2017

Advancing Vibrational Spectroscopy for Cellular and Sub Cellular Analysis: Raman Spectroscopy as a Novel In Vitro Nanotoxicological Assessment Protocol

Esen Efeoglu
Technological University Dublin

Advancing Vibrational Spectroscopy for Cellular and Sub Cellular Analysis: Raman Spectroscopy as a Novel *in vitro* Nanotoxicological Assessment Protocol

By

Esen Efeoglu

PhD Thesis

Supervisor

Prof. Hugh J. Byrne

Dr Alan Casey

FOCAS Research Institute
School of Physics
Dublin Institute of Technology
Kevin Street, Dublin 8

2017

Abstract

This work is designed to establish a 'High content Nanotoxicological Screening method' using *in vitro* Raman microspectroscopy. The undeniable increase of nanotechnology based products has brought challenges in terms of determining their toxicological properties. Considering the total time and cost of screening nanomaterials by conventional methods, the need for a rapid, label-free technique which will provide a wide range of information on multiple parameters is unquestionable.

This study investigated the applicability of Raman microspectroscopy as a High Content Screening technique to clarify cell-nanoparticle interaction by determining the localisation of the nanoparticles and consequent effects in these localised areas in terms of cyto- and geno- toxicity. For this purpose, in the first part of the study, the potential of Raman spectroscopy has been explored to monitor sequential trafficking of nanoparticles in cellular organelles and to determine the differing spectral signatures of the organelles. Human lung carcinoma cells (A549) were exposed to non-toxic carboxylate-modified and fluorescently-labelled polystyrene nanoparticles for 4, 12 and 24 hours and Raman spectral maps were acquired from the subcellular regions to determine their localisation. With the aid of multivariate analysis techniques, the study demonstrated the applicability of Raman microspectroscopy to provide information regarding localisation and to determine the local environment based on differing signatures of intracellular compartments such as endosomes, lysosomes and endoplasmic reticulum, in a completely label free manner.

Aminated polystyrene nanoparticles (PS-NH_2) and polyamidoamine (PAMAM) dendrimers are known to show acute toxicity and in order to observe this toxicity and corresponding responses, time and dose dependant Raman spectroscopic markers of

cellular toxic events were systematically monitored upon nanoparticle exposure to A549 cells. Alamar Blue (AB) and 3-(4,5-Dimethylthiazol-2-yl)-2,5diphenyltetrazoliumbromid (MTT) assays were employed to determine the mean effective concentration, EC_{50} and Raman spectroscopy was used to acquire multiple point spectra from the cytoplasm, nucleus and nucleolus. The most significant changes were observed in the cytoplasm for both time and dose dependent cases. The Raman spectral markers for lipidosis and oxidative stress were determined as a function of dose and time, and the responses were correlated with conventional cytotoxicity assays. With the aid of multivariate analysis techniques, the study showed the ability of Raman spectroscopy to provide information about cellular responses at different particle concentrations and exposure times.

Following this, the potential of Raman microspectroscopy was analysed by comparing spectral marker evolution in non-cancerous cells (immortalized human bronchial epithelium) with cancerous cells (A549 and human lung epidermoid). Spectral markers of oxidative stress, cytoplasmic RNA aberrations and liposomal rupture were identified and cell-line dependent variations in these spectral markers were observed, and were correlated with cellular assays and imaging techniques. The findings from the comparison of spectral markers, especially in the low wavenumber region, have shown the applicability of Raman spectroscopy to identify different cell death pathways in cancerous and non-cancerous cell lines.

Different cell death mechanisms were also identified based on common and/or differing spectral markers of cyto- and geno- toxicity upon PS-NH_2 and PAMAM exposure. The results were correlated with flow cytometry and cytotoxicity assays. The study further demonstrated the potential of Raman microspectroscopy to

differentiate apoptotic and necrotic cell death mechanisms, as a function of time (from 4 to 72 h) and applied dose (sub-lethal/lethal).

Finally, in order to establish a toxicological assessment protocol based on Raman microspectroscopy, 3D graphs of biomarker intensities are plotted as a function of time and dose and also intensities are correlated with % viability values. The established 3D models can be used to predict nanotoxicity, which can also be applied to nanomedicine.

Declaration

I certify that this thesis which I now submit for examination for the award Doctor of Philosophy (Ph.D), is entirely my own work and has not been taken from the work of others, save and to the extent that such work has been cited and acknowledged within the text of my work.

This thesis was prepared according to the regulations for postgraduate study by research of the Dublin Institute of Technology and has not been submitted in whole or in part for another award in any other third level institution. The work reported on in this thesis conforms to the principles and requirements of the DIT's guidelines for ethics in research.

DIT has permission to keep, lend or copy this thesis in whole or in part, on condition that any such use of the material of the thesis be duly acknowledged.

Signature _____ Date _____/_____/_____

Esen Efeoglu

Acknowledgements

I would like to take this opportunity to thank many people for their support and assistance through my project.

First of all, I would like to thank my supervisor, mentor, Prof. Dr. Hugh Byrne, for his support, incredible guidance, patience and encouragement throughout this project. He helped me to overcome all problems that I faced during the project. Moreover, he helped me to become much stronger whenever I needed motivation. I would also want to thank my supervisor Dr. Alan Casey for sharing his invaluable expertise since I started my study.

Also, I would like to express my great appreciation to FOCAS Research Institute and Dublin Institute of Technology and Science Foundation Ireland (SFI) for allowing me to carry out this study and provide an incredible work environment and facilities.

I would also like to thank Marcus Maher for his enormous help and endless support. When things went wrong he was the person who made me believe that everything is going to be great and who was there to celebrate every good moment! I would like to thank Mark Keating, Adrian Maguire and Franck Bonnier for their help whenever I needed a help during my data analysis. I also would like to thank my dearest friends Zeineb Farhane and Gabriele Dadalt Souto for their invaluable friendship, continuous support and understanding.

Last but not least, I would like to express my deepest gratitude to my family, Öner Efeoğlu and Zühal Efeoğlu, Eren Soyaltın, Utku Soyaltın and Deniz Soyaltın, for supporting me every stage of my life, their endless love and confidence in me.

Finally, I would like to say, since I started this project, these people and many others made me feel like home even though I'm 4000 km away. Thank you all!

List of Abbreviations

$O_2^{-\cdot}$	Superoxide anion
8-OHdG	8-hydroxy-2'-deoxyguanosine
A	Adenine
A549	Human lung adenocarcinoma cell line
AB	Alamar Blue
Abs	Absorption
AOP	Adverse Outcome Pathways
ATCC	American Type Culture Collection
BEAS-2B	Non-cancerous immortalized human bronchial epithelium
C	Cytosine
C_{60}	Fullerene
CaF_2	Calcium fluoride
Calu-1	Human lung epidermoid cells
carboxy-H_2DCFDA	6-carboxy-2',7'-dichlorodihydrofluorescein diacetate
CARS	Coherent anti Stokes Raman spectroscopy
CCD	Charge Coupled Device
CLS	Classical least squares
CLSM	Confocal Laser Scanning Microscopy
CNTs	Carbon nanotubes
CO_2	Carbondioxide
-COOH	Carboxyl group
DLS	Dynamic light scattering

DMEM F-12	Dulbecco's Modified Eagle Medium/F12
DMSO	Dimethyl sulfoxide
DNA	Deoxyribonucleic acid
EC	Effective concentration
ECACC	European Collection of Authenticated Cell Cultures
EM	Electron microscopy
Em	Emission
ER	Endoplasmic reticulum
EU	European Union
FBS	Foetal bovine serum
G	Guanine
h	Hour
H_2O_2	Hydrogen peroxide
HCA	High Content Analysis
HCS	High Content Screening
hMSCs	Human mesenchymal stem cells
$HO^{\cdot}$	Hydroxyl radicals
IF	Immunofluorescence
IR	Infrared
JACoP	Just Another Colocalisation Plugin
KMCA	K-means clustering Analysis
LDH	Lactate Dehydrogenase
MCR-ALS	Multivariate Curve Resolution Alternating Least Squares
MDA-MB-231	Human breast cancer cell line

MIE	Molecular initiating event
mL	Millilitre
MTS	(3-(4,5-dimethylthiazol-2-yl)-5-(3-carboxymethoxyphenyl)-2-(4-sulfophenyl)-2H-tetrazolium)
MTT	3-(4,5-Dimethylthiazol-2-yl)-2,5diphenyltetrazoliumbromid
MWCNTs	Multi-walled carbon nanotubes
N.A.	Numerical Aperture
NaCl	Sodium chloride
NADH	Nicotinamide adenine dinucleotide
NIR	Near Infrared
nm	Nanometer
NNLS	Non-negative least squares
NR	Neutral Red
OECD	Organisation for Economic Co-operation and Development
PAMAM	Polyamidoamine
PBS	Phosphate buffered saline
PCA	Principal components analysis
PCR	Polymerase chain reaction
PEG	Poly-ethylene glycol
Phe	Phenylalanine
PI	Propidium iodide
PLA	Poly-lactic acid
PLGA	Polylactic-co-glycolic acid
PLSR	Partial Least Squares Regression

PMT	Photomultiplier
PS	Polystyrene
PS-COOH	Carboxylated PSNPs
PS-NH_2	Aminated PSNPs
PSNPs	Polystyrene nanoparticles
RFP	Red Fluorescent Protein
RNA	Ribonucleic acid
ROS	Reactive Oxygen Species
RPMI-1640	Roswell Park Memorial Institute Medium
Saos-2	Human bone osteosarcoma cell line
SCC	Spectral cross correlation
SERS	Surface enhanced Raman spectroscopy
SiOH	Silanol
STM	Scanning Tunnelling Microscopy
SW-1353	Human chondro sarcoma cell line
SWCNTs	Single-walled carbon nanotubes
T	Thymine
TERS	Tip enhanced Raman spectroscopy
U	Uracil
WP	Work packages
WPMN	Working Party on Manufactured Nanomaterials
WST-1	(2-(2-methoxy-4-nitrophenyl)-3-(4-nitrophenyl)-5-(2,4-disulfophenyl)-2H-tetrazolium)

XTT	3-bis-(2-methoxy-4-nitro-5-sulfophenyl)-2H-tetrazolium-5-carboxanilide
YO-PRO-1	3-methyl-2-[{1-[3-(trimethylammonio)propyl]quinolin-4(1H)-ylidene}methyl]-1,3-benzoxazol-3-ium diiodide
μm	Micrometer
μM	Micromolar

Table of Contents

List of Tables

List of Figures

Figure 2.11. Schematic diagram of algorithm of K-means clustering.

Figure 3.1. Confocal Images of 40 nm carboxylated polystyrene nanoparticles (green) and lysosomes (red) of A549 cells after 24 hours (A) and 12 hours (C), confocal images of 40 nm carboxylated polystyrene nanoparticles (green) and endoplasmic reticulum (red) of A549 cells after 24 hours (B) and 12 hours (D) x60 magnification. Co-localisation is indicated by yellow/orange.

Figure 3.2. Confocal Images of 40 nm carboxylated polystyrene nanoparticles (green) and lysosomes (red) of A549 cells after 4 hours (A), confocal images of 40 nm carboxylated polystyrene nanoparticles (green) and early endosome stain (red) of A549 cells after 4 hours (B) x60 magnification. Co-localisation is indicated by yellow/orange.

Figure 3.3. **I**(A) Typical white-light microscope image of an A549 cell after 24 hour exposure. The selected area defined by the black line indicates the area selected for Raman mapping (B), Example of K-means reconstructed image from a Raman map on the selected area of an A549 cell including the polystyrene environment, polystyrene cluster and cytoplasm. **II);** Raman spectrum of raw polystyrene nanoparticle and mean spectrum calculated for the different clusters obtained after K-means clustering which correspond to polystyrene cluster (Cluster 6, pink) and polystyrene environment (Cluster 10, red). Grey shading is used as a guide for polystyrene related peaks in the mean spectra. Spectra are offset for clarity.

Figure 3.4. **I**(A), Scatter plot of the PCA of spectra corresponding to the KMCA clusters of polystyrene (pink) and polystyrene environment (red) for 24 hour particle exposure before PS subtraction. (B), Scatter plot of the PCA of spectra corresponding to polystyrene nanoparticles and polystyrene environment after raw polystyrene

spectrum subtracted for 24 hour particle exposure. **II);** Loading of PC1before (A) and after (B) polystyrene subtraction. In the loading of PC1 before PS subtraction, characteristic peaks of polystyrene are highlighted with grey and bands which can be attributed to the presence of nucleic acids, proteins and lipids were indicated with black circles (A). In the loading of PC1 of polystyrene cluster and polystyrene environment after PS subtraction, possible polystyrene residues are indicated with black circles and band assignments are made according to Table 3.3 (B). Spectra are offset for clarity. The dotted line represents the '0' line for each loading.

Figure 3.5. Mean spectra of PS environment cluster (Loading of PC1 ≥0) and PS cluster (Loading of PC1< 0) after PS subtraction for 24 hour exposure. Spectra are offset for clarity.

Figure 3.6. **I**(A) Typical white-light microscope image of an A549 cell after 12 hour exposure. The selected area defined by the black line indicates the area selected for Raman mapping (B), Example of K-means reconstructed image from a Raman map on the selected area of an A549 cell including the polystyrene environment, polystyrene cluster and cytoplasm and nucleus. **II);** Raman spectrum of raw polystyrene nanoparticle and mean spectrum calculated for the different clusters obtained after K-means clustering which correspond to polystyrene cluster (Cluster 5, brown) and polystyrene environment (Cluster 3, green). Grey shading is used as a guide for polystyrene related peaks in the mean spectra. Spectra are offset for clarity.

Figure 3.7. **I**(A), Scatter plot of the PCA of spectra corresponding to the polystyrene cluster (brown) and polystyrene environment (green) for 12 hour particle exposure before PS subtraction. (B), Scatter plot of the PCA of spectra corresponding to the polystyrene cluster and polystyrene environment for 12 hour particle exposure,

after subtraction of the raw polystyrene spectrum. **II);** Loading of PC1 before (A) and after (B) polystyrene subtraction. In the loading of PC 1 before subtraction, characteristic peaks of polystyrene are highlighted with grey and bands which can be attributed to presence of proteins and lipids were indicated with black circles (A). In the loading of PC1 after PS subtraction, possible polystyrene residues are indicated with black circles and band assignments are made according to Table 3.4 (B). Spectra are offset for clarity. The dotted line represents the '0' line for each loading.

Figure 3.8. Mean spectra of PS environment cluster (Loading of PC1 ≥0, red), PS cluster (Loading of PC 1< 0, blue) after PS subtraction for 12 hour exposure and spectrum of cytoplasm (black). Spectra are offset for clarity.

Figure 3.9. **I**(A) Typical white-light microscope image of an A549 cell after 4 hour exposure. The selected area defined by the black line indicates the area selected for Raman mapping (B), Example of K-means reconstructed image from a Raman map on the selected area of an A549 cell including the polystyrene environment, polystyrene cluster and cytoplasm, nucleus and substrate. **II);** Raman spectrum of raw polystyrene nanoparticle and mean spectrum calculated for the different clusters obtained after K-means clustering which correspond to polystyrene cluster (Cluster 8, light blue) and polystyrene environment (Cluster 4, dark blue). Grey shading is used as a guide for polystyrene related peaks in the mean spectra. '*' used as an indicator of polystyrene features in the polystyrene cluster. Spectra are offset for clarity.

Figure 3.10. (A), Scatter plot of the PCA of spectra corresponding to the polystyrene cluster (Cluster 8, light blue) and polystyrene environment (Cluster 4, dark blue) for 4 hour particle exposure, before PS subtraction (B), Loading of PC1 and PC2 before PS subtraction.

Figure 3.11. (A), Scatter plot of the PCA of spectra corresponding to the polystyrene cluster for 4 hour particle exposure (B), PC loadings of polystyrene cluster (C), Scatter plot of the PCA of spectra corresponding to the polystyrene cluster after polystyrene subtraction for 4 hour particle exposure (D), PC loadings of polystyrene subtracted polystyrene cluster. Spectra are offset for clarity. The dotted line represents the '0' line for each loading.

Figure 3.12. Mean spectra of cytoplasm (Loading of PC1 ≥0, red), early endosome (Loading of PC 1< 0, blue) after PC subtraction for 4 hour exposure and difference between mean spectra of cytoplasm and early endosome (green). Spectra are offset for clarity.

Figure 3.13. I; Comparison of mean spectra of 4, 12 and 24 hour nanoparticle exposure data sets. **II;** Comparison of PCA loadings of 4, 12 and 24 hour nanoparticle exposure data sets. The loadings of PC1 are used for 24 (Figure 3.4) and 12 hour (Figure 3.7) data sets while the loading of PC2 is used for the 4 hour data set (Figure 3.11). The main indicator bands for the different exposure time data sets were assigned according to Tables 3.3, 3.4 and 3.5. Spectra are offset for clarity. The dotted line represents the '0' line for each loading.

Figure 3.S1 Cytotoxicity of 40 nm carboxlylated polystyrene nanoparticles after 24, 48, 72 and 96 hour exposures determined by the Alamar Blue (A) and MTT assay (B). Data are expressed as % of control mean ± SD of three independent experiments. Negative control (NC): A549 cells; Positive control (PC): 10% Dimethyl sulfoxide (DMSO) 90 % media.

Figure 3.S2 (A), Scatter plot of the PCA of spectra correspond to polystyrene nanoparticles and their environment after raw polystyrene spectrum subtracted for 24

hour particle exposure, same colours with K-means maps were used to identify scatter plots, (B) PC loading of polystyrene nanoparticles and polystyrene subtracted environment. The characteristic peaks of polystyrene were indicated with black circles in Loading 1.

Figure 3.S3 (A), Scatter plot of the PCA of spectra correspond to polystyrene nanoparticles and their environment after raw polystyrene spectrum subtracted for 12 hour particle exposure, same colours with K-means maps were used to identify scatter plots, (B) PC loading of polystyrene nanoparticles and polystyrene subtracted environment. The characteristic peaks of polystyrene were indicated with black circles in Loading 1.

Figure 3.S4 (A), Scatter plot of the PCA of spectra correspond to polystyrene nanoparticles and their environment after raw polystyrene spectrum subtracted for 4 hour particle exposure, same colours with K-means maps were used to identify scatter plots, (B) PC loading of polystyrene nanoparticles and polystyrene subtracted environment. The characteristic peaks of polystyrene were indicated with black circles in Loading 1.

Figure 4.1. **I)** Cytotoxicity of 40 nm amine-modified polystyrene nanoparticles (PS-NH_2) after 4, 12, 24 and 48 hour exposures determined by the Alamar Blue assay. **II)** Cytotoxicity of 40 nm amine-modified polystyrene nanoparticles (PS-NH_2) after 8 exposure determined by the Alamar Blue and MTT assays. The concentrations (2.5, 5 and 10 μM) which are used throughout the study are indicated by red dashed lines. Data are expressed as % of control mean ± SD of three independent experiments.

Figure 4.2. **I)** Scatter plot of the PCA of spectra corresponding to cytoplasm, nucleus and nucleolus of the (8hour) unexposed and PS-NH_2 exposed cells for 10 μM

concentration of nanoparticles. Different cellular regions are coded as follows; red for cytoplasm, green for nucleus and blue for nucleolus. Exposed and unexposed cells are indicated by open circles and closed circles, respectively. **II)** First 2 loadings of PC analysis; loadings are offset for clarity and the dotted line represents the zero '0' point for each loading. In loading 1, notable bands which are used to differentiate the nuclear region from cytoplasm are indicated by black dashed outlines.

Figure 4.3. Mean difference spectra of cytoplasm (red), nucleus (green) and nucleolus (blue) obtained by subtraction of mean spectra of 8 hour PS-NH_2 exposed cells from mean spectra of unexposed cells. The spectra are offset for clarity, the dashed line indicating the zero point. The bands related to PS are indicated with grey highlights.

Figure 4.4. **I)** Scatter plot of the PCA of spectra corresponding to cytoplasm of the unexposed cells (closed circles) and cells exposed to 10 μM PS-NH_2 for 8 hour (open diamond). **II)** Loadings of PC1 for pairwise analysis of cytoplasm of exposed cells with the control for 10 μM (red), 5 μM (blue) and 2.5 μM (black) for 8 hour. The dotted line represents the zero '0' point for each loading. Loadings are offset for clarity.

Figure 4.5. **I)** Scatter plot of the PCA of spectra corresponding to cytoplasm of the unexposed cells (close circles) and PS-NH_2 exposed cells (2.5 μM) (open circles) for 24 hour, **II)** Comparison of the Loading of PC1s for different PS-NH_2 concentrations (cytoplasm). 4, 8, 12, 24 and 48 hour are indicated with black, blue, green, red and magenta, respectively. Positive features of the PCs are related to exposed cells while negative features of the PCs are related to their controls. Loadings are offset for clarity. The dotted line represents the zero '0' point for each loading.

Figure 4.6. Comparison of the changes in the Amide I region of loading 1 for 4 (I), 8 (II), 12 (III), 24 (IV) and 48 (V) hrs. The loadings and sum of the bands after fitting are indicated with blue and red lines, respectively. Each individual fitted band is represented by black lines. Peak positions are indicated on the top of the fitted figures.

Figure 4.7. Comparison of the Loading 1 of PCs of cytoplasm for exposed and unexposed cells after 8 hour exposure to 10 μM (red) and 48 hour 2.5 μM (blue) PS-NH_2. Positive and negative features of the loadings relate to exposed and unexposed cells, relatively. The significant differences between the loadings are indicated with black circles. Loadings are offset for clarity. The dotted line represents the zero '0' point for each loading.

Figure 4.8. Difference spectrum of nucleus of PS-NH_2 exposed cells and unexposed cells obtained by subtraction of mean spectra of 24 hour PS-NH_2 exposed cells from mean spectra of unexposed cells.

Figure 4.S1. Mean spectra of different cellular regions of unexposed cells. Nucleolus, nucleus and cytoplasm are indicated by blue, green and red, respectively. The differences in molecular composition (nucleic acids, proteins and lipids) of the regions are highlighted.

Figure 4.S2. Mean spectra of cytoplasm of exposed cells (blue) and unexposed cells (red). The 785 and 810 cm^{-1} region is indicated with dashed outline.

Figure 4.S3. Scatter plot of the PCA of spectra corresponding to cytoplasm of the unexposed cells (control) and cells exposed to PS-NH_2 for 8hr. The code for different concentrations from 2.5 to 10 μM (I-III) is, rectangle (I), square (II) and diamond (III), respectively. Unexposed cells and exposed cells are indicated by close circles and open circles, respectively.

Figure 4.S4. Raman intensities of the 785 cm^{-1} (blue) and 810 cm^{-1} (red) bands as a function of dose.

Figure 4.S5. Scatter plot of the PCA of spectra corresponding to cytoplasm of the unexposed cells (control) and PS-NH_2 exposed cells. The colour code for different exposure times from 4 to 48 (I-V) h is, black (I), blue (II), green (III), red (IV) and magenta (V), respectively. Unexposed cells and exposed cells are indicated by close circles and open circles, respectively.

Figure 5.1. Cytotoxicity of 100 nm amine-modified polystyrene nanoparticles (PS-NH_2) after 24 h (A and B), 48 h (C and D) and 72 h (E and F) exposures, as determined by the Alamar Blue (A, C and E) and MTT (B, D and F) assay, for A549, Calu-1 and BEAS-2B cell lines. The concentration range between 20 to 0.15 μM is used throughout the study. Data are expressed as % of control mean ± SD of three independent experiments.

Figure 5.2. CLSM images of BEAS-2B cells and BEAS-2B cells exposed to 100 nm aminated polystyrene nanoparticles (indicated with green fluorescent) from 24 to 72 hours.x60 magnification.

Figure 5.3. Loadings of the first component of PCA (PC1), each exposure time is indicated by a colour from 24 hour to 72 h as following; blue, red and black. The positive side of the loadings represents the spectral features of the particle exposed cells (0.6 μM of PS-NH_2), while the negative side represents the control cells for each loading. Loadings are offset for clarity and the dotted line represents the zero '0' point for each loading. The changing features with extended particle exposure times are indicated with black dashed area.

Figure 5.4. First loadings of PCA of cytoplasm of control and 72 hour particle exposed cells for BEAS-2B, A549 and Calu-1 cell lines, respectively; loadings are offset for clarity and the dotted line represents the zero '0' point for each loading. Positive side of the loadings (PC>0) represents the spectral features of the particle exposed cells, while the negative side (PC<0) represents the control cells for each loading. The areas with changing features between cell lines are indicated with dashed lines.

Figure 5.5. % of Reactive oxygen species (ROS) generation compared to controls for A549, Calu-1 and BEAS-2B cell line after 1, 2, 3, 4, 6 and 24 h PS-NH_2 exposure. The concentrations used for BEAS-2B, Calu-1 and A549 are 0.6, 1 and 2.5 μM, respectively.

Figure 5.6. Comparison of the first loadings of PCA of cytoplasm of control and particle exposed A549 (A) and Calu-1 (B) cell lines after 24, 48 and 72 hour particle exposure; loadings are offset for clarity and the dotted line represents the zero '0' point for each loading. The positive side of the loadings represents the spectral features of the particle exposed cells, while the negative side represents the control cells for each loading. The changing features between cell lines are indicated with dashed lines.

Figure 5.7. Changes in lysosomal protonation measured by Lysosensor activity in A549 (A), Calu-1 (B) and BEAS-2B (C) cell lines.

Figure 5.8. Schematic representation of different cell death pathways for A549, Calu-1 and BEAS-2B cell lines. Pathway for BEAS-2B cell line is indicated with red arrows, when A549 and Calu-1 is represented with black arrows.

Figure 5.S1. Scatter plot of the PCA of spectra corresponding to cytoplasm of unexposed cells (control) and PS-NH_2 exposed BEAS-2B cells after 24 (A), 48 (B) and 72 (C) h exposure. Unexposed cells and exposed cells are indicated with closed circles and open circles, respectively. '0' line for PC1 is indicated by black dashed outlines.

Figure 5.S2. Scatter plot of the PCA of spectra corresponding to cytoplasm cells of the unexposed cells (control) and PS-NH_2 exposed A549 (A), Calu-1 (B) cells after 72 h exposure. Unexposed cells and exposed cells are indicated with closed circles and open circles, respectively. '0' line for PC1 is indicated by black dashed outlines.

Figure 5.S3. Scatter plot of the PCA of spectra corresponding to cytoplasm cells of the unexposed cells (control) and PS-NH_2 exposed A549 and Calu-1 cells for 24 h exposure. Unexposed cells and exposed cells are indicated with close circles and open circles, respectively.

Figure 5.S4. White-light images of A549 cells (unexposed) after 48 (A) and 72 (B) h. x60 magnification. Vesicle formation is indicated with black arrows.

Figure 5.S5. CLSM images of A549 (A), Calu-1 (B) and BEAS-2B (C) cells exposed to 2.5, 1 and 0.6 μM of PS-NH_2 after 24 h with x60 magnification. Green fluorescent indicates the PS-NH_2.

Figure 6.1. Cytotoxicity of generation 5 polyamidoamine (PAMAM-G5) dendrimers after 24, 48 and 72 h exposures determined by the Alamar Blue (A) and MTT assays (B). Data are expressed as % of control mean ± SD of three independent experiments.

Figure 6.2. Loadings of PC1 for pairwise analysis of cytoplasm of exposed cells (EC_n) and corresponding control after 24 h PAMAM-G5 exposure. The negative side of the loading represents the spectral features of control, whereas positive side represents the cells exposed to PAMAM-G5. Loadings are offset for clarity and zero '0' line for each dose is indicated with black dashes. The progressive changes in the loadings are indicated with grey highlights and corresponding band assignments are provided on top of the highlights.

Figure 6.3. Loadings of PC1 for pairwise analysis of cytoplasm of exposed cells and corresponding control from 4 to 72 h PAMAM-G5 (EC_{25}) exposure. The negative side of the loading represents the spectral features of control, whereas positive side represents the cells exposed to PAMAM-G5. Loadings are offset for clarity and the zero '0' line for each dose is indicated with black dashes. The progressive changes in the loadings are indicated with grey highlights and corresponding band assignments are provided on top of the highlights.

Figure 6.4. Loadings of PC1 for pairwise analysis of nucleus of exposed cells and corresponding control from 4 to 72 h PAMAM-G5 (EC_{25}) exposure. The negative side of the loading represents the spectral features of control, whereas positive side represents the cells exposed to PAMAM-G5. Loadings are offset for clarity and the zero '0' line for each dose is indicated with black dashes. The progressive changes in the loadings are indicated with grey highlights and corresponding band assignments are provided on top of the highlights.

Figure 6.5. A) Comparison of time dependant changes on the band intensities of 728 and 756 cm^{-1} bands calculated from pairwise PCA of nucleus of exposed cells and corresponding control, B) Comparison of dose dependant changes on the band

intensities of 728 and 756 cm^{-1} bands calculated from pairwise PCA of nucleus of PAMAM exposed cells and corresponding control, in A and B error bars indicate ± SD of the band intensities, C) Loadings of PC1 for pairwise analysis of nucleus of exposed cells and corresponding control after 24h PAMAM-G5 exposure. The negative side of the loading represents the spectral features of control, whereas positive side represents the cells exposed to PAMAM-G5. Loadings are offset for clarity and zero '0' line is indicated with black dashes. The progressive changes in the loadings are indicated with grey highlights and corresponding band assignments are provided on top of the highlights.

Figure 6.6. **A)** Loadings of PC1 for pairwise analysis of nucleolus of exposed cells and corresponding control after 24 h PAMAM-G5 exposure. B) Loadings of PC1 for pairwise analysis of cytoplasm of exposed cells and corresponding control from 4 to 72 h PAMAM-G5 exposure. The negative side of the loading represents the spectral features of control, whereas positive side represents the cells exposed to PAMAM-G5. Loadings are offset for clarity and zero '0' line is indicated with black dashes. The progressive changes in the loadings are indicated with grey highlights and corresponding band assignments are provided on top of the highlights.

Figure 6.S1. Mean spectra of cytoplasm from control cells and exposed cells (PAMAM dendrimers) as a function of dose (24 hour exposure to EC_{75}) and time (72 hour exposure to EC_{25}).

Figure 6.S2. Mean spectra of nucleus from control cells and exposed cells (PAMAM dendrimers) as a function of dose (24 hour exposure to EC_{75}) and time (72 hour exposure to EC_{25}).

Figure 6.S3. Mean spectra of nucleolus from control cells and exposed cells (PAMAM dendrimers) as a function of dose (24 hour exposure to EC_{75}) and time (72 hour exposure to EC_{25}).

Figure 6.S4. Scatter plots of the PCA of spectra corresponding to cytoplasm of A549 cells (control) and A549 cells exposed to the EC_{10} (A), EC_{25} (B), EC_{50} (C) and EC_{75} (D) concentrations of PAMAM-G5 dendrimers after 24 h. Each graph indicates a pairwise comparison of exposed cells with corresponding control for 24 hour. Unexposed cells and exposed cells are indicated with closed circles and open circles, respectively. '0' line for PC1 is indicated by black dashed outlines.

Figure 6.S5. Scatter plot of the PCA of spectra corresponding to cytoplasm of A549 cells (control) and A549 cells exposed to the EC_{25} concentration of PAMAM-G5 dendrimers after 4 (A), 8 (B), 24 (C), 48 (D) and 72 hour. Each graph indicates a pairwise comparison of exposed cells with corresponding control for extending exposure times. Unexposed cells and exposed cells are indicated with closed circles and open circles, respectively. '0' line for PC1 is indicated by black dashed outlines.

Figure 6.S6. Scatter plot of the PCA of spectra corresponding to nucleus of A549 cells (control) and A549 cells exposed to the EC_{25} concentration of PAMAM-G5 dendrimers after 4 (A), 8 (B), 24 (C), 48 (D) and 72 (E) hour. Each graph indicates a pairwise comparison of exposed cells with corresponding control for extending exposure times. Unexposed cells and exposed cells are indicated with closed circles and open circles, respectively. '0' line for PC1 is indicated by black dashed outlines.

Figure 6.S7. Band intensities of 785 (nucleic acids) and 810 (RNA) cm^{-1} bands calculated from PC1 from pairwise PCA of nucleus of PAMAM-G5 exposed cells and corresponding controls from 4 to 72 h.

Figure 6.S8. Band intensities of 785 (nucleic acids) and 810 (RNA) cm^{-1} bands calculated from PC1 from pairwise PCA of nucleus of exposed cells and corresponding controls.

Figure 6.S9. Scatter plots of the PCA of spectra corresponding to nucleolus of A549 cells (control) and A549 cells exposed to the EC_{10} (A), EC_{25} (B), EC_{50} (C) and EC_{75} (D) concentrations of PAMAM-G5 dendrimers after 24 h. Each graph indicates a pairwise comparison of exposed cells with corresponding control for 24 hour. Unexposed cells and exposed cells are indicated with closed circles and open circles, respectively. '0' line for PC1 is indicated by black dashed outlines.

Figure 6.S10. Scatter plot of the PCA of spectra corresponding to nucleolus of A549 cells (control) and A549 cells exposed to the EC_{25} concentration of PAMAM-G5 after 4 (A), 8 (B), 24 (C), 48 (D) and 72 (E) hour. Each graph indicates a pairwise comparison of exposed cells with corresponding control for extending exposure times. Unexposed cells and exposed cells are indicated with closed circles and open circles, respectively. '0' line for PC1 is indicated by black dashed outlines.

Figure 7.1. Cytotoxicity of generation 5 polyamidoamine (PAMAM-G5) dendrimers and amine-modified polystyrene nanoparticles (PS-NH_2) after 24, 48 and 72 h exposures determined by the Alamar Blue and MTT assays. Data are expressed as % of control mean ± SD of three independent experiments.

Figure 7.2. Comparison of PC1 obtained from pairwise PCA of cytoplasm of exposed cells and corresponding control for 4(A), 8(B), 24(C), 48(D) and 72 (E) h PS-NH_2 (Blue) and PAMAM-G5 (Black) exposure. The negative side of the loading represents the spectral features of control, whereas positive side represents the cells exposed to PS-NH_2 and PAMAM-G5. Loadings are offset for clarity and the zero '0'

line is indicated with black dashes. The progressive changes in the loadings are indicated with grey highlights.

Figure 7.3. Comparison of Band intensities of 785 (nucleic acids), 810 (RNA), 1003 (Phenylalanine) and 1438 (Lipids) cm^{-1} bands calculated from PC1 from pairwise PCA of cytoplasm of exposed cells (EC_{25}) and corresponding controls. The changes in the band intensities for PS-NH_2 and PAMAM-G5 exposure are indicated with blue and red lines, respectively. Data are expressed as % of control mean ± SD.

Figure 7.4. Comparison of PC1 obtained from pairwise PCA of nucleus of exposed cells and corresponding control for 4, 8, 24, 48 and 72 h PAMAM-G5 (A) and PS-NH_2 (B) exposure. The negative side of the loading represents the spectral features of control, whereas positive side represents the cells exposed to PS-NH_2 and PAMAM-G5. Loadings are offset for clarity and the zero '0' line is indicated with black dashes. The progressive changes in the loadings are indicated with black dashes.

Figure 7.5. Representation of the percentage of cells in different cell death processes upon PAMAM-G5 and PS-NH_2 exposure. Live, apoptotic and necrotic cells were indicated with blue, red and green, respectively. Cells are exposed to 4 different concentrations of the nanomaterials for 24 h. A549 cells without exposure are used as control.

Figure 7.6. Comparison of Band intensities of 785 (nucleic acids), 810 (RNA), 1000 (Phenylalanine) and 1438 (Lipids) cm^{-1} bands calculated from PC1 from pairwise PCA of nucleus of exposed cells and corresponding control for The changes in the band intensities for PS-NH_2 and PAMAM-G5 exposure are indicated with blue and red lines, respectively. Data are expressed as % of control mean ± SD.

Figure 7.S1. Scatter plot of the PCA of spectra corresponding to cytoplasm of A549 cells (control) and A549 cells exposed to the EC_{25} concentration of PAMAM-G5 dendrimers after 4 (A), 8 (B), 24 (C), 48 (D) and 72 (E) hour. Unexposed cells and exposed cells are indicated with closed circles and open circles, respectively. The zero '0' line for PC1 is indicated by black dashes.

Figure 7.S2. Scatter plot of the PCA of spectra corresponding to cytoplasm of A549 cells (control) and A549 cells exposed to the EC_{25} concentration of PS-NH_2 after 4 (A), 8 (B), 24 (C), 48 (D) and 72 (E) hour. Unexposed cells and exposed cells are indicated with closed circles and open circles, respectively. The zero '0' line for PC1 is indicated by black dashes.

Figure 7.S3. Scatter plot of the PCA of spectra corresponding to nucleus of A549 cells (control) and A549 cells exposed to the EC_{25} concentration of PAMAM-G5 dendrimers after 4 (A), 8 (B), 24 (C), 48 (D) and 72 (E) hour. Unexposed cells and exposed cells are indicated with closed circles and open circles, respectively. The zero '0' line for PC1 is indicated by black dashes.

Figure 7.S4. Scatter plot of the PCA of spectra corresponding to nucleus of A549 cells (control) and A549 cells exposed to the EC_{25} concentration of PS-NH_2 after 4 (A), 8 (B), 24 (C), 48 (D) and 72 (E) hour. Unexposed cells and exposed cells are indicated with closed circles and open circles, respectively. The zero '0' line for PC1 is indicated by black dashes.

Figure 8.1. Comparison of PCA loadings of 4, 12 and 24 hour nanoparticle exposure data sets. Loadings are offset for clarity. The dotted line represents the zero '0' point for each loading and intensity scale of 0±0.1 is used for comparison. The figure is adapted from a published paper (Efeoglu *et al.* 2015).

Figure 8.2. Spectral Markers of acute toxic response in cytoplasm of A549 and Calu-1 cells after 24 hour exposure to PS-NH_2 and PAMAM nanoparticles. Positive and negative features of the loadings relate to exposed and unexposed cells, relatively. The 750-830 cm^{-1} and above 1000 cm^{-1} region are indicated with highlights. Loadings are offset for clarity. The dotted line represents the zero '0' point for each loading and intensity scale of 0±0.05 is used for comparison.

Figure 8.3. The schematic illustration of different cell death pathways on cancerous and non-cancerous cell lines and Raman spectral markers which are used to identify cell death pathways. Loadings are offset for clarity. The dotted line represents the zero '0' point for each loading and intensity scale of 0±0.05 is used for comparison (Efeoglu *et al.* 2017) .

Figure 8.4. Spectral marker profiles of apoptotic and necrotic cell death. Comparison of Band intensities of 1003 (Phenylalanine) (A) and 1438 (Lipids) (B) cm^{-1} bands calculated from PC1 from pairwise PCA of nucleus of exposed cells and corresponding control. Comparison of PC1 obtained from pairwise PCA of nucleus of exposed cells and corresponding control for 4, 8, 24, 48 and 72 h PAMAM-G5 (C) and PS-NH2 (D) exposure. The changes in the band intensities for PS-NH_2 and PAMAM-G5 exposure are indicated with blue and red lines, respectively. Data are expressed as % of control mean ± SD. The negative side of the loading represents the spectral features of control, whereas positive side represents the cells exposed to PS-NH_2 and PAMAM-G5. Loadings are offset for clarity. The dotted line represents the zero '0' point for each loading and intensity scale of 0±0.05 is used for comparison.

Figure 8.5. Comparisons of the loading 1 of PCA of cytoplasm for exposed and control cells. (A) After 8 h exposure to 10 μM (red) and 48 h 2.5 μM (blue) PS-NH_2.

(B) After 8 h exposure to EC_{25} (red) and 24 h EC_{10} μM (blue) PAMAM dendrimers. Positive and negative features of the loadings relate to exposed and control cells, relatively. The areas that show similar responses are indicated with highlights. Loadings are offset for clarity. The dotted line represents the zero '0' point for each loading and intensity scale of 0±005 is used for comparison.

Figure 8.6. Comparison of the loading 1 of PCs of cytoplasm, nucleus and nucleolus for exposed and unexposed cells after 8 h exposure to EC_{25} (red) and 24 h EC_{10} (blue) PAMAM dendrimers. Positive and negative features of the loadings relate to exposed and unexposed cells, relatively. The 750-830 cm^{-1} area is indicated with highlights. Loadings are offset for clarity. The dotted line represents the zero '0' point for each loading and intensity scale of 0±0.05 is used for comparison.

Figure 8.7. 3D mesh and contour plot of 785 (A, B) and 810 cm^{-1} (C, D) spectral marker intensity as a function of time (hour) and dose (EC_n). The 24 hour cellular viability at EC_{10}, EC_{25}, EC_{50} and EC_{75} determined by AB assay are indicated with percentages on the plot (white text).

Figure 8.8. 3D mesh plots representing the response of (A) Simulated model of Reactive oxygen species (B) 810 cm^{-1} spectral marker intensity (A) is adapted from Maher *et al.* (Maher *et al.* 2014)

Figure 8.9. 3D mesh and contour plot 1003 (A and B) and 1438 (C and D) cm^{-1}spectral marker intensity as a function of time and dose. The cellular viability at EC_{10}, EC_{25}, EC_{50} and EC_{75} are indicated with percentages on the plot (white text).

CHAPTER 1

Introduction

1.1. Introduction

Huge interest and accelerated research on nanoscience and nanotechnologies has brought nano-scale engineered products into our lives. Developments in visualisation, imaging and characterisation techniques have also provided more detailed information on naturally occurring nano-scale systems such as enzymes, protein complexes and manufactured nano-scale materials. Nano-scale materials have quickly found their place in different areas, from pharmacological science and medicine, to the cosmetics and textile industries. However, the concomitant increase of the possibility of exposure of humans to engineered nanomaterials has given rise to concerns over their potential health effects. The emergent field of Nanotoxicology addresses possible exposure routes, uptake and trafficking within cells. The understanding of the mechanism of action of nanomaterials in the human system and possible responses of the cells upon exposure to nanomaterials can also allow the developments of new application areas such as disease treatments and controlled drug delivery. In order to investigate the toxicity of nano-engineered or naturally formed nanomaterials, the Organisation for Economic Co-operation and Development (OECD) recommends generally known and common used protocols for nanotoxicological assessment such as cell viability tests (MTT, Neutral Red, Alamar Blue). However, direct visualisation of the nanomaterials within cells, and the resultant cellular responses remains a challenge.

Raman spectroscopy, as a vibrational spectroscopic technique, provides fingerprint information for chemical or biochemical structures. Also, the easy sample preparation, narrow spectral bandwidth and minimal influence from the water in the nature of

biological samples and the label free nature of technique have made the technique powerful for biological applications.

Therefore, in this thesis, the applicability of Raman spectroscopy to determine the cell-nanomaterial interaction in terms of particle localisation, possible trafficking routes and cellular responses is investigated, towards an ultimate aim of developing a nanotoxicological screening method and demonstrating the potential of Raman spectroscopic imaging as a truly label free, high content analysis technique, by establishing the spectroscopic signatures of nanoparticle localisation with identification of subcellular organelles and spectral markers of cyto-and geno- toxic events which lead to cell death.

1.2. Background

The term ‘Nanotechnology’ is derived from the words ‘nano’ and ‘technology’. The word ‘nano’ comes from Greek word ‘dwarf’ and it indicates 10^{-9}m as an operational scale for nanotechnology. Technology is aimed to generate goods or to perform functions that have benefit to human welfare. With the combination of the words, nanotechnology can be defined as a multidisciplinary scientific discipline which involves the manipulation of materials with a scale smaller than 100 nm to perform functions which benefit human life. It includes the design, production, characterization and application of matter and processes. It comprises many areas of science from engineering to life sciences. Although the concept of nanotechnology is considered to be new, human beings have been using nanostructures since the 4th and 5th century B.C.. The Lycurgus Cup (Freestone *et al.* 2007) and Damascus Steel that contain gold

colloids (Daniel & Astruc 2004) and nanowires and carbon nanotubes (CNTs) (Reibold *et al.* 2006), respectively, can be considered among the first products of nanotechnology.

In 1959, Richard Feynman first referred to the concept of nanoscience at his talk 'There's plenty of room at the bottom' (Feynman 1992). He suggested that materials can be manipulated at an atomic level, and this could lead to the formation of new structures with extraordinary properties. Such materials could have properties which extend beyond classical physics laws such as gravity and surface tension. On the other hand, weak interactions such as van der Waals forces become important for the manipulated material (Feynman 1992). 15 years later, the term nanotechnology was firstly used by Japanese scientist Norio Taniguchi and it was defined as 'production technology to get the extra high accuracy and ultrafine dimensions, i.e., the preciseness and fineness on the order of 1 nm (nanometre), 10^{-9} meter in length' (Taniguchi 1974). In the following period, the invention of more developed microscopy systems such as Scanning Tunnelling Microscopy (STM) in 1981 and the discovery of new structures like fullerenes and CNTs accelerated the development of nanotechnology. In 1986, K. Eric Drexler in his book 'Engines of Creation: The Coming Era of Nanotechnology' suggested a nanoscale "replicating assembler" which would be able to copy itself and of other structures of random complexity (Drexler 1986). In recent years, the term 'Nanobiotechnology' developed rapidly with the merger of the nanotechnology studies with the life sciences. Thus, 'Nanobiotechnology' can be defined as the use of nanomaterials and the application of them to biomolecules or biomolecular structures, living cells or microorganisms to characterize and identify biological structures and address on-going health issues.

The importance of the combination of biological sciences with physical sciences is beyond question. The materials and techniques developed based on the combination of these areas have a high impact on different areas from medicine to biotechnology. When the biological cell, as an essential element of life, is considered, it seems to be completely compatible to the nanotechnology concept. Cells consist of molecules and molecular structures- functional nanoscale machines. Cells can be considered as the most advanced nano-machine, due to their function in regulating and controlling biological systems, and the understanding of cells is one of the great challenges in science (Whitesides 2005). A eukaryotic cell can be defined as a structure in which many complex vital activities and biochemical reactions are carried out in an approximately 10 μm diameter three dimensional space that is bounded by a cell membrane. Each organelle within the cell performs a specific task and these are formed by the organization of many biological macromolecules which act as small nanomachines. When the extraordinary properties of materials on the nanoscale in nature are considered, it is not an exaggeration to assume that new structures and materials as well as tools with superior properties are waiting to be explored. Although there is still a vast array of concepts to be discovered, nanoscience holds great promise in the area of medicine. The emerging area 'Nanomedicine,' a combination of nanotechnology and medicine, deals with the use of nanomaterials and technology for the detection, diagnosis and treatment of diseases in a personalized platform. Engineered nanomaterials and tools can be used as screening and imaging agents, targeted drug delivery systems or regenerative medicines (Chen *et al.* 2005; Cui *et al.* 2008; Kumar *et al.* 2007; Pan *et al.* 2008; Weng *et al.* 2008). It is also possible to use them in tissue engineering (A Ito & Kamihira 2011). New contrast agents with improved quality can be used to detect problems in the human body at earlier stages

(Hahn *et al.* 2011). Moreover, tailored nanoparticles can be powerful tools to treat diseases with a minimum effect on healthy cells using targeting or controlled release of drugs (Ghosh *et al.* 2008).

The nanoparticles that are used in nanomedicine can be divided into different groups as follows: polymeric nanoparticles, metal nanoparticles, metal oxide nanoparticles, liposomes, dendrimers, quantum dots, viral nanoparticles, carbon nanotubes. Among these nanostructures, polymeric nanoparticles, both individually and as a coating, have been widely investigated for medical applications from diagnosis to drug delivery applications (Storrie & Mooney 2006). Due to the biodegradable nature of polylactic-co-glycolic acid (PLGA) and poly-lactic acid (PLA) polymers, they have been investigated and found highly useful in drug delivery studies (F Ito *et al.* 2008; Naha *et al.* 2008; Naha, Kanchan, & Panda 2008). Moreover, polymers have been used as coatings on the surface of liposomes, metal and metal oxide nanoparticles to improve biocompatibility and blood circulation (Dobrovolskaia & McNeil 2007). Poly-ethylene glycol (PEG) coated gold nanoparticles are also useful as imaging probes for *in vivo* biomedical applications (Kim *et al.* 2007). Metal and metal oxide nanoparticles and nanocomposites have also been investigated in drug delivery studies. In addition to drug delivery studies, they have been used in the detection, identification and differentiation of cell types (as diseased and not diseased) by using spectroscopic techniques, due to their optical and electronical properties. These nanoparticles are readily uptaken by cells because of their size and functionalisation of nanoparticles with dyes makes them visible for intracellular tracking (El-Sayed, Huang, & El-Sayed 2006; Sokolov *et al.* 2003).

Although nanostructures and nanostructured tools are applicable for medicine, challenges remain, such as blood circulation time and targeting efficiency. Furthermore, despite the undeniable potential of these particles, their toxicity is still a big challenge which has restricted their widespread use in medicine and has created the subcategory of toxicology, known as 'Nanotoxicology' (Oberdörster *et al.* 2005). Nanotoxicology mainly deals with the potential risks and adverse health effects that can be arise from their use and aims to achieve safe deployment of nanotechnologies (Donaldson *et al.* 2004). In this sense, Nanotoxicology deals with the potential toxic effect of nanomaterials or nanostructured materials which are not seen or rarely seen in macro or larger particles. Nanotoxicology involves different aspects in itself. Physicochemical properties of nanoparticles such as the size and the shape of nanoparticles, surface area and surface chemistry determine the potential risk of the material. Besides physicochemical determinants, molecular determinants can be considered as a different aspect of nanotoxicology. Nanoparticles may induce the formation of Reactive Oxygen Species (ROS) and expression of inflammatory markers (Curtis *et al.* 2006; Kabanov 2006). The production of ROS, due to their high chemical activity, can cause destruction of DNA, carbohydrates, proteins and lipids. The destruction of DNA and proteins causes a genotoxic response which may cause DNA adduct formation, DNA damage, chromosomal aberration, mutation, apoptosis and finally cell death (Driscoll *et al.* 1996; Englen *et al.* 1990). The possible routes of exposure and biodistribution of nanoparticles also effect their toxicity (Lewinski, Colvin, & Drezek 2008; Yah, Simate, & Iyuke 2012). The consideration of nanotoxicity therefore needs to take into account realistic exposure scenarios, and regulatory government agencies must work with the colloboration of academia and industry (Lanone & Boczkowski 2006; Nel *et al.* 2006).

The detailed understanding of the interaction of designed and delivered nanoparticles with tissues, cells and body fluids is of great importance to optimise these nanoparticles for medical applications such as drug delivery, molecular imaging and tissue implants. Endocytosis is known as the primary mechanism for the cellular uptake of nanoparticles into the cells (Treuel, Jiang, & Nienhaus 2013). At the early stage of endocytosis, nanoparticles are trafficked through endosomes and later lysosomes (Salvati *et al.* 2011; Shapero *et al.* 2011). Also, intracellular trafficking of nanoparticles, ROS production and inflammatory responses have been widely studied (see for example the review by (Nel *et al.* 2009)). Although it has been studied extensively, the complexity of the process and varied physicochemical properties of nanoparticles still raise question marks on this issue. For this reason, visualization of the uptake of nanoparticles and observation of their trafficking into the cell is of critical importance to develop novel tools for nanomedicine and to assess their potential toxic effects.

The tracking of nanomaterials, from the initial exposure of cells to nanomaterials to exocytosis or degradation, has been studied by microscopic and spectroscopic techniques. Standard Optical microscopy can be used for the visualization of cells. Although it makes it possible to image live cells, it is difficult to gain detailed information about subcellular structures due to the limited spatial resolution. Electron microscopy (EM) has also been used for the visualisation of nanoparticles in cells. However, sample preparation causes alteration on the structure of cells (Mu *et al.* 2012).

Nanoparticles which have been labeled by fluorescent dyes have been extensively studied (Fazlollahi *et al.* 2011; Jan *et al.* 2008; Sandin *et al.* 2012; Zhuang 2009). Confocal Laser Scanning Microscopy (CLSM) has also been used for the visualization of nanoparticles for *in vitro* studies (*Handbook of Biological Confocal Microscopy* 2006). By the use of these fluorescent based techniques, fluorescent emmission of nanoparticles and the subcellular location of nanoparticles have been determined. Using two photon exitation techniques and NIR fluorophores, the penetration depths of the detection techniques have been increased (Aparicio-Ixta *et al.* 2012; Yang *et al.* 2012). It is also possible to observe physological processes within a cell using fluorescent based techniques. The labeling of lysosomes and mitochondria can be achieved by using lyso and mitotracker which are available as commercial kits (Le *et al.* 2010). Although these techniques allow visualization of the nanoparticles *in vitro* and determination of their localisation in the cell, they have drawbacks as well. Fluorescent based microscopy is limited in resolution and all nanoparticles cannot be functionalized with flourescent dyes. Moreover, labeled nanoparticles may release the dye into the local environment from their surfaces such that the detection of fluorescence does not guarantee the presence of nanoparticles (Salvati *et al.* 2011; Suh *et al.* 1998; Win & Feng 2006).

Over the last decade, High Content Analysis/Screening (HCA/HCS), which can be described as automated imaging and analysis of ‘phenotypic assay endpoints for the evaluation of multiple information regarding to cell morphology, biochemical parameters in cells, tissue-level toxicity, as well as animal disease models, has brought a new perspective to, for example, drug discovery and academic research (Brayden *et al.* 2015; Liebel & Link 2007; Zock 2009). HCA has been used to replace cellular

assays for cell signalling (Ding *et al.* 1998; Sarker *et al.* 2008; Zock 2009), neurobiology (Radio *et al.* 2008; Ruan *et al.* 2008), *in vitro* toxicology (Anguissola *et al.* 2014; Brayden *et al.* 2015; Morelli *et al.* 2006), cell physiology (Dykens *et al.* 2008; Gasparri *et al.* 2004) and many other applications due to its speed, sensitivity and multifaceted data which provide advantages over conventional cellular assays. However, this technology still remains challenging because of the cost, problems in data management, development of application based models and lack of common standards (Liebel & Link 2007).

Spectroscopic techniques have also been studied for the visualisation of cellular and subcellular structures of cells (Dorney *et al.* 2012; Matthäus *et al.* 2007). In particular, vibrational spectroscopic techniques such as Infrared (IR) and Raman spectroscopy have been widely used for the localization studies of nanoparticles. Although IR spectroscopy can provide important information about the localisation of nanoparticles inside the cell, its limited spatial resolution can be a problem. Another challenge of the technique for biological samples is water, which gives strong signals in IR spectra (Keating & Byrne 2013). As an alternative and complementary vibrational spectroscopic technique, Raman spectroscopy is known as a powerful method to study different biolomolecules and biomolecular structures (Carey 1982). Raman scatterering can be defined as the inelastic collision of photons with molecules. Due to easy sample preperation steps, narrow spectral bandwidths and minimal influence from water, the technique can be used for biological samples (Moskovits 1985).

1.3. Aims and Objectives

The main aim of this thesis is to establish a novel nanotoxicological assessment protocol based on Raman microspectroscopy, which will allow the toxicity analysis of wide range of nanomaterials in a rapid and multi-parametric fashion.

The study is designed to investigate applicability of Raman microspectroscopy as a High Content Screening technique to clarify cell-nanoparticle interaction by determining the localisation of the nanoparticles and consequent effects in these localised areas in terms of cyto- and geno- toxicity.

Raman microspectroscopy, with the aid of multivariate analysis techniques, has been employed to determine nanoparticle localisation and to obtain information regarding to spectral signatures of the cellular compartments such as early endosomes, lysosomes and endoplasmic reticulum. Following their localisation, the effect of nanoparticles in a time and dose dependant manner has been studied and the spectral markers of the cytotoxic events have been identified. The consistency of the spectral markers on different cell lines (cancerous and non-cancerous) has been studied and different toxic pathways leading to cell death have been explored. In order to observe common and/or differing spectral markers of the cyto- and geno- toxicity, exposure to different nanoparticles has been studied in a time dependant fashion.

1.4. Thesis Summary

This thesis is designed to show the applicability of Raman spectroscopy as a high content analysis tool due to its fingerprint property to establish a novel nanotoxicological screening method.

Chapter 1 highlights the concept of Nanoscience, Nanotechnology and Nanotoxicology with the aims and objectives of the thesis. Also, the chapter provides background information about the techniques that are commonly used for the determination of nanoparticle localisation and as an emerging technique, the use of Raman spectroscopy for cellular analysis, nanoparticle localisation and toxicity.

Chapter 2 describes the methodology that has been used throughout the study in more detail. The principles of Raman microspectroscopy and the use of multivariate analysis techniques to extract information from the huge and complex Raman data sets are discussed. Moreover, the theory behind the bioimaging techniques, cytotoxicity assays and biochemical assays which are employed as a complementery technique to Nanotoxicological assesment by Raman microspectroscopy will be explained in detail.

Chapter 3 mainly focuses on the use of Raman spectroscopy to differentiate different subcellular structures as well as localisation of nontoxic nanoparticles within these compartments. The chapter will provide the biochemical composition of the different organelles such as early endosome, lysosome and endoplasmic reticulum based on their Raman characteristic bands upon different exposure times.

Chapter 3 has been adapted from the published journal article entitled 'Determination of Nanoparticle Localisation within Subcellular Organelles *in vitro* using Raman Spectroscopy', Analytical Methods, 2015, DOI: 10.1039/c5ay02661j.

Chapter 4 mainly focus on the identification of spectral markers of the cytotoxicity in a time and dose dependent manner by monitoring the effect of amine-modified polystyrene nanoparticles in human lung adenocarcinoma cells. The chapter will provide information regarding to spectral markers of the particle dependent (toxicity initiating event) and cellular dependant events (activation of caspases, protein and lipid damage and ultimately cell death) with the aid of multivariate analysis techniques. The Raman spectral markers for lipidosis, ROS formation and oxidative stress related biochemical damage will be introduced.

Chapter 4 has been adapted from the published journal article entitled '*In vitro* Monitoring of Time and Dose Dependent Cytotoxicity of Aminated Nanoparticles using Raman Spectroscopy', Analyst, 2016, 141, 5417-5431.

Chapter 5 shows the applicability of Raman microspectroscopy as a 'high content nanotoxicological screening technique with the aid of multivariate analysis on non-cancerous (immortalized human bronchial epithelium) and cancerous cell-lines (human lung carcinoma and human lung epidermoid cells). Spectral markers of cellular responses such as oxidative stress, cytoplasmic RNA aberrations and liposomal rupture were identified and cell-line dependent systematic variations in these spectral markers, as a function of the exposure time, were observed using Raman microspectroscopy.

Chapter 5 has been adapted from the published journal article entitled 'Label-Free, High Content Screening using Raman Microspectroscopy: The Toxicological Response of Different Cell Lines to Amine-modified Polystyrene Nanoparticles (PS-NH_2)', Analyst, 2017, DOI: 10.1039/C7AN00461C.

Chapter 6, Raman microspectroscopy is employed as an *in vitro* label free high content screening technique to observe toxicological changes within the cell in a multi-parametric fashion. The evolution of spectral markers as a function of time and applied dose has been used to elucidate the mechanism of action of polyamidoamine (PAMAM) dendrimers associated with cytotoxicity and their impact on nuclear biochemistry. The spectral markers of cytotoxicity and genotoxicity upon PAMAM dendrimer exposure is provided with information regarding to PAMAM-DNA/RNA interaction.

Chapter 6 has been adapted from the published journal article entitled 'Determination of Spectral Markers of Cytotoxicity and Genotoxicity Using *in vitro* Raman Microspectroscopy: Cellular Responses to Polyamidoamine Dendrimer Exposure', Analyst, 2017, DOI: 10.1039/C7AN00969K.

Chapter 7 demonstrates the common and/or differentiating spectral markers of cyto- and geno- toxicity, identified by comparing the spectral markers of the cellular responses upon exposure to two different toxic nanoparticles, PS-NH_2 and PAMAM. The chapter further demonstrates the potential of Raman microspectroscopy to differentiate apoptotic and necrotic cell death mechanisms. The spectral markers of the toxic events and ultimately cell death were identified and compared with the aid of

unsupervised Principal Component Analysis (PCA). The results were correlated with flow cytometry and cytotoxicity assays.

Chapter 7 has been adapted from the submitted journal article entitled 'Identification of Cell Death Mechanisms based on Raman Spectral Markers of Cyto-/Geno-Toxicity: Comparative Study of Polyamidoamine Dendrimers and Aminated Polystyrene Nanoparticles, Journal of Biophotonics, 2017.

Chapter 8 summarises the main findings of the thesis to build a more holistic approach to demonstrate cell-nanoparticle interaction and to determine nanoparticle toxicity using Raman microspectroscopy as a High Content Screening technique.

Chapter 8 has been adapted from the accepted journal article entitled 'Toxicological Assessment of Nanomaterials: The role of in vitro Raman Microspectroscopic Analysis', Analytical and Bioanalytical Chemistry, 2017.

In the chapters which are adapted from the papers, the format of the original has been retained, but changes in figure and section numbering have been made, as required for the thesis format. Supplementary material related to the corresponding work is also added at the end of the Chapters.

1.5. References

Anguissola, S, Garry, D, Salvati, A, O'Brien, P J and Dawson, K A (2014) High Content Analysis Provides Mechanistic Insights on the Pathways of Toxicity Induced by Amine-Modified Polystyrene Nanoparticles. *PLoS ONE*, 9(9), e108025.

Aparicio-Ixta, L, Ramos-Ortiz, G, Pichardo-Molina, J L, Maldonado, J L, Rodriguez, M, Tellez-Lopez, V M, Martinez-Fong, D, Zolotukhin, M G, Fomine, S, Meneses-Nava, M A and Barbosa-Garcia, O (2012) Two-Photon Excited Fluorescence of Silica Nanoparticles Loaded with a Fluorene-Based Monomer and Its Cross-Conjugated Polymer: Their Application to Cell Imaging. *Nanoscale,* 4(24), 7751-9.

Brayden, D J, Cryan, S-A, Dawson, K A, O'Brien, P J and Simpson, J C (2015) High-Content Analysis for Drug Delivery and Nanoparticle Applications. *Drug Discovery Today,* 20(8), 942-57.

Carey, P R (1982) *Biochemical Applications of Raman and Resonance Raman Spectroscopies / P.R. Carey*, Academic Press, New York.

Chen, C C, Liu, Y C, Wu, C H, Yeh, C C, Su, M T and Wu, Y C (2005) Preparation of Fluorescent Silica Nanotubes and Their Application in Gene Delivery. *Advanced Materials,* 17(4), 404-7.

Cui, D, Pan, B, Zhang, H, Gao, F, Wu, R, Wang, J, He, R and Asahi, T (2008) Self-Assembly of Quantum Dots and Carbon Nanotubes for Ultrasensitive Dna and Antigen Detection. *Anal Chem,* 80(21), 7996-8001.

Curtis, J, Greenberg, M, Kester, J, Phillips, S and Krieger, G (2006) Nanotechnology and Nanotoxicology: A Primer for Clinicians. *Toxicol Rev*, 25(4), 245-60.

Daniel, M C and Astruc, D (2004) Gold Nanoparticles: Assembly, Supramolecular Chemistry, Quantum-Size-Related Properties, and Applications toward Biology, Catalysis, and Nanotechnology. *Chem Rev*, 104(1), 293-346.

Ding, G J, Fischer, P A, Boltz, R C, Schmidt, J A, Colaianne, J J, Gough, A, Rubin, R A and Miller, D K (1998) Characterization and Quantitation of Nf-Kappab Nuclear Translocation Induced by Interleukin-1 and Tumor Necrosis Factor-Alpha. Development and Use of a High Capacity Fluorescence Cytometric System. *J Biol Chem*, 273(44), 28897-905.

Dobrovolskaia, M A and McNeil, S E (2007) Immunological Properties of Engineered Nanomaterials. *Nat Nanotechnol*, 2(8), 469-78.

Donaldson, K, Stone, V, Tran, C L, Kreyling, W and Borm, P J (2004). Nanotoxicology In *Occup Environ Med* Vol. 61 England.

Dorney, J, Bonnier, F, Garcia, A, Casey, A, Chambers, G and Byrne, H J (2012) Identifying and Localizing Intracellular Nanoparticles Using Raman Spectroscopy. *Analyst*, 137(5), 1111-9.

Drexler, K E (1986) *Engines of Creation: The Coming Era of Nanotechnology*, Anchor Books, New York.

Driscoll, K E, Carter, J M, Howard, B W, Hassenbein, D G, Pepelko, W, Baggs, R B and Oberdörster, G (1996) Pulmonary Inflammatory, Chemokine, and Mutagenic Responses in Rats after Subchronic Inhalation of Carbon Black. *Toxicology and Applied Pharmacology*, 136(2), 372-80.

Dykens, J A, Jamieson, J D, Marroquin, L D, Nadanaciva, S, Xu, J J, Dunn, M C, Smith, A R and Will, Y (2008) *In vitro* Assessment of Mitochondrial Dysfunction and Cytotoxicity of Nefazodone, Trazodone, and Buspirone. *Toxicol Sci,* 103(2), 335-45.

El-Sayed, I H, Huang, X and El-Sayed, M A (2006) Selective Laser Photo-Thermal Therapy of Epithelial Carcinoma Using Anti-Egfr Antibody Conjugated Gold Nanoparticles. *Cancer Lett,* 239(1), 129-35.

Englen, M D, Taylor, S M, Laegreid, W W, Silflow, R M and Leid, R W (1990) The Effects of Different Silicas on Arachidonic Acid Metabolism in Alveolar Macrophages. *Exp Lung Res,* 16(6), 691-709.

Fazlollahi, F, Angelow, S, Yacobi, N R, Marchelletta, R, Yu, A S L, Hamm-Alvarez, S F, Borok, Z, Kim, K-J and Crandall, E D (2011) Polystyrene Nanoparticle Trafficking across Mdck-Ii. *Nanomedicine : nanotechnology, biology, and medicine,* 7(5), 588-94.

Feynman, R P (1992) There's Plenty of Room at the Bottom [Data Storage]. *Journal of Microelectromechanical Systems,* 1(1), 60-6.

Freestone, I, Meeks, N, Sax, M and Higgitt, C (2007) The Lycurgus Cup- a Roman Nanotechnology. *Gold Bulletin,* 40(4), 270-7.

Gasparri, F, Mariani, M, Sola, F and Galvani, A (2004) Quantification of the Proliferation Index of Human Dermal Fibroblast Cultures with the Arrayscan™ High-Content Screening Reader. *Journal of Biomolecular Screening,* 9(3), 232-43.

Ghosh, P, Han, G, De, M, Kim, C K and Rotello, V M (2008) Gold Nanoparticles in Delivery Applications. *Adv Drug Deliv Rev,* 60(11), 1307-15.

Hahn, M A, Singh, A K, Sharma, P, Brown, S C and Moudgil, B M (2011) Nanoparticles as Contrast Agents for in-Vivo Bioimaging: Current Status and Future Perspectives. *Anal Bioanal Chem,* 399(1), 3-27.

Handbook of Biological Confocal Microscopy (2006), Springer US.

Ito, A and Kamihira, M (2011) Tissue Engineering Using Magnetite Nanoparticles. *Prog Mol Biol Transl Sci,* 104, 355-95.

Ito, F, Fujimori, H, Honnami, H, Kawakami, H, Kanamura, K and Makino, K (2008) Effect of Polyethylene Glycol on Preparation of Rifampicin-Loaded Plga Microspheres with Membrane Emulsification Technique. *Colloids Surf B Biointerfaces,* 66(1), 65-70.

Jan, E, Byrne, S J, Cuddihy, M, Davies, A M, Volkov, Y, Gun'ko, Y K and Kotov, N A (2008) High-Content Screening as a Universal Tool for Fingerprinting of Cytotoxicity of Nanoparticles. *ACS Nano,* 2(5), 928-38.

Kabanov, A V (2006) Polymer Genomics: An Insight into Pharmacology and Toxicology of Nanomedicines. *Advanced drug delivery reviews,* 58(15), 1597-621.

Keating, M E and Byrne, H J (2013) Raman Spectroscopy in Nanomedicine: Current Status and Future Perspective. *Nanomedicine (Lond),* 8(8), 1335-51.

Kim, D, Park, S, Lee, J H, Jeong, Y Y and Jon, S (2007) Antibiofouling Polymer-Coated Gold Nanoparticles as a Contrast Agent for in Vivo X-Ray Computed Tomography Imaging. *Journal of the American Chemical Society,* 129(24), 7661-5.

Kumar, S, Harrison, N, Richards-Kortum, R and Sokolov, K (2007) Plasmonic Nanosensors for Imaging Intracellular Biomarkers in Live Cells. *Nano Letters,* 7(5), 1338-43.

Lanone, S and Boczkowski, J (2006) Biomedical Applications and Potential Health Risks of Nanomaterials: Molecular Mechanisms. *Curr Mol Med,* 6(6), 651-63.

Le, T T, Duren, H M, Slipchenko, M N, Hu, C-D and Cheng, J-X (2010) Label-Free Quantitative Analysis of Lipid Metabolism in Living Caenorhabditis Elegans. *Journal of Lipid Research,* 51(3), 672-7.

Lewinski, N, Colvin, V and Drezek, R (2008) Cytotoxicity of Nanoparticles. *Small,* 4(1), 26-49.

Liebel, U and Link, W (2007) Meeting Report: Trends and Challenges in High Content Analysis. *Biotechnol J,* 2(8), 938-40.

Matthäus, C, Chernenko, T, Newmark, J A, Warner, C M and Diem, M (2007) Label-Free Detection of Mitochondrial Distribution in Cells by Nonresonant Raman Microspectroscopy. *Biophysical Journal,* 93(2), 668-73.

Morelli, J K, Buehrle, M, Pognan, F, Barone, L R, Fieles, W and Ciaccio, P J (2006) Validation of an *in vitro* Screen for Phospholipidosis Using a High-Content Biology Platform. *Cell Biol Toxicol,* 22(1), 15-27.

Moskovits, M (1985) Surface-Enhanced Spectroscopy. *Reviews of Modern Physics,* 57(3), 783-826.

Mu, Q, Hondow, N S, Krzeminski, L, Brown, A P, Jeuken, L J and Routledge, M N (2012) Mechanism of Cellular Uptake of Genotoxic Silica Nanoparticles. *Part Fibre Toxicol,* 9, 29.

Naha, P C, Kanchan, V, Manna, P K and Panda, A K (2008) Improved Bioavailability of Orally Delivered Insulin Using Eudragit-L30d Coated Plga Microparticles. *J Microencapsul,* 25(4), 248-56.

Naha, P C, Kanchan, V and Panda, A K (2008) Evaluation of Parenteral Depot Insulin Formulation Using Plga and Pla Microparticles. *Journal of Biomaterials Applications,* 24(4), 309-25.

Nel, A, Xia, T, Mädler, L and Li, N (2006) Toxic Potential of Materials at the Nanolevel. *Science,* 311(5761), 622.

Nel, A E, Madler, L, Velegol, D, Xia, T, Hoek, E M and Somasundaran, P (2009) Understanding Biophysicochemical Interactions at the Nano-Bio Interface. *Nat Mater,* 8.

Oberdörster, G, Maynard, A, Donaldson, K, Castranova, V, Fitzpatrick, J, Ausman, K, Carter, J, Karn, B, Kreyling, W, Lai, D, Olin, S, Monteiro-Riviere, N, Warheit, D and Yang, H (2005) Principles for Characterizing the Potential Human Health Effects from Exposure to Nanomaterials: Elements of a Screening Strategy. *Particle and Fibre Toxicology,* 2(1), 8.

Pan, B, Cui, D, Ozkan, C S, Ozkan, M, Xu, P, Huang, T, Liu, F, Chen, H, Li, Q, He, R and Gao, F (2008) Effects of Carbon Nanotubes on Photoluminescence Properties of Quantum Dots. *The Journal of Physical Chemistry C,* 112(4), 939-44.

Radio, N M, Breier, J M, Shafer, T J and Mundy, W R (2008) Assessment of Chemical Effects on Neurite Outgrowth in Pc12 Cells Using High Content Screening. *Toxicol Sci,* 105(1), 106-18.

Reibold, M, Paufler, P, Levin, A A, Kochmann, W, Patzke, N and Meyer, D C (2006) Materials: Carbon Nanotubes in an Ancient Damascus Sabre. *Nature,* 444(7117), 286.

Ruan, B, Pong, K, Jow, F, Bowlby, M, Crozier, R A, Liu, D, Liang, S, Chen, Y, Mercado, M L, Feng, X, Bennett, F, von Schack, D, McDonald, L, Zaleska, M M, Wood, A, Reinhart, P H, Magolda, R L, Skotnicki, J, Pangalos, M N, Koehn, F E, Carter, G T, Abou-Gharbia, M and Graziani, E I (2008) Binding of Rapamycin Analogs to Calcium Channels and Fkbp52 Contributes to Their Neuroprotective Activities. *Proc Natl Acad Sci U S A,* 105(1), 33-8.

Salvati, A, Aberg, C, dos Santos, T, Varela, J, Pinto, P, Lynch, I and Dawson, K A (2011) Experimental and Theoretical Comparison of Intracellular Import of Polymeric Nanoparticles and Small Molecules: Toward Models of Uptake Kinetics. *Nanomedicine,* 7(6), 818-26.

Sandin, P, Fitzpatrick, L W, Simpson, J C and Dawson, K A (2012) High-Speed Imaging of Rab Family Small Gtpases Reveals Rare Events in Nanoparticle Trafficking in Living Cells. *ACS Nano,* 6(2), 1513-21.

Sarker, K P, Kataoka, H, Chan, A, Netherton, S J, Pot, I, Huynh, M A, Feng, X, Bonni, A, Riabowol, K and Bonni, S (2008) Ing2 as a Novel Mediator of Transforming Growth Factor-Beta-Dependent Responses in Epithelial Cells. *J Biol Chem,* 283(19), 13269-79.

Shapero, K, Fenaroli, F, Lynch, I, Cottell, D C, Salvati, A and Dawson, K A (2011) Time and Space Resolved Uptake Study of Silica Nanoparticles by Human Cells. *Mol Biosyst,* 7(2), 371-8.

Sokolov, K, Follen, M, Aaron, J, Pavlova, I, Malpica, A, Lotan, R and Richards-Kortum, R (2003) Real-Time Vital Optical Imaging of Precancer Using Anti-Epidermal Growth Factor Receptor Antibodies Conjugated to Gold Nanoparticles. *Cancer Res,* 63(9), 1999-2004.

Storrie, H and Mooney, D J (2006) Sustained Delivery of Plasmid Dna from Polymeric Scaffolds for Tissue Engineering. *Adv Drug Deliv Rev,* 58(4), 500-14.

Suh, H, Jeong, B, Liu, F and Kim, S W (1998) Cellular Uptake Study of Biodegradable Nanoparticles in Vascular Smooth Muscle Cells. *Pharmaceutical Research,* 15(9), 1495-8.

Taniguchi, N. (1974). On the Basic Concept of Nanotechnology, *International Conference on Production Engineering*. Tokyo: Proceedings of the International Conference on Production Engineering.

Treuel, L, Jiang, X and Nienhaus, G U (2013) New Views on Cellular Uptake and Trafficking of Manufactured Nanoparticles. *J R Soc Interface,* 10(82), 20120939.

Weng, K C, Noble, C O, Papahadjopoulos-Sternberg, B, Chen, F F, Drummond, D C, Kirpotin, D B, Wang, D, Hom, Y K, Hann, B and Park, J W (2008) Targeted Tumor Cell Internalization and Imaging of Multifunctional Quantum Dot-Conjugated Immunoliposomes *in vitro* and in Vivo. *Nano Lett,* 8(9), 2851-7.

Whitesides, G M (2005) Nanoscience, Nanotechnology, and Chemistry. *Small,* 1(2), 172-9.

Win, K Y and Feng, S S (2006) *In vitro* and in Vivo Studies on Vitamin E Tpgs-Emulsified Poly(D,L-Lactic-Co-Glycolic Acid) Nanoparticles for Paclitaxel Formulation. *Biomaterials,* 27(10), 2285-91.

Yah, C S, Simate, G S and Iyuke, S E (2012) Nanoparticles Toxicity and Their Routes of Exposures. *Pak J Pharm Sci,* 25(2), 477-91.

Yang, Y, An, F, Liu, Z, Zhang, X, Zhou, M, Li, W, Hao, X, Lee, C-S and Zhang, X (2012) Ultrabright and Ultrastable near-Infrared Dye Nanoparticles for *in vitro* and in Vivo Bioimaging. *Biomaterials,* 33(31), 7803-9.

Zhuang, X (2009) Nano-Imaging with Storm. *Nat Photonics,* 3(7), 365-7.

Zock, J M (2009) Applications of High Content Screening in Life Science Research. *Combinatorial Chemistry & High Throughput Screening,* 12(9), 870-6.

CHAPTER 2

Methodology

2.1. Introduction

In the previous chapter, the background and aims of the study are discussed and the importance of tracking nanoparticles within cells as well as their mechanism of action in terms of toxicology highlighted. This chapter is designed to provide more background information about the techniques and assays which were employed throughout the study. Further details on sample preparation and general methodology are provided in the relevant chapters.

Commonly used and well-established cytotoxicity assays; Alamar Blue (AB) and 3-(4,5-dimethylthiazol-2-yl)-2,5-diphenyltetrazolium bromide (MTT), 6-carboxy-2',7'-dichlorodihydrofluorescein diacetate (carboxy-H_2DCFDA) assay for determination of reactive oxygen species (ROS), lysosensor for determination of cellular protonation and apoptosis-necrosis assay to determine cell death are used as a complementary techniques to Raman microspectroscopy, measured using plate readers or Confocal laser scanning microscopy (CLSM), and in this chapter they are explained in theory. Finally, the technique of Raman microspectroscopy, which is used to determine particle localisation and spectral signatures of the subcellular compartments, spectral markers of the time and dose dependant toxicity and cell death, is discussed. The unsupervised multivariate analysis techniques which are used to extract the information from the Raman data sets are also explained.

2.2. Nanoparticles

In this study, three different types of nanoparticles (40 nm carboxyl-modified and fluorescently labelled polystyrene nanoparticles (PS-NP), 100 nm amine-modified and fluorescently labelled polystyrene nanoparticles (PS-NH_2), polyamidoamine dendrimers (PAMAM)), are used as model nanoparticles to establish a Nanotoxicological assessment protocol using Raman microspectroscopy. The properties of the nanoparticles and the reason behind the selection of these nanoparticles as model are detailed below.

2.2.1. Polystyrene Nanoparticles

The applications potential of nanopolystyrene is beyond question, due to the wide ranging use of nanopolystyrene and its bulk form, for instance in food packaging, medical products and cell culture substrate materials (Balasundaram & Webster 2007; Kyoung Je Cha and Moon-Hee Na and Hyung Woo Kim and Dong Sung 2014; Wünsch 2000). It was included in 2006 in the Organisation for Economic Co-operation and Development (OECD) Working Party on Manufactured Nanomaterials (WPMN) list of priority nanomaterials for risk assessment, along with other nanostructured materials such as fullerenes (C_{60}), single-walled carbon nanotubes (SWCNTs), multi-walled carbon nanotubes (MWCNTs), silver nanoparticles, iron nanoparticles, titanium dioxide, aluminium oxide, cerium oxide, zinc oxide, silicon dioxide, dendrimers, nanoclays and gold nanoparticles (OECD, ENV/JM/MONO(2010)46) (OECD 2010). However, based on emerging knowledge of nanopolystyrene, it was removed from the list in 2010. Nevertheless, it is commercially available in a range of

sizes with different surface modifications and fluorescent labels and can serve as a model for the study of nanoparticle interactions with cells (Anguissola *et al.* 2014).

Among the range of different size and surface modifications, 40 nm carboxylated (PSNP) and 100 nm aminated (PS-NH_2) fluorescently labelled polystyrene nanoparticles are chosen and used in this study, as they perform as a model for non-toxic and toxic nanoparticles, respectively (Dorney *et al.* 2012; Efeoglu, Casey, & Byrne 2016; Efeoglu *et al.* 2015).

The PSNPs, trade name FluoroSpheres® Fluorescent Microspheres (F8795), were obtained from Molecular Probes, Invitrogen (USA) and kept at 4 ^{o}C in the dark according to manufacturer's instructions. The carboxyl groups on the surface of the nanoparticles render the surface effectively anionic and they show intense fluorescence when excited with the 488nm argon-ion laser line, emitting in the yellow-green region of the spectrum (505/515 nm). The choice of the size and surface modification has been made based on literature on internalization and uptake studies of PSNPs, which indicates that particles smaller than 100 nm are better for internalisation studies (Rejman *et al.* 2004; Shapero *et al.* 2011). Furthermore, the study by Dorney.*et al.* (2012) showed the applicability of Raman spectroscopy to determine the presence of PSNPs within cells due to their strong, distinct Raman signature (Figure 2.1). For further investigation of trafficking and localisation of nanoparticles within cellular compartments based on particle exposure times, PSNPs were thus deemed to be suitable.

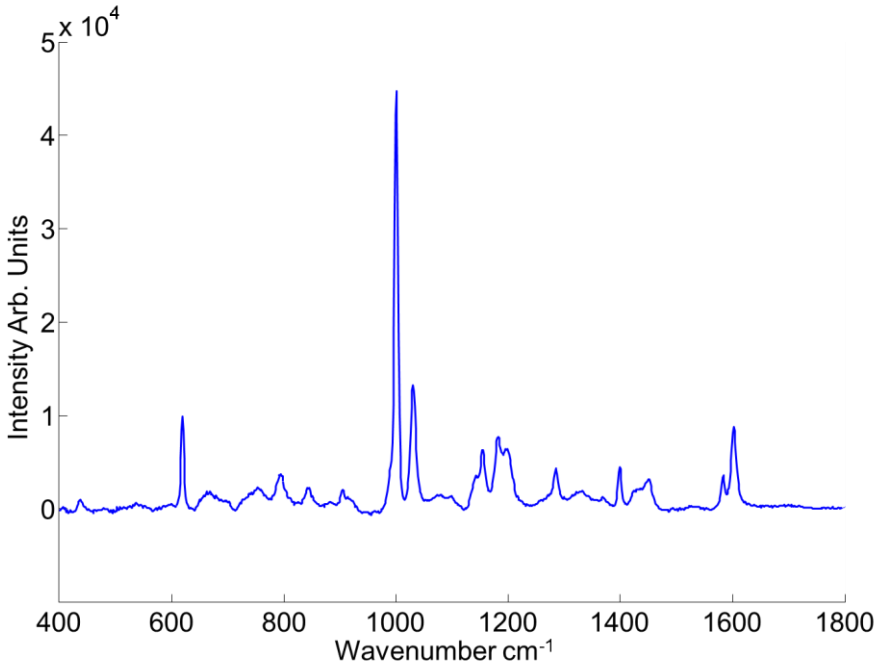

Figure 2.1. Raman spectrum of polystyrene nanoparticles.

The 100 nm PS-NH_2 (L9904), were obtained from Sigma-Aldrich (Ireland) and kept at 4 ^oC in the dark according to manufacturer's instructions. The amino groups on the surface of the nanoparticles render the surface effectively cationic and they show intense fluorescence when excited with the 488 nm argon-ion laser line, emitting in the orange region of the spectrum (664 nm). PS-NH_2 are chosen as model nanoparticles due to their well-documented cytotoxic mechanisms (Anguissola *et al.* 2014; Lunov, Syrovets, Loos, Beil, *et al.* 2011; Lunov, Syrovets, Loos, Nienhaus, *et al.* 2011; Ruenraroengsak *et al.* 2012; Wang *et al.* 2013; Xia *et al.* 2008). The primary uptake mechanism for PS-NH_2 has been identified as endocytosis, which involves the uptake of particles across the cell membrane by the formation of early endosomes and trafficking to lysosomes where they induce ROS formation and ultimately trigger the cell death mechanisms (Xia *et al.* 2008) due to their highly cationic surface. (Anguissola *et al.* 2014; Bexiga *et al.* 2011; Ruenraroengsak *et al.* 2012; Xia *et al.*

2008). Therefore, in order to observe toxic effects of the nanoparticles in human cells, PS-NH_2 are chosen as model nanoparticles. The cells are exposed to different doses of the PS-NH_2 for various time points to determine dose and time dependant responses. The time and dose dependant spectral markers of the toxicity are identified using Raman spectroscopy.

A stock solution of known concentration of PSNPs and PS-NH_2 in a 1 mL bottle was prepared as per the manufacturer's instructions, in accordance with Equation 2.1.

$$\text{Number of microspheres/mL} = \frac{6C \times 10^{12}}{\rho \times \pi \times \emptyset^3} \qquad \textbf{Equation 2.1.}$$

where;

C= Concentration of PSNPs in g/mL (% solid supplied in aqueous suspension, 5%, 0.05 g/mL and 2%, 0.02 g/mL for 40 nm carboxlylated and 100 nm aminated microspheres, respectively)

ρ = density of polymer in g/mL (value for polystyrene is 1.05)

$\emptyset$ = diameter of NPs in μm.

Further dilutions of the stock solutions were made to reach the desired amount of particles for each experiment, specific details of which are provided in the respective chapters.

2.2.2. Polyamidoamine (PAMAM) dendrimers

In order to see consistency of the spectral markers of toxicity determined by Raman microspectroscopy, a second toxic nanoparticle is introduced to the human cells. PAMAM nanoparticles have attracted attention due to their unique, tuneable properties and potential applications in gene and/or drug delivery, miRNA delivery and MRI contrast agents (Bourne *et al.* 1996; Twyman *et al.* 1999; Zhou *et al.* 2006). The toxic effects of the PAMAM dendrimers have also been widely studied using cytotoxicity assays such as Alamar Blue (AB), MTT, Neutral Red (NR) and Clonogenic assays (Maher & Byrne 2016; Maher *et al.* 2014; S P Mukherjee & Byrne 2013; S P Mukherjee, Davoren, & Byrne 2010; Naha & Byrne 2013; Naha *et al.* 2010). As a general mechanism, dendrimers are found to cause a generation dependent, systematic cytotoxicity, oxidative stress and genotoxicity due to the proton sponge effect in endosomes and/or lysosomes, which causes endosomal rupture and mitochondrial accumulation, resulting in oxidative stress, activation of inflammatory cascades and ultimately cell death. Therefore, PAMAM dendrimers are chosen as model nanoparticles due to their widely studied and well-defined toxic properties and commercial availability.

PAMAM dendrimers consist of a tree-like structure which includes an etylenediamine core and branching amidoamine internal structure with amine groups on the surface. The number of amidoamine branches determines the number of surface amino groups and defines the ‘generation’ of the dendrimer. A representative example for generation 1 PAMAM dendrimer is provided in Figure 2.2.

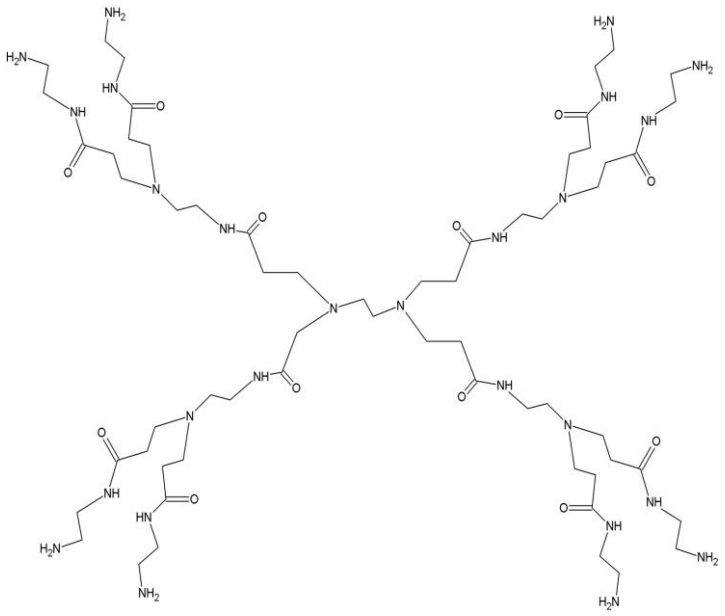

Figure 2.2. Generation 1 PAMAM dendrimer.

The number of surface groups increases with increasing generation, as shown in Table 2.1. A direct relationship between structure and toxic effects due to increasing amount of surface amino groups has been shown by Mukherjee *et al.* (S P Mukherjee, Davoren, & Byrne 2010). In this study, generation 5 PAMAM dendrimers are used to achieve mid-range toxic response.

Table 2.1. Properties of PAMAM dendrimers based on generation. (The table is adapted from Dendritech Inc. (Dendritech 2017).

Generation	Number of Surface Amino groups(nm)	Diameter(nm)
0	4	1.5
1	8	2.2
2	16	2.9
3	32	3.6
4	64	4.5
5	128	5.4
6	256	6.7
7	512	8.1
8	1024	9.7
9	2048	11.4
10	4096	13.5

2.3. Cell Lines

All the cell lines chosen for this study were purchased from American Type Culture Collection (ATCC) and European Collection of Authenticated Cell Cultures (ECACC). The human lung adenocarcinoma cell line (A549) was chosen as a model cell line (ATCC number CCL-185) to determine localisation of the nanoparticles within the cell and to identify spectral markers of time and dose dependant toxicity. Human lung epidermoid cells (Calu-1, ECACC 93120818) and non-cancerous immortalized human bronchial epithelium (BEAS-2B, ATCC® CRL-9609™) cells

are also used to identify common and/or differentiating spectral markers of the toxicity in different cell lines. All cell lines were chosen from cancerous and non-cancerous lung cells, as they mimic one of the primary routes for nanoparticle exposure, inhalation. Cell micrographs of the cell lines are provided in Figure 2.3.

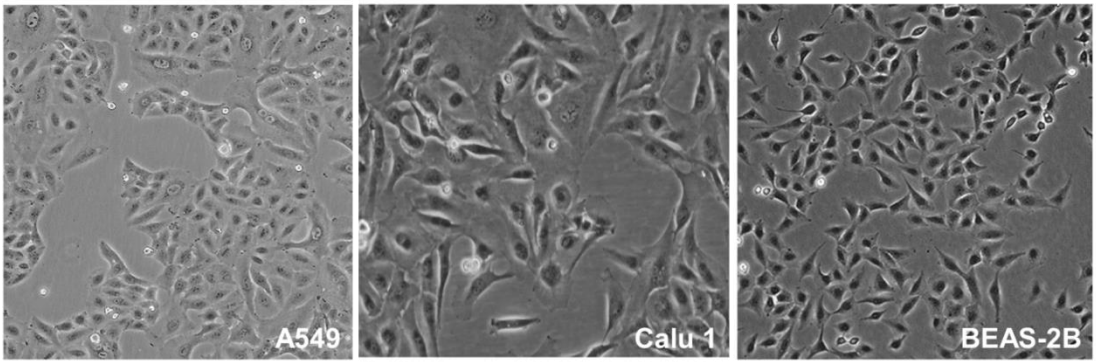

Figure 2.3. Cell Micrographs of A549, Calu-1 and BEAS-2B cell lines. (The figure is adapted from the images provided by ATCC and ECACC (ATCC-A549 ; ATCC-BEAS-2B ; ECACC-Calu-1)

2.4. Cellular Assays

2.4.1. Cytotoxicity Evaluation

For cytotoxicity evaluation, Alamar Blue (AB) and 3-(4,5-dimethylthiazol-2-yl)-2,5-diphenyltetrazolium bromide (MTT) were purchased from Biosciences (Ireland) and Sigma Aldrich Ltd. (Ireland), respectively.

2.4.1.1. Alamar Blue (AB) Assay

The AB dye is known as a redox indicator, which undergoes a colorimetric change and emits a string fluorescent signal (590 nm) as a result of metabolic activity for the whole population of cells when excited at 530-560 nm (O'Brien *et al.* 2000). The AB dye is water soluble and non-toxic and has many applications, from determination of cell proliferation to cytokine assaying (Rampersad 2012; Vega-Avila & Pugsley 2011; White, DiCaprio, & Greenberg 1996). When cells are exposed to the nanoparticles, their metabolic activity changes and cell damage may occur. The changing metabolic activity or cell damage can result in formation of a reducing environment for Resazurin sodium salt which causes a change in the state of the dye and the difference can be quantified by measuring fluorescence (Bonnier *et al.* 2015; Mosmann 1983). The conversion of Resazurin to fluorescently active reduced form, Resofurin is depicted in Figure 2.4.

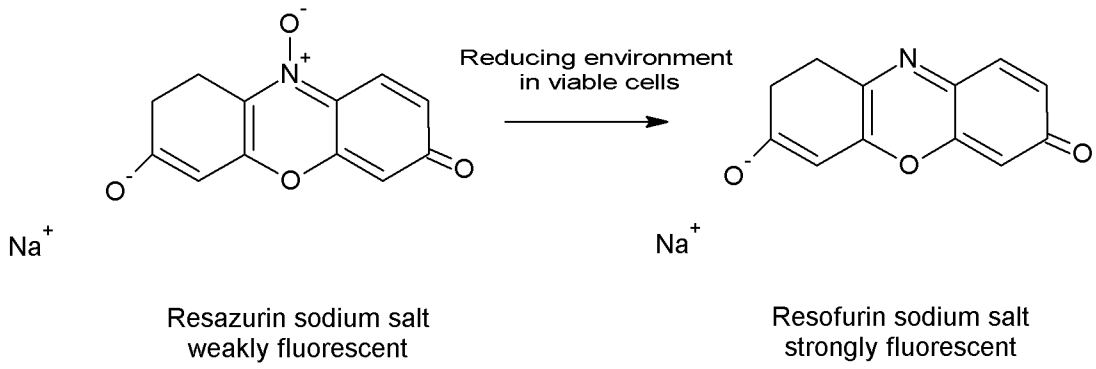

Figure 2.4. Reduction of Resazurin sodium salt to strongly fluorescent Resofurin sodium salt.

2.4.1.2. MTT Assay

The function of the MTT assay is mainly based on cleavage of tetrazolium salts to formazan dye by succinate-tetrazolium reductase (mitochondrial reductase) (Figure 2.5). Therefore, the assay is based primarily on mitochondrial activity. Formazan dye does not dissolve in water and it needs another dissolution step by using DMSO to obtain dissolved dye. The MTT assay can be used to measure cell proliferation in the presence of growth factors, growth inhibitors, cytokines, nutrients as well as nanoparticles and pharmaceutical compounds (Biovision).

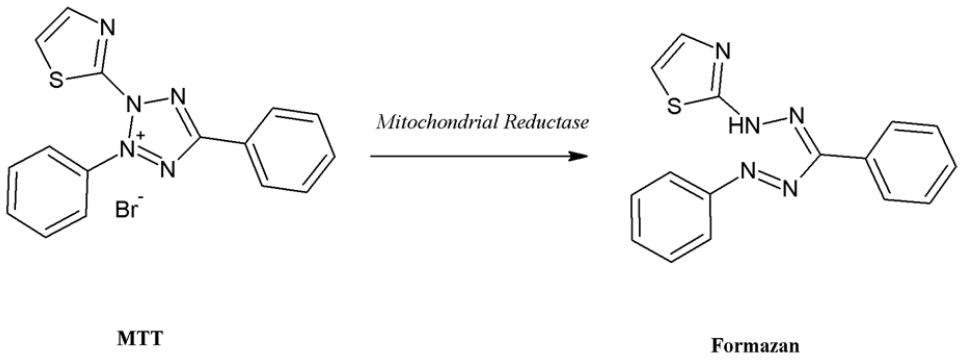

Figure 2.5. Reduction of MTT to insoluble Formazan product by mitochondrial reductase as a result of metabolic activity.

2.4.2. Determination of Reactive oxygen species (ROS): 6-carboxy-2',7' dichlorodihydrofluorescein diacetate (carboxy-H_2DCFDA) assay

Reactive oxygen species can be defined as endogenous and highly reactive molecules containing oxygen and/or nitrogen ions which are generated as a result of mitochondrial oxidative metabolism and also as a response to exogenous factors such infection, xenobiotics (Krumova & Cosa 2016; Ray, Huang, & Tsuji 2012). The reactive oxygen

species are consumed rapidly in cells following their synthesis and excess amounts are controlled by antioxidant mechanisms of the cells. Distortion in the homeostasis as a result of cellular response and/or abnormalities in mitochondrial mechanism or antioxidant mechanisms can result in oxidative stress (Betteridge DJ, Ray, Krumova). The effect of nanoparticles on ROS formation and oxidative stress has been widely studied and demonstrated by different research groups (S P Mukherjee & Byrne 2013; S P Mukherjee, Davoren, & Byrne 2010; Naha *et al.* 2010; Xia *et al.* 2006). In this study, Carboxy-H_2DCFDA is used to determine ROS levels in the cells upon nanoparticle exposure to different cell lines as a complementary technique to Raman microspectroscopy.

The acetylated form of fluorescein, Carboxy-H_2DCFDA, can be used as a general ROS indicator in cells, although there are different types of ROS. The change in the ROS activity of the cell causes formation of intracellular esterases and oxidated states in cells which removes the acetate groups from the surface of the dye and prevents its leakage out of the cell. The fluorescence emission of oxidized Carboxy-H_2DCFDA dye (Excitation/Emission; 485/535 nm) can be measured at 535 nm (ThermoFisherScientific).

2.4.3. Determination of Cellular Protonation): Lysosensor

Surface charges of the nanomaterials can result in changes in pH of the cells upon exposure. Lysosensor dyes can be defined as pH indicators due to their accumulation in acidic compartments of the cells. The fluorescence quenching of the dye results in an increase in fluorescent intensity which allows quantification of protonation inside the cell (Figure 2.6). The lysosensor probes can be used on their own or in combination with other assay to determine cellular protonation. For this study, Lysosensor™ was

purchased from Life Technologies, Ireland and used to identify acidification of the cancerous and non-cancerous cells upon nanoparticle exposure.

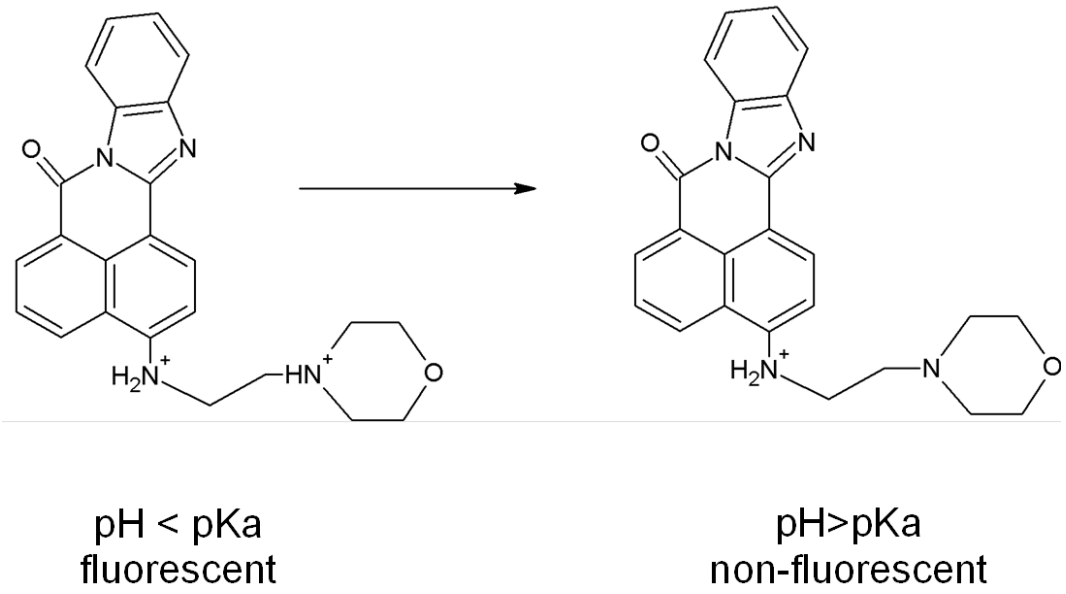

Figure 2.6. Lysosensor^{TM} at different pH (The figure is adapted from the study of Li *et al.* (Y Li *et al.* 2016)).

2.5. Flow Cytometry

Flow cytometry enables the measurement of optical and fluorescent characteristics of the cell populations, particles, microorganisms in a rapid and reproducible way. The specimen under investigation is presented to a light source through a hydrodynamic chamber. The scattered light and fluorescence are collected and converted to electronic pulses which are digitized using computer analysis to create single and/or multiple-variable histograms (Brown & Wittwer 2000; Johnson 1992). The technique can be used for cell sorting based on size also can provide information about cellular labelling

of nuclear material, antibody binding etc. with the use of multiple labels. In this study, flow cytometry is used to determine cell death mechanisms.

A representative schematic of the Flow cytometer is provided in Figure 2.7. In this thesis, BD Biosciences Accuri C6 Flow Cytometer (Becton Dickinson, Oxford, UK) was used for determination of cell death mechanisms.

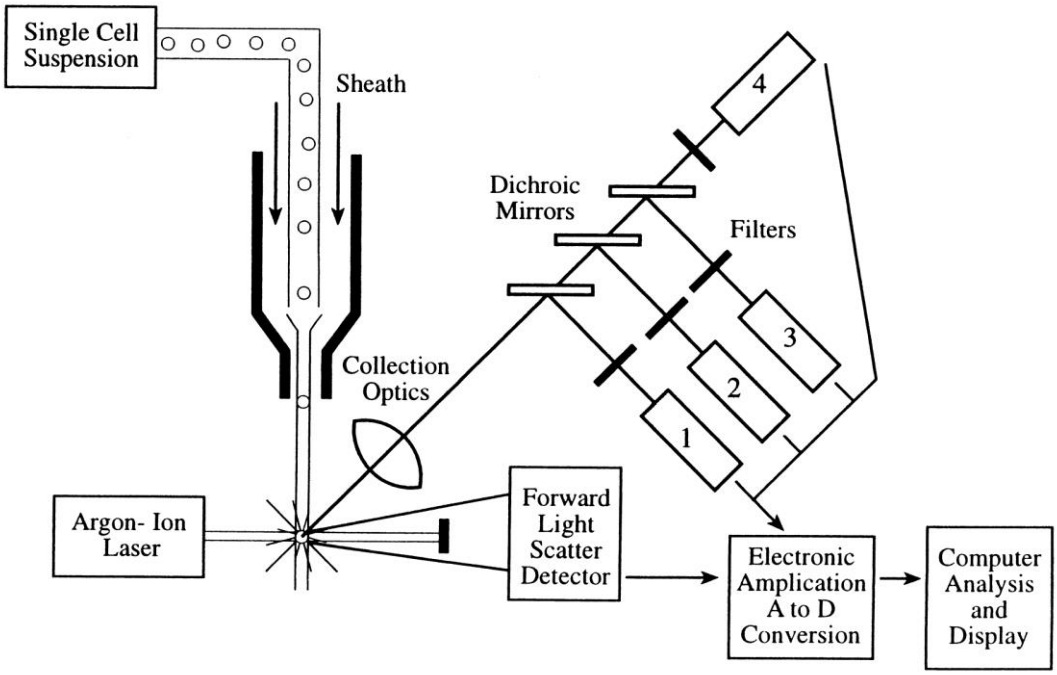

Figure 2.7. Schematic of Flow Cytometry (Brown & Wittwer 2000).

Membrane Permeability/Dead Cell Apoptosis Kit with YO-PRO®-1 and PI was purchased from Molecular Probes (Invitrogen). The cell membrane loses its integrity during necrotic cell death, whereas it slightly loses the integrity upon apoptotic cell death which allows the entrance of the YO-PRO-1 dye and restricts the entrance of PI into the cell. Therefore, the use of YO-PRO-1 and PI provides a sensitive analysis of apoptotic and necrotic cell death (ThermoFisherScientific).

2.6. Confocal Microscopy

Conventional microscopy is based on the visualisation of an entire field of an illuminated specimen placed on the microscope stage. However, conventional microscopy suffers from blurring of images and loss of spatial resolution. In confocal laser microscopy, this problem is overcome by focusing the excitation beam on a small spot inside the sample. Moreover, instead of viewing the back light directly, the light to be imaged is projected and goes through a small pinhole aperture which allows the light originating only from the focal plane to be imaged, while other scattered light is blocked. Confocal light is detected by a sensitive light detector on the other side of pinhole aperture. Briefly, confocal microscopy provides the visualisation of one selected spot on the sample at a time and with continuous scanning of sections through the X-Y plane a 2-D image can be achieved. Z-stacks can be produced by repeating the process at different focal planes in the sample. Compared to conventional microscopy techniques, it provides high-contrast and sharp images (Nwaneshiudu *et al.* 2012; ZEISS). A schematic illustration of Confocal microscopy is shown in Figure 2.8.

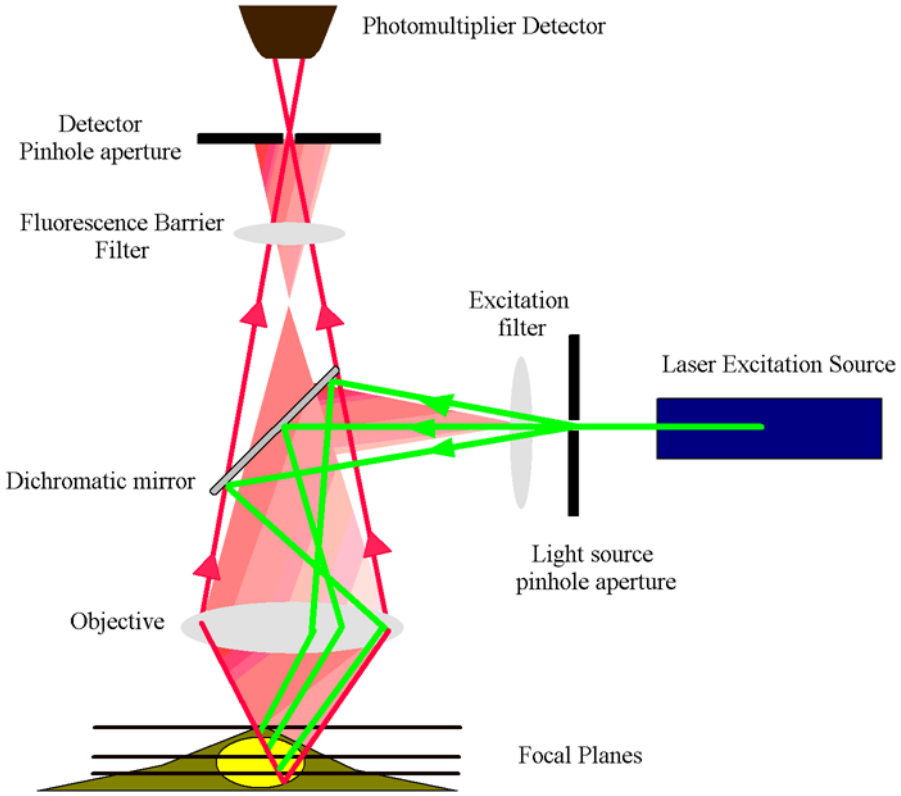

Figure 2.8. Schematic illustration of optical configuration of Confocal microscope.

An inverted, Zeiss LSM510 Meta, confocal laser scanning microscope (Carl Zeiss Inc.) equipped with a x60 oil immersion objective and Argon (488 nm) and HeNe (543 nm) lasers was used throughout this study.

2.6.1. Confocal Fluorescence Imaging of Cell Compartments

Organelle staining, specific to early endosome, lysosome and endoplasmic reticulum (ER), was used to identify organelles which are the possible trafficking route of PSNPs. Lysotracker (Red DND-99), Endoplasmic Reticulum (ER)-Tracker and Cell Light Early Endosome-RFP Bacmam 2.0 stains were purchased from Life Technologies, Ireland. All organelle stains were prepared according to manufacturer's

instructions. LysoTracker® probes can be described as fluorescent acidic probes with are localised in cellular compartments with low pH and mainly localise in spherical organelles (Tian *et al.* 2010; Wiederschain 2011). ER-Tracker™ Red dye is a drug conjugate glibenclamide BODIPY® TR which binds to ER prominent receptors and is known to be highly selective for ER (ER-Tracker™ Dyes for Live-Cell Endoplasmic Reticulum Labeling). Unlike LysoTracker® probes and ER-Tracker™ Red dye, CellLight® reagents were used to determine the localisation of early endosomes. Instead of using of a fluorescent dye directly to label an organelle, CellLight® reagents contain a signal peptide or protein fused to a fluorescent label. The labelling of the cell compartment utilizes BacMam Technology which can be defined as the use of the baculo virus as a vector coupled with a mammalian promoter for the expression of transgenes. For early endosome staining, the transgene encodes the Rab5a protein which is specific to membranes and early endosomes (Bucci *et al.* 1992; Horiuchi *et al.* 1997).

In this study, confocal microscopy was used for the determination of fluorescently labelled and carboxylated PSNPs and organelle staining, with and without the presence of PSNPs to confirm and quantify co-localisation. The absorption and emission characteristics for the both the stains and particles are provided in Table 2.2.

Table 2.2. Spectral Characteristics of 40 nm carboxylated and fluorescently labelled polystyrene nanoparticles and organelle probes.

Organelle Probes and PSNPs	Abs*(nm)	Em*(nm)
40 nm carboxylated-nanoparticles	505	515
Lysotracker®Red DND-99	577	590
ER-Tracker™	587	615
Cell Light® Early Endosome-RFP BacMam 2.0	543	560

2.6.2. Quantification of Co-localization of Nanoparticles within Cell Compartments

In this part of the study, to quantify the degree of colocalisation of PSNPs within different organelles such as early endosomes, lysosome and endoplasmic reticulum, based on exposure time of cells to the particles, overlay confocal images of cells with organelle staining and particles were used. Analysis of the images was carried out using LSM 510 software and quantification of colocalisation within cellular compartments was performed using ImageJ with the JACoP Plugin.

Although the importance of quantification of colocalisation in confocal images is beyond question, the quantification analysis is still challenging and can have inconsistencies due to multiple morphologies within cell structures, the possibility of

complete or partial overlap, bleaching of the fluorescent dye and sample preparation and acquisition differences. Mainly, colocalisation analysis is based on the coefficient calculations which are specialised for intensity distribution and pixel area for overlapping pixels. Most commonly, colocalisation analysis techniques are based on pixel intensity distributions (Bolte & Cordelieres 2006; Costes *et al.* 2004; Q Li *et al.* 2004; Manders *et al.* 2003; Zinchuk & Zinchuk 2008). In the analysis of confocal images, pre-processing such as background corrections carries a significant importance as much as sample preparation and image acquisition for efficient calculation of coefficients and data interpretation.

In this study, images were preproccessed by using imageJ to remove background prior to calculations of colocalisation coefficients by using Just Another Co-localization Plugin (JACoP). JACoP is a recently established toolbox to integrate global statistical methods with an object-based approach for colocalisation analysis (Bolte & Cordelieres 2006). Pearson's and Mander's coefficients were calculated to quantify the amount of colocalisation. Pearson's coefficient gives information about intensity distribution between channels correlated to each other. On the other hand, Mander's coefficient describes the actual overlap of the signals from two channels. The difference of Mander's coefficient from Pearson coefficient is the average intensities of the each channel are taken out from the equation. The mathematical expressions for the calculation of Pearson's and Mander's coefficients are shown in equation 2.3 and Equation 2.3.

$$r = \frac{\sum_i (S1_i - S1_{average}) x (S2_i - S2_{average})}{\sqrt{\sum_i (S1_i - S1_{average})^2 \, x \sum_i (S2_i - S2_{average})^2}}$$

Equation 2.2. Pearson‘s correlation coefficient

$$R = \frac{\sum_i S1_i x S2_1}{\sqrt{\sum_i (S1_i)^2 x \sum_i (S2_1)^2}}$$

Equation 2.3. Overlap coefficient according to Manders (R)

where:

S1= Signal intensity of 1st Channel*

S2= Signal intensity of 2nd Channel*

*Each Channel represents the related fluorescent species. For instance, in this study, one channel belongs to green fluorescent image from particles and second one belongs to red fluorescent image from organelle stain.

$S1_{average}$= Average intensity of 1st channel

$S2_{average}$= Average intensity of 2nd channel

2.7. Raman Spectroscopy

Although the Raman-effect was first demonstrated by Sir C. V. Raman and K. S. Krishnan in 1928 (ACS), the developments in high powered light sources such as ion lasers widened the applications of Raman spectroscopy in the late 1960’s. Raman spectroscopy, as a vibrational spectroscopic technique, has now become a really powerful technique for the characterisation and identification of biomolecules and biomolecular species, due to the narrow spectral bandwidths and ease of sample

preparation (Butler *et al.* 2016). Raman Spectroscopy deals with the collection and measurement of scattering light from a sample. The technique provides a chemical fingerprint of the specimen under investigation.

When light interacts with a sample, it causes a perturbation of the eigenstate of the molecule and causes the formation of time-dependent virtual states. The concept of a virtual state can be explained by the formation of a short-lived complex between light and electrons during the polarization of electrons and dipole moment formation in the molecule as a result of distortion in electron cloud following light-molecule interaction (Figure 2.9.I). If the initial state and final state of a molecule are the same, the energy of the incident light does not show any net change and this phenomenon is called Rayleigh scattering. On the other hand, if there is a change of the initial and final state frequency of the light (energy gain or loss), they are called Stokes scatter and anti-Stokes Scatter, respectively (Figure 2.9.II). The difference in the energy state and frequency of the incident light creates a vibration in the molecular state and this difference is known to be characteristic to the molecule. In this manner, Raman spectroscopy provides fingerprint information which is characteristic of molecule.

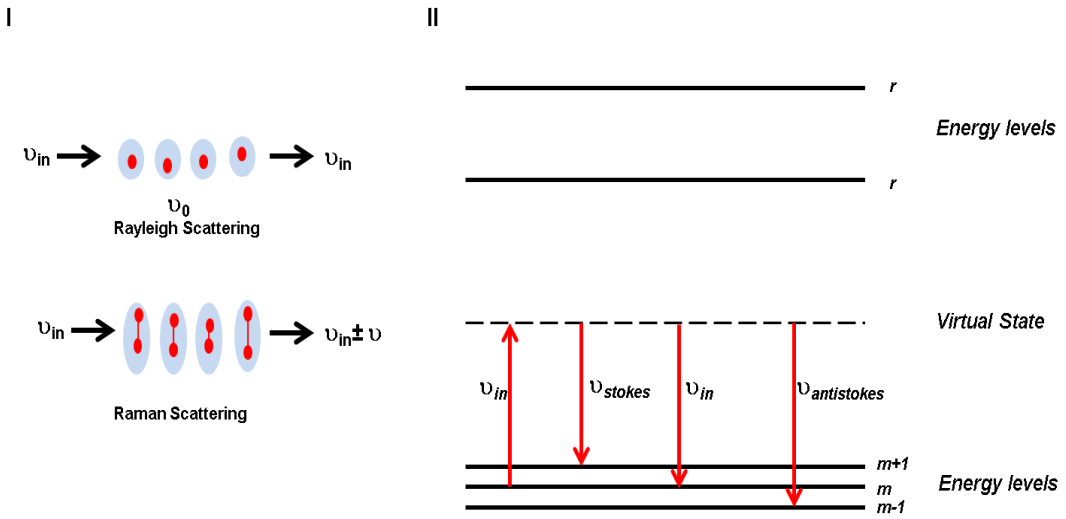

Figure 2.9. Rayleigh scattering-Raman scattering, **I.** Dipole moment formation and change in electron density. **II.** Schematic illustration of quantum mechanical view of Raman and Rayleigh scattering. Where, m indicates the initial and final energy levels and r indicates the higher energy levels. υ_{in} relates to the initial state of incident light. Rayleigh scattering at $\upsilon_{in}=\upsilon_{sc}$. Stokes scattering at $\upsilon_{in}>\upsilon_{sc}$. antiStokes scattering at $\upsilon in<\upsilon sc$.

When light interacted with a molecule, it causes changes in its conformation by perturbing the electron cloud and oscillation. As a result, molecular bands such as C-C, C-N, C=O, or ring structures can rotate, vibrate or stretch. The whole chemical structure of molecule can be determined by the number of bands which are known as 'fingerprint bands' and their location in Raman spectroscopy. Due to the fingerprinting capability of the technique, Raman spectroscopy can be used to identify biomolecules and biomolecular species *in situ*.

A Raman spectrophotometer typically consists of 4 major parts; the light source (laser), optics (filters and focussing objective), wavelength selector (grating) and the detector (Photodiode, CCD, PMT). The set-up for a typical Raman spectrometer is shown in Figure 2.10.

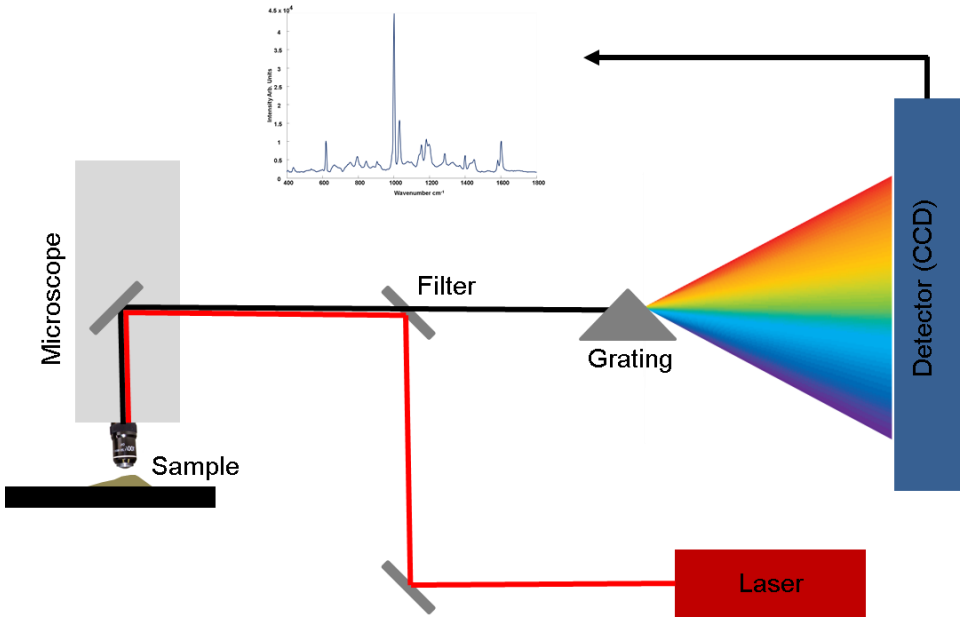

Figure 2.10. Schematic illustration of Raman Spectroscopy set up.

The developing technology of Raman Spectroscopy and high potential of the technique in different areas, from medicine to industry, has led to the development of variants of the Raman spectroscopy technique itself, such as surface enhanced Raman spectroscopy (SERS) (Stiles *et al.* 2008), tip enhanced Raman spectroscopy (TERS) (Zhang *et al.* 2016) and coherent anti Stokes Raman spectroscopy (CARS) (Pezacki *et al.* 2011; Zheltikov 2000). These techniques enable Raman spectroscopy to be more sensitive, to perform molecule specific analysis with enhanced signal.

In this study, Raman spectroscopy was used to determine the localisation of the PSNPs within cellular compartments. A Horiba Jobin-YvonLabRAM HR800 spectrometer equipped with a 785 nm diode laser was used. All measurements were acquired by using a x100 water immersion objective (LUMPlanF1, Olympus, N.A. 1), producing a spot size on the sample of ~1μm. Before spectral acquisition, the system was calibrated to the 520.7 cm^{-1} line of silicon. A 300 lines per mm grating (approximately 1.5 cm^{-1} per pixel spectral dispersion) and a 100 μm confocal pinhole were used throughout this study. The spectra were dispersed onto a 16-bit dynamic range Peltier cooled CCD detector. All white-light images of the cells were taken by using the integrated video camera. Raman maps were acquired over selected areas.

2.8. Data Analysis

Although Raman spectroscopy has been attracting increasing interest in different areas and the applications has been widened, the analysis of the huge spectral data sets and possible interferences from the spectrometer itself is still challenging and under question. Especially, the analysis of spectra or groups of spectra based on molecular differences between them, requires the use of statistical methods to remove side effects which are known as 'artefacts' such as background which can produce a significant effect on sample signal. Analysis of spectral data sets and comparison of different spectral data sets including disease markers, presence of nanomaterials, pharmacological substances or external agents with control groups by using Raman spectroscopy requires multivariate analysis of the hyperspectral data to extract information in an effective manner. The extracted data with the information gained through statistical analysis can be applied in different areas of science from geology,

pharmacology to bioimaging and chemistry. Multivariate analysis techniques are the most common used and well known techniques to reduce the dimensionality and complexity of data and they allow very effective and simultaneous analysis of Raman spectral data sets.

2.8.1. K-means Clustering

In this study, K-means clustering was used to identify different regions and compartments of cells as well as to identify the localisation of PSNPs inside these compartments. K-means clustering separates the Raman spectral data into the groups or classes based on their similarity. The method is known as 'Hard Clustering Method'. In principle, a number of seed locations are chosen by user and algorithm forms initial centroid locations independently based on similarity. The mean of the each cluster serves as cluster centroid. In the case of Raman spectroscopy, each spectrum is assigned to one of these cluster locations based on the Euclidean distance between the spectrum and cluster centroid. After the 1st centroid locations are formed and all data is assigned into a cluster, the Euclidean distance is re-calculated and the process continues until each data point (spectrum) reaches a static position. In hard clustering methods, each pixel in the image relates specifically to a certain value to form a cluster and the whole image is formed by a group of clusters related to the different values and each pixel can be assigned just to one cluster. The general algorithm for K-means clustering is shown schematically in Figure 2.11.

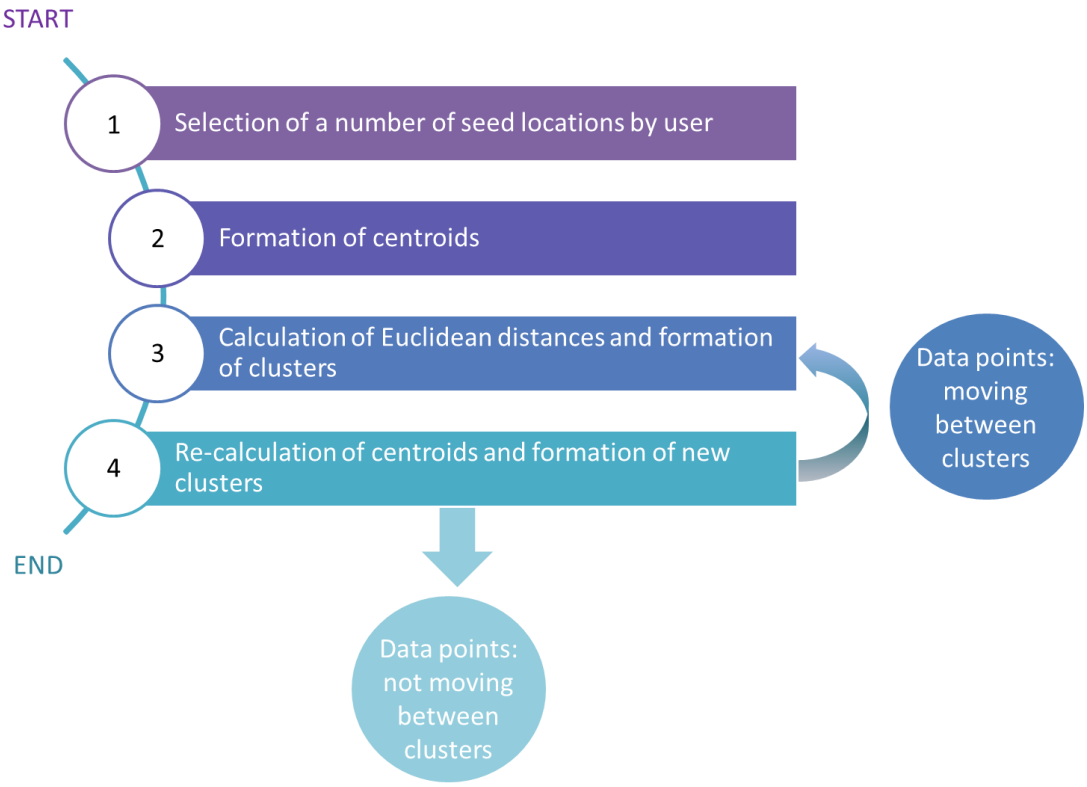

Figure 2.11. Schematic diagram of algorithm of K-means clustering.

Although K-means clustering is widely utilised in biospectroscopy (Bonnier *et al.* 2008; Wolthuis *et al.* 2008), there remains limitations of the technique, such as the subjectivity of the choice of initial cluster number, the fact that it delivers the mean spectral information from a cluster, and that it hard clusters each point exclusively to a single cluster.

2.8.2. Principal Component Analysis (PCA)

In order to overcome the limitations of the K-means clustering and also to obtain information regarding to biochemical information from cells and cellular compartments, Principal Components analysis (PCA) was used on Raman spectral data sets. Moreover, the biochemical changes in the cellular regions, such as nucleus,

nucleolus and cytoplasm, upon a toxicant exposure is determined by pairwise comparisons of control cells with nanoparticle exposed cells. PCA is based on determination of a number of principal components which correspond to the variables in the data sets to reduce dimensionality. In each data set, data is separated into the groups based on variances (principal components) in data sets. A number of principal components are determined according to their efficiency to separate the data sets from each other; the 1^{st} principal component shows the highest variance in the data set and the other principal components follow it as 2^{nd} most, 3^{rd} most and 4^{th} most variance and so on.

2.9. Chapter Summary

In this chapter, materials and theories behind the methodologies that used during the study are given. The experimental details are provided in relevant chapters.

2.10. References

ACS *American Chemical Society International Historic Chemical Landmarks. The Raman Effect.* [Online]. Available: http://www.acs.org/content/acs/en/education/whatischemistry/landmarks/ramaneffect.html [Accessed July]

Anguissola, S, Garry, D, Salvati, A, O'Brien, P J and Dawson, K A (2014) High Content Analysis Provides Mechanistic Insights on the Pathways of Toxicity Induced by Amine-Modified Polystyrene Nanoparticles. *PLoS ONE,* 9(9), e108025.

ATCC-A549 *A549 (Atcc ® ccl-185 ™)* [Online]. Available: https://www.lgcstandardsatcc.org/~/media/26179D062B9C4F49B79C311851B1C154.ashx [Accessed July]

ATCC-BEAS-2B *Beas-2b (Atcc ® crl-9609 ™)* [Online]. Available: https://www.lgcstandardsatcc.org/~/media/B80F9ED2BDD44668A26C57DEB5386940.ashx [Accessed July]

Balasundaram, G and Webster, T J (2007) An Overview of Nano-Polymers for Orthopedic Applications. *Macromolecular Bioscience,* 7(5), 635-42.

Bexiga, M G, Varela, J A, Wang, F, Fenaroli, F, Salvati, A, Lynch, I, Simpson, J C and Dawson, K A (2011) Cationic Nanoparticles Induce Caspase 3-, 7- and 9-Mediated Cytotoxicity in a Human Astrocytoma Cell Line. *Nanotoxicology,* 5(4), 557-67.

Biovision *Mts Cell Proliferation Colorimetric Assay Kit* [Online]. Available: http://www.biovision.com/mts-cell-proliferation-colorimetric-assay-kit.html [Accessed July]

Bolte, S and Cordelieres, F P (2006) A Guided Tour into Subcellular Colocalization Analysis in Light Microscopy. *J Microsc,* 224(Pt 3), 213-32.

Bonnier, F, Bertrand, D, Rubin, S, Venteo, L, Pluot, M, Baehrel, B, Manfait, M and Sockalingum, G D (2008) Detection of Pathological Aortic Tissues by Infrared Multispectral Imaging and Chemometrics. *Analyst,* 133(6), 784-90.

Bonnier, F, Keating, M E, Wrobel, T P, Majzner, K, Baranska, M, Garcia-Munoz, A, Blanco, A and Byrne, H J (2015) Cell Viability Assessment Using the Alamar Blue Assay: A Comparison of 2d and 3d Cell Culture Models. *Toxicol In vitro,* 29(1), 124-31.

Bourne, M W, Margerun, L, Hylton, N, Campion, B, Lai, J-J, Derugin, N and Higgins, C B (1996) Evaluation of the Effects of Intravascular Mr Contrast Media (Gadolinium Dendrimer) on 3d Time of Flight Magnetic Resonance Angiography of the Body. *Journal of Magnetic Resonance Imaging,* 6(2), 305-10.

Brown, M and Wittwer, C (2000) Flow Cytometry: Principles and Clinical Applications in Hematology. *Clinical Chemistry,* 46(8), 1221.

Bucci, C, Parton, R G, Mather, I H, Stunnenberg, H, Simons, K, Hoflack, B and Zerial, M (1992) The Small Gtpase Rab5 Functions as a Regulatory Factor in the Early Endocytic Pathway. *Cell,* 70(5), 715-28.

Butler, H J, Ashton, L, Bird, B, Cinque, G, Curtis, K, Dorney, J, Esmonde-White, K, Fullwood, N J, Gardner, B, Martin-Hirsch, P L, Walsh, M J, McAinsh, M R, Stone, N and Martin, F L (2016) Using Raman Spectroscopy to Characterize Biological Materials. *Nat. Protocols,* 11(4), 664-87.

Costes, S V, Daelemans, D, Cho, E H, Dobbin, Z, Pavlakis, G and Lockett, S (2004) Automatic and Quantitative Measurement of Protein-Protein Colocalization in Live Cells. *Biophys J,* 86(6), 3993-4003.

Dendritech, I (2017) *Pamam Dendrimers* [Online]. Available: http://www.dendritech.com/pamam.html

Dorney, J, Bonnier, F, Garcia, A, Casey, A, Chambers, G and Byrne, H J (2012) Identifying and Localizing Intracellular Nanoparticles Using Raman Spectroscopy. *Analyst,* 137(5), 1111-9.

ECACC-Calu-1 *Ecacc General Cell Collection: Calu-1* [Online]. Available: https://www.pheculturecollections.org.uk/products/celllines/generalcell/detail.jsp?refId=93120818&collection=ecacc_gc [Accessed July]

Efeoglu, E, Casey, A and Byrne, H J (2016) *In vitro* Monitoring of Time and Dose Dependent Cytotoxicity of Aminated Nanoparticles Using Raman Spectroscopy. *Analyst,* 141(18), 5417-31.

Efeoglu, E, Keating, M, McIntyre, J, Casey, A and Byrne, H J (2015) Determination of Nanoparticle Localisation within Subcellular Organelles *in vitro* Using Raman Spectroscopy. *Analytical Methods,* 7(23), 10000-17.

Horiuchi, H, Lippe, R, McBride, H M, Rubino, M, Woodman, P, Stenmark, H, Rybin, V, Wilm, M, Ashman, K, Mann, M and Zerial, M (1997) A Novel Rab5 Gdp/Gtp Exchange Factor Complexed to Rabaptin-5 Links Nucleotide Exchange to Effector Recruitment and Function. *Cell,* 90(6), 1149-59.

Johnson, K L (1992) Basics of Flow Cytometry. *Clin Lab Sci,* 5(1), 22-4.

Krumova, K and Cosa, G (2016). Chapter 1 Overview of Reactive Oxygen Species In *Singlet Oxygen: Applications in Biosciences and Nanosciences, Volume 1* Vol. 1, The Royal Society of Chemistry.

Kyoung Je Cha and Moon-Hee Na and Hyung Woo Kim and Dong Sung, K (2014) Nano Petri Dishes: A New Polystyrene Platform for Studying Cell-Nanoengineered Surface Interactions. *Journal of Micromechanics and Microengineering,* 24(5), 055002.

Li, Q, Lau, A, Morris, T J, Guo, L, Fordyce, C B and Stanley, E F (2004) A Syntaxin 1, Galpha(O), and N-Type Calcium Channel Complex at a Presynaptic Nerve Terminal: Analysis by Quantitative Immunocolocalization. *J Neurosci,* 24(16), 4070-81.

Li, Y, Zhao, T, Wang, C, Lin, Z, Huang, G, Sumer, B D and Gao, J (2016) Molecular Basis of Cooperativity in Ph-Triggered Supramolecular Self-Assembly. *Nat Commun,* 7, 13214.

Lunov, O, Syrovets, T, Loos, C, Beil, J, Delacher, M, Tron, K, Nienhaus, G U, Musyanovych, A, Mailander, V, Landfester, K and Simmet, T (2011) Differential Uptake of Functionalized Polystyrene Nanoparticles by Human Macrophages and a Monocytic Cell Line. *ACS Nano,* 5(3), 1657-69.

Lunov, O, Syrovets, T, Loos, C, Nienhaus, G U, Mailander, V, Landfester, K, Rouis, M and Simmet, T (2011) Amino-Functionalized Polystyrene Nanoparticles Activate the Nlrp3 Inflammasome in Human Macrophages. *ACS Nano,* 5(12), 9648-57.

Maher, M A and Byrne, H J (2016) Modification of the *in vitro* Uptake Mechanism and Antioxidant Levels in Hacat Cells and Resultant Changes to Toxicity and

Oxidative Stress of G4 and G6 Poly(Amidoamine) Dendrimer Nanoparticles. *Anal Bioanal Chem,* 408(19), 5295-307.

Maher, M A, Naha, P C, Mukherjee, S P and Byrne, H J (2014) Numerical Simulations of *in vitro* Nanoparticle Toxicity – the Case of Poly(Amido Amine) Dendrimers. *Toxicology in vitro,* 28(8), 1449-60.

Manders, E M M, Visser, A E, Koppen, A, de Leeuw, W C, van Liere, R, Brakenhoff, G J and van Driel, R (2003) Four-Dimensional Imaging of Chromatin Dynamics During the Assembly of the Interphase Nucleus. *Chromosome Research,* 11(5), 537-47.

Mosmann, T (1983) Rapid Colorimetric Assay for Cellular Growth and Survival: Application to Proliferation and Cytotoxicity Assays. *J Immunol Methods,* 65(1-2), 55-63.

Mukherjee, S P and Byrne, H J (2013) Polyamidoamine Dendrimer Nanoparticle Cytotoxicity, Oxidative Stress, Caspase Activation and Inflammatory Response: Experimental Observation and Numerical Simulation. *Nanomedicine,* 9(2), 202-11.

Mukherjee, S P, Davoren, M and Byrne, H J (2010) *In vitro* Mammalian Cytotoxicological Study of Pamam Dendrimers - Towards Quantitative Structure Activity Relationships. *Toxicol In vitro,* 24(1), 169-77.

Naha, P C and Byrne, H J (2013) Generation of Intracellular Reactive Oxygen Species and Genotoxicity Effect to Exposure of Nanosized Polyamidoamine (Pamam) Dendrimers in Plhc-1 Cells *in vitro*. *Aquat Toxicol,* 132-133, 61-72.

Naha, P C, Davoren, M, Lyng, F M and Byrne, H J (2010) Reactive Oxygen Species (Ros) Induced Cytokine Production and Cytotoxicity of Pamam Dendrimers in J774a.1 Cells. *Toxicology and Applied Pharmacology,* 246(1–2), 91-9.

Nwaneshiudu, A, Kuschal, C, Sakamoto, F H, Anderson, R R, Schwarzenberger, K and Young, R C (2012) Introduction to Confocal Microscopy. *J Invest Dermatol,* 132(12), e3.

O'Brien, J, Wilson, I, Orton, T and Pognan, F (2000) Investigation of the Alamar Blue (Resazurin) Fluorescent Dye for the Assessment of Mammalian Cell Cytotoxicity. *Eur J Biochem,* 267(17), 5421-6.

OECD. (2010). Oecd, Series on the Safety of Manufactured Nanomaterials (pp. 46).

Rampersad, S N (2012) Multiple Applications of Alamar Blue as an Indicator of Metabolic Function and Cellular Health in Cell Viability Bioassays. *Sensors,* 12(9).

Ray, P D, Huang, B-W and Tsuji, Y (2012) Reactive Oxygen Species (Ros) Homeostasis and Redox Regulation in Cellular Signaling. *Cellular signalling,* 24(5), 981-90.

Rejman, J, Oberle, V, Zuhorn, I S and Hoekstra, D (2004) Size-Dependent Internalization of Particles Via the Pathways of Clathrin- and Caveolae-Mediated Endocytosis. *Biochem J,* 377(Pt 1), 159-69.

Ruenraroengsak, P, Novak, P, Berhanu, D, Thorley, A J, Valsami-Jones, E and Gorelik, J (2012) Respiratory Epithelial Cytotoxicity and Membrane Damage (Holes) Caused by Amine-Modified Nanoparticles. *Nanotoxicology,* 6.

Shapero, K, Fenaroli, F, Lynch, I, Cottell, D C, Salvati, A and Dawson, K A (2011) Time and Space Resolved Uptake Study of Silica Nanoparticles by Human Cells. *Mol Biosyst,* 7(2), 371-8.

ThermoFisherScientific *Carboxy-H_2DCFDA(General Oxidative Stress Indicator)* [Online]. Available: https://www.thermofisher.com/order/catalog/product/C400 [Accessed July]

Tian, Y, Su, F, Weber, W, Nandakumar, V, Shumway, B R, Jin, Y, Zhou, X, Holl, M R, Johnson, R H and Meldrum, D R (2010) A Series of Naphthalimide Derivatives as Intra and Extracellular Ph Sensors. *Biomaterials,* 31(29), 7411-22.

Twyman, L J, Beezer, A E, Esfand, R, Hardy, M J and Mitchell, J C (1999) The Synthesis of Water Soluble Dendrimers, and Their Application as Possible Drug Delivery Systems. *Tetrahedron Letters,* 40(9), 1743-6.

Vega-Avila, E and Pugsley, M K (2011) An Overview of Colorimetric Assay Methods Used to Assess Survival or Proliferation of Mammalian Cells. *Proc West Pharmacol Soc,* 54, 10-4.

Wang, F, Yu, L, Monopoli, M P, Sandin, P, Mahon, E, Salvati, A and Dawson, K A (2013) The Biomolecular Corona Is Retained During Nanoparticle Uptake and Protects the Cells from the Damage Induced by Cationic Nanoparticles until Degraded in the Lysosomes. *Nanomedicine,* 9(8), 1159-68.

White, M J, DiCaprio, M J and Greenberg, D A (1996) Assessment of Neuronal Viability with Alamar Blue in Cortical and Granule Cell Cultures. *J Neurosci Methods,* 70(2), 195-200.

Wiederschain, G Y (2011) The Molecular Probes Handbook. A Guide to Fluorescent Probes and Labeling Technologies. *Biochemistry (Moscow),* 76(11), 1276-.

Wolthuis, R, Travo, A, Nicolet, C, Neuville, A, Gaub, M P, Guenot, D, Ly, E, Manfait, M, Jeannesson, P and Piot, O (2008) Ir Spectral Imaging for Histopathological Characterization of Xenografted Human Colon Carcinomas. *Anal Chem,* 80(22), 8461-9.

Wünsch, J R (2000) *Polystyrene:Synthesis, Production and Application* Vol. 10, Rapra Technology Limited.

Xia, T, Kovochich, M, Brant, J, Hotze, M, Sempf, J and Oberley, T (2006) Comparison of the Abilities of Ambient and Manufactured Nanoparticles to Induce Cellular Toxicity According to an Oxidative Stress Paradigm. *Nano Lett,* 6.

Xia, T, Kovochich, M, Liong, M, Zink, J I and Nel, A E (2008) Cationic Polystyrene Nanosphere Toxicity Depends on Cell-Specific Endocytic and Mitochondrial Injury Pathways. *ACS Nano,* 2(1), 85-96.

ZEISS *Education in Microscopy and Digital Imaging* [Online]. Available:

http://zeiss-campus.magnet.fsu.edu/articles/livecellimaging/techniques.html

[Accessed July]

Zhou, J, Wu, J, Hafdi, N, Behr, J P, Erbacher, P and Peng, L (2006) Pamam Dendrimers for Efficient Sirna Delivery and Potent Gene Silencing. *Chem Commun (Camb)*(22), 2362-4.

Zinchuk, V and Zinchuk, O (2008) Quantitative Colocalization Analysis of Confocal Fluorescence Microscopy Images. *Curr Protoc Cell Biol,* Chapter 4, Unit 4.19.

CHAPTER 3

Determination of Nanoparticle Localisation within Subcellular Organelles *in vitro* using Raman Spectroscopy

The following chapter has been adapted from the published journal article entitled 'Determination of Nanoparticle Localisation within Subcellular Organelles *in vitro* using Raman Spectroscopy', Analytical Methods, 2015, **7**, 10000-10017.

Author list: Esen Efeoglu, Mark Keating, Jennifer McIntyre, Alan Casey, Hugh J. Byrne

EE performed all measurements and data analysis and is the main drafting author. MK contributed to data analysis, JM contributed to confocal images. AC and HJB contributed to manuscript design and final drafting.

3.1. Abstract

Ease of sample preparation, narrow spectral bandwidth and minimal influence from water are features of Raman spectroscopy which make it a powerful, label-free way to study a wide range of biological structures and phenomena. In this context, given the concerns over their toxicology arising from their increased production and use, evaluation of nanoparticle uptake and localisation in biological systems and determination of the mechanisms of subcellular interaction and trafficking can provide long-term solutions for nanotoxicology, and potential strategies for nanomedicine. In this study, Raman spectroscopy is explored to monitor the sequential trafficking of nanoparticles through subcellular organelles *in-vitro* and to establish the spectroscopic signatures of those organelles. A549 human lung carcinoma cells were exposed to 40 nm carboxylate-modified and fluorescently-labelled polystyrene nanoparticles for 4, 12 and 24hrs. Raman spectroscopy was applied to nanoparticle exposed cells to determine the localisation within cellular compartments. Confocal laser scanning fluorescence microscopy (CLSM) with different organelle staining kits confirmed the localisation of the nanoparticles in organelles at the chosen exposure periods and co-localization was quantified using ImageJ with the JACoP colocalisation plugin. To confirm nanoparticle localisation and elucidate the spectroscopic signatures of the different subcellular organelles, a combination of K-means clustering (KMCA) and Principal components analysis (PCA) was applied to the Raman spectroscopic maps. The study showed the applicability of the techniques for elucidation of the localisation of polystyrene nanoparticles within the cell as well as determination of their local environment, differentiating the spectral signatures of intracellular compartments such

as endosomes, lysosomes and endoplasmic reticulum, in a completely label free manner.

3.2. Introduction

Increased production and extended use of nanomaterials in different application areas, from composites to cosmetics, has highlighted the necessity of evaluation of every aspect of their biological interactions. Although nanostructures and nanostructured tools have been considered in recent years to be suitable for medical applications, challenges remain, such as blood circulation time and targeting efficiency. Furthermore, despite the undeniable potential of these particles, questions remain concerning their toxicity which has restricted their widespread use in medicine and has created the subcategory of toxicology, known as 'Nanotoxicology' (Donaldson *et al.*, 2004). Nanotoxicology deals with the potential risks and adverse health effects that can arise from nanomaterial use and aims to achieve safe deployment of nanotechnologies (Curtis *et al.*, 2006). The physicochemical properties of nanoparticles such as the size and the shape of nanoparticles, surface area and surface chemistry can determine the potential risk of the material. Besides physico-chemical determinants, molecular level determinants can be considered as a different aspect of nanotoxicology. Nanoparticles may induce the formation of Reactive Oxygen Species (ROS) and expression of inflammatory markers (Kabanov, 2006; Driscoll *et al.*, 1996). The production of ROS, due to their high chemical activity, can cause destruction of DNA, carbohydrates, proteins and lipids (Naha *et al.*, 2013). The destruction of DNA and proteins causes a genotoxic response which may cause DNA adduct formation, DNA damage, chromosomal aberration, mutation, apoptosis and finally cell death (Englen *et al.*, 1990; Lewinski *et al.*, 2008). The possible routes of exposure and biodistribution of nanoparticles also effect their toxicity (Yah *et al.*, 2012; Lanone *et al.*, 2006). The consideration of nanotoxicity therefore needs to take into account

realistic exposure scenarios, and regulatory government agencies must work with the colloboration of academia and industry (Nel *et al.*, 2006; Treuel *et al.*, 2013). A detailed understanding of the interaction of engineered nanoparticles with tissues, cells and bodily fluids is also of great importance for optimisation in medical applications such as drug delivery, molecular imaging and tissue implants.

Intracellular trafficking of nanoparticles, ROS production and inflammatory responses have been widely studied (see for example the review by Nel *et al.*, 2009). Endocytosis is accepted as the primary mechanism for the cellular uptake of nanoparticles into cells (Salvati *et al.*, 2011). Subsequently, nanoparticles are trafficked through endosomes and later lysosomes (Shapero *et al.*, 2011; Mu *et al.*, 2012). Although it has been studied extensively, the complexity of the process and varied physicochemical properties of nanoparticles still raise question marks on this issue. For this reason, direct visualization of the uptake of nanoparticles and observation of their trafficking within the cell is of critical importance to develop routine toxicological screening protocols and novel tools for nanomedicine.

The tracking of nanomaterials, from the initial exposure of cells to nanomaterials, to exocytosis or degradation has been studied by microscopic and spectroscopic techniques (Dorney *et al.*, 2012; Keating *et al.*, 2012; Keating *et al.*, 2013). Electron microscopy (EM) has also been used for the visualisation of nanoparticles in cells. However, not all nanoparticles are visible by EM within the cellular environment, and sample preparation can furthermore cause alteration on the structure of cells (Davoren *et al.*, 2007; Shapero *et al.*, 2011). Standard optical microscopy can be used for the visualization of cells. Although it is possible to image live cells, it is difficult to gain

detailed information about subcellular structures due to the limited spatial resolution. Nanoparticles which have been labeled by fluorescent dyes have been extensively studied and Confocal Laser Scanning Microscopy (CLSM) is an invaluable tool for the visualization of nanoparticles for *in vitro* studies (Sandin *et al.*, 2012; Fazlollahi *et al.*, 2011; Jan *et al.*, 2008; Pawley, 2006). By the use of these fluorescent based techniques, fluorescent emmission of nanoparticles and the subcellular location of nanoparticles have been determined. Two photon exitation techniques and NIR fluorophores can increase the penetration depths of the detection techniques (Aparicio-Ixta *et al.*, 2012; Yang *et al.*, 2012; Le *et al.*, 2010; Suh *et al.*, 1998). Using fluorescent based techniques, it is also possible to observe physological processes within a cell. The labeling of lysosomes and mitochondria can be achieved by using lyso and mitotracker which are available as commercial kits (Matthaus *et al.*, 2007). Although these techniques allow visualization of the nanoparticles *in vitro* and determination of their localisation in the cell, they have drawbacks. Fluorescent based microscopy is limited in resolution and all nanoparticles cannot be functionalized with flourescent dyes. Moreover, labeled nanoparticles may release the dye into the local environment from their surfaces such that the detection of fluorescence does not guarantee the presence of nanoparticles (Salvati *et al.*, 2011; Dorney *et al.*, 2012; Suh *et al.*, 1998).

Spectroscopic techniques have also been studied for the visualisation of cellular and subcellular structures of cells (Dorney *et al.*,2012; Keating *et al.*, 2012; Keating *et al.*, 2013; Carey, 1982; Mattson *et al.*,2013). In particular, vibrational spectroscopic techniques such as Infrared absorption (IR) and Raman spectroscopy have been widely used for the localisation studies of nanoparticles (Carey, 1982; Li *et al.*, 2013; Rhiem *et al.*, 2015; Li *et al.*, 2015). Although IR spectroscopy can provide important

information about the localisation of nanoparticles inside the cell, its limited spatial resolution can be a problem. Another challenge of the technique for biological samples is water, which gives strong signals in IR spectra (Draux *et al.*, 2009). As an alternative vibrational spectroscopic technique, Raman spectroscopy has been demonstrated to be a powerful technique to study different biolomolecules and biomolecular structures (Miljkovic *et al.*, 2010). Due to the ease of sample preparation, narrow spectral bandwidths and minimal influence from water, the technique can be used for biological samples and the optical wavelengths commonly employed render it particularly suitable for subcellular analysis (Nawaz *et al.*, 2010). Label-free imaging of live cells has been studied by Klein *et al.* (2012), by combining immunofluorescence (IF) imaging with Raman spectroscopy to identify cellular structures such as nucleus, cytoplasm and cellular organelles. Also, coregistration of flourescence images with Raman images has been studied by Krauss *et al.* (2015). The study by Dorney et. al. (2012) shows the ability of Raman spectroscopy to observe nanopaparticles in intracellular compartments as well as the biochemical responses and information from their subcellular environment based on their intrinsic spectroscopic signatures which makes the technique completely label free (Dorney *et al.*, 2012). Moreover, different supervised and unsupervised data mining techniques such as spectral cross correlation and classical least squares (CLS) analysis have been used by Keating *et al.* (2012) to extract cellular information directly from complex Raman data sets in the presence of nanoparticles.

This study extends the work of Dorney *et al.*(2012) and Keating *et al.* (2012), which demonstrated the ability of Raman spectroscopy to localise polystyrene nanoparticles in cells after a 24hr exposure, to monitor the evolution of the intracellular environment

of nanoparticles as they are progressively trafficked through the different subcellular organelles of the cell, from 4hrs to 24hrs exposure, and further demonstrate the potential of Raman spectroscopic imaging as a truly label free, high content analysis technique, by establishing the spectroscopic signatures of these subcellular organelles. Nontoxic, 40 nm carboxylated and flourescently labelled polystyrene nanoparticles were used as a model nanoparticles to show the applicability of Raman Spectroscopy as an analytical tool to determine particle localisation within subcellular compartments and establish the spectral fingerprint of these compartments. Nontoxic particles were chosen in order to minimise the perturbation to the cell metabolism, and the nontoxic nature of the particles was confirmed using conventional cytotoxicity assays. CLSM and Raman Spectroscopy were applied to polystyrene nanoparticles and their localisation was determined within cell compartments at different exposure times. A549 human lung carcinoma cells were chosen as a model cell line and cells were exposed to nanoparticles for 4, 12 and 24 hrs. Confocal images with different cell compartment staining kits was used to confirm their localisation at different exposure times and quantification of co-localisation were made by using ImageJ and the JACoP colocalisation plugin. Raman mapping was applied for unlabelled single cells and Raman datasets were analyzed by using unsupervised K-means clustering (KMCA) and principal components (PCA) analysis. The applicability of Raman Spectroscopy was assessed for the determination of the characteristic spectra of subcellular organelles in which nanoparticles are enveloped and trafficked in a comletely label free manner.

3.3. Materials and Methods

3.3.1. Nanoparticles

Commercially available, 40 nm carboxylate-modified and fluorescently labelled polystyrene nanoparticles (F8795) were purchased from Invitrogen (USA). The characteristic properties such as size and emission spectra are supplied by Invitrogen (Thermofisher Scientific, 2015) and have been further characterised in house using a Malvern Zetasizer ZS for size and surface potential measurements, Atomic Force microscopy (AFM) and UV-Vis spectroscopy (Dorney, 2013).

3.3.2. Cell Culture and Cytotoxicity

A549 cells from human lung carcinoma (ATCC number CCL-185) were chosen as a model cell line in this study. Cells were cultured in Dulbecco's Modified Eagle's Medium Nutrient Mixture F-12 HAM (DMEM-F12) with 2 mM L-glutamine and 10% foetal bovine serum (FBS) at 37 °C in 5% CO_2. DMEM-F12 cell culture medium and trypsination solution were purchased from Sigma Aldrich, Ireland. For cytotoxicity evaluation, commonly used Alamar Blue (AB) and 3-(4,5-dimethylthiazol-2-yl)-2,5-diphenyltetrazolium bromide (MTT) assays were purchased from Biosource (UK) and Sigma Aldrich Ltd. (Dublin, Ireland), respectively. Details about cytotoxicity assay and results are given in Supplementary Information (SI.1).

3.3.2.2. Preparation of nano-polystyrene solutions

Polystyrene nanoparticle solutions were prepared by dispersing nanoparticles directly into the 10% FBS and 2 mM L-glutamine supplemented DMEM-F12 medium. The initial stock concentration of the polystyrene nanoparticle solution was chosen as $1x10^{12}$ particles per ml (ppml).

3.3.3. Confocal Laser Scanning Fluorescence Microscopy

3.3.3.1. Sample Preparation for Confocal Microscopy

Samples for CLSM were prepared by seeding approximately 16,000 A549 cells onto 35 mm uncoated glass bottom dishes purchased from MatTek Corporation, USA. For effective adherence of the cells on the glass surface, 200 µl of cell suspension at a density of 16,000 cells were dropped onto the glass surface and incubated for 1 hr. Following 1 hr incubation, 2 ml of DMEM-F12 medium with 10% FBS and 2mM L-glutamine were added, and the cells were incubated for 24 hrs. After 24 hr incubation, the medium was removed and nanoparticles suspended in medium (DMEM-F12 with 10% FBS and 2mM L-glutamine) were added. For all confocal imaging studies, nanoparticle suspensions of concentration $1x10^{12}$ ppml were used. In order to determine the time evolution of the subcellular localisation of nanoparticles, 4, 12 and 24 hrs exposure times were chosen. Following exposure, the medium containing nanoparticles was removed and the cells were rinsed with PBS and the samples were imaged in sterile 0.9% NaCl saline solution.

3.3.3.2. Confocal Fluorescence Imaging of Cell Compartments

Lysotracker (Red DND-99), Endoplasmic Reticulum (ER)-Tracker and Cell Light Early Endosome-RFP Bacmam 2.0 stains were purchased from Life Technologies, Ireland. All organelle stains were prepared according to manufacturer's instructions. 200 µl of A549 cells suspension at a density of 16,000 cells were seeded onto the glass bottom dishes and cells were incubated for 1 hr. After initial attachment, 2 ml of DMEM-F12 medium with supplements were added. The cells were incubated overnight at 37 °C in 5% CO_2. The culture medium was then removed and the cells were exposed to the nanoparticle solution of concentration $1x10^{12}$ ppml for 4, 12 and 24 hrs. For Lysotracker and ER stains, the effective concentrations used were 75 nM and 1 µM, respectively, according to manufacturer instructions, and probes were diluted to final concentrations from their stocks. Medium, containing nanoparticles, was removed from the dishes and the pre-warmed (37 °C) medium containing the cellular stains was added separately. Cells were then incubated for 30 min at 37 °C in 5% CO_2. After incubation, the stain containing medium was removed and the dishes were rinsed with PBS three times. Confocal images were captured in sterile pre-warmed PBS saline solution. For endosomal staining, cells were seeded onto the glass bottom dishes with the same density with other staining and 2 ml of DMEM-F12 medium was added following the initial attachment. After 24 hour, cells were exposed to CellLight Reagent BacMam 2.0-RFP for 16 hrs at 37 °C for expression of Red fluorescent protein. Cells were exposed to the polystyrene particles prepared in pre-warmed medium at 37 °C with a concentration of $1x10^{12}$ ppml for 4 hours. After 4 hr particle exposure, cells were washed three times with PBS and observed in PBS.

For confocal imaging of nanoparticles and organelles within the cell, an inverted Zeiss LSM510 Meta, confocal laser scanning microscope (Carl Zeiss Inc.) equipped with a x60 oil immersion objective and Argon (488 nm) and HeNe (543 nm) lasers was used to determine the localisation of polystyrene nanoparticles within cell compartments. Table 3.1 lists the absorption and emission characteristics for the target species.

A 505-530 nm band pass filter was used to collect the fluorescence of 40 nm carboxylated and fluorescently labelled polystyrene nanoparticles. In order to observe nanoparticle localisation within intracellular compartments, images were acquired by using the combination of a 505-530 nm band pass filter to collect the fluorescence of nanoparticles and a 560 nm long pass filter for the organelle staining dye fluorescence. Analysis of images was carried out using LSM 510 software and quantification of colocalisation was calculated using the JACoP colocalisation plugin with ImageJ.

Table 3.1. Spectral Characteristics of 40 nm carboxylated and fluorescently labelled polystyrene nanoparticles and organelle probes.

Organelle Probes	Abs*(nm)	Em*(nm)
40 nm carboxylated-nanoparticles	505	515
Lysotracker®Red DND-99	577	590
ER-Tracker™	587	615
Cell Light® Early Endosome-RFP Bacmam 2.0	543	560

3.3.4. Raman Spectroscopy

3.3.4.1. Sample preparation for Raman Spectroscopy

To prepare samples for Raman spectroscopic analysis, approximately 16,000 cells per substrate were seeded on CaF_2 slides and they were incubated for 24 hrs in 2 mls 10% FBS DMEM - F12 medium at 37 °C in 5% CO_2. After 24 hrs, the medium was removed and 40 nm polystyrene nanoparticles suspended in 10% FBS DMEM - F12 media were added. A549 cells were exposed to the nanoparticles for 4, 12 and 24 hrs. A concentration of $1x10^{12}$ ppml was used for 24 hr exposure. The exposure time affects the degree of uptake of nanoparticles, aggregate formation and thus the intensity of the characteristic Raman bands of polystyrene nanoparticles, and therefore doses of $5x10^{12}$ ppml were chosen to achieve clearer spectra for earlier exposure times. Following nanoparticle exposure, cells were rinsed three times with PBS and fixed with 10%

formalin for 10 min. Cells were washed with water to remove formalin and spectra were acquired in water.

In this study, a Horiba Jobin-Yvon LabRAM HR800 spectrometer equipped with a 785 nm diode laser was used. All measurements were acquired by using a x100 water immersion objective (LUMPlanF1, Olympus, N.A. 1), producing a spotsize on the sample of ~1μm. Before spectral acquisition, the system was calibrated to the 520.7 cm^{-1} line of silicon. A 300 lines per mm grating (approximately 1.5 cm^{-1} per pixel spectral dispersion) and a 100 μm confocal pinhole were used throughout this study. The spectra were dispersed onto a 16-bit dynamic range Peltier cooled CCD detector. All white-light images of the cells were taken by using the integrated video camera. Raman maps were acquired over selected areas. Spectra were acquired for 2 x 10 seconds per spot, to achieve acceptable signal to noise ratios. The spectral range was chosen from 400 to 1800 cm^{-1}. The step size between two measurements was set to 1 μm for all exposure times.

3.3.5. Data Analysis

Unsupervised KMCA and PCA were performed on different Raman data sets by using Matlab (Mathworks, USA) in order to extract information from complex and huge datasets. Data pre-processing was also carried out using Matlab. First, mild smoothing by using a Savitsky-Golay filter (3th order, 9 points) was applied to lightly smooth the data. The background, predominantly water in the immersion geometry, was subtracted with unsupervised Classical Least Squares (CLS) analysis to minimize the possible background contributions into the spectra (Draux *et al.*, 2009). Following

smoothing and background subtraction, spectra were vector normalized before analysis to improve spectral quality.

KMCA, considered the simplest unsupervised learning algorithm, was used as a first step of spectral map analysis. It is a spectral image analysis technique which uses the similarities in the spectra to form clusters; each representing the specific biomolecular signature of a selected area. Briefly, in KMCA, the number of clusters (k) is defined *a priori* by the operator to initialize the classification. K centroids were formed by the programme randomly but as far as possible from each other and then each point around centroids is associated the nearest point on data set for initial classification. Following initial classification, barycentres are formed by rearranging the first centroids and the process continues until convergence is reached and there is no further change in the centroids. The final k-means clusters and associated mean spectra give information about molecular similarities within data sets and can be used to differentiate regions with different molecular features.

For further analysis, PCA was employed to examine and differentiate the spectral characteristics of specific k-means clusters. Thus, PCA was used to highlight the changes on the biochemical composition based on nanoparticle exposure which may clarify the mode of interaction and particle localisation with cells. Specifically, the loadings of the PC were used to identify and differentiate the spectroscopic signatures of the different cell compartments in which the nanoparticles are localised, including early endosomes, lysosomes and endoplasmic reticulum.

3.4. Results and Discussion

3.4.1. Nanoparticle Cytotoxicity

In advance of further analysis, the cytotoxicity of the polystyrene nanoparticles to the cells over the range of doses and exposure times employed was examined using standard cytotoxic assays, as described in the Supplemental Material (3.S1). Consistent with previous reports for neutral and carboxylated polystyrene particles (Dorney *et al.*, 2012), no significant cytotoxicity was recorded.

3.4.2. Confocal Laser Scanning fluorescence microscopy

Because the uptake of nanoparticles within a cell population is a continuous process, it is possible to observe the progressive trafficking through different cell compartments as a function of incubation time. The intracellular localisation of particles as a function of nanoparticle exposure time was examined using CLSM. Cells were exposed to a dose of $1x10^{12}$ ppml of media for 4, 12 and 24 hrs. Localisation of fluorescently labelled and carboxylated polystyrene nanoparticles in the perinuclear region of A549 cells after 24 hr particle exposure has previously been shown by Dorney et. al..

In order to determine the localisation of nanoparticles in a more specific manner, organelle staining kits were used to further examine the localisation environment for 24 hrs and earlier exposure times. Cells were exposed to 40 nm carboxylated and fluorescently labelled polystyrene nanoparticles for 24, 12 and 4 hrs. Following the incubation period, the medium was removed, cells were washed with PBS thrice and

cells were incubated with 1 μM Endoplasmic Reticulum staining and 75 nM Lysotracker for 30 min. For early endosome staining, cells were exposed to CellLight BacMam 2.0 reagent for 16 hrs at 37 °C after initial 24 hr incubation. After incubation with the organelle staining agents, cells were washed with PBS and observed in NaCl solution.

To demonstrate the amount of co-localisation of the nanomaterial within the different subcellular compartments, fluorescent images of polystyrene particles and organelle staining and their overlay images were recorded for each incubation time. An example of the images taken for each exposure time and organelle staining are shown in Figure 3.1 and Figure 3.2. These images were then used to quantify the degree of co-localization of polystyrene nanoparticles and cellular compartments. The overall calculation of colocalisation coefficients was made based on the average of 3 images for each particle exposure time and organelle staining.

Figure 3.1 shows the CLSM images of A549 cells after 24 and 12 hr particle exposure (green) with Lysosome and Endoplasmic Reticulum staining (red). Co-localisation is indicted by yellow/orange colouring. The confocal images of 40 nm carboxylated polystyrene particles indicate that, although some of the particles localise in the lysosomes after 24 hr incubation (Figure 3.1A), the nanoparticles are predominantly associated with endoplasmic reticulum at this time point (Figure 3.1B). On the other hand, as seen in Figure 3.1C, when the exposure time of A549 cells to the polystyrene particles is reduced to 12 hrs, most of the particles are observed in the lysosomes and, there is less co-localization with the ER at this time point (Figure 3.1D). The small

amount of co-localisation in lysosomes at the 24 hr time point and the ER at the 12 hr time point demonstrates the continuity of the trafficking process.

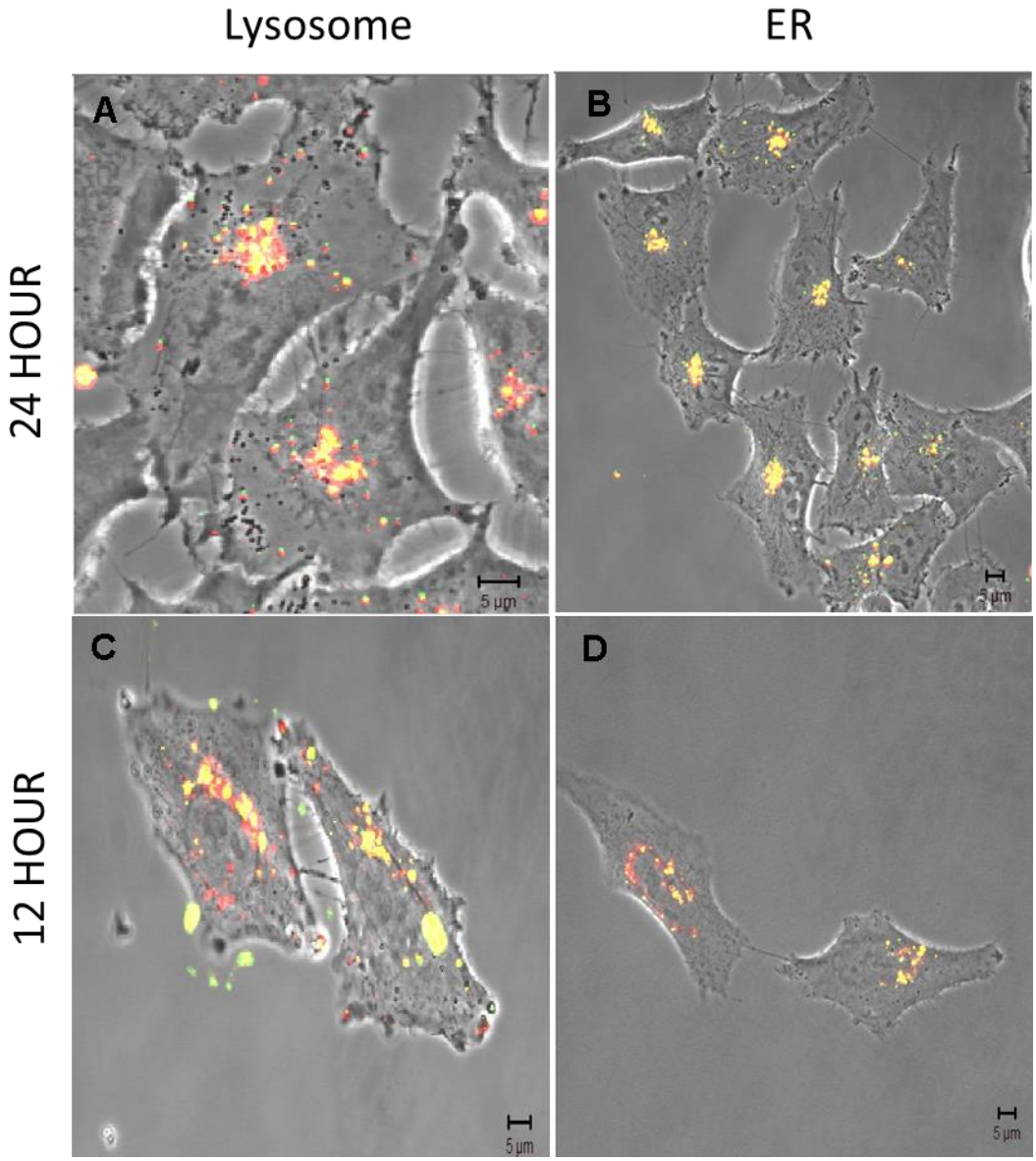

Figure 3.1. Confocal Images of 40 nm carboxylated polystyrene nanoparticles (green) and lysosomes (red) of A549 cells after 24 hours (A) and 12 hours (C), confocal images of 40nm carboxylated polystyrene nanoparticles (green) and endoplasmic reticulum (red) of A549 cells after 24 hours (B) and 12 hours (D) x60 magnification. Co-localisation is indicated by yellow/orange.

After 4 hr exposure, the nanoparticles are seen to be more diffusely distributed throughout the cytoplasm, as shown in Figure 3.2. Figure 3.2A shows some degree of co-localization with lysosomes, whereas Figure 3.2B demonstrates that there is a significantly higher amount of co-localization in endosomes.

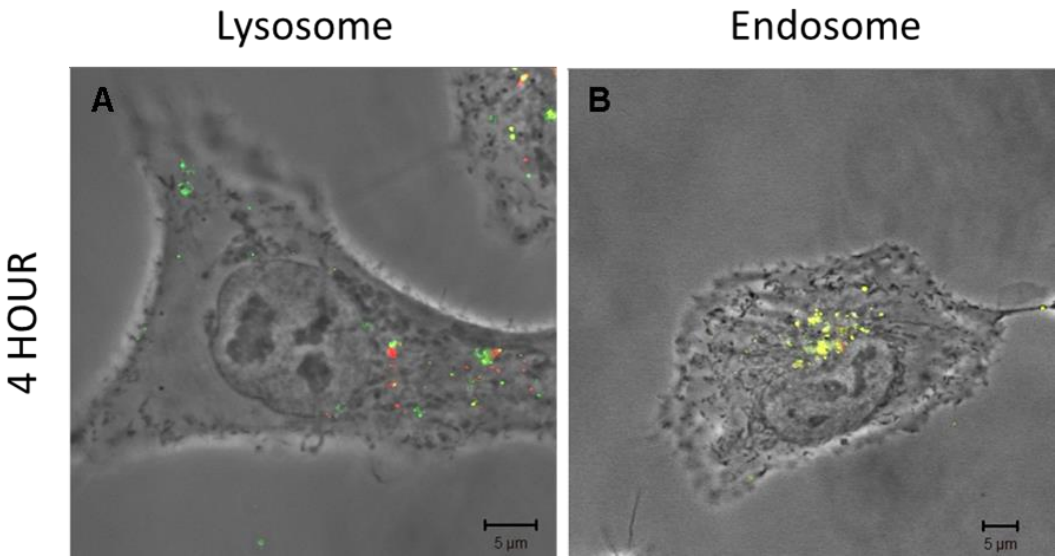

Figure 3.2. Confocal Images of 40nm carboxylated polystyrene nanoparticles (green) and lysosomes (red) of A549 cells after 4 hours (A), confocal images of 40 nm carboxylated polystyrene nanoparticles (green) and early endosome stain (red) of A549 cells after 4 hours (B) x60 magnification. Co-localisation is indicated by yellow/orange.

Quantification of the degree of subcellular organelle colocalisation at the chosen exposure periods was performed by using the JACoP plugin of ImageJ (Bolte *et al.*, 2006). The quantification of co-localization relies on the estimation of overlay in stained sections with at least two different fluorescent dyes. In the current study, the multicolour confocal microscopic images of green fluorescent polystyrene particles and organelle staining kits were used to obtain quantitative amount of overlay. Even

though co-localization can be due to the close physical proximity of different labelled species, it can clarify the common localisation points for nanoparticles within the cell. The preparation steps, image acquisition and pre-process of images play an important role in achieving a precise quantification of co-localisation. Therefore, all acquired images were subjected to background correction. Co-localisation coefficients were calculated for background corrected images. Pearson's coefficient and Mander's coefficients were used to calculate the quantitative amount of co-localisation. As seen in Table 3.2, 90% of early endosomes contain polystyrene nanoparticles after 4 hr exposure. When cells are exposed to the nanoparticles, all particles are not taken up by cell at the same time. Therefore, 52% of lysosomes contain polystyrene nanoparticles at the same incubation time. 72% of lysosomes are associated with nanoparticles after 12 hr incubation, while, when cells were exposed to nanoparticles for 24 hrs, this amount was reduced to 53%. On the other hand, the amount of endoplasmic reticulum which contains nanoparticles was calculated as 58% after 12 hr incubation, whereas this amount increased to 80% after 24 hrs.

Table 3.2. Quantification of Co-localisation of Nanoparticles with Cellular Structures.

	Exposure Time(hr)	**Pearson Coefficient(r)**	**Overlap Coefficient(R)**	**k_1&k_2**	**Mander's Coefficient(M)**
Early Endosome	4	0.919	0.965	k1=1.107 k2=0.84	M=0.911
Lysosome	4	0.471	0.816	k1=1.222 k2=0.546	M=0.521
	12	0.837	0.945	k1=0.954 k2=0.936	M=0.72
	24	0.665	0.892	k1=1.165 k2=0.682	M=0.53
ER	12	0.794	0.923	k1=1.201 k2=0.713	M=0.58
	24	0.832	0.921	k1=1.0 k2=0.837	M=0.80

3.4.3. Raman Spectroscopy

Having confirmed the intracellular localisation of the nanoparticles at different exposure times using CLSM, Raman spectroscopy was employed to establish the spectroscopic signatures of the environment of the respective subcellular organelles. The software of the instrument (LabSpec6) allows the mapping of customized areas and when the total acquisition time for spectral maps and step size was considered, the

total mapping time for each selected area of the cell was around 2-5 hrs. The use of selected areas instead of whole cell mapping decreases the total map acquisition time which provides stable conditions and increases sample integrity with higher resolution of the cellular compartments with small step sizes.

Polystyrene nanoparticles exhibit a characteristic Raman spectrum, as shown in Figure 3.3 II. They exhibit a strong Raman spectral signature, and the peaks around 620 cm^{-1}, 1001 cm^{-1}, 1031 cm^{-1}, 1182 cm^{-1}, 1399 cm^{-1}, 1583 $cm^{-1}$and 1602 cm^{-1}. Therefore, they can easily be identified within the cells (Dorney *et al.*, 2012). A combination of multivariate analysis techniques can then be employed to extract the spectroscopic signatures of the subcellular environment of the cell.

After spectral maps were acquired, the data was analysed using KMCA and PCA in the Matlab platform. Before analysis, mild smoothing and normalisation were applied to the spectra to improve spectral quality (Section 2.5). The background, predominantly water in the immersion geometry (Bonnier *et al.*, 2011), was subtracted with Classical Least Squares (CLS) analysis. Following the pre-processing of data, KMCA was used to determine the localisation of nanoparticles within cells and PCA was applied to gain further information about the environment of the nanoparticles within the cell. The applicability of Raman spectroscopy with the aid of KMCA and PCA to differentiate different cellular regions as well as presence of particles within the cell after 24 hr exposure has been shown and the results of the study were similar to Raman spectral maps of an A549 cell which were used as control in our study (Data not shown) (Dorney *et al.*, 2012; Bonnier *et al.*, 2010). Once the nanoparticles were identified within the cells, in order to analyse the spectral signature of the subcellular

environment further, the raw polystyrene spectrum was subtracted from the spectra of the K-means clusters associated with the polystyrene and polystyrene environment by using Non-negative least squares (NNLS) analysis. The underlying spectral signatures were further analysed using PCA, and the signatures for each time point are compared.

The Raman spectral map of an A549 cell acquired following 24 hr particle exposure is shown in Figure 3.3. The white-light image of cells was obtained using the x100 immersion objective and the mapping area is indicated by the black line (Figure 3.3 IA). The mapping area, which includes the perinuclear region and neighbouring cytoplasm, was chosen according to the expected particle localisation area indicated by confocal microscopy to reduce the mapping time (Figure 3.1). The KMCA clearly differentiates a large perinuclear region (cluster 10, red in Figure 3.3 IB), as well as other regions of the neighbouring cytoplasm. A single K-means cluster containing clear signatures of polystyrene (PS) nanoparticles was clearly identified, as seen in Figure 3.3 II (cluster 6, pink in Figure 3.3 IB). For 24 hr particle exposure, most of the particles were observed in the perinuclear region which is consistent with the CLSM results (Figure 3.1 and Table 3.2). However, a few particles were observed in different K-means clusters of the neighbouring cytoplasm due to the continuity of particle uptake over 24 hrs. Some particles can be taken up later by the cell resulting in localisation in other subcellular vesicles such as lysosomes in the outer cytoplasmic area (cluster 1 and 7) as seen in Figure 3.1 and Table 3.2. When the mean spectra of K-means clusters were compared, characteristic polystyrene bands were clearly observed with high intensity in cluster 6, compared to cluster 10 (Figure 3.3 II). Grey shading is used to identify polystyrene related bands. Notably, polystyrene bands with low intensity were also observed in the mean spectrum of the polystyrene environment.

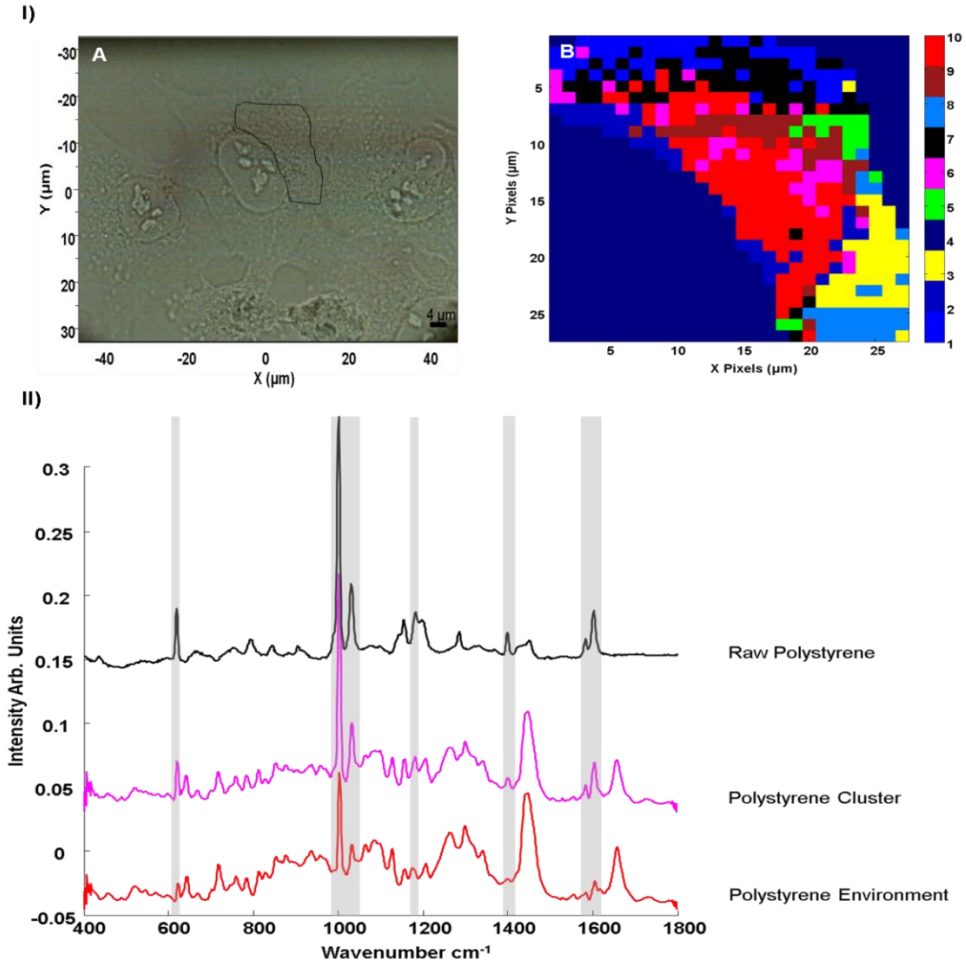

Figure 3.3. **I**(A) Typical white-light microscope image of an A549 cell after 24 hour exposure. The selected area defined by the black line indicates the area selected for Raman mapping (B), Example of K-means reconstructed image from a Raman map on the selected area of an A549 cell including the polystyrene environment, polystyrene cluster and cytoplasm. **II);** Raman spectrum of raw polystyrene nanoparticle and mean spectrum calculated for the different clusters obtained after K-means clustering which correspond to polystyrene cluster (Cluster 6, pink) and polystyrene environment (Cluster 10, red). Grey shading is used as a guide for polystyrene related peaks in the mean spectra. Spectra are offset for clarity.

PCA was carried out to further explore the differentiation between the polystyrene cluster (K-means Cluster 6, pink) and polystyrene subcellular environment (K-means

cluster 10, red). Figure 3.4 IA shows the scatter plot of the PCA of spectra which correspond to the clusters. The KMCA cluster which is associated with polystyrene nanoparticles (pink) is clearly differentiated from that of the nanoparticle environment (red), according to PC1, the loading of which is dominated by negative features corresponding to the spectrum of raw polystyrene, indicated by the grey shading in Figure 3.4 IIA. On the other hand, the positive loading of PC1 provides information about the biochemical composition of the polystyrene environment and many peaks can be clearly observed which can be attributed to specific biochemical constituents: features at 718-733 $cm^{-1}$are related to lipids and nucleic acids, 1231-1284 cm^{-1} to nucleic acids, lipids and proteins and several bands between 1400-1600 cm^{-1} are related to proteins and lipids and the Amide I of proteins features strongly at 1600 cm^{-1} (Figure 3.4 IIA) (Notingher *et al.*, 2003; Notingher *et al.*, 2006; Movasaghi *et al.*, 2007).

It is noted that some spectra identified by KMCA as neighbouring environment can be seen in the negative side of scatter plot, indicating polystyrene contributions to the spectra which is similar to the observations of Dorney *et al.* (2012). KMCA is a hard clustering algorithm which clusters spectra of similar character but does not account for mixed contributions. PCA clearly indicates contributions of PS in these spectra. In order to show the contribution of the raw polystyrene spectrum in the environment cluster, the raw polystyrene spectrum was subtracted from the spectra of the environmental cluster by using CLS (Supplementary Information 3.S2). After polystyrene subtraction from the spectra of the environment cluster, the explained variance was increased from 42% to 62% and the spectra of the two clusters were better separated and clustered.

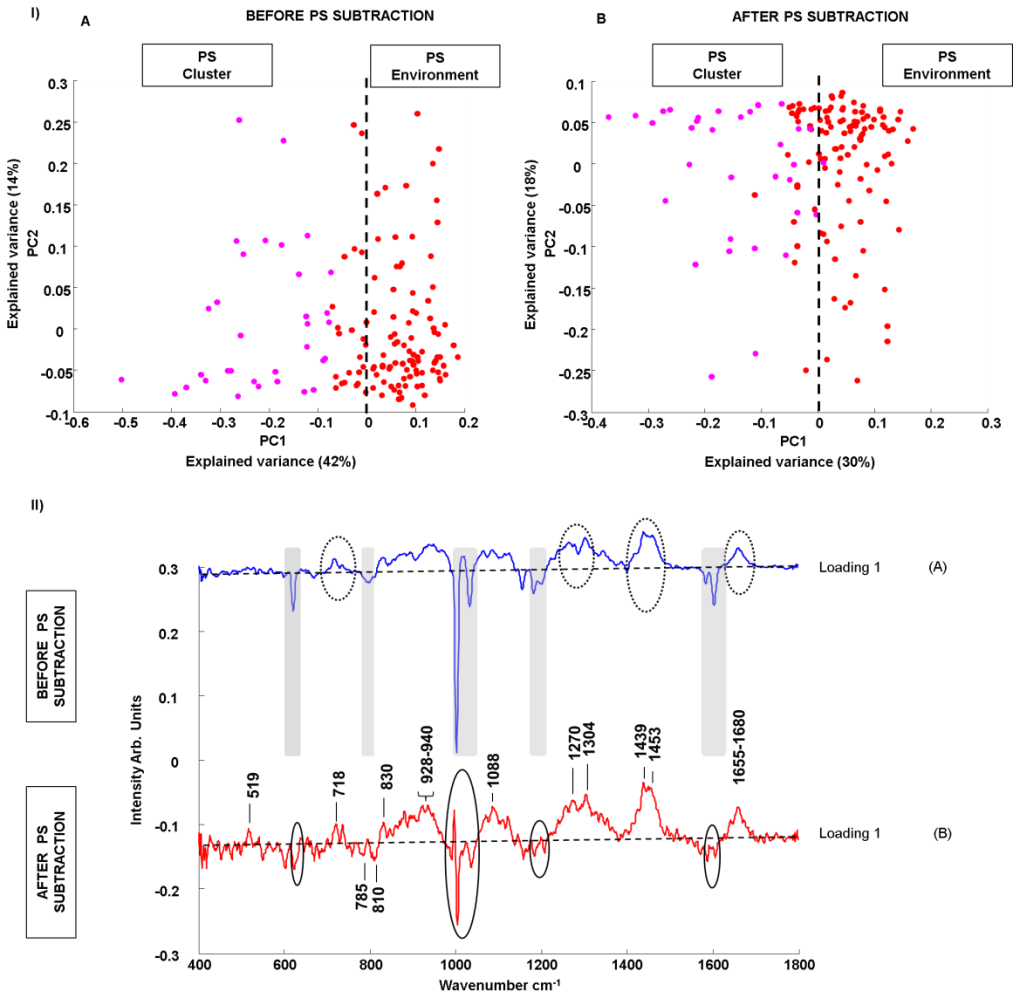

Figure 3.4. **I**(A), Scatter plot of the PCA of spectra corresponding to the KMCA clusters of polystyrene (pink) and polystyrene environment (red) for 24 hour particle exposure before PS subtraction. (B), Scatter plot of the PCA of spectra corresponding to polystyrene nanoparticles and polystyrene environment after raw polystyrene spectrum subtracted for 24 hour particle exposure. **II);** Loading of PC1 before (A) and after (B) polystyrene subtraction. In the loading of PC1 before PS subtraction, characteristic peaks of polystyrene are highlighted with grey and bands which can be attributed to the presence of nucleic acids, proteins and lipids were indicated with black circles (A). In the loading of PC1 of polystyrene cluster and polystyrene environment after PS subtraction, possible polystyrene residues are

indicated with black circles and band assignments are made according to Table 3.3 (B). Spectra are offset for clarity. The dotted line represents the '0' line for each loading.

In order to further elucidate the spectroscopic signatures of the neighbouring environment and the area which includes polystyrene nanoparticles, the raw spectrum of polystyrene was subtracted from the spectra of each of the respective K-means clusters. Figure 3.4 IB shows the scatter plot of the PCA of spectra after subtraction of the raw polystyrene spectrum from both the polystyrene and neighbouring environment clusters. After subtraction, the explained variance in the scatter plot of the PCA was reduced to 30% from 42%, which indicates that the spectrum of the underlying biological environment of the nanoparticle cluster itself is similar to that of the neighbouring environment cluster. Nevertheless, the two clusters are differentiated negatively and positively with respect to PC1, although again there is some overlap of the environment cluster on the negative side. In order to compare spectral differences between spectra which are loaded positively and negatively with respect to PC1, mean spectra related to PC1≥0 and PC1<0 are calculated. Figure 3.5 presents the mean of all points which score positively (PS neighbouring environment) or negatively (underlying PS biological environment) with respect to PC1 in Figure 3.4 IB. Residual PS is clearly evidenced in both spectra by the feature at ~1004cm^{-1}. Moreover, polystyrene bands at 620 cm^{-1} and 1600 cm^{-1} are observed in the mean spectra of the underlying PS biological environment. The specific differences between the spectra of the underlying PS biological environment and the neighbouring environment are better visualised in the PC loading after raw polystyrene subtraction, shown in Figure 3.4 IIB.

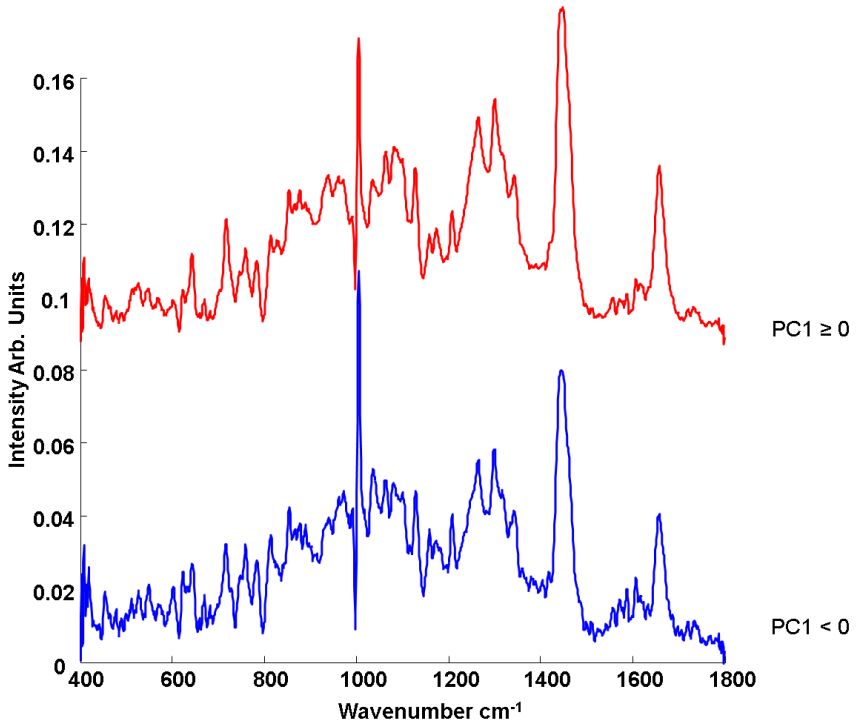

Figure 3.5. Mean spectra of PS environment cluster (Loading of PC1 ≥0) and PS cluster (Loading of PC1< 0) after PS subtraction for 24 hour exposure. Spectra are offset for clarity.

The bands observed in the loading of PC1 can be attributed to differences in the biological environment underlying the polystyrene cluster and the neighbouring environment cluster. Although subtraction of the raw polystyrene spectrum has significantly reduced the negative differentiating features of the raw polystyrene spectrum, some residual polystyrene bands can be observed after subtraction due to the high variability of the intensity of bands in the large Raman map data sets. Therefore, in Figure 3.4 IIB, possible residues of polystyrene bands at 620 cm^{-1}, 1001 cm^{-1}, 1182 cm^{-1} and 1602 cm^{-1} are indicated with black circles and they are excluded from band assignments.

When the bands in the loading of PC1 after raw polystyrene subtraction are analysed in further detail, it can be seen that the positive contributions which relate to the neighbouring PS environment are dominated by bands at 519 cm^{-1}, 718 cm^{-1}, which are indicative of the presence of phosphatidylinositol and membrane lipids, respectively. Moreover, the bands at around 1088 cm^{-1}, 1270 cm^{-1},1304 cm^{-1} and 1439 cm^{-1}, are also associated with lipids, while protein related bands are observed at ~830 cm^{-1}, 928-940 cm^{-1} and 1453 cm^{-1}. The band around 1660 cm^{-1} can be attributed to the Amide I (C-N stretch) of proteins, but also in the same region, bands in the range between 1655 - 1680 cm^{-1} can be attributed to C=O stretch of lipids (Figure 3.4 IIB)(Notingher *et al.*, 2003; Notingher *et al.*, 2006; Movasaghi *et al.*, 2007). On the other hand, the negative loading of PC1 is dominated by polystyrene features with two bands which can be attributed to the presence of RNA, necessary for protein synthesis, at 785 cm^{-1} and 810 cm^{-1}. When the results are compared with the CLSM results, it is clear to say that particles localise in a perinuclear area which is rich in lipid and protein content. The endoplasmic reticulum is known to be the largest organelle within cells with varying size depending on cell type (generally more than 10% of cell composition) and the spatially organized structure of the endoplasmic reticulum is mainly located in the perinuclear region (Terasaki *et al.*, 1991), and thus the underlying spectral signature can be associated with that of the endoplasmic reticulum (Figure 3.4 IIB and Table 3.3).

Table 3.3. Band assignments related to polystyrene cluster and polystyrene environment after 24 hour particle exposure (Notingher *et al.*, 2003; Notingher *et al.*, 2006; Movasaghi *et al.*, 2007).

Band Assignment (cm^{-1})	**Polystyrene Cluster**	**Polystyrene Environment**
519	-	Phosphatidylinositol
718	-	Membrane lipids
785	RNA	-
810	Nucleic acids	-
830	-	Proteins
928-940	-	Proteins
1088	-	Lipids
1270	-	Proteins&Lipids
1304	-	Lipids
1439	-	Lipids
1453	-	Proteins
1655-1680	-	Proteins&Lipids

After polystyrene particles are taken up by cell, they are carried to lysosomes by endosomes and, after 12 hrs, they mainly localize in lysosomes, as seen in Table 3.2, and Figure 3.1. For this reason, the second exposure time to examine the particle localisation and neighbouring environment within the cell using Raman spectroscopy was chosen as 12 hrs and Raman maps were acquired as before from A549 cells (Figure 3.6). As seen in the CLSM images (Figure 3.1), the distribution of lysosomes within the cell is much wider than the endoplasmic reticulum. Therefore, the customised Raman mapping area was chosen to be larger for 12 hr exposure time compared to the 24 hr exposure (Figure 3.6 IA). The selected area for mapping shows K-means clustering due to the influence of different thickness of the nucleus,

cytoplasm and the edge of cell. When the mapped area includes the edge and outside of the cell, the use of higher number of clusters is needed because of the variety in composition (Dorney *et al.*, 2012). In the 12 hr data set, the customised area was composed of the nuclear area and inner cytoplasm (Figure 3.6 IA). For this reason, 6 different clusters of K-means were used to determine the polystyrene localisation. As seen in Figure 3.6 IB, a number of distinct clusters were identified and polystyrene nanoparticles are clearly identifiable in the mean spectra of cluster 5 (brown), compared to the neighbouring environment of cluster 3 (green) (Figure 3.6 II.).

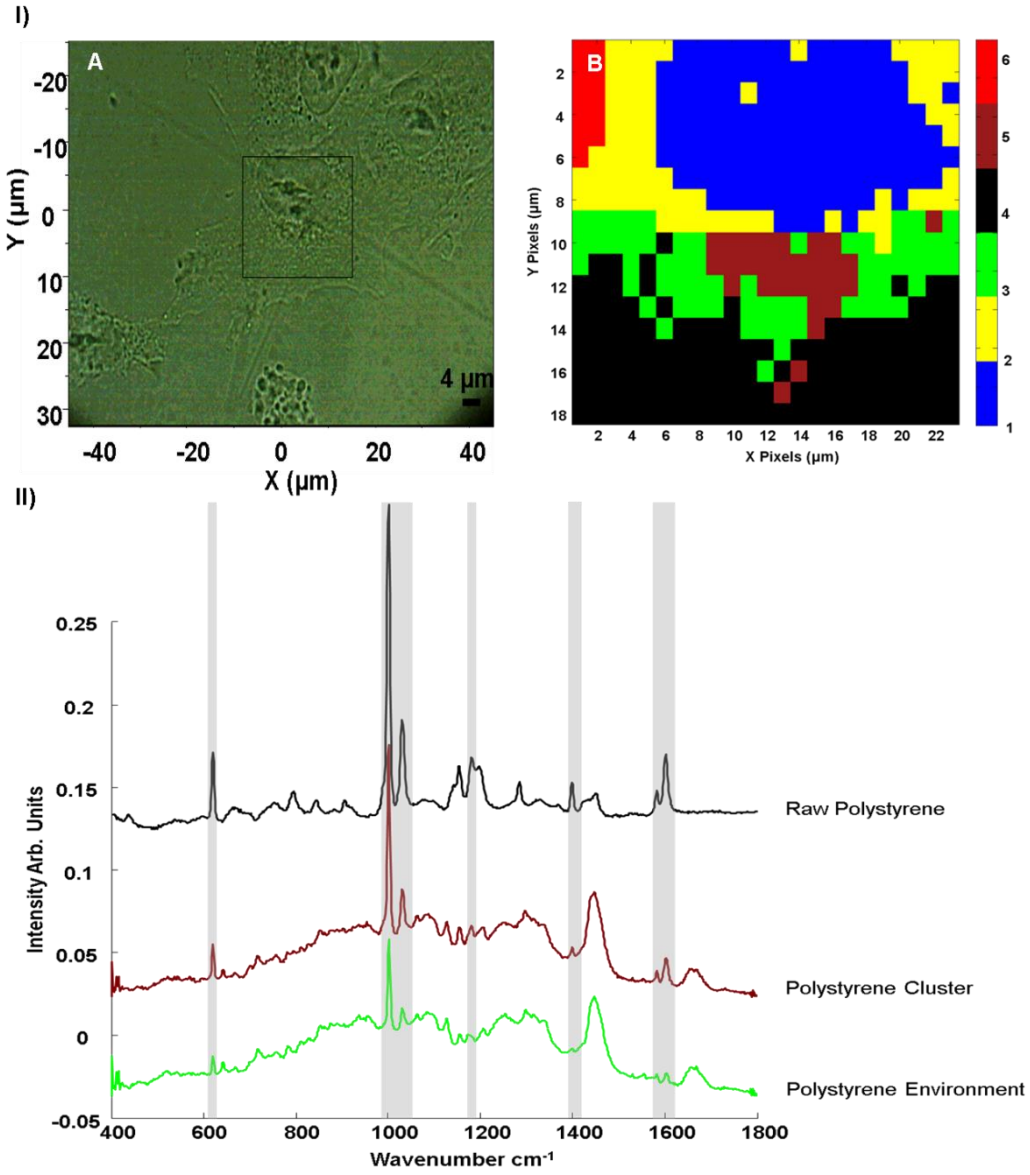

Figure 3.6. **I**(A) Typical white-light microscope image of an A549 cell after 12 hour exposure. The selected area defined by the black line indicates the area selected for Raman mapping (B), Example of K-means reconstructed image from a Raman map on the selected area of an A549 cell including the polystyrene environment, polystyrene cluster and cytoplasm and nucleus. **II);** Raman spectrum of raw polystyrene nanoparticle and mean spectrum calculated for the different clusters obtained after K-means clustering which correspond to polystyrene cluster (Cluster 5, brown) and polystyrene environment (Cluster 3, green). Grey shading is used as a guide for polystyrene related peaks in the mean spectra. Spectra are offset for clarity.

Figure 3.7 IA shows the PCA scatter plot of the spectra associated by KMCA with the polystyrene nanoparticles (Cluster 5, brown) and their neighbouring environment (Cluster 3, green) for 12 hr exposure, colour coded as per Figure 3.6 IB. The clusters are well differentiated according to the loading of PC1 (44% Explained Variance) and the loading is dominated by strong negative peaks of polystyrene at 620 cm^{-1}, 800 cm^{-1}, 1001 cm^{-1}, 1031 cm^{-1}, 1182 cm^{-1}, 1583 cm^{-1} and 1602 cm^{-1}, as shown in Figure 3.7 IIA. As was observed for the 24 hr exposure data set, some spectra of the polystyrene neighbouring environment KMCA cluster are identified by PCA as containing strong polystyrene contributions, in addition to cellular Raman bands at 1280 cm^{-1} and 1439 cm^{-1}, which are related to the Amide III of proteins and lipids, respectively (Notingher *et al.*, 2003; Notingher *et al.*, 2006; Movasaghi *et al.*, 2007). When the polystyrene spectrum is subtracted from the spectra of the polystyrene neighbouring environment cluster, the explained variance is increased to 60% and the spectra related to the polystyrene environment cluster became significantly differentiated from the polystyrene cluster in the scatter plot (Supplementary Information Figure 3.S2).

In order to extract information about the underlying biochemical composition of the polystyrene cluster which possibly derives from the lysosomal biochemical content, the raw polystyrene spectrum was subtracted from both the spectra of the polystyrene cluster and the polystyrene neighbouring environment cluster of the 12 hr exposure data set. The explained variance of the PCA scatter plot is reduced to 26% from 44%, as seen in Figure 3.7 IB.

Lysosomes can typically vary from 0.1 to 1.2 μm in size (Kuehnel, 2003). Whereas the Raman spot size is significantly smaller that the ER, it is comparable to the size of the

lysosomes and thus a more significant contrast may be expected between the underlying biological content of the PS cluster, which should be characteristic of lysosomes and their neighbouring environment, the cytoplasm.

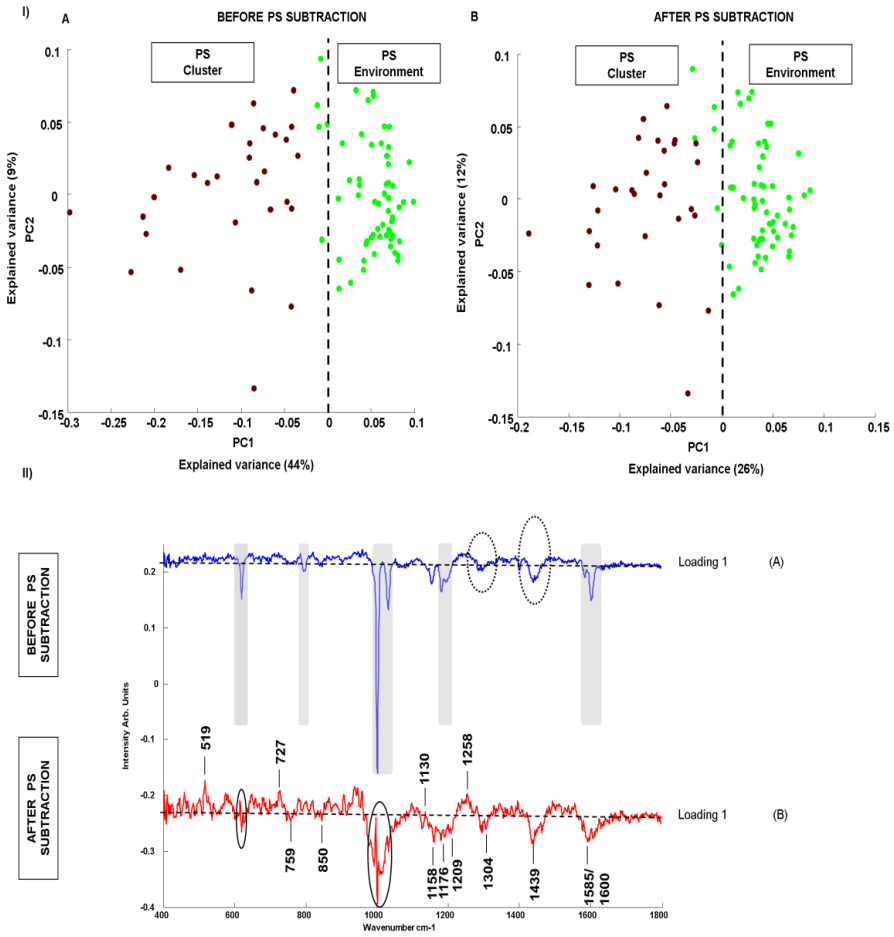

Figure 3.7. **I**(A), Scatter plot of the PCA of spectra corresponding to the polystyrene cluster (brown) and polystyrene environment (green) for 12 hour particle exposure before PS subtraction. (B), Scatter plot of the PCA of spectra corresponding to the polystyrene cluster and polystyrene environment for 12 hour particle exposure, after subtraction of the raw polystyrene spectrum. **II);** Loading of PC1 before (A) and after (B) polystyrene subtraction. In the loading of PC 1 before subtraction, characteristic peaks of polystyrene are highlighted with grey and bands which can be attributed to presence of proteins and lipids were indicated with black circles (A). In the loading of PC1 after PS subtraction, possible polystyrene residues are indicated with black circles and band assignments are made according to Table 3.4 (B). Spectra are offset for clarity. The dotted line represents the '0' line for each loading.

Similar to 24 hr exposure data set, although they are well differentiated by PC1, some overspill of the neighbouring environment cluster into the polystyrene cluster is observed, both before and after subtraction of the PS spectrum from that of both clusters. After subtraction, when mean spectra are calculated for the positive and negative sides of PC1, similar spectra are obtained, as shown in Figure 3.8. Moreover, the mean spectrum of the cytoplasm (Cluster 4) is also shown to highlight the similarities of the spectra of the biological environment underlying the polystyrene and the neighbouring environment after 12 hr exposure. Residual PS features are apparent in both spectra, to a lesser extent than for the 24 hr exposure, and some differentiating bands at 1607 and 1617 cm^{-1} which are related to the C=C bond in Tyr, Trp and Phe and a broad band in the range between 1231-1284 cm^{-1} which can be attributed the Amide III (both α-helix and ß-sheet) region of proteins as well as lipids are evident. On the other hand, the most significant differentiating bands for the cytoplasm are observed at 508 and 1254 cm^{-1} which relates to the disulfide bond (S-S stretch) and Amide III (ß-sheet) of proteins. These differentiating bands are best visualised in the loading of PC1 (Figure 3.7 IIB).

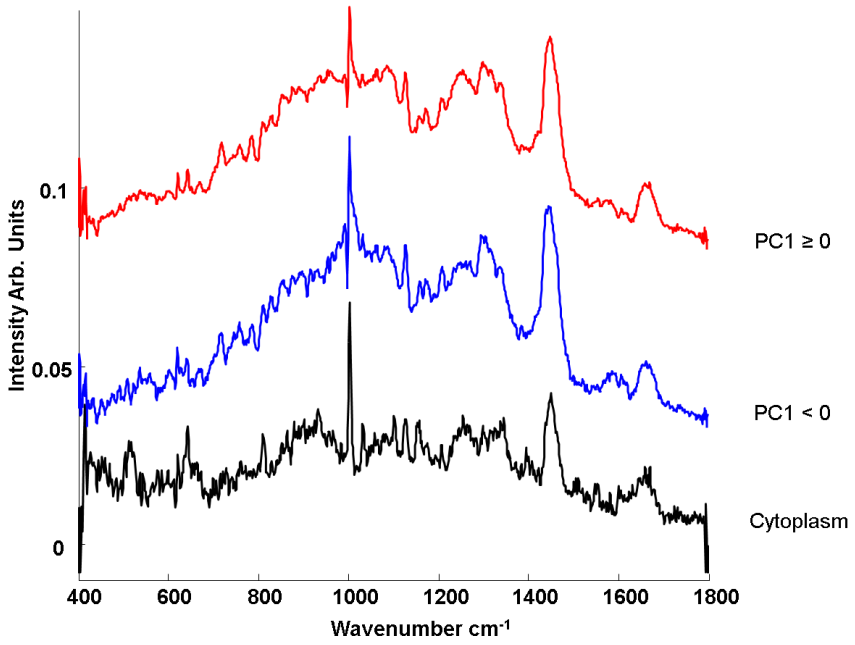

Figure 3.8. Mean spectra of PS environment cluster (Loading of PC1 ≥0, red), PS cluster (Loading of PC 1< 0, blue) after PS subtraction for 12 hour exposure and spectrum of cytoplasm (black). Spectra are offset for clarity.

As seen in Figure 3.7 IIB, some polystyrene residues, indicated by the black circles, at 620 cm^{-1} and 1001 cm^{-1}, remain after subtraction and these are excluded from the band assignments (Table 3.4). Many peaks related to lipids can be seen clearly at 519 cm^{-1} (phosphatidylinositol) and 1130 cm^{-1} (structural changes of phospholipids) in the positive loading of PC1, associated with the spectra of the neighbouring environment (Notingher *et al.*, 2003; Notingher *et al.*, 2006; Movasaghi *et al.*, 2007). Moreover, bands at 727 cm^{-1} and 1258 cm^{-1} (Amide III), which can be attributed to presence of proteins in the neighbouring environment cluster, can be seen in the positive loading of PC1. In contrast to the case for 24 hr exposure, the dominant, negative features of the loading of PC1, associated with the underlying biological content of the PS cluster, feature negative loadings of lipid bands at 759 cm^{-1} (phosphatidylethanolamine), 1304

cm^{-1} and 1439 cm^{-1} (Klein *et al.*, 2012). Even though they are not as dominant as in the 24 hr exposure data, some protein bands can be identified at 850 cm^{-1}, 1158 cm^{-1}, 1176 cm^{-1}, 1209 cm^{-1}, 1600 cm^{-1} (Amide I) in the negative loading of PC1. For the 12 hr exposure data set, the band at 1585 cm^{-1} can be attributed to Phe, which has associated bands across the rest of the spectrum at 1209 cm^{-1} and 1607 cm^{-1}. Also, the wider band around 1010 cm^{-1} compared to the 24 hr exposure data set can be explained by symmetric ring breathing of Phe. Band assignments can be seen in detail in Table 3.4.

Table 3.4. Band assignments related to the underlying biological environment of the polystyrene cluster and the neighbouring polystyrene environment after 12 hour particle exposure (Notingher *et al.*, 2003; Notingher *et al.*, 2006; Movasaghi *et al.*, 2007).

Band Assignment (cm^{-1})	**Polystyrene Cluster**	**Polystyrene Environment**
519	-	Phosphatidylinositol
727	-	Protein
759	phosphatidylethanolamine	-
850	Protein	-
1004	Phe	-
1130	-	Lipids
1158	Protein	-
1176	Protein	-
1209	Protein	-
1258	-	Protein
1304	Lipids	-
1439	Lipids	-
1585-1600	Proteins	-

The band assignments of Figure 3.7 IIB can be used to elucidate the biochemical content of the underlying PS biological environment and the neighbouring environment, which are related to lysosomes and cytoplasm, respectively. The negative bands in the loading of PC1, associated with the polystyrene cluster, indicate the presence of lipids and proteins, as shown in table 3.4. There are some negatively loaded peaks in PC1, associated with the polystyrene cluster, but those that are identifiable are largely associated with high intensity Raman bands of lipids. Notably, there is no indication of the presence of nucleic acids, which were prominent in the environment of the 24 hr exposure (Table 3.3). In the 12 hr exposure data set, the dominance of the negative features of the underlying PS biochemical environment in the loading of PC1 after raw polystyrene subtraction can be attributed to localisation within the higher density lysosomes in cytoplasm, which has quite low Raman signal.

For 4 hr exposure, particles mainly localize in early endosomes, as seen by CLSM with early endosome staining (Figure 3.2) and it has previously been shown that the nanoparticles are largely present in vesicles individually rather than as aggregates, as in the case of lysosomes (Shapero *et al.*, 2011). As a result, the associated Raman signals are significantly lower than at longer exposure times. Moreover, the wide distribution of early endosomes in the cytoplasm and low inherent signal of the relatively thin outer cytoplasm makes the observation of nanoparticles for 4 hr exposure time challenging. Figure 3.9 shows the results of Raman spectral mapping of an A549 cell after 4 hr exposure. The white-light image of the cells was obtained using a x100 immersion objective and the customised mapping area is indicated with the black line (Figure 3.9 IA). The mapping was performed over a larger area and 10 different K-means clusters were used in the analysis. Clusters containing signatures of

PS nanoparticles were identifiable although the suggested polystyrene related clusters (Cluster 8) cover most of the area of the cytoplasm, surrounded by Cluster 4, as seen in Figure 3.9 IB. The presence of polystyrene nanoparticles can be still recognized by the slightly higher intensity of the characteristic bands of polystyrene in some clusters, as shown in Figure 3.9 II. The characteristic polystyrene band at 1004 cm^{-1} overlaps with the band from phenylalanine, and therefore the polystyrene band at 1602 cm^{-1}, which is marked with '*' in Figure 3.9 II, can be used as a clearer indicator band for the presence of polystyrene.

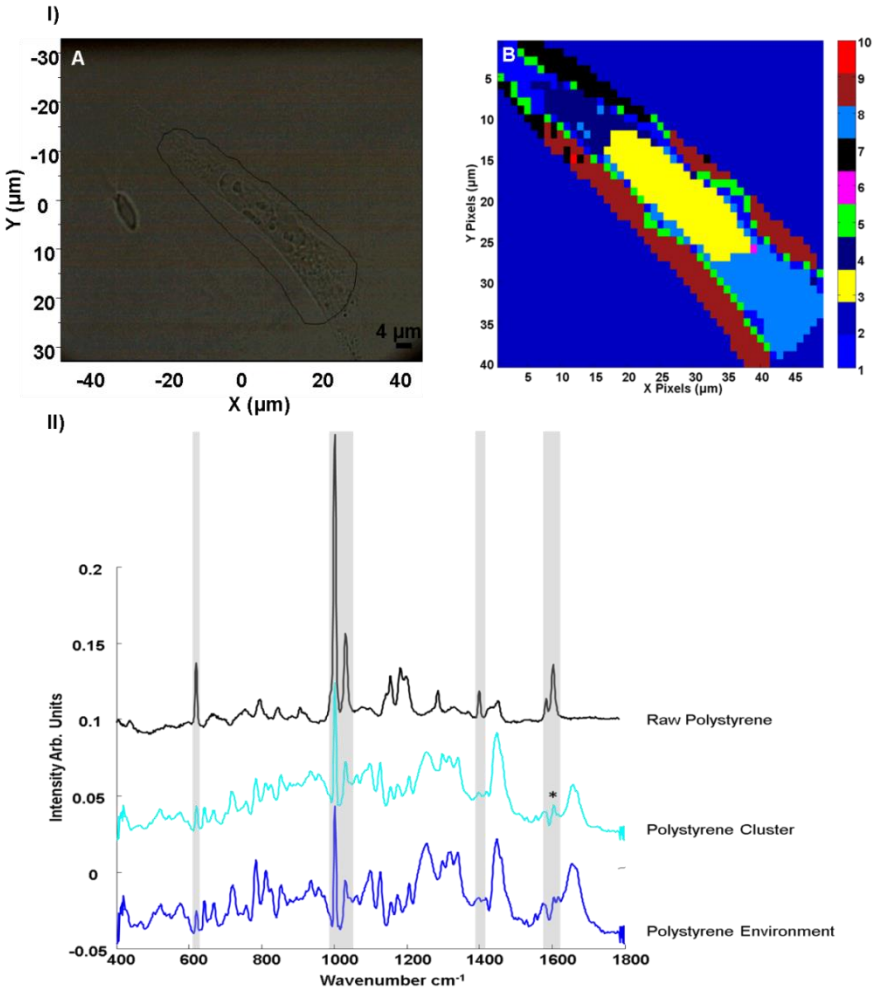

Figure 3.9. **I**(A) Typical white-light microscope image of an A549 cell after 4 hour exposure. The selected area defined by the black line indicates the area selected for Raman mapping (B), Example of K-means reconstructed image from a Raman map on the selected area of an A549 cell including the polystyrene environment, polystyrene cluster and cytoplasm, nucleus and substrate. **II);** Raman spectrum of raw polystyrene nanoparticle and mean spectrum calculated for the different clusters obtained after K-means clustering which correspond to polystyrene cluster (Cluster 8, light blue) and polystyrene environment (Cluster 4, dark blue). Grey shading is used as a guide for polystyrene related peaks in the mean spectra. '*' used as an indicator of polystyrene features in the polystyrene cluster. Spectra are offset for clarity.

Figure 3.10A shows the scatter plot of the PCA of spectra which correspond to clusters identified as having spectral signatures of polystyrene nanoparticles and their neighbouring environment. The KMCA cluster which is associated with polystyrene nanoparticles (Cluster 8, light blue) is largely differentiated from that of the neighbouring environment (Cluster 4, dark blue), according to PC1. As can be seen from the loading of PC1 in Figure 3.10B, however, no strong features associated with polystyrene nanoparticles are observable. Positive features of the loading of PC1 can be seen at 785 cm^{-1} (U, T, C bases of RNA) and 810 cm^{-1} (Phosphodiester Z marker), indicating the presence of nucleic acids. On the other hand, a 1004 cm^{-1} peak relates to protein, a 1280 cm^{-1} peak relates to the Amide III band of proteins and a strong lipid band at 1439 cm^{-1} are observed as negative loadings of PC1. As seen in Figure 3.9 IB, the neighbouring environment cluster (Cluster 4) includes both the outer cytoplasm and perinuclear area. Therefore, the separation according to PC1 reflects the differing subcellular environments rather than the specific environment of polystyrene itself.

The loading of PC2, however, shows some indication of the characteristic polystyrene peaks, although PC2 does not differentiate the two KMCA clusters. Some biochemical signatures of lipids at 718 cm^{-1} (membrane lipids), 1065 cm^{-1}, 1088 cm^{-1}, 1304 cm^{-1}, 1439 cm^{-1} and 1656 cm^{-1}(Phospholipids) can be seen in the positive loading of PC2 while bands at 873 cm^{-1} and 1600 cm^{-1} indicates the presence of proteins. Moreover, the band at 1656 cm^{-1}, indicating the presence of phospholipids in the biological content of the environment cluster, may be associated with the membrane derived structure of early endosomes. A sharp L-α-phosphatidylcholine band at around 790 cm^{-1} is also observed in the negative loading of PC2 (Klein *et al.*, 2012).

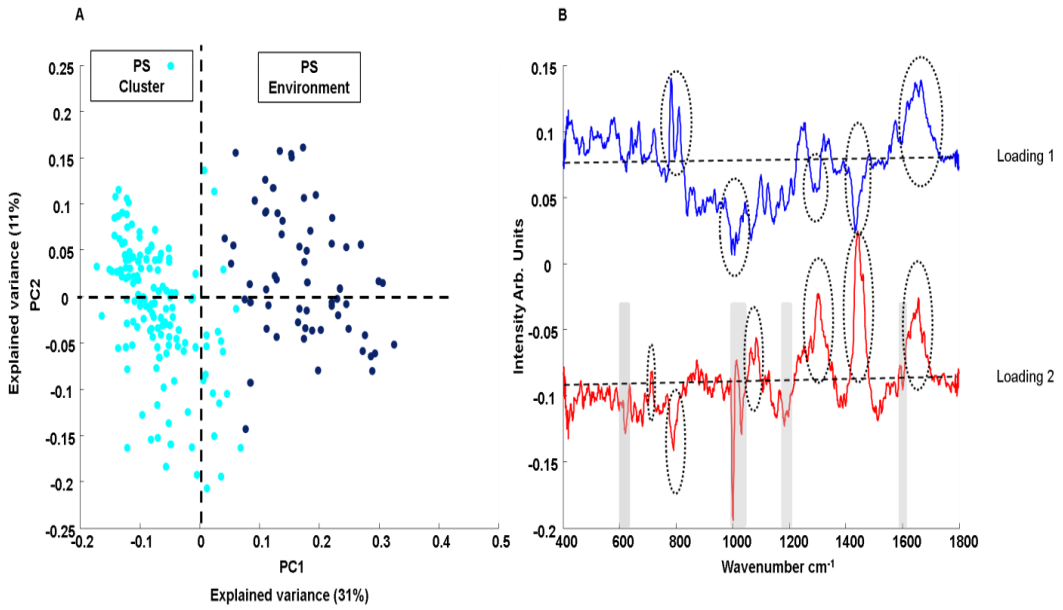

Figure 3.10. (A), Scatter plot of the PCA of spectra corresponding to the polystyrene cluster (Cluster 8, light blue) and polystyrene environment (Cluster 4, dark blue) for 4 hour particle exposure, before PS subtraction (B), Loading of PC1 and PC2 before PS subtraction.

When the size of early endosomes (200-500 µm), the Raman source spot size and step size (1 µm) are considered, contributions to each mapped spot of at least three different spectral profiles can be expected; that of polystyrene, early endosomes and the surrounding cytoplasm. Among these structures, the separation in spectra mainly arises from the biochemical differences of the cytoplasm and early endosomes, rather than the presence of polystyrene nanoparticles, due to the low signal from individual or small clusters of nanoparticles. The spectra of the polystyrene cluster identified by KMCA (Cluster 8) were therefore further analysed on their own using PCA. In the PCA scatter plot of Figure 3.11A, spectra are separated by both PC1 and PC2. Notably, the negative loading of PC2 is clearly dominated by the spectral features of polystyrene (Figure 3.11B, Loading 2), although some cellular molecular signatures are also

present (1158 cm^{-1} related to proteins, 1180 cm^{-1} related to nucleic acids and 1439 cm^{-1} related to lipids). The positive loading of PC2 shows bands which can be attributed to the presence of nucleic acids (~ 785 cm^{-1} and 810 cm^{-1} which are related to RNA and phosphodiester Z marker, respectively), and lipids (1255 cm^{-1}). In order to further elucidate the spectral signatures of the underlying biochemical structure, the raw polystyrene spectrum was subtracted from the Polystyrene cluster. As seen in Figure 3.11C, the spectra are again distributed in all quadrants of the PC1/PC2 scatterplot. The loadings of PC1 and PC2 in Figure 3.11D contain the same biological features as that of the un-subtracted spectra in Figure 3.11B and, as the loading of PC2 in Figure 3.11B is differentiated according to polystyrene content, the loading of PC2 in Figure 3.11D is interpreted as the differentiation between early endosome (negative) and neighbouring cytoplasm (positive). Band assignments can be seen in detail in Table 3.5.

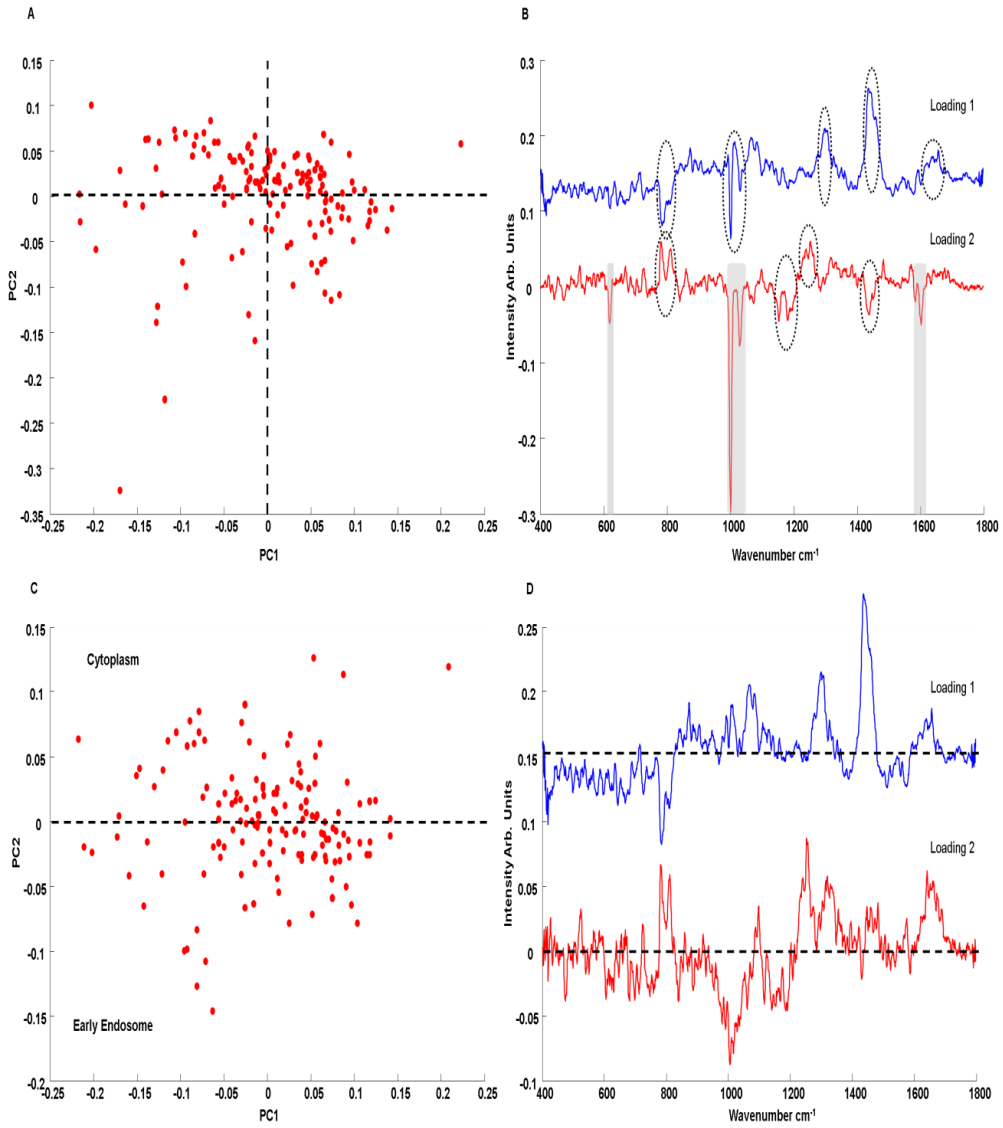

Figure 3.11. (A), Scatter plot of the PCA of spectra corresponding to the polystyrene cluster for 4 hour particle exposure (B), PC loadings of polystyrene cluster (C), Scatter plot of the PCA of spectra corresponding to the polystyrene cluster after polystyrene subtraction for 4 hour particle exposure (D), PC loadings of polystyrene subtracted polystyrene cluster. Spectra are offset for clarity. The dotted line represents the '0' line for each loading.

In order to identify spectral differences between cytoplasm and early endosome, positively (PC2≥0) and negatively (PC2<0) scored mean spectra related to PC2

(Figure 3.11C) were calculated as seen in Figure 3.12. When the mean spectra which are negatively and positively scored are subtracted from each other to show biochemical differences between early endosome and cytoplasm, similar features with Figure 3.11D- Loading 2 are obtained.

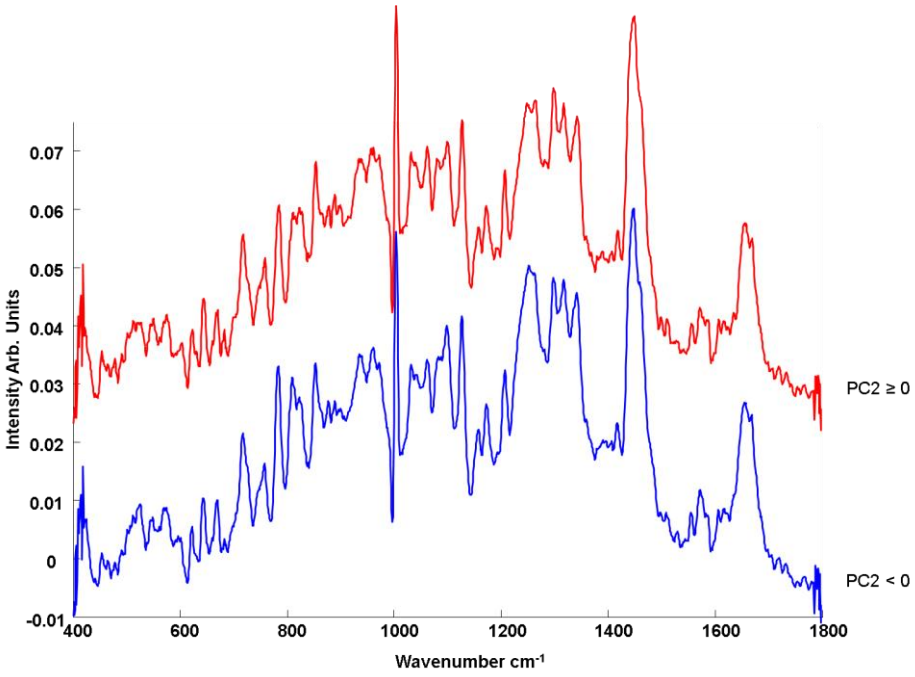

Figure 3.12. Mean spectra of cytoplasm (Loading of PC1 ≥0, red), early endosome (Loading of PC 1< 0, blue) after PC subtraction for 4 hour exposure and difference between mean spectra of cytoplasm and early endosome (green). Spectra are offset for clarity.

Briefly, the cytoplasm is differentiated from the early endosome by the bands at 785 and 810 cm^{-1} which are related to presence of nucleic acids. Also, spectra are differentiated by the band at 1237 cm^{-1}, which can be attributed to Amide III band of proteins as a result of higher protein content in the cytoplasm compared to the early endosomes. On the other hand, early endosomes are differentiated from the cytoplasm

by bands at 1066 and 1439 cm^{-1} which indicate the presence of lipids (Notingher *et al.*, 2003; Notingher *et al.*, 2006; Movasaghi *et al.*, 2007).

Table 3.5. Band assignments related to polystyrene cluster and polystyrene environment after 4 hour particle exposure (Notingher *et al.*, 2003; Notingher *et al.*, 2006; Movasaghi *et al.*, 2007).

Band Assignment (cm^{-1})	Polystyrene Cluster	Polystyrene Environment
718	-	Membrane Lipids
790	L-α-phosphatidylcholine	-
970	Proteins	-
1031	Proteins	-
1080	-	Phosopholipids
1304	-	Lipids
1656-1600	-	Phospholipids& Proteins

Finally, the extracted Raman spectral profiles associated with the underlying biochemical environment of the polystyrene nanoparticles for each exposure time, 24, 12, and 4 hrs, were compared, to demonstrate the applicability of Raman spectroscopy to determine and differentiate particle localisation within different subcellular compartments. Results showed that the extracted spectra and characteristics for different organelles are well differentiated, as seen in Figure 3.13A. The respective PC loadings which differentiated them from their immediate environment are shown in Figure 3.13B. According to the CLSM observations, nanoparticles are expected to be seen in endoplasmic reticulum, lysosomes and early endosomes, respectively, from longer to shorter exposure times. Therefore, the spectra for 24, 12 and 4 hr may be associated with the spectrum of endoplasmic reticulum, lysosomes and early

endosomes, which can be used as a guide to evaluate nanoparticle localisation with Raman spectroscopy.

Polystyrene nanoparticles are taken into cells by the process of endocytosis[12], where after they are bound by membrane derived endosomal vesicles, as confirmed by the CLSM images after 4 hr exposure. Considering the Raman spectrum related to 4 hr particle exposure, strong bands in the spectral range between 700 and 900 cm^{-1} are observed in the mean spectra, compared to 12 and 24 hr particle exposure. This region can be attributed to proteins which naturally exist in membrane structure (Notingher *et al.*, 2003; Notingher *et al.*, 2006; Movasaghi *et al.*, 2007). Lipid and phospholipid related bands are also prominent in the spectra associated with early endosomes due to their membrane derived nature.

Following the particle exposure and uptake, early endosomes are internally trafficked and become engulfed by lysosomes. Lysosomes originate from the golgi apparatus, and therefore, as a biochemical structure, they show similar properties to the golgi apparatus or endoplasmic reticulum. Considering the Raman signature derived from the 12 hr exposure data set, the PC loading is dominated by features of proteins and lipids. The signatures of both are significantly different to those associated with the early endosomes, however. In 12 hr exposure test which relates to biochemical content of lysosomes, the bands at around 519, 759, 1130, 1304 and 1439 cm^{-1} are observed which are related to phosphatidylinositol, phosphatidylethanolamine, C-C stretch of lipids, CH_2 twist of lipids and CH_{def} of lipids, respectively. On the other hand, for early endosomes, lipid bands showed more phospholipid related bands at around 1080 and 1656 cm^{-1} with phosphatidylcholine and membrane lipids at 790 and 718 cm^{-1},

respectively. Compared to 4 hr spectrum, the features in the 700-900 cm^{-1} region disappear, and clear differences can be observed in Amide I and Amide III regions.

Lysosomes containing polystyrene nanoparticles are further trafficked to the golgi apparatus or endoplasmic reticulum (Dorney *et al.*, 2012; Chang *et al.*, 2008). The mean spectrum related to the endoplasmic reticulum shows prominent nucleic acid bands at 785 cm^{-1} and 810 cm^{-1}, indicating the presence of RNA for protein synthesis around the perinuclear region and granular endoplasmic reticulum. Moreover, the prominence of protein and lipid related bands is consistent with the lipid and protein rich nature of the endoplasmic reticulum. The PC loading is also differentiated from that of 12 hr exposure time by the bands around 718 cm^{-1}, 733 cm^{-1} which are related to membrane lipids, produced in the endoplasmic reticulum.

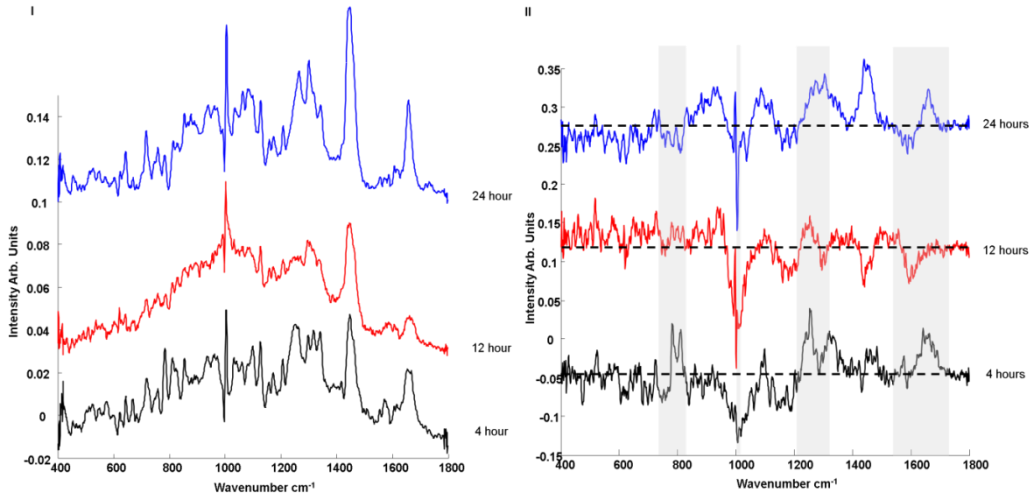

Figure 3.13. **I;** Comparison of mean spectra of 4, 12 and 24 hour nanoparticle exposure data sets. **II;** Comparison of PCA loadings of 4, 12 and 24 hour nanoparticle exposure data sets. The loadings of PC1 are used for 24 (Figure 3.4) and 12 hour (Figure 3.7) data sets while the loading of PC2 is used for the 4 hour data set (Figure 3.11). The main indicator bands for the different exposure time data sets were assigned according to Tables 3.3, 3.4 and 3.5. Spectra are offset for clarity. The dotted line represents the '0' line for each loading.

One of the biggest and most consistent differences for the different exposure times is observed in the spectral range between 1585 cm^{-1} and 1660 cm^{-1} (Notingher *et al.*, 2003; Notingher *et al.*, 2006; Movasaghi *et al.*, 2007). Raman bands in this region can be attributed to a number of distinct biochemical structures. They include the vibration of C=C bond of phospholipids, C=O bond of lipids and Amide I band of proteins (Notingher *et al.*, 2003; Notingher *et al.*, 2006; Movasaghi *et al.*, 2007). However, proteins containing electron rich amino acid residues such as Phe, Tyr and Thr have a characteristic band at 1004 cm^{-1}, due to the symmetric ring breathing. For the 4 hr exposure data set, this broad band is observed at 1656 cm^{-1}, which, coupled with the

1080 cm^{-1} phospholipid related band and no significant evidence of a protein band at 1004 cm^{-1}, indicates the presence of phospholipids. On the other hand, the 12 hr data set exhibits a strong band at 1004 cm^{-1} and therefore the band at around 1585-1600 cm^{-1} may be associated with the presence of proteins. For the 24 hr exposure data set, the broad band in the spectral range between 1655-1680 cm^{-1} can therefore be attributed to lipids, due to absence of the band at around 1004 cm^{-1} band. The second notable differentiating band range is that of the Amide III region of proteins from 1231 cm^{-1} to 1284 cm^{-1}, which shows the differences in protein secondary structures (Notingher *et al.*, 2003; Notingher *et al.*, 2006; Movasaghi *et al.*, 2007).

Raman spectroscopy, with the aid of multivariate analysis, can therefore clearly be used to not only identify the presence of nanoparticles within cells, based on their chemical signatures, but also explore the local environment, identifying different spectroscopic signatures of that environment as the nanoparticles are progressively trafficked through the cell. The study demonstrates the principle based on analysis of individual cells at each time-point, although over the course of the study, multiple cells were analysed at each time-point, representative examples being shown here. The CLSM analysis, consistent with literature, demonstrates that the subcellular processes are uniform within a cell culture, and indeed a general phenomenon *in vitro*.

It is noted, however, than while organic polymeric nanoparticles have distinctive spectra with features spanning the fingerprint region, inorganic nanoparticles may not have as rich spectra which can be used for identification purposes. For example, silica nanoparticles have relatively few distinguishing bands and furthermore their vibrational properties can be affected by the formation of lattice like structure due to

hydrogen bonds between SiOH groups within neighbouring silica nanoparticles (Meier *et al.*, 2006). Iron Oxide nanoparticles are also renowned for their weak Raman spectrum in the fingerprint region (Madhavi *et al.*, 2013). However, the weak signal of inorganic nanoparticles can be increased by the use of Raman reporter molecules and preparation of bio-composites or core-shell structures of inorganic nanoparticles. In order to overcome the lattice formation problems in silica nanoparticles, the use of organosilane compounds and the effect of vacuum drying of the samples have been shown in the study of Volovšek *et. al.* (2008). Semiconductor quantum dots are often functionalised for biological applications with coatings such as poly ethylene glycol (PEG), PEG-amines or carboxylic acids, and may therefore also be identified by the Raman signature of the coating, although this may challenge the sensitivity of the technique (Byrne *et al.*, 2006 ; Lu *et al.*, 2007 ; Lee *et al.*, 2008).

3.5. Conclusion

The study showed the applicability of Raman spectroscopy to determine the localisation of nanoparticles within cellular compartments, based on their intrinsic chemical structures without labelling at different incubation times. The study also demonstrates the power of Raman spectroscopy with different multivariate analysis techniques to extract biochemical information from intracellular compartments as a non-invasive and completely label free technique. Spectral differences between nanoparticles and their environment were analysed and spectral features related to endoplasmic reticulum, lysosome and early endosome were investigated at different particle exposure times. Although the data aquistion speed is currently somewhat slow, improved system performance and sensitivities will enable more rapid and ultimately

realtime monitoring, towards the realisation of Raman spectroscopy as a label free, high content analysis technique for *in vitro* screening of toxicity and drug efficacy.

3.6. References

Aparicio-Ixta, L., Ramos-Ortiz, G., Pichardo-Molina, J. L. (2012) 'Two-photon excited fluorescence of silica nanoparticles loaded with a fluorene-based monomer and its cross-conjugated polymer: their application to cell imaging', Nanoscale, 4(24), pp. 7751–7759.

Bolte, S., Cordelieres, F. P.(2006) 'A guided tour into subcellular colocalisation analysis in light microscopy', Journal of Microscopy, 224(3), pp. 213-232.

Bonnier, F., Knief, P., Lim, B., Meade, A. D., Dorney, J., Bhattacharya, K., Lyng, F. M., Byrne, H. J. (2010) 'Imaging live cells grown on a three dimensional collagen matrix using Raman Microspectroscopy', Analyst, 135(12), pp. 3169-3177.

Bonnier, F., Mehmood, A., Knief, P., Meade, A., Hornebeck, W., Lambkin, H., Flynn, K., McDonagh, V., Healy, C., Lee, T. C., Lyng, F. M., Byrne, H. J. (2011) '*In vitro* analysis of immersed human tissues by Raman microspectroscopy", Journal of Raman Spectroscopy', Journal of Raman Spectroscopy, 42(5), pp. 888–896.

Byrne, S. J., Corr, S. A., Rakovich, T. Y., Gun'ko, Y. K., Rakovich, Y. P., Donegan, J. F., Mitchell, S., Volkov, Y. (2006) 'Optimisation of the synthesis and modification of CdTe quantum dots for enhanced live cell imaging', J. Mater. Chem., 16, pp. 2896 – 2902.

Carey, P. R. (1982) 'Biochemical Applications of Raman and Resonance Raman Spectroscopies'. Academic Press, New York.

Chang, M. Y., Shiau, A. L., Chen, Y. H., Chang, C. J., Chen, H. H., Wu, C. L. (2008) 'Increased apoptotic potential and dose-enhancing effect of gold nanoparticles in

combination with single-dose clinical electron beams on tumor-bearing mice', Cancer Sci., 99(7), pp. 1479-1484.

Curtis, J., Greenberg, M., Kester, J., Phillips, S., Krieger, G. (2006) 'Nanotechnology and nanotoxicology: a primer for clinicians', Toxicol. Sci., 25(4), pp. 245-260.

Davoren, M., Herzog, E., Casey, A., Cottineau, B., Chambers, G., Byrne, H. J., Lyng, F. M. (2007) '*In vitro* toxicity evaluation of single walled carbon nanotubes on human A549 lung cells', Toxicology *in vitro*, 21(3), pp. 438-448.

Donaldson, K., Stone, V., Tran, C. L., Kreyling, W., Borm, P. J. (2004) 'Nanotoxicology', Occup. Environ. Med., 61(9), pp. 727-728.

Dorney, J. (2013) 'Polystyrene: A Potential Standard For Developing *In vitro* Cellular Tracking Methods For Nanotoxicology'. PhD, Dublin Institute of Technology.

Dorney, J., Bonnier, F., Garcia, A., Casey, A., Chambers, G., Byrne, H. J. (2012) 'Identifying and localizing intracellular nanoparticles using Raman Spectroscopy', Analyst, 137(5), pp. 1111-1119.

Draux, F., Jeannesson, P., Beljebbar, A., Tfayli, A., Fourre, N., Manfait, M., Sule-Suso, J., Sockalingum, G. D. (2009) 'Raman spectral imaging of single living cancer cells: a preliminary study', Analyst, 134(3), pp. 542-548.

Driscoll, K. E., Carter, J. M., Howard, B. W., Hassenbein, D.G., Pepelko, W., Baggs, R. B., Oberdoerster, G. (1996) 'Pulmonary inflammatory, chemokine, and mutagenicresponses in rats after subchronic inhalation of carbon black', Toxicol. Appl. Pharmacol., 136(2), pp. 372-380.

Englen, M. D., Taylor, S. M., Laegreid, W. W., Silflow, R. M., Leid, R. W. (1990) 'The effect of different silicas on arachidonic acid metabolism in alveolar macrophages', Exp. Lung. Res., 16(6), pp. 691-709.

Fazlollahi, F., Angelow, S., Yacobi, N. R. (2011) 'Polystyrene nanoparticle trafficking across MDCK-II', Nanomedicine: nanotechnology, biology, and medicine, 7(5), pp. 588–594.

Jan, E., Byrne, S. J., Cuddihy, M. (2008) 'High-content screening as a universal tool for fingerprinting of cytotoxicity of nanoparticles', ACS nano, 2(5), pp. 928–938.

Kabanov, A. V. (2006) 'Polymer genomics: an insight into pharmacology and toxicology of nanomedicines', Adv. Drug. Deliv. Rev., 58(15), pp. 1597-1621.

Keating, M., Bonnier, F., Byrne, H. J. (2012) 'Spectral Cross Correlation as a Supervised Approach for the Analysis of Complex Raman Datasets: The Case of Nanoparticles in Biological Cells', Analyst, 137, pp. 5792-5802.

Keating, M., Byrne, H. J. (2013) 'Raman spectroscopy in nanomedicine: current status and future perspectives', NanoMedicine, 8(8), pp. 1335-1351.

Klein, K., Gigler, A. M., Aschenbrenner, T., Monetti, R., Bunk, W., Jamitzky, F., Morfill, G., Stark, R. W., Schlegel, J. (2012) 'Label-free live-cell imaging with confocal Raman microscopy', Biophys J., 102(2), pp. 360–368.

Krauss, S. D., Petersen, D., Niedieker, D., Fricke, I., Freier, E., El-Mashtoly, S. F., Gerwert, K., Mosig, A. (2015) 'Colocalisation of fluorescence and Raman microscopic images for the identification of subcellular compartments: a validation study', Analyst, 140(7), pp. 2360-2368.

Kuehnel, W. (2003) ‘Color atlas of Cytology, Histology, and Microscopic Anatomy’, Thieme, Germany.

Lanone, S., Boczkowski, J. (2006) ‘Biomedical applications and potential health risks of nanomaterials: molecular mechanisms’, Curr. Mol. Med., 6(6), pp. 651-663.

Le, T. T., Duren, H. M., Slipchenko, M. N., Hu, C. D., Cheng, J. X. (2010) ‘Label-free quantitative analysis of lipid metabolism in living Caenorhabditis elegans’, Journal of Lipid Research, 51(3), pp. 672–677.

Lee, J., Kim, J., Park, E., Jo, S., Song, R. (2008) ‘PEG-ylated cationic CdSe/ZnS QDs as an efficient intracellular labeling agent’, Phys Chem Chem Phys., 10, pp. 1739-1742.

Lewinski, N., Colvin, V., Drezek, R. (2008) ‘Cytotoxicity of nanoparticles’, Small, 4(1), pp. 26–49.

Li, J., Strong, R., Trevisan, J., Fogarty, S. W., Fullwood, N. J., Jones, K. C., Martin, F. L. (2013) ‘Dose-related alterations of carbon nanoparticles in Mammalian cells detected using biospectroscopy: potential for real-world effects’, Environ. Sci. Technol., 47(17), pp. 10005−10011.

Li, J., Ying, G., Jonesa, K. C., Martin, F. L. (2015) ‘Real-world carbon nanoparticle exposures induce brain and gonadal alterations in zebrafish (Danio rerio) as determined by biospectroscopy techniques’, Analyst, 140, pp. 2687-2695.

Lu, L., Xu, XL., Liang, WT., Lu, HF. (2007) ‘Raman analysis of CdSe/CdS core-shell quantum dots with different CdS shell thickness.’ J. Phys., Condens. Matter, 19(40), 406221.

Madhavi, V., Prasad, T., Madhavi, G. (2013) 'Synthesis and spectral characterization of iron based micro and nanoparticles', International Journal of Nanomaterials and Biostructures, 3(2), pp. 31-34.

Matthaus, C., Chernenko, T., Newmark, J. A., Warner, C. M., Diem, M. (2007) 'Label-Free Detection of Mitochondrial Distribution in Cells by Nonresonant Raman Microspectroscopy', Biophysical Journal, 93(2), pp. 668–673.

Mattson, E. C., Aboualizadeh, E., Barabas, M. E., Stucky, C. L., Hirschmugl, C. J. (2013) 'Opportunities for Live Cell FT-Infrared Imaging: Macromolecule Identification with 2D and 3D Localization', Int. J. Mol. Sci., 14(11), pp. 22753-22781.

Meier, C., Lüttjohann, S., Kravets, V. G., Nienhaus, H., Lorke, A., Wiggers, H. (2006) 'Raman properties of silicon nanoparticles', Physica E, 32(1), pp. 155-158.

Miljkovic, M., Chernenko, T., Romeo, M. J., Bird, B., Matthaus, C., Diem, M. (2010) 'Label-free imaging of human cells: algorithms for image reconstruction of Raman hyperspectral datasets', Analyst, 135(8), pp. 2002-2013.

Movasaghi, Z., Rehman, S., Rehman, I. U. (2007) 'Raman Spectroscopy of Biological Tissues', Applied Spectroscopy Reviews, 42(5), pp. 493-541.

Mu, Q., Hondow, N. S., Krzemiński, L., Brown, A. P., Jeuken, L. J., Routledge, M. N. (2012) 'Mechanism of cellular uptake of genotoxic silica nanoparticles', Part. Fibre. Toxicol., 23, pp. 9-29.

Naha, P., Byrne, H. J. (2013) 'Generation of intracellular reactive oxygen species and genotoxicity effect to exposure of nanosized polyamidoamine (PAMAM) dendrimers in PLHC-1 cells *in vitro*', Aquatic Toxicology, 132–133, 61-72.

Nawaz, H., Bonnier, F., Knief, P., Howe, O., Lyng, F. M., Meade, A. D., Byrne, H. J. (2010) 'Evaluation of the Potential of Raman Microspectroscopy for Prediction of Chemotherapeutic Response to Cisplatin in Lung Adenocarcinoma', Analyst, 135(12), pp. 3070-3076.

Nel, A., Xia, T., Madler, L., Li, N. (2006) 'Toxic potential of materials at the nanolevel', Science, 311(5761), pp. 622-627.

Notingher, I., Hench, L. L. (2006) 'Raman microspectroscopy: a non-invasive tool for studies of individual living cells *in vitro*', Expert Rev. Med. Devices, 3(2), pp. 215–234.

Notingher, I., Verrier, S., Haque, S., Polak, J. M., Hench, L. L. (2003) 'Spectroscopic Study of Human Lung Epithelial Cells (A549) in Culture: Living Cells Versus Dead Cells', Biopolymers (Biospectroscopy), 72(4), pp. 230–240.

Pawley, J. (2006) Handbook of biological confocal microscopy 3rd ed., Springer-Verlag, Heidelberg.

Rhiem, S., Riding, M. J., Baumgartner, W., Martin, F. L., Semple, K. T., Jones, K. C., Schaffer, A., Maes, H. M. (2015) 'Interactions of multiwalled carbon nanotubes with algal cells: quantification of association, visualization of uptake, and measurement of alterations in the composition of cells', Environmental Pollution, 196, pp. 431-439.

Salvati, A., Aberg, C., Dos Santos, T. (2011) 'Experimental and theoretical comparison of intracellular import of polymeric nanoparticles and small molecules: toward models of uptake kinetics', Nanomedicine: nanotechnology, biology, and medicine, 7(6), pp. 818-826.

Sandin, P., Fitzpatrick, L. W., Simpson, J. C., Dawson, K. (2012) 'High-speed imaging of Rab family small GTPases reveals rare events in nanoparticle trafficking in living cells', ACS nano, 6(2), pp. 1513–1521.

Shapero, K., Fenaroli, F., Lynch, I., Cottell, D. C., Salvati, A., Dawson, K. A. (2011) ' Molecular BioSystems, 2011, 7(2), pp. 371-378.

Suh, H., Jeong, B., Liu, F. K. S. (1998) 'Cellular uptake study of biodegradable nanoparticles in vascular smooth muscle cells', Pharm. Res., 15(9), pp. 1495–1498.

Terasaki, M., Jaffe, L. A. (1991) 'Organization of the sea urchin egg endoplasmic reticulum and its reorganization at fertilization', J. Cell Biol., 114(5), pp. 929–940.

Thermofisher Scientific (2015) Molecular Probes, http://tools.thermofisher.com/content/sfs/manuals/mp05000.pdf. Accessed 07 October 2015.

Treuel, L., Jiang, X., Nienhaus, G. U. (2013) 'New views on cellular uptake and trafficking of manufactured nanoparticles', J. R. Soc. Interface, 10(82), 20120939.

Volovšek, V., Furić, K., Bistričić, L., Leskovac, M. (2008) 'Micro Raman Spectroscopy of Silica Nanoparticles Treated with Aminopropylsilanetriol', Macromol. Symp. 265(1), pp. 178–182.

Yah, C. S., Simate, G. S., Iyuke, S. E. (2012) 'Nanoparticles toxicity and their routes of exposures', Pak. J. Pharm. Sci., 25(2), pp. 477-491.

Yang, Y., An, F., Liu, Z. (2012) 'Ultrabright and ultrastable near-infrared dye nanoparticles for *in vitro* and in vivo bioimaging', Biomaterials, 33(31), pp. 7803–7809.

3S Supplementary Material:

3.S1. Cytotoxicity Evaluation

The toxicological characteristics of 40 nm carboxlylated and fluorescently labelled polystyrene particles were evaluated by the Alamar Blue (AB) and 3-(4,5-dimethylthiazol-2-yl)-2,5-diphenyltetrazolium bromide (MTT) assays, in each case following manufacturer's instructions. Alamar Blue (AB) and 3-(4,5-dimethylthiazol-2-yl)-2,5-diphenyltetrazolium bromide (MTT) were purchased from Biosource (UK) and Sigma Aldrich Ltd. (Dublin, Ireland), respectively. Serial dilutions of the initial stock were made and nanoparticle solutions within the concentration range from $5x10^{12}$to $7.8x10^{9}$were prepared in order to evaluate the cytotoxic effect of nanoparticles on A549 cells.

A549 cells and 10% Dimethyl sulfoxide (DMSO)-90% medium solution were used as positive and negative controls, respectively. Cells were seeded in 96-well plates (Nunc, Denmark) with densities of 1 x 10^5 cells/ml, 7 x 10^4 cells/ml, 3 x 10^4cells/ml and 2 x 10^4 cells/ml for 24, 48, 72 and 96 hr exposures, respectively, to achieve the desired confluence for each incubation period. Seeded cells were incubated for 24 hr for cell attachment. After 24 hr incubation, the medium was removed and the plates were rinsed with 100 µl/well phosphate buffered saline (PBS). Cells were exposed to different concentrations of nanoparticles ($5x10^{12}$, $1x10^{12}$, $5x10^{11}$, $2.5x10^{11}$, $1.25x10^{11}$, $6.25x10^{10}$, $3.13x10^{10}$, $1.56x10^{10}$, $7.80x10^{9}$ ppml) for the desired time period. Each cytotoxicity test was repeated 3 times as independent experiments with six replicates for each concentration and positive and negative control per micro plate.

The Alamar Blue and MTT assays were conducted on same plate. After the desired exposure time, the nanoparticle containing medium was removed and the plates were washed with 100 µl/well PBS. 100 µl of AB/ MTT solution (5% [v/v] solution of AB and 10% [v/v] of MTT dye) prepared in fresh medium without FBS and supplements were added to each well. The plates were incubated for 3 hr. AB fluorescence was measured by using a microplate reader (TECAN GENios, Grodig, Austria) at the excitation and emission wavelengths of 540 and 595 nm. For the MTT assay, the plates were washed with PBS to remove AB and 100 µl of DMSO were added to each well. The plates were shaken for 10 min at 200 rpm and the absorbance was quantified at 570 nm using the same microplate reader (reference filter 340 nm).

Both assays showed that the nanoparticles do not elicit a significant cytotoxic response over the applied concentration range. The elevated AB response (>100%) in Figure 3.S1.A may be due to interaction of the nanoparticles with the assay at these high doses The results are consistent with previous reports for carboxylated, fluorescently labelled particles of polystyrene, which demonstrated negligible toxic response.

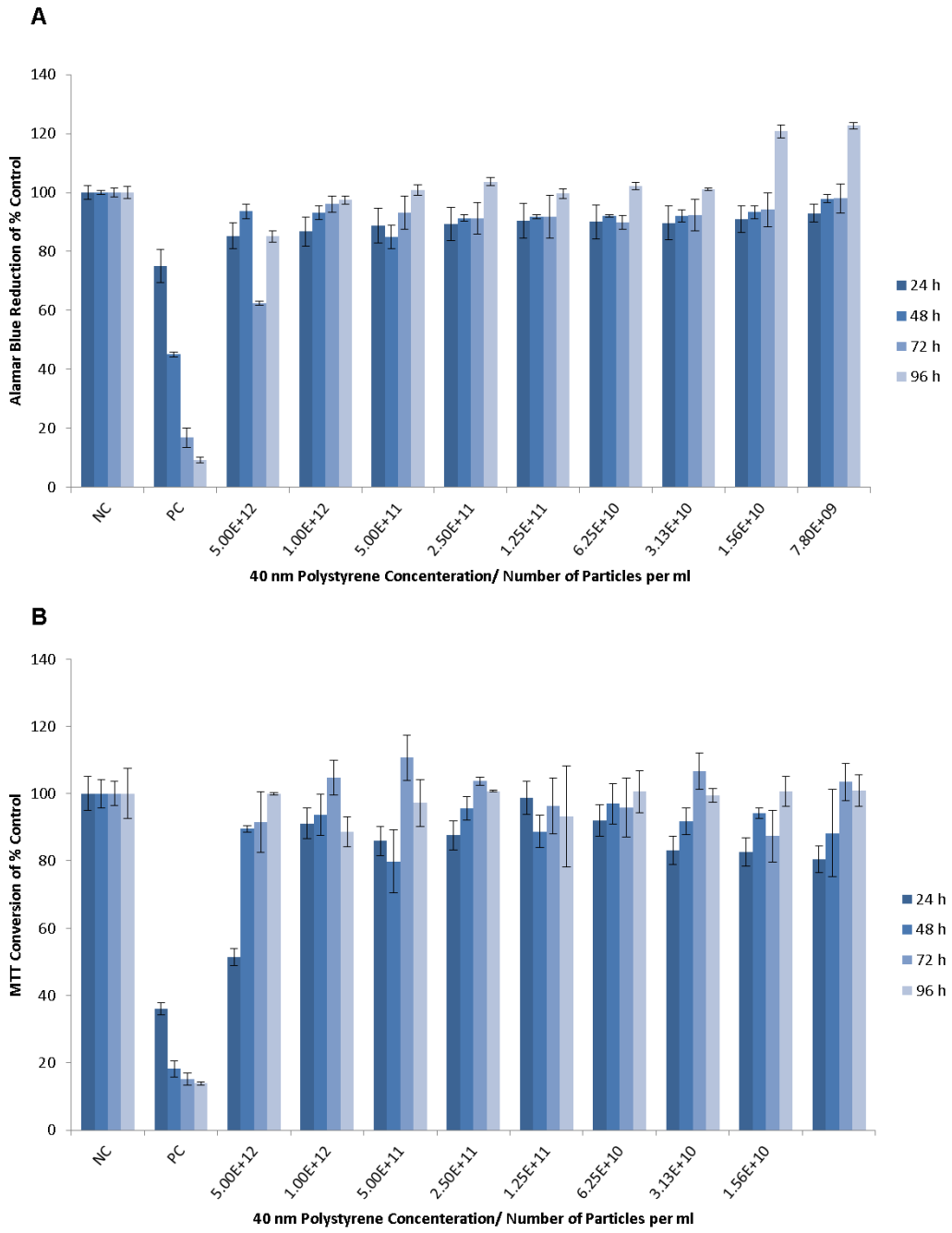

Figure 3.S1. Cytotoxicity of 40 nm carboxylated polystyrene nanoparticles after 24, 48, 72 and 96 hr exposures determined by the Alamar Blue (A) and MTT assay (B). Data are expressed as % of control mean ± SD of three independent experiments. Negative control (NC): A549 cells; Positive control (PC): 10% Dimethyl sulfoxide (DMSO) 90 % media.

3.S2. Polystyrene Subtraction From Environment Cluster

In order to better differentiate clusters, the raw polystyrene spectrum was subtracted from the environment cluster by using CLS. Figure 3.S2, Figure 3.S3 and Figure 3.S4 shows the scatter plots of PC and related loadings for 24 hr, 12 hr and 4 hr exposure data sets, respectively.

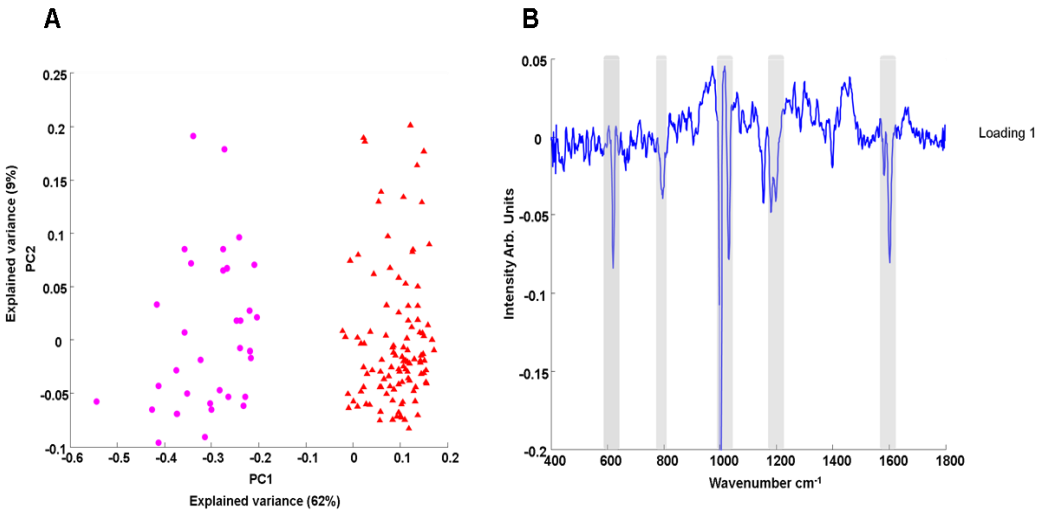

Figure 3.S2. (A), Scatter plot of the PCA of spectra correspond to polystyrene nanoparticles and their environment after raw polystyrene spectrum subtracted for 24 hr particle exposure, same colours with K-means maps were used to identify scatter plots, (B) PC loading of polystyrene nanoparticles and polystyrene subtracted environment. The characteristic peaks of polystyrene were indicated with black circles in Loading 1.

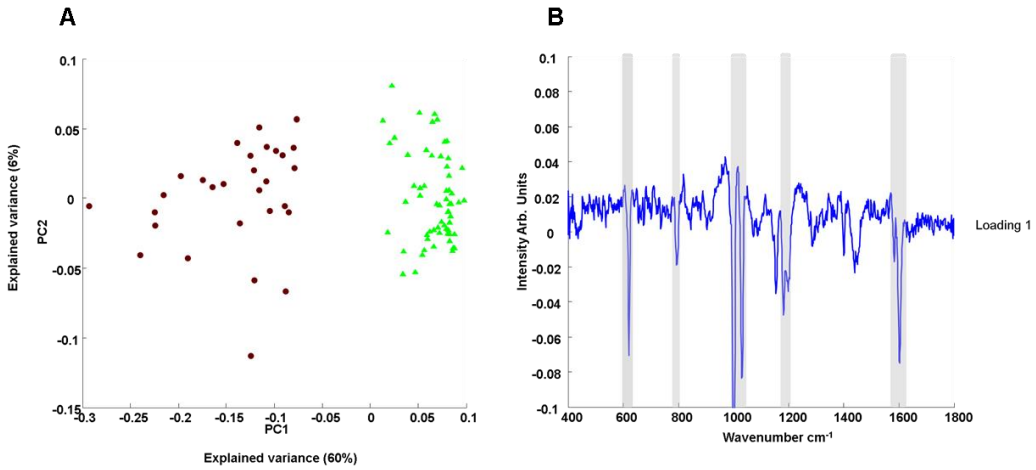

Figure 3.S3. (A), Scatter plot of the PCA of spectra correspond to polystyrene nanoparticles and their environment after raw polystyrene spectrum subtracted for 12 hr particle exposure, same colours with K-means maps were used to identify scatter plots, (B) PC loading of polystyrene nanoparticles and polystyrene subtracted environment. The characteristic peaks of polystyrene were indicated with black circles in Loading 1.

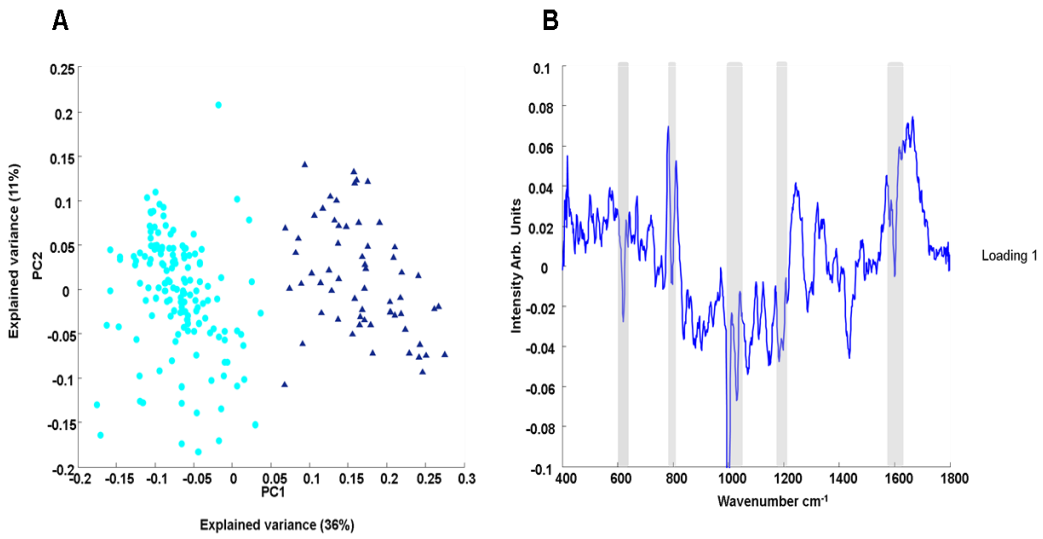

Figure 3.S4. (A), Scatter plot of the PCA of spectra correspond to polystyrene nanoparticles and their environment after raw polystyrene spectrum subtracted for 4 hr particle exposure, same colours with K-means maps were used to identify scatter plots, (B) PC loading of polystyrene nanoparticles and polystyrene subtracted environment. The characteristic peaks of polystyrene were indicated with black circles in Loading 1.

CHAPTER 4

In vitro Monitoring of Time and Dose Dependent Cytotoxicity of Aminated Nanoparticles using Raman Spectroscopy

The following chapter has been adapted from the published journal article entitled '*In vitro* Monitoring of Time and Dose Dependent Cytotoxicity of Aminated Nanoparticles using Raman Spectroscopy', Analyst, 2016, **141**, 5417-5431.

Author list: Esen Efeoglu, Alan Casey, Hugh J. Byrne

EE performed all measurements and data analysis and is the main drafting author. AC and HJB contributed to manuscript design and final drafting.

4.1. Abstract

Investigation of possible adverse health effects of nanomaterials, in a rapid multi-parametric fashion, has become increasingly important, due to their increased production and potential uses in a wide range of application areas, from cosmetics to pharmaceutics. Although conventional *in-vitro* cytotoxicological techniques provide valuable information about the particle toxicity, the importance of gaining high content information in a single assay with the analysis of multiple parameters in a non-invasive and label-free way is still one of the biggest challenges in nanotoxicology. As a vibrational spectroscopic technique, the power of Raman spectroscopy for the analysis of cells, tissues and also nanoparticle localization within cells has been shown previously. In this study, the ability of Raman spectroscopy to fingerprint the dose and time dependent cellular responses and effect of cytotoxic events on biochemical constituents of the cells is monitored. A549 human lung carcinoma cells and aminated polystyrene nanoparticles (PS-NH_2) are used as a model cell line and nanoparticle, respectively. Following the determination of cellular responses in the presence of toxic PS-NH_2 by using conventional cellular assays, Alamar Blue (AB) and 3-(4,5-Dimethylthiazol-2-yl)-2,5diphenyltetrazoliumbromid (MTT), and calculation of EC_{50} values for both assays, Raman spectroscopy was employed at response related doses and time points. Multiple point spectra from the cytoplasm, nucleus and nucleolus of 20 cells were acquired using Raman spectroscopy for each exposure dose and time point. Unsupervised principle components analysis (PCA) was applied to the Raman data sets for the comparison of exposed and unexposed cells as well as different exposure doses and times. The study shows the ability of Raman spectroscopy to provide information about cellular responses at different particle concentrations and

exposure times with the aid of multivariate analysis. In the chosen range of concentrations, the most significant changes were observed in the cytoplasm for both time dependent and dose dependent cases due to the route of endocytosis The Raman spectral markers for lipidosis, ROS formation and oxidative stress related biochemical damage are determined and correlated with exposure dose and time, and the responses are correlated with conventional cytotoxicity assays.

4.2. Introduction

The growing interest and research in nanoscience and nanotechnology has introduced a plethora of nanomaterials into human life. More than 1600 products of nanotechnology have already found their place in the market, ranging from cosmetics to pharmaceutics (more information about nanotechnology based products can be found at http://www.nanotechproject.org/) (*Consumer Products Inventory* 2016). From their production, to use and disposal by consumers, nanomaterials interact with living systems and the environment via different exposure routes. Due to their size, different surface properties and reactivity, related to their physicochemical properties, these novel materials can easily interact with biological systems. The emergence of Nanoscience and Nanotechnology has therefore given rise to the fields of Nanotoxicology (Oberdörster *et al.* 2005) and Nanomedicine (Webster 2006). Nanotoxicology mainly deals with the possible adverse biological effects of nanomaterials for humans and ultimately the environment(Donaldson *et al.* 2004). The Organisation for Economic Co-operation and Development (OECD) recommends established and commonly used protocols for nanotoxicological assessment (*Oecd Oecd Guidelines for the Testing of Chemicals* 2013), such as cell viability tests (3-(4,5-Dimethylthiazol-2-yl)-2,5diphenyltetrazoliumbromid (MTT), Neutral Red (NR) and Alamar Blue (AB)). On the other hand, Nanomedicine promises new paradigms in targeted drug delivery, diagnostics and imaging (Godbey, Wu, & Mikos 1999; Tosi *et al.* 2013). However, direct visualisation of the nanomaterials within cells, and the resultant cellular responses remains a challenge.

Raman spectroscopy has origin in inelastic collision of photons with molecules and provides fingerprint information about the specimen under investigation (Byrne, Sockalingum, & Stone 2011; Ferraro, Nakamoto, & Brown 2003). Due to the nature of the technique, fingerprint information at a molecular level, easy sample preparation steps, narrow spectral bandwidth and minimal influence from the water, a natural component of biological samples, the technique has attracted interest for the analysis of biological structures. The applicability of Raman spectroscopy as a tool for analysis of cells, tissues and biofluids has been demonstrated in recent years (Bonnier *et al.* 2011; Bonnier *et al.* 2014; Breve 1996; Dorney *et al.* 2012; Efeoglu *et al.* 2015; Walton, Deveney, & Koenig 1970). The technique has also been widely used for the analysis of cell-drug and cell-nanoparticle interactions at a sub-cellular level (Chernenko *et al.* 2009; Farhane *et al.* 2015; Farhane *et al.* 2016; Nawaz *et al.* 2010; Nawaz *et al.* 2011; Nawaz *et al.* 2013; Owen *et al.* 2006; Zoladek *et al.* 2011). The study of Dorney *et al.* demonstrated the ability of Raman spectroscopy to identify and discriminate different subcellular regions as well as the presence of the nanoparticles within these regions (Dorney *et al.* 2012). Moreover, the study of Keating *et al.* demonstrated the importance of multivariate analysis techniques on huge Raman data sets to gain further information about cell-nanoparticle localisation (Mark E. Keating, Bonnier, & Byrne 2012). Also, the ability of the Raman spectroscopy to differentiate different cellular compartments, such as endosomes and lysosomes, as well as localisation of the nanoparticles in these compartments has been demonstrated (Efeoglu *et al.* 2015). For the case of Carbon Nanotubes, Knief *et al.* (Knief *et al.* 2009) probed the correlation of Raman biospectroscopic markers with conventional cytotoxicity assays, indicating that Raman spectroscopy can potentially be employed as a single, label free assay to localise nanoparticles, identify trafficking mechanisms

and evaluate nanoparticle toxicity. However, an extensive study of dose and time dependent cellular responses to nanoparticle exposure has not as yet been reported.

The toxicity of aminated PSNPs (PS-NH_2) has been extensively studied by different research groups to determine the mode of interaction of these nanoparticles with different types of human cell lines by using conventional cytotoxic and microscopic techniques (Anguissola *et al.* 2014; Lunov, Syrovets, Loos, Beil, *et al.* 2011; Lunov, Syrovets, Loos, Nienhaus, *et al.* 2011; Ruenraroengsak *et al.* 2012; Wang *et al.* 2013; Xia *et al.* 2008). Polystyrene nanoparticles are taken up by most of the cell lines through endocytosis, which is accepted as the primary mechanism for nanomaterial uptake into the cells (Treuel, Jiang, & Nienhaus 2013). Basically, particles are taken up across the cell membrane by the formation of early endosomes which carry the nanoparticles to the lysosomes. After particles are engulfed by lysosomes, they are carried to the endoplasmic reticulum (Efeoglu *et al.* 2015; Mu *et al.* 2012; Shapero *et al.* 2011). In the case of PS-NH_2, exposure of cells to the nanoparticles can induce toxicity due to the formation of Reactive oxygen species (ROS). The formation of ROS starts with the endocytosis of nanoparticles and continues throughout their trafficking within cells. The resultant oxidative stress causes the release of inflammatory factors and triggers apoptosis. Also, release of cationic nanoparticles into the cytosol due to endosomal or lysosomal rupture resulting from membrane damage allows nanoparticles to reach the mitochondria and cause a change in mitochondrial membrane potential, also initiating the apoptotic process (Xia *et al.* 2008). Aminated polystyrene particles induce cytotoxicity by triggering caspase mediated apoptotic pathways, even at low exposure doses, due to their cationic properties. Basically, pro-apoptotic Bcl-2 proteins are located on the mitochondrial membrane and cause the

formation of holes which will release apoptogenic factors and trigger the caspase activity (Anguissola *et al.* 2014; Bexiga *et al.* 2011; Ruenraroengsak *et al.* 2012; Xia *et al.* 2008). As the responses of cells to commercially available PS-NH_2 exposure *in vitro* have been extensively documented, they can serve as ideal model nanoparticles to explore the capabilities of Raman spectroscopy to monitor cellular responses.

In this study, the dose and time dependent cellular responses and effect of cytotoxic events on biochemical constituents of the cells are monitored using Raman spectroscopy. Aminated polystyrene nanoparticles (PS-NH_2) are chosen as model nanoparticles due to their well-documented cytotoxic mechanisms. Human lung adenocarcinoma (A549) cells were chosen for consistency with other studies (Anguissola *et al.* 2014; Efeoglu *et al.* 2015), which show common modes of action in a number of cell lines, and as they act as models for human exposure by inhalation. Cells were exposed to PS-NH_2 in different doses and for different exposure times. In order to determine toxic effects of the PS-NH_2 in A549 cells, the conventional cytotoxic assay, Alamar Blue was carried out for 4, 8, 12 and 24 hr particle exposure. The 3-(4,5-dimethylthiazol-2-yl)-2,5-diphenyltetrazolium bromide (MTT) assay was also used to determine cytotoxic effect of PS-NH_2 in A549 cells after 8 hr particle exposure to compare the responses from different cytotoxicity assays. A549 cells were exposed to 2.5, 5 and 10 μM concentrations of the PS-NH_2 for the evaluation of spectroscopic signatures of the dose-dependent toxic responses in the fingerprint region of the Raman spectrum. Also, cells were exposed to 2.5 μM of PS-NH_2 for 4, 8, 12 and 24 hrs for the assessment of toxicity related changes in biomolecules such as the proteins, lipids and nucleic acids. In order to elucidate the roles of different cellular regions and related toxic responses, Raman spectra were acquired from cytoplasm,

nucleus and nucleolus. Raman datasets and unsupervised Principal Component analysis (PCA) was used for the elucidation and comparison of dose and time dependent biomolecular changes in the cells upon nanoparticle exposure.

4.3. Materials and Methods

4.3.1. Nanoparticles

100 nm amine-modified and fluorescently labelled, latex type, polystyrene nanoparticles (PS-NH_2, Product Number: L9904) were chosen as model nanoparticles for this study and purchased from Sigma-Aldrich (Ireland). The peak excitation and emission wavelengths of the PS-NH_2 are specified by the manufacturer as 481 and 644 nm, respectively. The PS-NH_2 were further characterised using a Malvern Zetasizer ZS to determine their size and surface potential in phosphate buffered saline (PBS) and cell culture medium. The nanoparticles were freshly prepared in pre-warmed cell culture medium containing supplements on the day of exposure.

4.3.2. Cell Culture

The human lung adenocarcinoma cell line, A549, was purchased from ATCC (ATTC. No: CCL-185) and cultured in Dulbecco's Modified Eagle's Medium Nutrient Mixture F-12 HAM (DMEM-F12) supplemented with 2mM L-glutamine and 10% foetal bovine serum (FBS, Sigma Aldrich) at 37 °C in a humidified 5% CO_2 incubator. Cells were sub-cultured at three days intervals to 60%-70% confluency.

4.3.3. Preparation of nanoparticle solutions

The PH-NH_2 solutions for both Raman measurements and cytotoxicity assays were prepared to the desired concentrations from initial concentrations by diluting the nanoparticles directly in 10% FBS and 2mM L-glutamine supplied DMEM-F12.

4.3.4. Cytotoxicity Assays and Determination of half-maximal effective concentration (EC_{50})

Alamar Blue (AB) and 3-(4,5-dimethylthiazol-2-yl)-2,5-diphenyltetrazolium bromide (MTT) assays were used to evaluate dose and time dependent cytotoxicity responses of 100 nm PS-NH_2 in A549 cells. AB and MTT assays were purchased from Biosciences Ltd. (Ireland) and Sigma-Aldrich (Dublin, Ireland), respectively and both assays were carried out on the same 96-well plate (Nunc, Denmark) by following manufacturer's instructions. A549 cells were seeded onto 96-well plates with densities of $1x10^5$ cells/mL and incubated at 37 °C in 5% CO_2 for 24 hrs for initial attachment and to achieve the desired confluency. PS-NH_2 solutions were prepared in the concentration range from 40 to 0.3125 μM by serial dilutions in pre-warmed DMEM-F12 medium supplemented with 10% FBS and 2mM L-glutamine. Following 24 hr initial attachment, the medium was removed and cells were rinsed with 100 μl/well PBS. A549 cells were exposed to the range of PS-NH_2 concentrations for each of the time points, 4, 8, 12, 24 and 48 hr. 10% Dimethyl sulfoxide (DMSO), prepared in cell culture medium, was used as a positive control. Six replicates of each different nanoparticle concentration, negative (A549 cells) and positive (DMSO) controls were used in each 96-well plate and 3 independent experiments were used to evaluate cytotoxic response of the PS-NH_2 on A549 cells for both assays. After particle

exposures, the cell medium containing nanoparticles was removed and cells were washed with PBS three times. AB/MTT solution was prepared in the ratio of 5% [v/v] solution of AB and 10% [v/v] of MTT dye in un-supplemented DMEM-F12. A 100 µl/well of MTT/AB solution was added to A549 cells and they were incubated for 3 hrs at 37 °C in 5% CO_2. A microplate reader (SpectraMax-M3, Molecular Devices, USA) was used to measure AB fluorescence emission at 595 nm (excitation/emission 540/595 nm, respectively). Following AB measurement, the cell medium containing AB and MTT is removed and cells were rinsed with PBS. 100 µl/well of DMSO were added to the 96-well plates and plates were agitated at 200 rpm for 10 mins. MTT absorbance was measured at 570 nm by using same plate reader system. The EC_{50} calculation was made by using a four parameter sigmoidal fit in SigmaPlot.

4.3.5. Raman Spectroscopy

Raman spectroscopy was used to monitor dose and time dependent changes of cellular constituents of A549 cells upon PS-NH_2 exposure. Approximately ~16000 cells per substrate were seeded onto CaF_2 disks and incubated for 24 hrs at 37 °C in 5% CO_2 for initial attachment. After initial attachment of the cells, cell medium was removed and cells were rinsed with PBS. The cell medium of A549 cells, which were used as control and will be referred to as unexposed cells throughout the study, was replaced with fresh 10% FBS and 2mM L-glutamine supplemented DMEM-F12. For the preparation of exposed cells, PS-NH_2 solutions with concentrations of 2.5, 5 and 10 µM were prepared in FBS and L-glutamine supplemented DMEM-F12 for the evaluation of dose dependent responses. A549 cells were exposed to the each concentration of PS-NH_2 for 8 hrs. Exposures to 2.5 µM PS-NH_2 were used for the

assessment of time-dependent cellular responses, at 4, 8, 12, 24 and 48 hrs. In parallel, unexposed cells were incubated in fresh medium at 37 °C in 5% CO_2 for periods equivalent to the PS-NH_2 exposure times. Following the particle exposures and incubation of unexposed cells, medium containing PS-NH_2 for exposed cells and cell medium for unexposed cells was removed and cells were washed with PBS thrice. 10% formalin was used to fix cells for 10 mins. After fixation of cells, formalin was removed and cells were washed three times with distilled and sterilised water. Throughout the study, Raman measurements were acquired by using water-immersion objective. Therefore, after fixation and washing steps, cells were kept in water and spectra were acquired in water.

A Horiba Jobin-Yvon LabRAM HR800 spectrometer, equipped with a 785 nm diode laser as source was used throughout the study. All measurements were acquired in water by using a x100 water immersion objective (LUMPlanF1, Olympus, N.A. 1). The spectrometer was calibrated to the 520.7 cm^{-1} line of silicon prior to spectral acquisition. A 300 lines per mm grating was chosen, which provides approximately 1.5 cm^{-1} per pixel spectral dispersion. A 100 μm confocal pinhole was used for all measurements. The spectra were dispersed onto a 16 bit dynamic range Peltier cooled CCD detector. Point spectra from the cytoplasm, nucleus and nucleolus of 20 cells were acquired for each dose and exposure time. The spectral range from 400 to 1800 cm^{-1}, the so-called fingerprint region, was chosen and spectra were acquired for 2x30 seconds at each spot. Unexposed cells were used as control for comparisons of the different doses and exposure times.

4.3.6. Data Analysis

Raman data sets were transferred to Matlab (Mathworks, USA) for data analysis. Pre-processing was carried out in the same data analysis platform to improve spectral quality. For pre-processing, first, a mild smoothing was applied to data sets by using Savitsky-Golay filter (3^{rd} order and 9 points). Classical Least Squares (CLS) analysis was employed to minimize contributions from the background which is dominantly water in the immersion geometry (Bonnier *et al.* 2014; Miljkovic *et al.* 2010). Spectra were vector normalized following smoothing and background subtraction. Principle Component Analysis (PCA) was applied to pre-processed Raman data sets to differentiate the spectral changes in fingerprint region of the nucleus, nucleolus and cytoplasm upon PS-NH_2 exposure.

4.4. Results and Discussion

The well-established and commonly used cytotoxicity assay, AB, was carried out to determine the dose and time dependent toxic effect of PS-NH_2 on A549 cells (Berridge, Herst, & Tan 2005; Rampersad 2012; Vega-Avila & Pugsley 2011). Figure 4.1.I shows the plots of cytotoxic response of PS-NH_2 on A549 cells determined by the AB assay. Half-maximal concentration for cellular viability, EC_{50}, values relating to the different particle exposure times were calculated in SigmaPlot by a four parameter sigmoidal fit. For 4 hr PS-NH_2 exposure, the EC_{50} value was calculated to be 20±1 μM. After 12 hr particle exposure, the EC_{50} value was decreased to 11±4 μM. For 24 hr exposure of A549 cells to the PS-NH_2, a median cytotoxic effect at a concentration of 10±2 μM was observed, while when cells were exposed to the PS-

NH_2 for 48 hrs, the EC_{50} value is calculated as 2.8±0.2 μM .The degree of toxicity is inversely related to the EC_{50} (Ragnvaldsson *et al.* 2007) and thus, when all exposure times are compared, the cytotoxicity of PS-NH_2 progressively increases from 4 hr to 48 hr exposure.

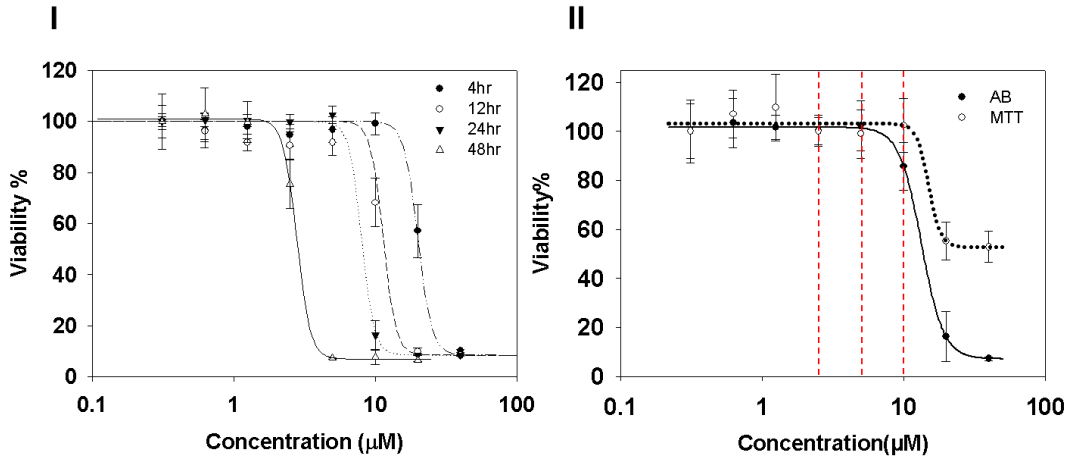

Figure 4.1. **I)** Cytotoxicity of 40 nm amine-modified polystyrene nanoparticles (PS-NH_2) after 4, 12, 24 and 48 hr exposures determined by the Alamar Blue assay. **II)** Cytotoxicity of 40 nm amine-modified polystyrene nanoparticles (PS-NH_2) after 8 exposure determined by the Alamar Blue and MTT assays. The concentrations (2.5, 5 and 10 μM) which are used throughout the study are indicated by red dashed lines. Data are expressed as % of control mean ± SD of three independent experiments.

As an alternative and complementary measure of cytoxic response, the MTT assay was also employed to monitor the toxic response of A549 cells to PS-NH_2 exposure. Figure 4.1.II compares the dose dependent responses for 8 hr PS-NH_2 exposure from the two assays, MTT and AB. EC_{50} values for both assays were observed similar to each other which are 13±1 and 15±5 μM for AB and MTT, respectively. Although EC_{50} values

were calculated to be similar, the difference in the underlying mechanism of toxicity changes according to concentration of PS-NH_2. The increasing concentrations of PS-NH_2 cause a rapid decrease in cell viability when it is determined by the AB assay, compared to that which is determined by MTT after 8hr exposure. For this reason, significantly different toxicological profiles can be obtained from well-established cytotoxicity assays due to the limitations of specific colorimetric label based assays.

The dose and time dependent cytotoxic response of a cytotoxicological assay reflects a complex cascade of events, triggered by endocytosis of the nanoparticles, giving rise to subsequent oxidative stress, inflammatory responses, apoptosis and cell death, as described for example by Maher *et al.* (Maher *et al.* 2014). Each cytotoxicity assay measures the toxic response of cells in different ways, and the relative sensitivity of the assay depends on the events in the cascade to which it is sensitive. AB is a measure of overall cellular activity as measured by the transformation of Rezazurin Sodium Salt (weak fluorescence) into Resofurin Sodium salt which has a strong fluorescence. Although the exact mechanism of the reduction reaction is unknown, as there are multiple cellular sites of conversion, AB assay provides valuable information about the overall activity of the cell population (O'Brien *et al.* 2000; Rampersad 2012; Vega-Avila & Pugsley 2011; White, DiCaprio, & Greenberg 1996). On the other hand, the MTT assay measures the cell activity based on formazan product formation which relates to the mitochondrial activity of cells (Mosmann 1983). In cases such as cellular exposure to poly (amido amine) (PAMAM) dendrimer nanoparticles, in which endosomolysis leads to translocation of the nanoparticles to the mitochondria, MTT is seen to be significantly more sensitive than AB, which measures the subsequent change to the cytosolic activity (S G Mukherjee *et al.* 2012). The formation of ROS

inside the cell is regulated by different factors such as protective enzymes and antioxidant mechanisms. The ROS formation and cell protection mechanism works through the cross-talk between cytosolic events and mitochondrial events upon the presence of ROS. In the case of PS-NH_2 exposure, the nanoparticles are trafficked from endosomes to lysosomes, and the toxic insult is first manifest through generation of ROS in the cytosol (around cell membrane and lysosomes), which subsequently impacts on the mitochondria (Casteilla, Rigoulet, & Pénicaud 2001; Pobezhimova & Voinikov 2000).

Although cytotoxicity assays such as AB, Neutral Red, and those based on tetrazolium salts (MTT, MTS, WST-1), provide valuable information about the toxic effect of material the under investigation, these techniques are not a definitive measure of cell viability and provide little information about the mechanism of action of the toxicants in terms of molecular determinants and pathways. In contrast, as a label free technique, Raman spectroscopy can potentially provide a high content spectroscopic profile of the cells and complete biochemical response at a given exposure time and dose (as illustrated by the mean spectra of the subcellular regions of the unexposed cell population, Supplementary Figure 4.S1). The dose dependent cytotoxicity measurements serve as a range finding test for Raman analysis.

Figure 4.2 shows the PCA of spectra corresponding to cytoplasm, nucleus and nucleolus of the 8hr unexposed control and 10 μM PS-NH_2 exposed cells. Although this dose is less than the EC_{50} for both assays at this time point, it induces a significant reduction in viability, as registered using the AB assay (Figure 4.1.II). Figure 4.2.I shows the scatter plots of PCA and the data sets relating to unexposed and exposed

cells are indicated with closed circles and open circles, respectively and coded with colours according to the different cellular regions. Cytoplasm, nucleus and nucleolus are indicated with red, green and blue, respectively. The same colour coding system is used for exposed cells, but with the use of open circles. The spectra corresponding to the nuclear areas (nucleus and nucleolus) and cytoplasm are clearly differentiated for both exposed and unexposed cells according to PC1, which represents the most significant variance (46%) among the data, originating from biochemical differences between the combined nuclear area and cytoplasm. The spectra relating to the cytoplasm of both exposed and unexposed cells score negatively according to Loading 1 ($PC1<0$), while nuclear and nucleolar spectra score positively according to Loading 1 ($PC1\geq0$). PC2 gives information about the second highest variance (16%) among the data sets, and differentiates each region for exposed and unexposed cells. For all cellular regions, exposed cells are clearly differentiated from unexposed cells, indicating that the spectral differences are larger than the intrinsic variability of each region, and score positively according to PC2 (indicated by open circles) while unexposed cells score negatively ($PC2<0$) (indicated by closed circles).

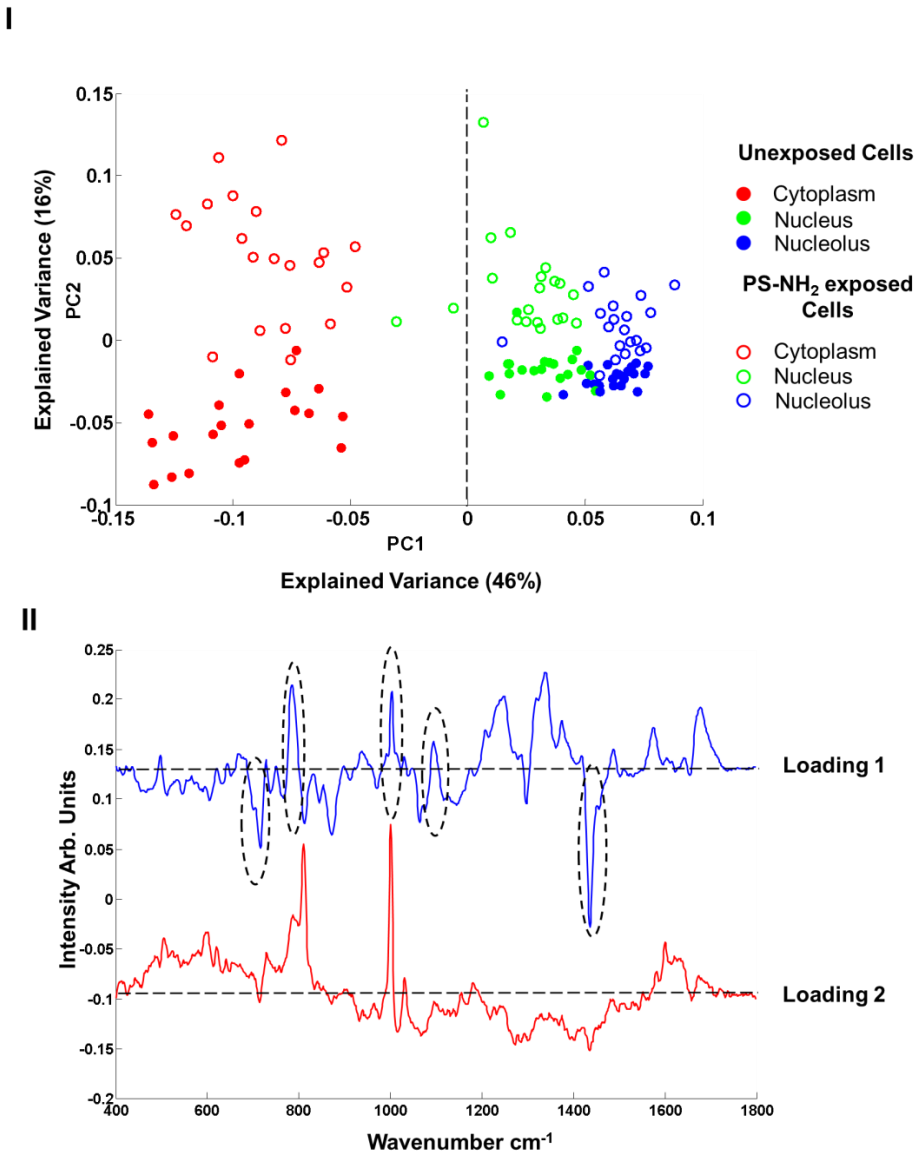

Figure 4.2. **I)** Scatter plot of the PCA of spectra corresponding to cytoplasm, nucleus and nucleolus of the (8hr) unexposed and PS-NH_2 exposed cells for 10 μM concentration of nanoparticles. Different cellular regions are coded as follows; red for cytoplasm, green for nucleus and blue for nucleolus. Exposed and unexposed cells are indicated by open circles and closed circles, respectively. **II)** First 2 loadings of PC analysis; loadings are offset for clarity and the dotted line represents the zero '0' point for each loading. In loading 1, notable bands which are used to differentiate the nuclear region from cytoplasm are indicated by black dashed outlines.

Figure 4.2.II shows the first two loadings of the PCA, corresponding to all regions of exposed and unexposed cells. As seen in Figure 4.2.I, exposed and unexposed cells differentiate from each other based on the differences in biochemical composition of nuclear regions and cytoplasm according to PC1. The spectra of the nuclear area of the cell, which is composed of nucleus and nucleolus, score positively, while spectra corresponding to cytoplasm score negatively, according to PC1, for both exposed and unexposed cells. For this reason, the positive features of loading 1 are dominated by nuclear and nucleolar related bands, while negative features relate to the cytoplasm. The most dominant features which are used to differentiate the nuclear area (nucleus and nucleolus) and cytoplasm, the positive features at 785, 1003, 1094 cm^{-1} and the negative features ~ 719, 1437 cm^{-1}, are indicated with black outlines in Figure 4.2.II. Amongst the positive features, the bands at ~ 785 cm^{-1} (Nucleic acids uracil (U), thymine (T), cytosine(C) ring breathing modes in the DNA/RNA bases, O-P-O backbone), 1003 (phenylalanine(Phe)), 1094 cm^{-1} (DNA), 1248 cm^{-1} (Guanine(G) and cytosine (NH_2), Amide III), 1339 cm^{-1} (Phe, tyrosine(Tyr), nucleic acid), 1373 cm^{-1} T, G, adenine(A) bases of deoxyribonucleic acid (DNA) and ribonucleic acid (RNA)), 1575 cm^{-1} (G, A of nucleic acids) and 1678 cm^{-1} (bound or free NAHD, Amide I region) indicate the predominance of nucleic acids and proteins which are abundant in the nuclear area (Movasaghi, Rehman, & Rehman 2007; Notingher & Hench 2006; Notingher *et al.* 2003). On the other hand, the dominant negative features include those at ~719 cm^{-1} (membrane phospholipid head, phosphatidylcholine), 873 cm^{-1} (hydroxyproline, tryptophan (Trp)), 1064 cm^{-1} (acyl chains, υ(C-C)), 1078 cm^{-1} (phospholipids), 1298 cm^{-1} (fatty acids) and 1437 cm^{-1} (Lipids, acyl chains, CH_2 deformation), which are more characteristic of the lipid rich cytoplasm. Unexposed and exposed cells are differentiated mainly according to loading 2, as seen in Figure

4.2.II. Although there are some contributions to the loading 2 from PS-NH_2 in the positive features, cells exposed for 8 hr to 10 μM of PS-NH_2 are mainly differentiated from the unexposed cells by increases in the intensities of nucleic acid bands at 785 cm^{-1} and 810 cm^{-1} (RNA, O-P-O stretching) and protein Amide I band at 1604 cm^{-1}. For loading 2, the bands derived from PS-NH_2 at 620, 1003, 1030 and 1600 cm^{-1} have been excluded from discussion.

Polystyrene nanoparticles are taken into the cells by the mechanism known as endocytosis. Previous studies have confirmed that the polystyrene nanoparticles (PS-COOH) are taken up into endosomes and carried to lysosomes (Anguissola *et al.* 2014; Efeoglu *et al.* 2015; Ekkapongpisit *et al.* 2012; Frohlich *et al.* 2012; Loos *et al.* 2014). Most of the nanoparticles are observed in lysosomes after 8 hr particle exposure. For this reason, after shorter exposure times, for example 8 hr, most of the cytotoxic responses can be attributed to changes in the cytoplasm and due to a cascade of processes including ROS formation, mitochondrial damage and lipidosis (Anguissola *et al.* 2014; Maher *et al.* 2014), but notably, the nucleus and nucleolus are not affected as much as cytoplasm. In order to better identify changes in the biomolecular composition of the cytoplasm, nucleus and nucleolus upon PS-NH_2 exposure, the mean spectra of particle exposed cells and unexposed cells were obtained and the spectral differences for each individual cellular region are evaluated by subtracting the mean spectra of exposed cells from the mean spectra of unexposed cells (Figure 4.3). When the mean spectra of cytoplasm, nucleus and nucleolus are analysed, the most significant changes are observed in the cytoplasm (red) of exposed cells compared to the corresponding control, as seen in Figure 4.3. For all cellular regions, some

contributions from the PS-NH_2 are observed in PS-NH_2 exposed cells and the bands related to PS are highlighted with grey and excluded from band assignments.

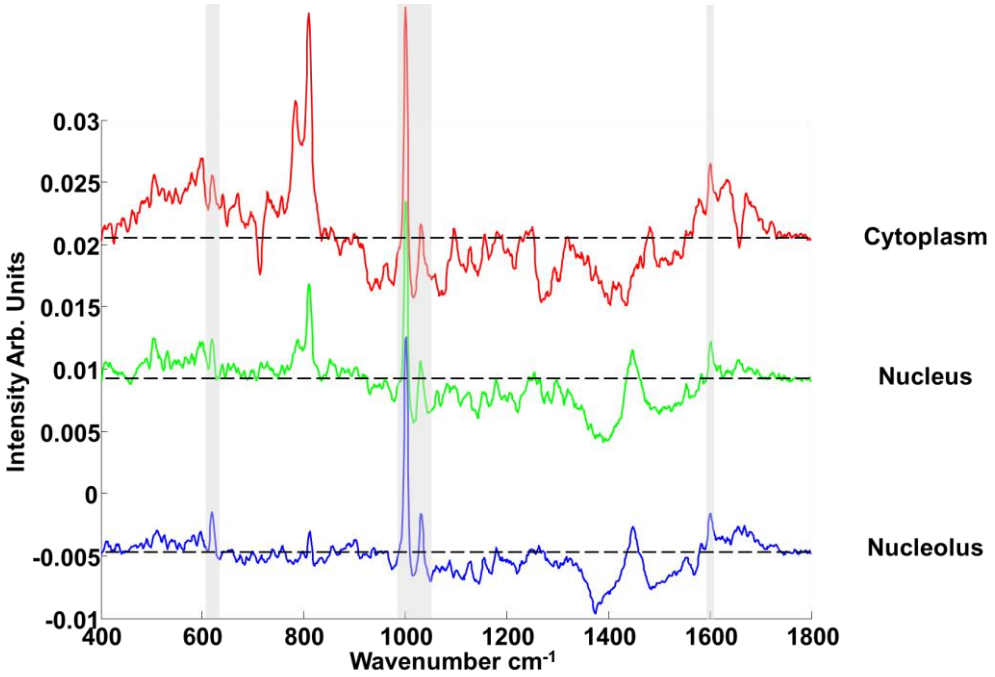

Figure 4.3. Mean difference spectra of cytoplasm (red), nucleus (green) and nucleolus (blue) obtained by subtraction of mean spectra of 8 hr PS-NH_2 exposed cells from mean spectra of unexposed cells. The spectra are offset for clarity, the dashed line indicating the zero point. The bands related to PS are indicated with grey highlights.

Cellular events as a result of nanoparticle exposure to, and uptake of, a toxicant cause the production, consumption and/or damage of biochemical constituents inside the cells. The changes in the biochemical constituents are reflected in the Raman spectral data sets and can be used to identify different cellular events. When cells are exposed to 10 μM PS-NH_2 for 8 hr, the most significant changes are observed in the cytoplasm, as seen in Figure 4.3. The intensity of the bands at 785 and 810 cm^{-1} become significantly higher compared to the controls. The band at 785 cm^{-1} can be attributed

to the ring breathing mode of nucleic acid bases (U, T and C) or O-P-O backbone stretching of nucleic acids, as so can be attributed to either RNA or DNA (Movasaghi, Rehman, & Rehman 2007; Notingher & Hench 2006; Notingher *et al.* 2003). The band at 810 cm^{-1} is attributed to RNA structures (Small & Peticolas 1971; Thomas, Medeiros, & Hartman 1971) and relates to asymmetric stretching of the sugar-phosphate diester. The presence of 785 and 810 cm^{-1} bands in Raman spectra of the cytoplasm has been examined in the study of Ghita *et al.* (Ghita *et al.* 2012), which showed that an increase of the RNA bands during cell differentiation can be attributed to repressed translation of mRNAs and increasing amounts of noncoding RNAs in the cytoplasm. As seen in Figure 4.3, upon PS-NH_2 exposure, the band at 810 cm^{-1} shows a significant increase compared to its control with a concomitant increase in the band at 785 cm^{-1}, while control cells did not show any significant band at 810 cm^{-1} for cytoplasm (Supplementary Figure 4.S2).

The exposure of cells to toxic PS-NH_2 is known to result in ROS formation (Ruenraroengsak & Tetley 2015). Increased ROS levels in the cell first impacts on the mitochondria and causes the mediation of cytotoxic effects and release of pro-apoptotic factors with increasing production of mitochondrial ROS (Xia *et al.* 2006), which in turn can cause deformation of cytoplasmic RNAs which generally localises in close proximity to the mitochondria and results in repression of translation and accumulation of noncoding RNAs in the cytoplasm of exposed cells. The role of oxidative stress in the repression of mRNA translation has been shown previously (Czech *et al.* 2013; Saikia *et al.* 2012; Yamasaki *et al.* 2009). For this reason, an increase in the intensity of the 810 cm^{-1} band in the cytoplasm can be attributed to changes in RNA content, as a result of oxidative stress and can be used as a

mitochondrial damage marker in a label-free way. Although the band at 785 cm^{-1} can be attributed to either DNA or RNA, the concomitant increase in the 810 cm^{-1} for short exposure times is consistent with a primary attribution of increased RNA accumulation in cytoplasm.

The cytoplasmic responses upon particle exposure are further explored according to their correlation with the concentration of toxicant. The effect of PS-NH_2 exposure on A549 cells was also monitored using intermediate (5 μM) and sub-lethal doses (2.5 μM), for 8hrs. PCA clearly differentiates unexposed and exposed cells according to PC1 for all exposure doses. Scatter plots of unexposed and exposed cells for each exposure dose are provided in Supplementary Figure 4.S3, and a representative example of scatter plot of cytoplasm of exposed and unexposed cells for 10 μM PS-NH_2 is shown in Figure 4.4.I. The respective loadings for the cytoplasmic regions of 2.5, 5 and 10 μM are shown in Figure 4.4.II.

For 10 μM PS-NH_2, which is close to the EC_{50} value for AB, exposed cells are differentiated from unexposed cells due to a significant increase of the intensity of nucleic acid bands represented by positive features of loading 1 (785 and 810 cm^{-1}), which can also be seen in the difference of mean spectra of exposed and unexposed cells (Figure 4.3). Notably, the changes in this region are seen to evolve monotonically with exposure dose (Figure 4.4, Figure 4.S4), confirming a direct correlation between the changes in nucleic acid spectral signatures and particle exposure.

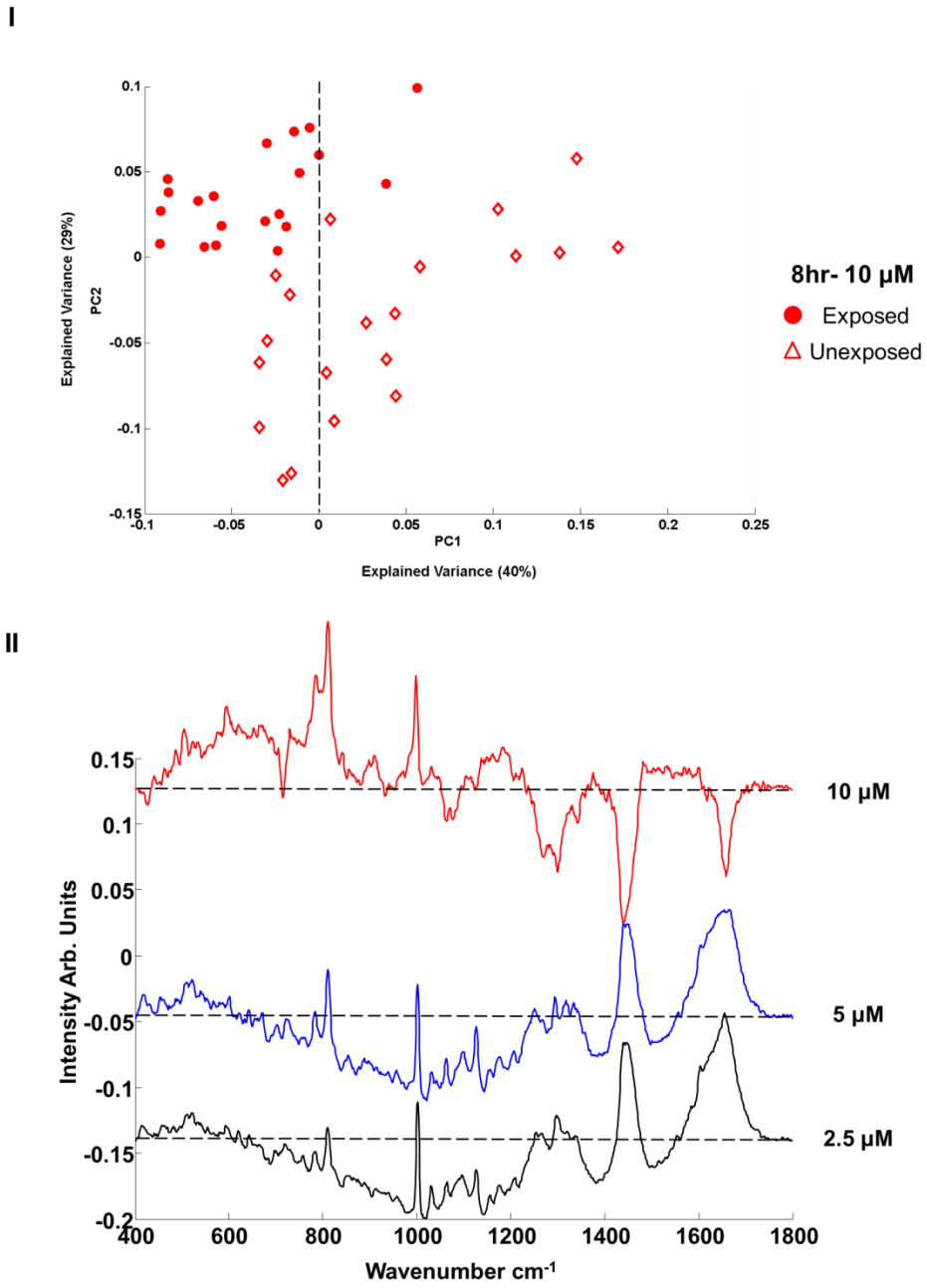

Figure 4.4. **I)** Scatter plot of the PCA of spectra corresponding to cytoplasm of the unexposed cells (closed circles) and cells exposed to 10 µM PS-NH_2 for 8 hr (open diamond). **II)** Loadings of PC1 for pairwise analysis of cytoplasm of exposed cells with the control for 10 µM (red), 5 µM (blue) and 2.5 µM (black) for 8 hr. The dotted line represents the zero '0' point for each loading. Loadings are offset for clarity.

Negative features of the loading (unexposed cells) are observed to be richer in protein and lipid content (bands at 1062, 1080, 1270, 1299 and 1438 cm^{-1}). The relatively higher amount of the lipids in unexposed cells compared to PS-NH_2 exposed cells can be attributed to damage of the lipidic structures such as lysosomes and membrane bounded cellular compartments upon PS-NH_2 exposure. When the nanoparticles are localised inside the lysosomes after 8 hrs, they become trapped due to the protonation of their surface in low lysosomal pH (~4.5). Protonation and the change in the lysosomal pH cause formation of a gradient for lipids to traffic into the lysosomes from the cytosol and finally the formation of enzymatically unbreakable complexes (Myeloid bodies) (Anguissola *et al.* 2014). The lipid transfer from cytoplasm to lysosomes and accumulation of lipids in lysosomes, a phenomenon known as lipidosis, causes the loss of lipid related bands in the spectral profile of the cytoplasm. Moreover, later stages of lipidosis cause a distortion and rupture of the lysosomal membrane (Asokan & Cho 2002; Drenckhahn, Kleine, & Lullmann-Rauch 1976; Lullmann, Lullmann-Rauch, & Wassermann 1978; Sonawane, Thiagarajah, & Verkman 2002). Therefore, changes in the intensities of the bands at 719 cm^{-1} (membrane phospholipids), 1270-1301 cm^{-1} (phospholipids, lipids), 1437 cm^{-1} (acyl chain of lipids) can be used to track lysosomal damage during nanotoxicological screening of toxic nanoparticles.

As seen in Figure 4.4, with the exception of the monotonic increase in the nucleic acid related bands at 785 and 810 cm^{-1}, sub lethal doses of PS-NH_2, result in significantly different spectral profiles compared to the cells exposed to 10 μM PS-NH_2. When the concentration of PS-NH_2 was reduced to 5 μM, the exposed cells show increased amounts of lipid, protein and nucleic acid in the cytoplasm compared to unexposed

cells (the positive features of loading 1). Also, nucleic acid related bands are prominent at around 1095 cm^{-1} (PO_2^-), 1177 cm^{-1} (C, G) and 1292 cm^{-1} (C) , but are not evident in the 10 μM PS-NH_2 exposed cells. The 5 μM PS-NH_2 exposed cells also show increases in the intensity of protein (1030, 1208, 1250 and 1654 cm^{-1}) and lipid bands (1064 cm^{-1}), compared to unexposed cells. A similar PC Loading profile was observed when the dose was reduced to 2.5 μM, exhibiting a decrease in the intensities of the bands at 785 cm^{-1} (Nucleic acids), 810 cm^{-1} (RNA), 1127 cm^{-1} (υ(C-N)), 1266 cm^{-1} (Amide III (α-helix)), 1319 cm^{-1} (G), 1333 cm^{-1} (G) and an increase in the intensity of the band at 1655 cm^{-1} (Amide I). When the respective loadings for each dose are compared, lipid and protein related bands are inverted in going from lethal (10 μM) to sub lethal (2.5 μM) PS-NH_2 doses. The change in the amount of lipid and protein structures with increasing dose can be related to damage of protein and lipid structures as a result of increasing amount of ROS inside the cell for toxic exposures.

Following the effect of dose of PS-NH_2 on A549 cells, the effect of exposure time was monitored by comparing particle exposed cells with their controls. In order to evaluate spectral differences progressively as a function of time, a sub lethal dose of PS-NH_2 (2.5 μM) was chosen and cells were exposed to the nanoparticles from 4 to 48 hrs. Figure 4.5.I shows the scatter plots of the PCA of spectra corresponding to cytoplasm of exposed and unexposed cells for 24 hr (2.5 μM), as a representative example of separation between exposed and unexposed cells. Scatter plots of cytoplasm of exposed and unexposed cells for each exposure time are provided in Supplementary Figure 4.S5. As seen in Figure 4.5.I, for the case of 24 hr, exposed and unexposed cells are largely differentiated according to PC1 (Explained Variance 45%). Figure 4.5.II

shows the comparison of the loadings of PC1 of cytoplasm of exposed and unexposed cells for 4, 8, 12, 24 and 48 hrs.

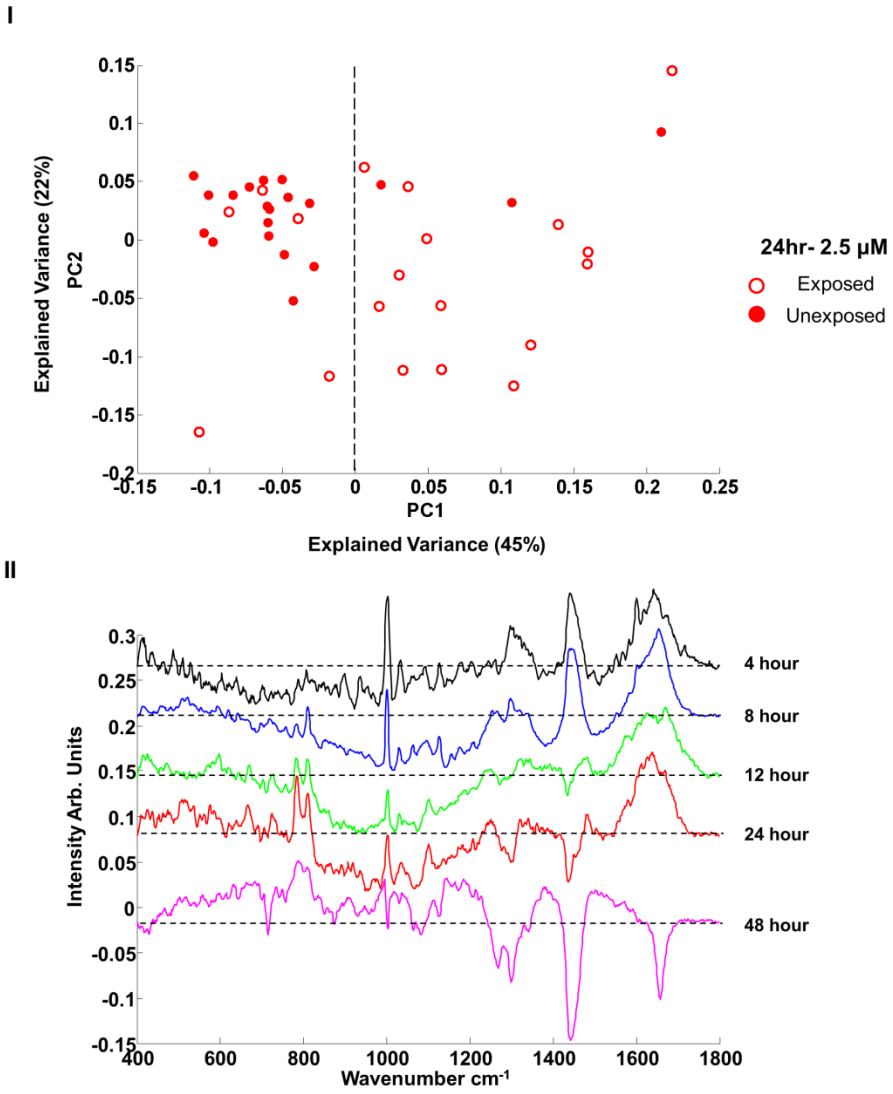

Figure 4.5. **I)** Scatter plot of the PCA of spectra corresponding to cytoplasm of the unexposed cells (close circles) and PS-NH_2 exposed cells (2.5 µM) (open circles) for 24 hr, **II)** Comparison of the Loading of PC1s for different PS-NH_2 concentrations (cytoplasm). 4, 8, 12, 24 and 48 hr are indicated with black, blue, green, red and magenta, respectively. Positive features of the PCs are related to exposed cells while negative features of the PCs are related to their controls. Loadings are offset for clarity. The dotted line represents the zero '0' point for each loading.

As in the case of the exposure dose dependent spectral profiles, the evolution of the nucleic acid features at 780 cm^{-1} and 810 cm^{-1} is observed to be prominent. However, these features are weak after 4 hr PS-NH_2 exposure, and the particle exposed cells differentiate from the unexposed cells largely due to their protein and lipid content. The bands at 1003 cm^{-1} (Phe), 1602 cm^{-1} (Phe) and 1640 cm^{-1} (Amide I) can be attributed to damaged protein structures resulting from the damage in the mRNA template and the distorted proteins accumulate inside the cell as well as normal proteins due to lysosomal damage (Frohlich *et al.* 2012). The increasing intensity of the lipid bands at 1298 and 1440 cm^{-1} indicates an increasing amount of lipids in the cytoplasm due to increasing amount of endosomes and lysosomes upon PS-NH_2 exposure. When the time of exposure of the cells to the PS-NH_2 is increased to 8 hr, following the increases in protein and lipid bands, some changes start to occur in RNA accumulation in the cytoplasm due to the onset of repression of mRNA translation, which are manifest in the Raman spectra of PS-NH_2 exposed cells (positive features of loading 1) as an increase in the band at 810 cm^{-1}. An increase in the intensity of bands at 1319 (G) cm^{-1} and 1333 (G) cm^{-1} can also be observed with increasing exposure time. For this exposure time, the sharp band at 1602 cm^{-1}(Phe) disappears and the intensity of the 1003 cm^{-1} band reduces, which can be attributed to the onset of degradation of proteins.

After 12 hr exposure of A549 cells to PS-NH_2, more significant changes occur in the biochemical composition of particle exposed cells compared to previous exposure times. For this exposure time, as seen in Figure 4.5.II, the nucleic acid band at 785 cm^{-1} shows an increase in its intensity which indicates the increasing amount of nucleic acids in cytoplasm. Similar to the effect of dose, in the case of increased exposure time,

the increase of nucleic acids in the cytoplasm can be observed at 810 cm^{-1} (RNA), with a larger increase in 785 cm^{-1} (RNA and DNA) compared to 8 hr exposure. Although the increase in the 785 cm^{-1} band was attributed to RNA accumulation for shorter exposure times (up to 8 hr), an independent increase is observed on the 785 cm^{-1} band compared to 810 cm^{-1} with increasing exposure time, which can be attributed to an increase of DNA content in the cytoplasm. The increasing amount of DNA in the cytoplasm can be attributed to the decay of mitochondrial membrane and release of mitochondrial DNA into the cytoplasm, at this time point. ROS formation and mitochondrial decay affect the spectral profile of proteins and lipids in particle exposed cells and this is reflected in the Raman spectra of unexposed cells and causes the appearance of the bands at 1200-1300 cm^{-1} (Amide III) and 1438 cm^{-1} (Protein, Lipids) as negative features of PC1, which represent the unexposed cells. Also notable is the emergence in the loadings spectrum of bands at 1299 and 1438 cm^{-1}. They are both associated with lipid content inside the cytoplasm and the change in the intensity of the bands can be attributed to damage of lipidic structures due to lipidosis after PS-NH_2 exposure. The intensity changes in the 1438 cm^{-1} band can be further used determine cytotoxic events in the cytosol and damage of lysosomes. The band at 1299 cm^{-1} is progressively reduced until 12 hour particle exposure and becomes inverted for 24 and 48 hr particle exposure, which indicates that lipids are more abundant in unexposed cells compared to exposed ones. The intensity of the band at 1438 cm^{1} did not show any change up to 8 hr, but this band is inverted with increasing intensity from 12 to 48 hr, such that it becomes a dominant feature of the discriminating loading. Moreover, the intensity of the 1003 cm^{-1} (Phe) band reduces significantly, while there is a clear broadening of the Amide I band (1550-1700 cm^{-1}). The intensities of the nucleic acid (785 cm^{-1}) and RNA (810cm^{-1}) bands increase further for 24 hr exposure,

while the protein and lipid bands (1266, 1299 and 1438 cm^{-1}) become more significant as negative features (unexposed cells) of PC1. The further increase in the intensity of the band at 785 cm^{-1} can be attributed to disruption of membrane structures and release of DNA into the cytoplasm (Elmore 2007).

When cells were exposed to PS-NH_2 for 48 hrs, the exposed cells are differentiated from unexposed cells according to their nucleic acid content, as the bands at 785 and 810 cm^{-1} are observed in the positive features of the loading 1. The band at 1003 cm^{-1}, which indicates the presence of Phe, becomes inverted for the 48 hr exposure. Moreover, the bands at 1299 and 1438 cm^{-1} become dominant in the negative features of the loading 1. The change in the lipid bands can be attributed to further decomposition of lipid structures in cell upon longer exposure. Also, the band at 1268 cm^{-1} appears for this exposure time in the negative features, which indicates a change in the conformational structures of the proteins. The contribution of the Amide I band at 1658 cm^{-1} has become inverted following 48 hr particle exposure. The inverted bands on loading 1 of PC can be attributed to less abundance of proteins and lipids in particle exposed cells.

The spectra of the cytoplasm of PS-NH_2 exposed cells are mainly differentiated from unexposed cells by the intensities of the bands at 785 and 810 cm^{-1}. Moreover, another significant change is observed in the Amide I region of proteins, with increasing exposure time. In order to monitor spectral changes in the Amide I region, the Amide I band (1550-1700 cm^{-1}) was analysed separately in detail. Oxidative stress in a cell causes damage in protein structures and changes the protein secondary structure and tertiary conformation. The changes in protein conformations are reflected in the Amide

I region of the Raman spectrum. With increasing exposure time, a broadening and shift is observed in the Amide I band. The Amide I band represents the different secondary structures of the proteins, such as α-helix, ß-sheet, loops (Stuart 1997), and the broadening or shift in Amide I band can be attributed to a change in secondary structure of proteins as a result of oxidative stress.

The Amide I region of proteins in the cytoplasm of PS-NH_2 exposed cells and changes in the bands upon particle exposure are detailed in Figure 4.6 and Table 4.1, for different exposure times (I-V) from 4 to 48 hr. The loadings of PC1 of cytoplasm of unexposed and exposed cells were used and peak fitting was carried out for all exposure times, using LabSpec Software. As seen in Figure 4.6, the band at 1602 cm^{-1}, which indicates the presence of Phe, is observed for all exposure times, and a change in the total area of the band is observed as a function of time. The band area increases from 0.51 to 1.88, from 4 to 12 hr exposure, but then decreases to 0.34 for 24 hr exposure. Following 48 hr exposure, this band has totally disappeared from the positive features of loading 1. For the first 4 hr particle exposure, both α-helix and ß-sheet structures of protein are observed. However, with increasing exposure time, α-helix structures become dominant and the bands related to the presence of ß-sheet structure disappear (1674 and 1679 cm^{-1}). Thus, with increasing exposure, the Amide I band becomes dominated by α-helix bands, resulting in an apparent shift to lower wavenumbers up to 24 hr exposure. When cells are exposed to the PS-NH_2 for 48 hrs, the Amide I band becomes completely inverted and a sharp band at 1658 cm^{-1}(Amide I, α-helix) is observed in the negative features of the loading 1 (Movasaghi, Rehman, & Rehman 2007; Notingher & Hench 2006; Notingher *et al.* 2003) .

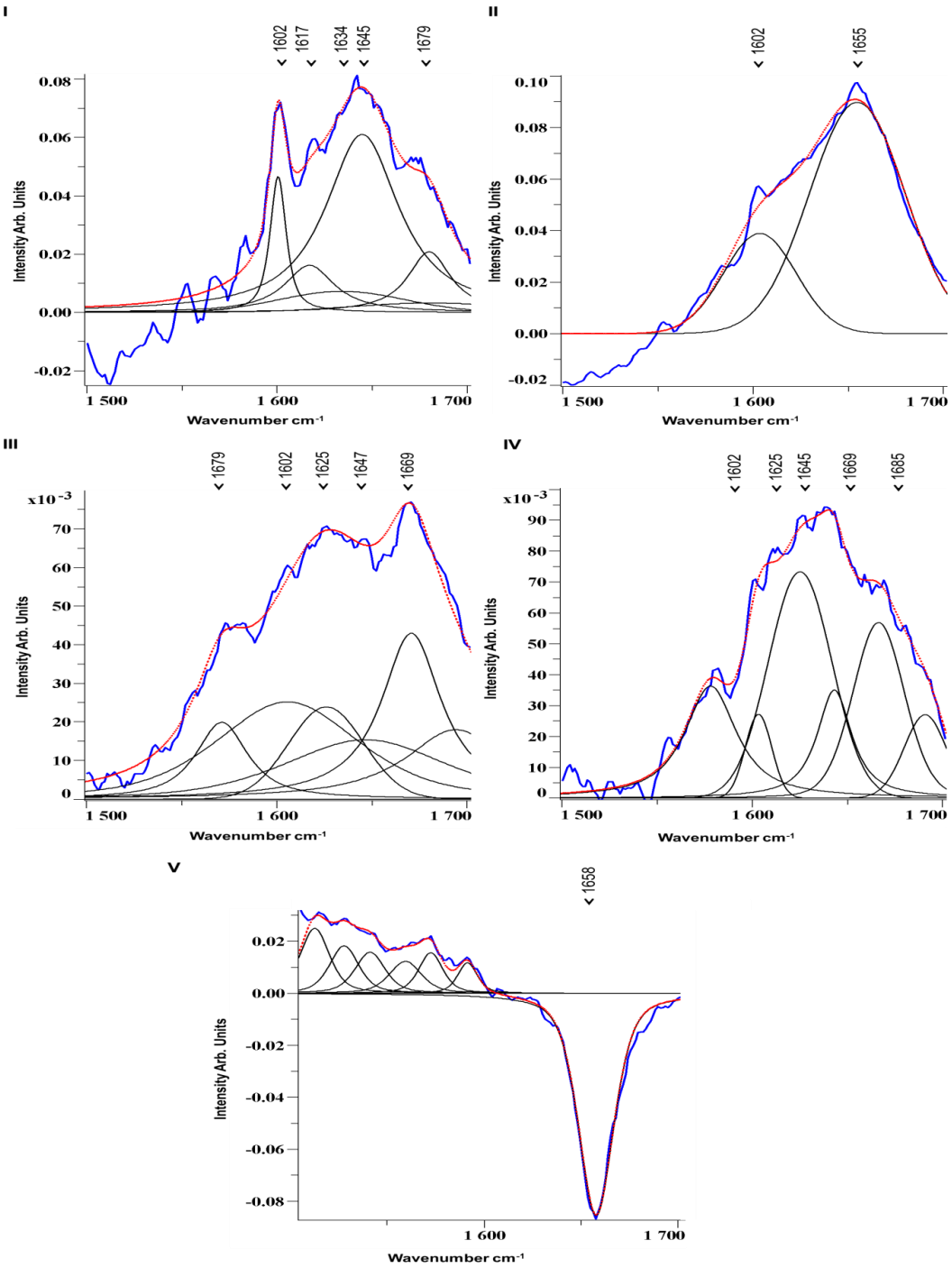

Figure 4.6. Comparison of the changes in the Amide I region of loading 1 for 4 (I), 8 (II), 12 (III), 24 (IV) and 48 (V) hrs. The loadings and sum of the bands after fitting are indicated with blue and red lines, respectively. Each individual fitted band is represented by black lines. Peak positions are indicated on the top of the fitted figures.

Table 4.1. Assignments of Raman Bands of proteins in Amide I Region (Movasaghi, Rehman, & Rehman 2007; Notingher & Hench 2006; Notingher *et al.* 2003).

		Band Positions (1550-1700 cm^{-1})	**Band Assignments**
PS-NH_2 Exposed Cells	**4 hour**	1602	Phe
		1618	Trp, Tyr (δ(C=C) stretch.)
		1634	Amide I (Both α-helix and ß sheet)
		1645	Amide I (α-helix)
		1679	Amide I (ß sheet)
	8 hour	1602	Phe
		1655	Amide I (α-helix)
	12 hour	1569	Trp (Indole Ring)
		1602	Phe
		1625	Trp
		1647	Random coils
		1669	Amide I (α-helix)
	24 hour	1582	Phe
		1602	Phe
		1625	Trp
		1645	α-helix
		1669	Amide I (C=O)
		1685	Amide I (disordered structure; non hydrogen bonded)
	48 hr	1658	Amide I (inverted)

Time and dose dependent cytotoxicity can be seen as a 3D response surface rather than a 2D curve, due to the variance of molecular determinants forming overall cytotoxicity (Maher *et al.* 2014). Thus, sublethal concentrations can elicit a similar effect to higher concentrations at different time points. Figure 4.7 shows the comparison of loading 1 of PC of cytoplasm of unexposed and exposed cells for cytoplasm for 8hr exposure 10 μM and 48hr exposure 2.5 μM PS-NH_2. Both loadings show similar positive (exposed cells) and negative features (unexposed cells), with the possible exception of the band at 810 cm^{-1} which indicates the presence of accumulated noncoding RNA in the cytoplasm. This difference can be explained by the more acute toxic effect of repression of translation of mRNA of higher exposure doses. More molecular determinants of toxicity are manifest for the nucleic acid constituents for all exposure times, although more prominently for high doses and long exposure times. For this reason, the difference in the bands related to nucleic acids can be attributed to changing amounts of molecular determinants. Compared to their controls, exposed cells showed lower contributions of protein and lipids, which can be attributed to damage to these biochemical constituents in particle exposed cells due to oxidative attack.

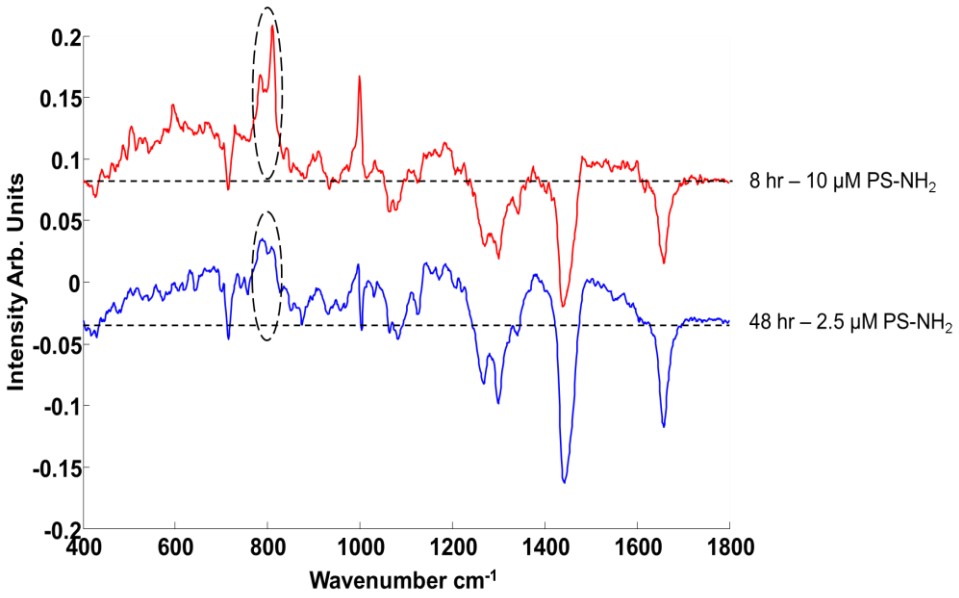

Figure 4.7. Comparison of the Loading 1 of PCs of cytoplasm for exposed and unexposed cells after 8 hr exposure to 10 μM (red) and 48 hr 2.5 μM (blue) PS-NH_2. Positive and negative features of the loadings relate to exposed and unexposed cells, relatively. The significant differences between the loadings are indicated with black circles. Loadings are offset for clarity. The dotted line represents the zero '0' point for each loading.

As shown in Figure 4.2, comparatively fewer changes are observable in the spectral signature of the nucleus and nucleolus, as might be expected, given the uptake and trafficking of the PS-NH_2 is through the cytoplasm, over a period of up to 24 hrs. No localisation of PS-HN_2 nanoparticles in the nucleus has been reported and, indeed, it has been seen that neutral PS nanoparticles are stored in lysosomal vesicles over several passages of the cells (Salvati *et al.* 2011; Shapero *et al.* 2011). Nevertheless, as shown in Figure 4.8, the mean difference spectrum of the nuclear region does show indications of reduced contributions of nucleic acids at 785 and 810 cm^{-1}, after 24 hr exposure, consistent with leakage of nuclear material into the cytoplasm after the onset

of apoptosis. This is also consistent with the larger increase of nucleic acid features in cytoplasm of PS-NH_2 exposed cells after 24 hr exposure (Figure 4.5.II).

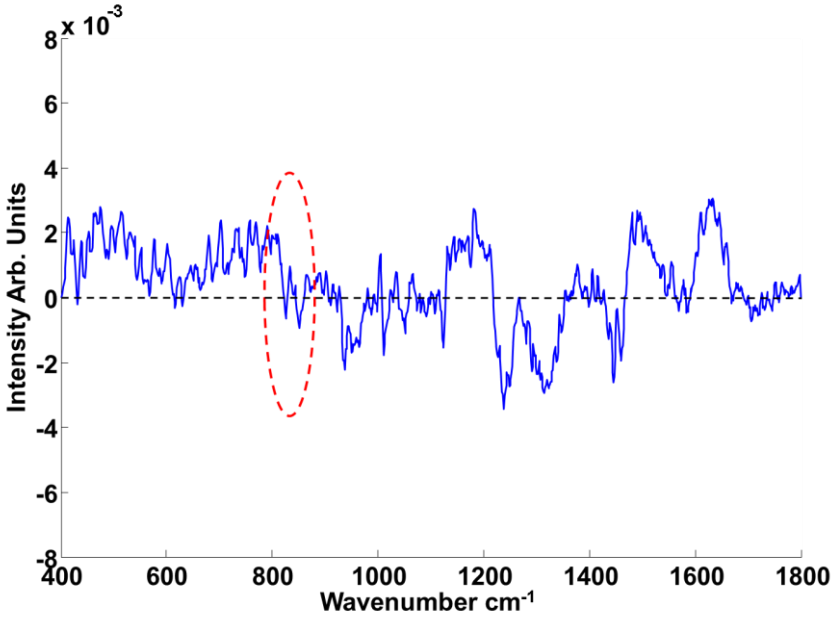

Figure 4.8. Difference spectrum of nucleus of PS-NH_2 exposed cells and unexposed cells obtained by subtraction of mean spectra of 24 hr PS-NH_2 exposed cells from mean spectra of unexposed cells.

In the case of exposure to the PS-NH_2, the most significant changes are observed in the cytoplasm, as expected due to the uptake mechanism and cellular trafficking of the PS-NH_2. The uptake mechanism by endocytosis and subsequent cellular trafficking initiates a series of molecular events and hence molecular determinants of the cytotoxicity. In endocytosis, toxic PS-NH_2 particles are carried to lysosomes by endosomes resulting in lipidosis, lysosomal membrane rupture and ROS in the cytosolic region. The mitochondria of the particle exposed cells are affected as a result of cytosolic changes and mediate the release of pro-inflammatory factors as signals of cytotoxicity. On the other hand, for example doxorubicin, commonly used anti-cancer

chemotherapy drug, is taken into cells by passive diffusion and targets the nuclear region directly. The cytotoxic effects are manifest initially in the nuclear and nucleolar regions of the cell, and only later in the cytoplasm (Farhane *et al.* 2015). The process is inverse for PS-NH_2, whereby the toxic effects of the particles are initially seen in the cytoplasmic region for shorter exposure times, although changes in the nuclear area may be more significant in chronic exposures, and linked with genotoxic effects.

In this study, the cytoplasmic changes relating to molecular events upon particle exposure due to the uptake mechanism and cellular trafficking the PS-NH_2, have been evaluated in a dose and time dependent manner, using Raman spectroscopy. The established initial response of oxidative stress is not evident in the spectral response, however. ROS such as hydrogen peroxide (H_2O_2), superoxide anion ($O_2^{-\cdot}$) and hydroxyl radicals ($HO^{\cdot}$) are known to be Raman inactive and, in addition, they are consumed rapidly after initial generation (Casteilla, Rigoulet, & Pénicaud 2001; S G Mukherjee *et al.* 2012). Nevertheless, although the molecular signatures of ROS are not possible to identify with Raman spectroscopy, the signatures of the resultant oxidative stress can be monitored via the signatures of the changes in biochemical constituent of the cells. Oxidative stress in the cytoplasm triggers a complex cascade of events which can include mitochondrial membrane potential decay, caspase activation, apoptosis and ultimately cell death. For a more extensive discussion of the responses, see for example references Xia *et al.* (Xia *et al.* 2008) and Maher *et al.* (Maher *et al.* 2014). The Raman spectral biomarkers of ROS formation, lysosomal damage and biochemical composition changes upon nanoparticle exposure are identified and the most dominant features changing inside the cytoplasm of the cells upon particle exposure are determined to be the bands at 785 and 810 cm^{-1} which can

be attributed to nucleic acids inside the cytosol. It is notable, however, that the spectral changes are dominated by the 785 and 810 cm^{-1} bands, rather that the whole spectrum of RNA or DNA (Bonnier *et al.* 2010), suggesting that the spectral signature is due to conformational changes in the nucleic acid structures due to change in the environment rather than production or consumption of the nucleic material. Especially for sub-lethal doses of PS-NH_2, some contributions are observed to the spectra of cells which indicate higher protein content compared to control cells. Cells use a recovery mechanism to stabilize the increased ROS levels inside the cells upon exposure to a toxicant (Casteilla, Rigoulet, & Pénicaud 2001). Increased production of enzymes such as superoxide dismutase, catalase, glutathione peroxidase, glutathione reductase, causes an increase in protein related bands. For this reason, the changes in cytosolic acids followed by increased protein profile can be attributed to increased ROS levels and the Raman profile can be used as a Nanotoxicological assay biomarker for a wide variety of nanomaterials.

In comparison with the responses of the classical cytotoxic assays, (Figure 4.1.II), significant spectral changes are observed over a dose range (from 2.5 to 10 μM), in which MTT shows no change, but AB shows significant change. These spectroscopic changes are therefore better correlated with AB, consistent with an interpretation of origin in cytosolic RNA which subsequently accumulates around the mitochondria. The changes in 1299 and 1438 cm^{-1} bands, which are associated with the later stage toxic response and become inverted after 12 hr particle exposure with an increasing intensity in the negative features of the loading 1, may be better correlated with the MTT response and therefore mitochondrial decay (Figure 4.5.II). Mitochondrial ROS

production can cause significant oxidative stress, damaging protein and lipid structures and mediating the release of factors to initiate the apoptotic process.

Spectral changes, as elucidated by PCA, are complex combinations of contributions of the multitude of biomolecules involved in the cellular responses. However, the combination signature shows consistency in its evolution as a function of time and dose, and correlates well with the known cytotoxic responses. Therefore, not individual spectra, but signatures at 785 cm^{-1} (either RNA or DNA), 810 cm^{-1} (RNA), 1299 cm^{-1} (lipids) and 1435 cm^{-1} (lipids) and proteins Amide I (1550-1700 cm^{-1}) region can be a guide to nanotoxicological screening.

4.5. Conclusion

Classical colorometric cytotoxicological assays monitor a single endpoint by which the cellular response to a toxicant is quantified in terms of the IC_{50}. The response is, however, a complex cascade of events, and different assays can report significantly different viability results, and yield little information about the mechanisms of response. The use of a label-free and rapid technique which provides multiparametric information about the changes in the biomolecular structures such as proteins, lipids and nucleic acids following exposure to a toxicant can accelerate the toxicological screening of nanomaterials. This study has identified spectral signatures which are correlated with nanoparticle exposure dose and time, and therefore the known mechanisms of cellular response and toxicity, demonstrating the potential of Raman spectroscopy as a label-free technique to provide multi-parametric information about the biomolecular changes upon a toxicant exposure. It is demonstrated that spectral

profiles of the particle exposed cells can be used to track the fingerprint of the molecular responses. Time and dose dependent cytotoxic responses and their reflection to the biochemical fingerprint of the cells can be monitored by using Raman spectroscopy in a progressive way. For all exposure times and doses, the most prominent Raman spectral marker, reflecting the cytotoxic response to exposure to model PS-NH_2 nanoparticles, is found to be the bands at 785 and 810 cm^{-1} in the cytoplasm, reflecting changes in cytoplasmic nucleic acid content. Notably, this response is not normally identified by conventional cytotoxicity assays. The concomitant and subsequent changes in the intensity of the bands corresponding to proteins (Amide I region, 1550-1700 cm^{-1}) and lipids (1229 and 1438 cm^{-1}) can also be used to determine toxic effect of nanoparticles. The use of Raman spectroscopy helps to corroborate and further elucidate the mechanism of action of the nanoparticles within cells and Raman cytotoxicity spectral-markers identified for model nanoparticles can potentially be used to screen for the mode of action and degree of toxicity of novel nanoparticles, in a single label-free assay.

4.6. References

Anguissola, S, Garry, D, Salvati, A, O'Brien, P J and Dawson, K A (2014) High Content Analysis Provides Mechanistic Insights on the Pathways of Toxicity Induced by Amine-Modified Polystyrene Nanoparticles. *PLoS ONE*, 9(9), e108025.

Asokan, A and Cho, M J (2002) Exploitation of Intracellular Ph Gradients in the Cellular Delivery of Macromolecules. *J Pharm Sci*, 91(4), 903-13.

Berridge, M V, Herst, P M and Tan, A S (2005) Tetrazolium Dyes as Tools in Cell Biology: New Insights into Their Cellular Reduction. *Biotechnol Annu Rev*, 11, 127-52.

Bexiga, M G, Varela, J A, Wang, F, Fenaroli, F, Salvati, A, Lynch, I, Simpson, J C and Dawson, K A (2011) Cationic Nanoparticles Induce Caspase 3-, 7- and 9-Mediated Cytotoxicity in a Human Astrocytoma Cell Line. *Nanotoxicology*, 5(4), 557-67.

Bonnier, F, Knief, P, Lim, B, Meade, A D, Dorney, J, Bhattacharya, K, Lyng, F M and Byrne, H J (2010) Imaging Live Cells Grown on a Three Dimensional Collagen Matrix Using Raman Microspectroscopy. *Analyst*, 135(12), 3169-77.

Bonnier, F, Mehmood, A, Knief, P, Meade, A D, Hornebeck, W, Lambkin, H, Flynn, K, McDonagh, V, Healy, C, Lee, T C, Lyng, F M and Byrne, H J (2011) *In vitro* Analysis of Immersed Human Tissues by Raman Microspectroscopy. *Journal of Raman Spectroscopy*, 42(5), 888-96.

Bonnier, F, Petitjean, F, Baker, M J and Byrne, H J (2014) Improved Protocols for Vibrational Spectroscopic Analysis of Body Fluids. *Journal of Biophotonics*, 7(3-4), 167-79.

Breve, G J P a J (1996). Whole Cell Studies and Tissue Characterization by Raman Spectroscopy In *"Biomedical Applications of Spectroscopy"* Vol. 25, John Wiley and Sons, New York.

Byrne, H J, Sockalingum, G D and Stone, N (2011). Chapter 4 Raman Microscopy: Complement or Competitor? In *Biomedical Applications of Synchrotron Infrared Microspectroscopy: A Practical Approach*, The Royal Society of Chemistry.

Casteilla, L, Rigoulet, M and Pénicaud, L (2001) Mitochondrial Ros Metabolism: Modulation by Uncoupling Proteins. *IUBMB Life,* 52(3-5), 181-8.

Chernenko, T, Matthaus, C, Milane, L, Quintero, L, Amiji, M and Diem, M (2009) Label-Free Raman Spectral Imaging of Intracellular Delivery and Degradation of Polymeric Nanoparticle Systems. *ACS Nano,* 3(11), 3552-9.

Consumer Products Inventory (2016) [Online]. Available: http://www.nanotechproject.org/cpi/ [Accessed June]

Czech, A, Wende, S, Mörl, M, Pan, T and Ignatova, Z (2013) Reversible and Rapid Transfer-Rna Deactivation as a Mechanism of Translational Repression in Stress. *PLoS Genet,* 9(8), e1003767.

Donaldson, K, Stone, V, Tran, C L, Kreyling, W and Borm, P J (2004). Nanotoxicology In *Occup Environ Med* Vol. 61 England.

Dorney, J, Bonnier, F, Garcia, A, Casey, A, Chambers, G and Byrne, H J (2012) Identifying and Localizing Intracellular Nanoparticles Using Raman Spectroscopy. *Analyst,* 137(5), 1111-9.

Drenckhahn, D, Kleine, L and Lullmann-Rauch, R (1976) Lysosomal Alterations in Cultured Macrophages Exposed to Anorexigenic and Psychotropic Drugs. *Lab Invest,* 35(2), 116-23.

Efeoglu, E, Keating, M, McIntyre, J, Casey, A and Byrne, H J (2015) Determination of Nanoparticle Localisation within Subcellular Organelles *in vitro* Using Raman Spectroscopy. *Analytical Methods,* 7(23), 10000-17.

Ekkapongpisit, M, Giovia, A, Follo, C, Caputo, G and Isidoro, C (2012) Biocompatibility, Endocytosis, and Intracellular Trafficking of Mesoporous Silica and Polystyrene Nanoparticles in Ovarian Cancer Cells: Effects of Size and Surface Charge Groups. *Int J Nanomedicine,* 7, 4147-58.

Elmore, S (2007) Apoptosis: A Review of Programmed Cell Death. *Toxicologic pathology,* 35(4), 495-516.

Farhane, Z, Bonnier, F, Casey, A and Byrne, H J (2015) Raman Micro Spectroscopy for *in vitro* Drug Screening: Subcellular Localisation and Interactions of Doxorubicin. *Analyst,* 140(12), 4212-23.

Farhane, Z, Bonnier, F, Maher, M A, Bryant, J, Casey, A and Byrne, H J (2016) Differentiating Responses of Lung Cancer Cell Lines to Doxorubicin Exposure: *In vitro* Raman Micro Spectroscopy, Oxidative Stress and Bcl-2 Protein Expression. *J Biophotonics*.

Ferraro, J R, Nakamoto, K and Brown, C W (2003). Chapter 1 - Basic Theory In *Introductory Raman Spectroscopy (Second Edition),* Academic Press, San Diego.

Frohlich, E, Meindl, C, Roblegg, E, Ebner, B, Absenger, M and Pieber, T R (2012) Action of Polystyrene Nanoparticles of Different Sizes on Lysosomal Function and Integrity. *Part Fibre Toxicol,* 9, 26.

Ghita, A, Pascut, F C, Mather, M, Sottile, V and Notingher, I (2012) Cytoplasmic Rna in Undifferentiated Neural Stem Cells: A Potential Label-Free Raman Spectral Marker for Assessing the Undifferentiated Status. *Anal Chem,* 84(7), 3155-62.

Godbey, W T, Wu, K K and Mikos, A G (1999) Tracking the Intracellular Path of Poly(Ethylenimine)/Dna Complexes for Gene Delivery. *Proceedings of the National Academy of Sciences of the United States of America,* 96(9), 5177-81.

Keating, M E, Bonnier, F and Byrne, H J (2012) Spectral Cross-Correlation as a Supervised Approach for the Analysis of Complex Raman Datasets: The Case of Nanoparticles in Biological Cells. *Analyst,* 137(24), 5792-802.

Knief, P, Clarke, C, Herzog, E, Davoren, M, Lyng, F M, Meade, A D and Byrne, H J (2009) Raman Spectroscopy - a Potential Platform for the Rapid Measurement of Carbon Nanotube-Induced Cytotoxicity. *Analyst,* 134(6), 1182-91.

Loos, C, Syrovets, T, Musyanovych, A, Mailänder, V, Landfester, K, Nienhaus, G U and Simmet, T (2014) Functionalized Polystyrene Nanoparticles as a Platform for Studying Bio–Nano Interactions. *Beilstein Journal of Nanotechnology,* 5, 2403-12.

Lullmann, H, Lullmann-Rauch, R and Wassermann, O (1978) Lipidosis Induced by Amphiphilic Cationic Drugs. *Biochem Pharmacol,* 27(8), 1103-8.

Lunov, O, Syrovets, T, Loos, C, Beil, J, Delacher, M, Tron, K, Nienhaus, G U, Musyanovych, A, Mailander, V, Landfester, K and Simmet, T (2011) Differential

Uptake of Functionalized Polystyrene Nanoparticles by Human Macrophages and a Monocytic Cell Line. *ACS Nano,* 5(3), 1657-69.

Lunov, O, Syrovets, T, Loos, C, Nienhaus, G U, Mailander, V, Landfester, K, Rouis, M and Simmet, T (2011) Amino-Functionalized Polystyrene Nanoparticles Activate the Nlrp3 Inflammasome in Human Macrophages. *ACS Nano,* 5(12), 9648-57.

Maher, M A, Naha, P C, Mukherjee, S P and Byrne, H J (2014) Numerical Simulations of *in vitro* Nanoparticle Toxicity – the Case of Poly(Amido Amine) Dendrimers. *Toxicology in vitro,* 28(8), 1449-60.

Miljkovic, M, Chernenko, T, Romeo, M J, Bird, B, Matthaus, C and Diem, M (2010) Label-Free Imaging of Human Cells: Algorithms for Image Reconstruction of Raman Hyperspectral Datasets. *Analyst,* 135(8), 2002-13.

Mosmann, T (1983) Rapid Colorimetric Assay for Cellular Growth and Survival: Application to Proliferation and Cytotoxicity Assays. *J Immunol Methods,* 65(1-2), 55-63.

Movasaghi, Z, Rehman, S and Rehman, I U (2007) Raman Spectroscopy of Biological Tissues. *Applied Spectroscopy Reviews,* 42(5), 493-541.

Mu, Q, Hondow, N S, Krzeminski, L, Brown, A P, Jeuken, L J and Routledge, M N (2012) Mechanism of Cellular Uptake of Genotoxic Silica Nanoparticles. *Part Fibre Toxicol,* 9, 29.

Mukherjee, S G, O'Claonadh, N, Casey, A and Chambers, G (2012) Comparative *in vitro* Cytotoxicity Study of Silver Nanoparticle on Two Mammalian Cell Lines. *Toxicol In vitro,* 26(2), 238-51.

Nawaz, H, Bonnier, F, Knief, P, Howe, O, Lyng, F M, Meade, A D and Byrne, H J (2010) Evaluation of the Potential of Raman Microspectroscopy for Prediction of Chemotherapeutic Response to Cisplatin in Lung Adenocarcinoma. *Analyst,* 135(12), 3070-6.

Nawaz, H, Bonnier, F, Meade, A D, Lyng, F M and Byrne, H J (2011) Comparison of Subcellular Responses for the Evaluation and Prediction of the Chemotherapeutic Response to Cisplatin in Lung Adenocarcinoma Using Raman Spectroscopy. *Analyst,* 136(12), 2450-63.

Nawaz, H, Garcia, A, Meade, A D, Lyng, F M and Byrne, H J (2013) Raman Micro Spectroscopy Study of the Interaction of Vincristine with A549 Cells Supported by Expression Analysis of Bcl-2 Protein. *Analyst,* 138(20), 6177-84.

Notingher, I and Hench, L L (2006) Raman Microspectroscopy: A Noninvasive Tool for Studies of Individual Living Cells *in vitro*. *Expert Rev Med Devices,* 3(2), 215-34.

Notingher, I, Verrier, S, Haque, S, Polak, J M and Hench, L L (2003) Spectroscopic Study of Human Lung Epithelial Cells (A549) in Culture: Living Cells Versus Dead Cells. *Biopolymers,* 72(4), 230-40.

O'Brien, J, Wilson, I, Orton, T and Pognan, F (2000) Investigation of the Alamar Blue (Resazurin) Fluorescent Dye for the Assessment of Mammalian Cell Cytotoxicity. *Eur J Biochem,* 267(17), 5421-6.

Oberdörster, G, Maynard, A, Donaldson, K, Castranova, V, Fitzpatrick, J, Ausman, K, Carter, J, Karn, B, Kreyling, W, Lai, D, Olin, S, Monteiro-Riviere, N, Warheit, D and Yang, H (2005) Principles for Characterizing the Potential Human Health Effects from

Exposure to Nanomaterials: Elements of a Screening Strategy. *Particle and Fibre Toxicology*, 2(1), 8.

Oecd Oecd Guidelines for the Testing of Chemicals (2013) [Online]. Available: http://www.oecd.org/chemicalsafety/testing/oecdguidelinesforthetestingofchemicals.htm [Accessed 01/03/2017]

Owen, C A, Selvakumaran, J, Notingher, I, Jell, G, Hench, L L and Stevens, M M (2006) *In vitro* Toxicology Evaluation of Pharmaceuticals Using Raman Micro-Spectroscopy. *J Cell Biochem,* 99(1), 178-86.

Pobezhimova, T P and Voinikov, V K (2000) Biochemical and Physiological Aspects of Ubiquinone Function. *Membr Cell Biol,* 13(5), 595-602.

Ragnvaldsson, D, Berglind, R, Tysklind, M and Leffler, P (2007) Environmental Hazard Screening of a Metal-Polluted Site Using Pressurized Liquid Extraction and Two *in vitro* Bioassays. *Ambio,* 36(6), 494-501.

Rampersad, S N (2012) Multiple Applications of Alamar Blue as an Indicator of Metabolic Function and Cellular Health in Cell Viability Bioassays. *Sensors,* 12(9).

Ruenraroengsak, P, Novak, P, Berhanu, D, Thorley, A J, Valsami-Jones, E and Gorelik, J (2012) Respiratory Epithelial Cytotoxicity and Membrane Damage (Holes) Caused by Amine-Modified Nanoparticles. *Nanotoxicology,* 6.

Ruenraroengsak, P and Tetley, T D (2015) Differential Bioreactivity of Neutral, Cationic and Anionic Polystyrene Nanoparticles with Cells from the Human Alveolar Compartment: Robust Response of Alveolar Type 1 Epithelial Cells. *Part Fibre Toxicol,* 12, 19.

Rygula, A, Majzner, K, Marzec, K M, Kaczor, A, Pilarczyk, M and Baranska, M (2013) Raman Spectroscopy of Proteins: A Review. *Journal of Raman Spectroscopy,* 44(8), 1061-76.

Saikia, M, Krokowski, D, Guan, B J, Ivanov, P, Parisien, M, Hu, G F, Anderson, P, Pan, T and Hatzoglou, M (2012) Genome-Wide Identification and Quantitative Analysis of Cleaved Trna Fragments Induced by Cellular Stress. *J Biol Chem,* 287(51), 42708-25.

Salvati, A, Aberg, C, dos Santos, T, Varela, J, Pinto, P, Lynch, I and Dawson, K A (2011) Experimental and Theoretical Comparison of Intracellular Import of Polymeric Nanoparticles and Small Molecules: Toward Models of Uptake Kinetics. *Nanomedicine,* 7(6), 818-26.

Shapero, K, Fenaroli, F, Lynch, I, Cottell, D C, Salvati, A and Dawson, K A (2011) Time and Space Resolved Uptake Study of Silica Nanoparticles by Human Cells. *Mol Biosyst,* 7(2), 371-8.

Small, E W and Peticolas, W L (1971) Conformational Dependence of the Raman Scattering Intensities from Polynucleotides. *Biopolymers,* 10(1), 69-88.

Sonawane, N D, Thiagarajah, J R and Verkman, A S (2002) Chloride Concentration in Endosomes Measured Using a Ratioable Fluorescent Cl- Indicator: Evidence for Chloride Accumulation During Acidification. *J Biol Chem,* 277(7), 5506-13.

Stuart, B H (1997) *Biological Applications of Infrared Spectroscopy* Chichester, UK.

Thomas, G J, Medeiros, G C and Hartman, K A (1971) The Dependence of Raman Scattering on the Conformation of Ribosomal Rna. *Biochemical and Biophysical Research Communications,* 44(3), 587-92.

Tosi, G, Bortot, B, Ruozi, B, Dolcetta, D, Vandelli, M A, Forni, F and Severini, G M (2013) Potential Use of Polymeric Nanoparticles for Drug Delivery across the Blood-Brain Barrier. *Curr Med Chem,* 20(17), 2212-25.

Treuel, L, Jiang, X and Nienhaus, G U (2013) New Views on Cellular Uptake and Trafficking of Manufactured Nanoparticles. *J R Soc Interface,* 10(82), 20120939.

Vega-Avila, E and Pugsley, M K (2011) An Overview of Colorimetric Assay Methods Used to Assess Survival or Proliferation of Mammalian Cells. *Proc West Pharmacol Soc,* 54, 10-4.

Walton, A G, Deveney, M J and Koenig, J L (1970) Raman Spectroscopy of Calcified Tissue. *Calcified Tissue Research,* 6(1), 162-7.

Wang, F, Yu, L, Monopoli, M P, Sandin, P, Mahon, E, Salvati, A and Dawson, K A (2013) The Biomolecular Corona Is Retained During Nanoparticle Uptake and Protects the Cells from the Damage Induced by Cationic Nanoparticles until Degraded in the Lysosomes. *Nanomedicine,* 9(8), 1159-68.

Webster, T J (2006) Nanomedicine: What's in a Definition? *Int J Nanomedicine,* 1(2), 115-6.

White, M J, DiCaprio, M J and Greenberg, D A (1996) Assessment of Neuronal Viability with Alamar Blue in Cortical and Granule Cell Cultures. *J Neurosci Methods,* 70(2), 195-200.

Xia, T, Kovochich, M, Brant, J, Hotze, M, Sempf, J and Oberley, T (2006) Comparison of the Abilities of Ambient and Manufactured Nanoparticles to Induce Cellular Toxicity According to an Oxidative Stress Paradigm. *Nano Lett,* 6.

Xia, T, Kovochich, M, Liong, M, Zink, J I and Nel, A E (2008) Cationic Polystyrene Nanosphere Toxicity Depends on Cell-Specific Endocytic and Mitochondrial Injury Pathways. *ACS Nano*, 2(1), 85-96.

Yamasaki, S, Ivanov, P, Hu, G F and Anderson, P (2009) Angiogenin Cleaves Trna and Promotes Stress-Induced Translational Repression. *J Cell Biol*, 185(1), 35-42.

Zoladek, A, Pascut, F C, Patel, P and Notingher, I (2011) Non-Invasive Time-Course Imaging of Apoptotic Cells by Confocal Raman Micro-Spectroscopy. *Journal of Raman Spectroscopy*, 42(3), 251-8.

4S Supplementary Material:

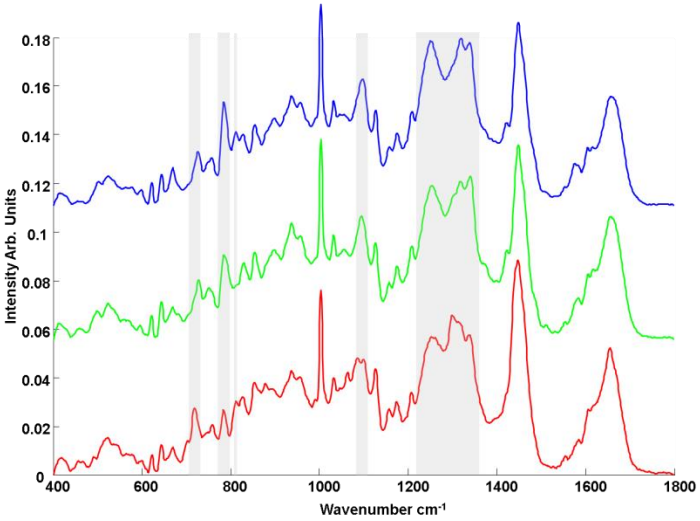

Figure 4.S1. Mean spectra of different cellular regions of unexposed cells. Nucleolus, nucleus and cytoplasm are indicated by blue, green and red, respectively. The differences in molecular composition (nucleic acids, proteins and lipids) of the regions are highlighted.

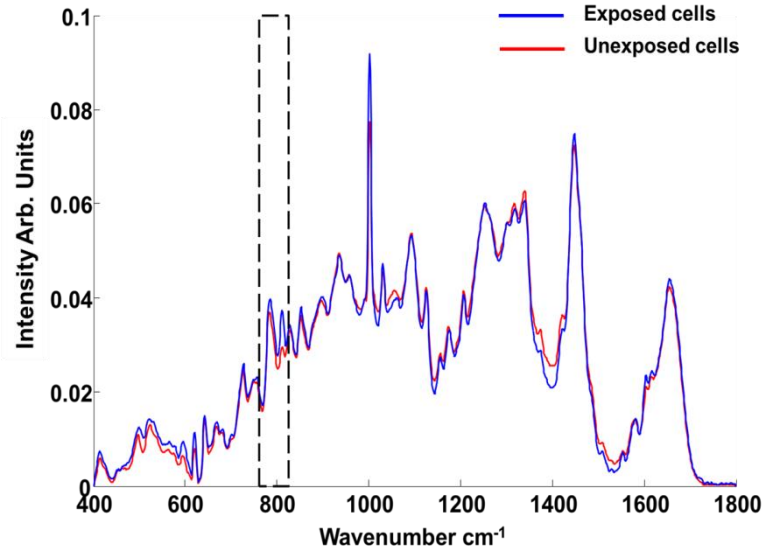

Figure 4.S2. Mean spectra of cytoplasm of exposed cells (blue) and unexposed cells (red). The 785 and 810 cm^{-1} region is indicated with dashed outline.

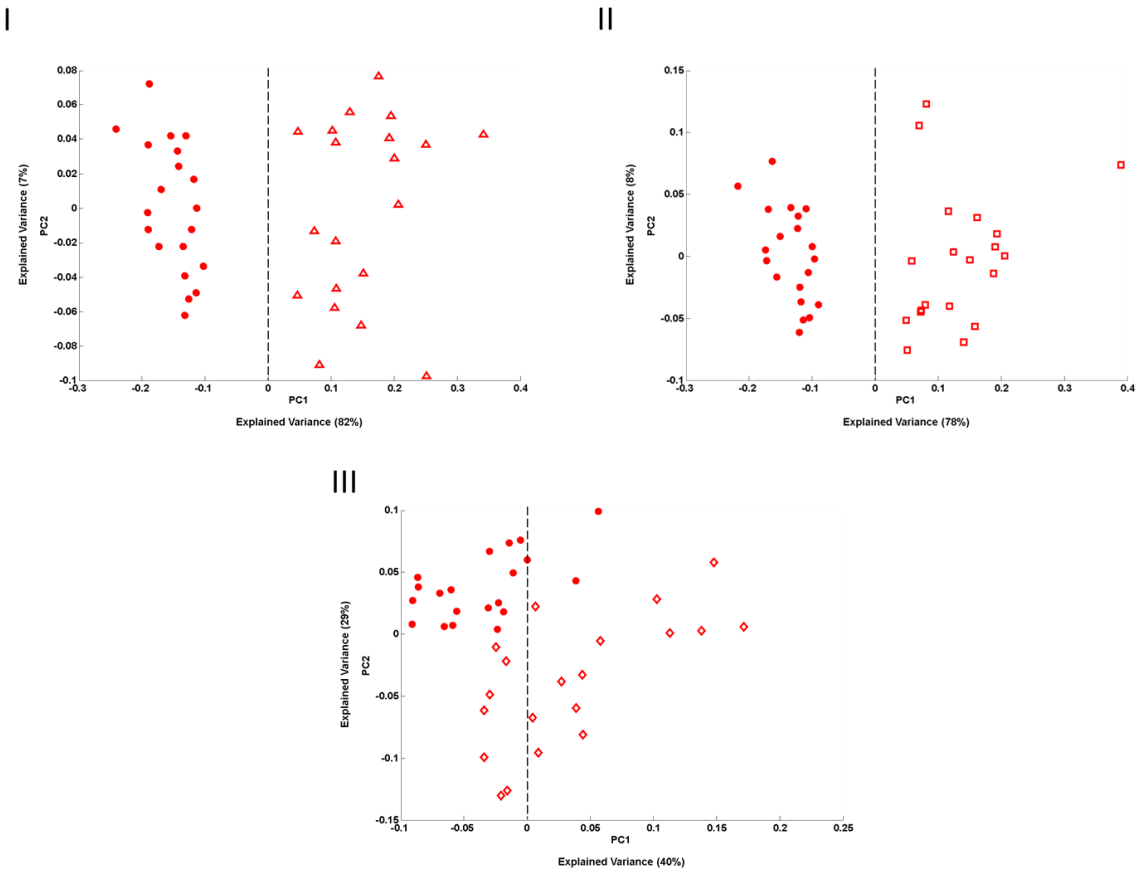

Figure 4.S3. Scatter plot of the PCA of spectra corresponding to cytoplasm of the unexposed cells (control) and cells exposed to PS-NH_2 for 8hr. The code for different concentrations from 2.5 to 10 μM (I-III) is, rectangle (I), square (II) and diamond (III), respectively. Unexposed cells and exposed cells are indicated by close circles and open circles, respectively.

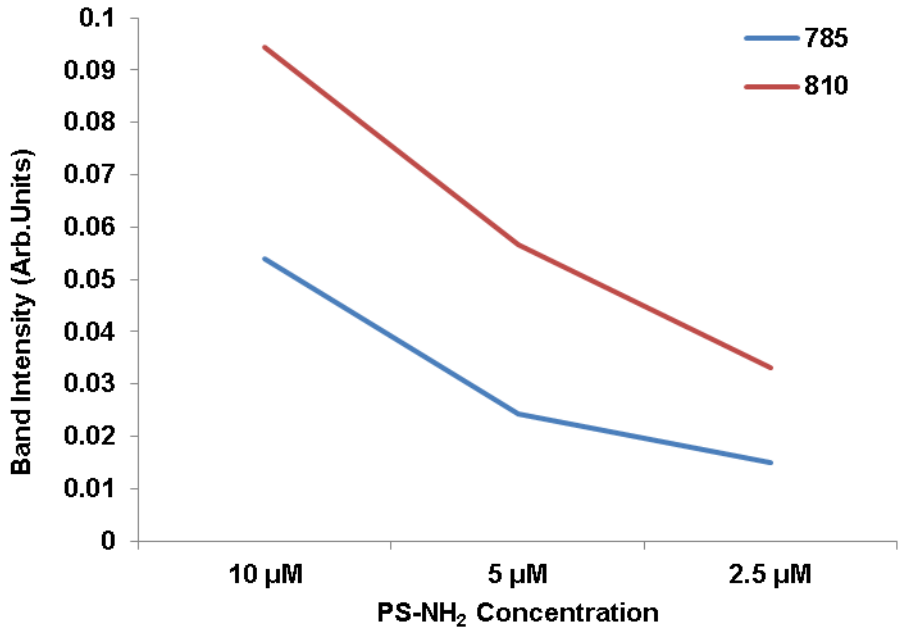

Figure 4.S4. Raman intensities of the 785 cm^{-1} (blue) and 810 cm^{-1} (red) bands as a function of dose.

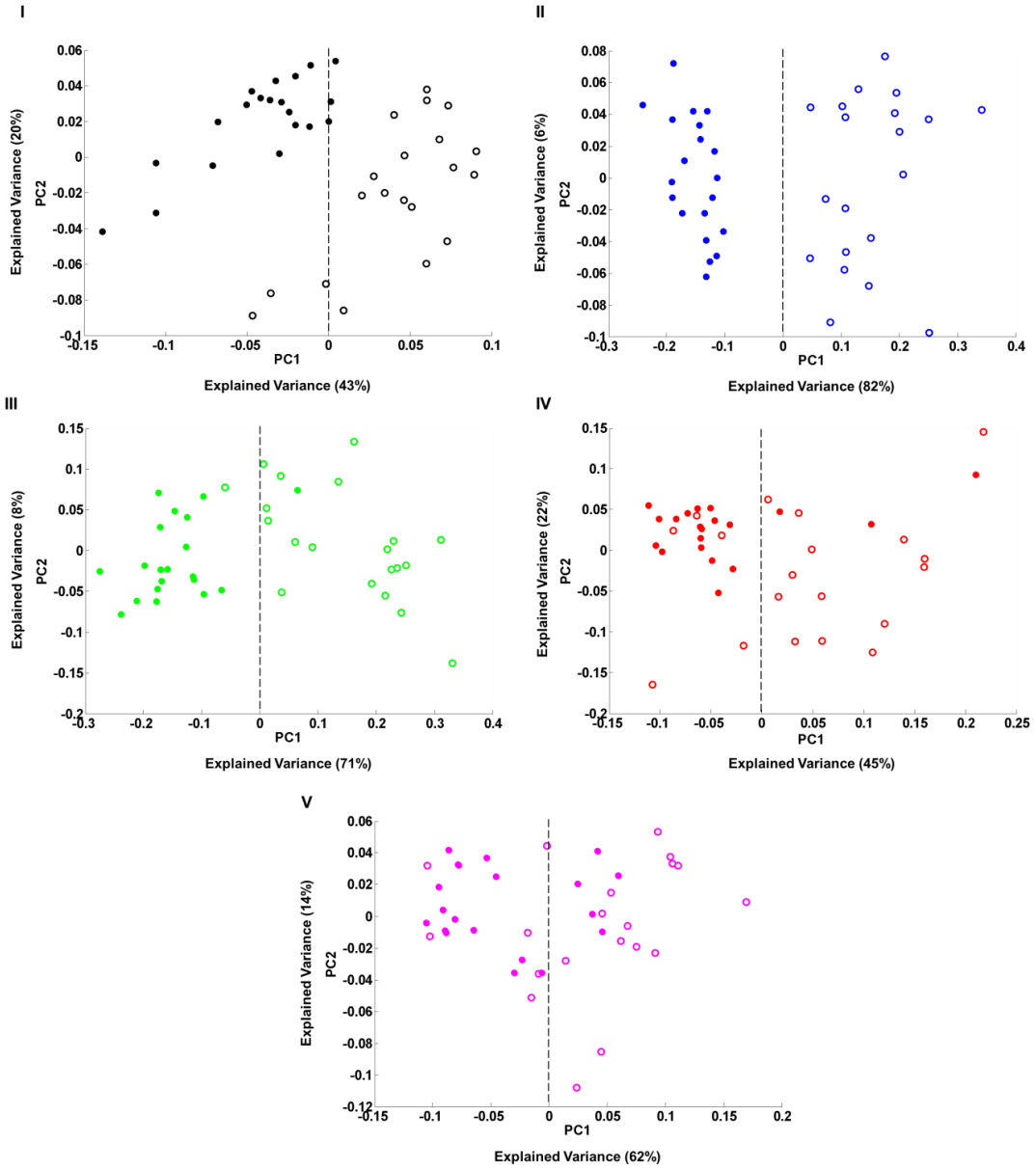

Figure 4.S5. Scatter plot of the PCA of spectra corresponding to cytoplasm of the unexposed cells (control) and PS-NH_2 exposed cells. The colour code for different exposure times from 4 to 48 (I-V) is, black (I), blue (II), green (III), red (IV) and magenta (V), respectively. Unexposed cells and exposed cells are indicated by close circles and open circles, respectively.

CHAPTER 5

Label-Free, High Content Screening using Raman Microspectroscopy: The Toxicological Response of Different Cell Lines to Amine-modified Polystyrene Nanoparticles (PS-NH_2)

The following chapter has been adapted from the published journal article entitled 'Label-Free, High Content Screening using Raman Microspectroscopy: The Toxicological Response of Different Cell Lines to Amine-modified Polystyrene Nanoparticles (PS-NH_2)', Analyst, 2017, DOI: 10.1039/C7AN00461C.

Author list: Esen Efeoglu, Marcus A. Maher, Alan Casey, Hugh J. Byrne

EE performed all measurements, data analysis and is the main drafting author, MAM contributed to ROS measurements. AC and HJB contributed to manuscript design and final drafting.

5.1. Abstract

Nanotoxicology has become an established area of science due to growing concerns over the production and potential uses of the nanomaterials in wide-range of areas from pharmaceutics to nanomedicine. Although different cytotoxicity assays have been developed and become widely used to determine the toxicity of nanomaterials, the production of multi-parametric information in a rapid and non-invasive way is still challenging, when the amount and diversity of physicochemical properties of nanomaterials are considered. High content screening can provide such analysis, but is often prohibitive in terms of capital and recurrent costs in academic environments. As a label-free technique, the applicability of Raman microspectroscopy for the analysis of cells, tissues and bodily fluids has been extensively demonstrated. The multi-parametric information in the fingerprint region has also been used for the determination of nanoparticle localisation and toxicity. In this study, the applicability of Raman microspectroscopy as a 'high content Nanotoxicological screening technique' is demonstrated, with the aid of multivariate analysis, on non-cancerous (immortalized human bronchial epithelium) and cancerous cell-lines (human lung carcinoma and human lung epidermoid cells). Aminated polystyrene nanoparticles are chosen as model nanoparticles due to their well-established toxic properties and cells were exposed to the nanoparticles for periods from 24-72 hour. Spectral markers of cellular responses such as oxidative stress, cytoplasmic RNA aberrations and liposomal rupture are identified and cell-line dependent systematic variations in these spectral markers, as a function of the exposure time, are observed using Raman microspectroscopy, and are correlated with cellular assays and imaging techniques.

5.2. Introduction

The ease of interaction of nanomaterials with biological molecules and living systems can be utilized to design novel nanoparticles for gene and drug delivery, personalised medicine, diagnosis as well as imaging technologies (Brigger, Dubernet, & Couvreur 2012; Godbey, Wu, & Mikos 1999; Nune *et al.* 2009; Tosi *et al.* 2013). Conversely, the physicochemical properties which give rise to this interaction and the high reactivity with biological systems can make them potentially toxic to humans (Andre E. Nel *et al.* 2009; Oberdörster *et al.* 2005). When the amount and physicochemical diversity of naturally occurring and manufactured nanomaterials are considered, determination of the toxic properties, possible adverse health effects and mechanism of action in a rapid, *in vitro* and multi-parametric fashion with a single assay carries significant importance to take full advantage from nanomaterials in wide range of application areas. Various biological assays and imaging technologies have been introduced for the determination of cell-nanoparticle interactions, monitoring of nanoparticle uptake and localisation. The commercially available and well established cytotoxicity assays, Alamar Blue (AB), 3-(4,5-Dimethylthiazol-2-yl)-2,5diphenyltetrazoliumbromid (MTT) and Neutral red (NR), are nanotoxicological assessments recommended by the Organisation for Economic Co-operation and Development (OECD) for the determination of the nanoparticle toxicity (OECD, OECD Guidelines for the Testing of Chemicals, 2013). However, the established techniques have remained limited due to the time needed for each experiment, requirement of multiple-labels and/or their invasive nature.

Over the last decade, High Content Analysis/Screening (HCA/HCS), which can be described as automated imaging and analysis of 'phenotypic assay endpoints' for the evaluation of multiple information regarding to cell morphology, biochemical parameters in cells, tissue-level toxicity, as well as animal disease models, has brought a new perspective to, for example, drug discovery and academic research (Brayden *et al.* 2015; Liebel & Link 2007; Zock 2009). HCA has been used to replace cellular assays for cell signalling (Ding *et al.* 1998; Sarker *et al.* 2008; Zock 2009), neurobiology (Radio *et al.* 2008; Ruan *et al.* 2008),*in vitro* toxicology (Anguissola *et al.* 2014; Brayden *et al.* 2015; Morelli *et al.* 2006), cell physiology (Dykens *et al.* 2008; Gasparri *et al.* 2004) and many other applications due to its speed, sensitivity and multifaceted data which provide advantages over conventional cellular assays. However, this technology still remains challenging because of the cost, problems in data management, development of application based models and lack of common standards (Liebel & Link 2007).

The applicability of Raman microspectroscopy to the investigation of biological systems has been demonstrated previously for tissues, cells, body fluids and also drug and nanoparticle screening (Bonnier *et al.* 2011; Bonnier *et al.* 2014; Breve 1996; Dorney *et al.* 2012; Efeoglu, Casey, & Byrne 2016; Efeoglu *et al.* 2015; Farhane *et al.* 2016; Walton, Deveney, & Koenig 1970). The power of the Raman microspectroscopy to differentiate cellular regions such as nucleus, nucleolus and cytoplasm along with the localisation of nanoparticles has been shown by Dorney *et al.* (Dorney *et al.* 2012). The localisation of the carboxyl modified-polystyrene nanoparticles (PS-COOH) at certain time points has been also demonstrated using Raman microspectroscopy and spectral biomarkers corresponding to cellular compartments such as endosomes,

lysosomes and endoplasmic reticulum have been identified (Efeoglu *et al.* 2015).The correlation of Raman signatures with cytotoxicity assays for carbon nanotubes was demonstrated by Knief *et al.* (Knief *et al.* 2009). The importance of the combination of multivariate analysis techniques to extract information from Raman data sets regarding nanoparticle localisation in cellular regions has been demonstrated by Keating *et al.* (Mark E. Keating, Bonnier, & Byrne 2012). The ability of Raman microspectroscopy to determine spectral markers of the dose and time dependent cellular responses and the corresponding changes in biochemical constituents of the cells upon exposure to aminated polystyrene ($PS\text{-}NH_2$) nanoparticles has been also studied(Efeoglu, Casey, & Byrne 2016).

Hereby, this study focuses on validation of the technique of Raman microspectroscopy as a label free, 'high content nanotoxicological screening' method in cancerous and non-cancerous cell lines based on spectral markers of cellular responses triggered by nanoparticle uptake. For this purpose, a non-cancerous, immortalized human bronchial epithelium cell line (BEAS-2B), and cancerous cell lines, human lung carcinoma (A549) and human lung epidermoid (Calu-1), are used, as they acts as models for human exposure by inhalation. Aminated polystyrene nanoparticles ($PS\text{-}NH_2$) were chosen as model nanoparticles due to their extensively-studied toxic properties (Anguissola *et al.* 2014; Lunov, Syrovets, Loos, Beil, *et al.* 2011; Lunov, Syrovets, Loos, Nienhaus, *et al.* 2011; Ruenraroengsak & Tetley 2015; Wang *et al.* 2013; Xia *et al.* 2008). The toxic forms of the polystyrene nanoparticles (PS), *e.g*. $PS\text{-}NH_2$, have previously been demonstrated to result in ROS formation and oxidative stress upon exposure which triggers apoptosis by the release of inflammatory factors (Anguissola *et al.* 2014; Bexiga *et al.* 2011; Ruenraroengsak & Tetley 2015; Xia *et al.* 2008). In

this study, the effect of the PS-NH_2 on the cancerous and non-cancerous cell lines were evaluated by using the commercially available and well-established toxicity assays AB and MTT from 24 to 72 h for each cell line. Raman microspectroscopic studies were carried out at sublethal doses in order to observe the progressive evolution of the spectroscopic signatures of the toxicity in the fingerprint region for BEAS-2B, A549 and Calu-1 cells. Cells were exposed to PS-NH_2 from 24 to 72 h and corresponding controls for each cell line were prepared for the comparison with the exposed cells. Raman spectra were acquired from the cytoplasm of the exposed and control cells and unsupervised Principal Component analysis (PCA) was used to evaluate changes upon PS-NH_2 exposure. Predicted toxic events based on Raman microspectroscopy such as oxidative stress, lysosomal damage were determined by using 6-carboxy-2',7'-dichlorodihydrofluorescein diacetate (carboxy-H_2DCFDA) dye and lysosensor, respectively and results were-correlated with the Raman spectral markers.

5.3. Materials and Methods

5.3.1. Nanoparticles and preparation of PS-NH_2 solutions

Commercially available, 100 nm amine-modified and fluorescently labelled polystyrene nanoparticles (PS-NH_2) were purchased from Sigma-Aldrich (L9904) and used throughout the study. The calculation of the stock concentration was made by using manufacturer's instructions. Excitation and emission spectra are supplied by Sigma-Aldrich and have maxima at 481/644 nm, respectively.

PS-NH_2 working solutions were prepared by dispersing nanoparticles directly into the pre-heated (37 °C), 10% foetal bovine serum (FBS)and 2 mM L-glutamine

supplemented in Dulbecco's Modified Eagle's Medium Nutrient Mixture F-12 HAM (DMEM-F12) or Roswell Park Memorial Institute (RPMI-1640)Medium, depending on the cell line. Initial stock concentration was calculated as 2.05 mM and working concentrations were freshly prepared prior to exposure. More information about working solutions and concentrations is supplied in the relevant sections of the following.

5.3.2. Reagents

For cytotoxicity evaluation of 100 nm PS-NH_2, 3-(4,5-dimethylthiazol-2-yl)-2,5-diphenyltetrazolium bromide (MTT) and Alamar blue (AB) assays were purchased from Sigma Aldrich Ltd. (Dublin, Ireland) and Biosource (UK), respectively. For determination of reactive oxygen species (ROS), 6-carboxy-2',7'-dichlorodihydrofluorescein diacetate (carboxy-H_2DCFDA) was purchased from Invitrogen (Ireland). In order to observe lysosomal activity and aberrations in intracellular pH, Lysosensor^{TM} green DND-189 (L7535) was purchased from Life Technologies, Ireland.

5.3.3. Cell Culture

Toxicological effects of 100 nm PS-NH_2 on cancerous and non-cancerous cell lines were evaluated. BEAS-2B (ATCC® CRL-9609™), a normal immortalized human bronchial epithelium cell line, was used as a model non-cancerous cell line, whereas A549 (ATCC number CCL-185^{TM}), human lung carcinoma, and Calu-1 (ECACC 93120818), human lung epidermoid cells, were chosen as model cancerous cell lines. BEAS-2B and A549 cell lines were purchased from American Type Culture Collection

(ATTC) and Calu-1 cells were obtained from the European Collection of Authenticated Cell Cultures (ECACC).

A549 and BEAS-2B cells were cultured in (DMEM-F12) with 2 mM L-glutamine and 10% foetal bovine serum (FBS) at 37 °C in 5% CO_2. For Calu-1 cells, the growth conditions were the same as for A549 and BEAS-2B, with the exception that the culture medium used was RPMI-1640, with 10% FBS and 2 mM L-glutamine supplement. A549 and Calu-1 cells were sub-cultured every 3 days, the BEAS-2B cell line every 4 days, until cells reached approximately 60-70% confluency.

5.3.4. AB (Alamar Blue) and MTT (3-(4, 5-dimethylthiazol-2-yl)-2, 5-diphenyltetrazolium bromide) assays and calculation of half-maximal effective concentration EC_{50} values

Both assays for evaluation of cytotoxicity of the 100 nm PS-NH_2 to the chosen cell lines were conducted in the same plate. For cytotoxicity evaluation, each cell line was seeded onto 96-well plates at densities of $1x10^5$, $5x10^4$ and $3x10^4$ cell/mL for 24, 48 and 72 hour, respectively. Cells were incubated at 37 °C in a 5% CO_2 humidified incubator for 24 h to achieve the initial attachment and desired confluency. For each cell line, six replicates of the positive (10% Dimethyl sulfoxide (DMSO)) and negative (cell lines) control and particle exposures were used and 3 independent experiments were carried out from the same batch of the cells after different passages to evaluate toxicity.

PS-NH_2 solutions within the concentration range of 20 μM to 0.15 μM were freshly prepared in pre-heated cell medium with 10%FBS and 2 μM L-glutamine. For A549

and BEAS-2B cell lines, particles were prepared in DMEM-F12, whereas RPMI medium with 10% FBS and 2 μM L-glutamine was used for particle exposures to the Calu-1 cells.

Following 24 h initial attachment, cells were rinsed with 100 μL/well of pre-warmed PBS and exposed to the test materials for 24, 48 and 72h. After the desired exposure time, cells were washed with PBS twice and exposed to the AB/MTT solution prepared in un-supplemented medium (A549 and BEAS-2B; DMEM-F12, Calu-1; RPMI) in the ratio of 5% [v/v] of AB and 10% [v/v] of MTT. Cells were incubated with AB/MTT solution at 37 °C in 5% CO_2 for 3 h. A micro plate reader (SpectraMax-M3, Molecular Devices, USA) was used to measure AB fluorescence emission at 595 nm. Following AB measurements, the AB/MTT solution was removed and cells were washed with 100 μL/well of PBS, twice. 100 μL/well of DMSO were added to 96-well plates and plates were agitated at 200 rpm for 10 min. MTT absorbance was measured in the micro plate reader at 570 nm. Data were transferred to SigmaPlot to fitEC_{50}curve by using a four parameter sigmoidal fit.

5.3.5. Confocal laser scanning fluorescence microscopy

Confocal laser scanning microscopy (CLSM) was used to determine nanoparticle uptake and to observe cellular changes upon nanoparticle exposure as well as morphological changes in control cells over the exposure time. For each cell line, $1x10^5$ cells/ per substrate were seeded onto glass bottom Petri dishes in respective medium and incubated for 24 h at 37 ºC in 5% CO_2. Following 24 h initial growth, cell medium was changed for control cells and test samples were exposed to 2.5, 1 and 0.6

μM of PS-NH_2 (calculated EC_{25} values) for A549, Calu-I and BEAS-2B, respectively and cells were incubated for 24, 48 and 72 h. After the desired exposure time, cells were rinsed with PBS three times and kept in PBS for Confocal studies. CLSM images were taken by using Zeiss Confocal Fluorescence Microscope (LSM 510 META, Carl Zeiss, Germany) with a x63 oil immersion objective

5.3.6. Raman Microspectroscopy

In this study, Raman microspectroscopy is used to monitor cellular responses upon 100nm PS-NH_2 exposure in cancerous (A549, Calu-1) and non-cancerous (BEAS-2B) cell lines to compare spectral fingerprints of molecular initiating events as well as cell death signatures. Cells were seeded onto CaF_2 discs at a density of approximately 16,000 cells/per substrate and incubated for 24 h at 37 °C in 5% CO_2 in the respective medium for the cell line. Following initial attachment and growth, the cell medium was removed and cells were rinsed with pre-warmed PBS. Cells were exposed to 2.5, 1 and 0.6 μM of 100 nm PS-NH_2 in cell medium supplemented with 10% FBS and 2 μM L-glutamine for A549, Calu-1 and BEAS-2B, respectively. Cells were incubated at 37 °C in 5% CO_2 for periods of 24, 48 and 72 h. For control cells, the cell medium was replaced by fresh pre-warmed medium for a period equivalent to the PS-NH_2 exposure times. Following exposure times, cell medium was removed and the cells were washed with 2 mL of PBS three times. 10% Formalin was used as a fixative reagent and incubated with cells in room temperature for 10 min. After fixation, cells were washed with PBS twice and kept in sterile dH_2O for Raman studies.

Throughout the study, a Horiba Jobin-Yvon LabRAM HR800 spectrometer, equipped with a 785 nm diode laser as source, was used with a x100 immersion objective (LUMPlanF1, Olympus, N.A. 1). The 520.7 cm^{-1} line of silicon was used to calibrate the spectrometer prior to spectral acquisition. A 300lines per mm grating and a 100 μm confocal pinhole was chosen for all measurements and spectra were collected by a 16 bit dynamic range Peltier cooled CCD detector. 20 point spectra from the cytoplasm of A549, Calu-1 and BEAS-2B cells and the corresponding controls for the each exposure time were acquired for 2 × 30 seconds at each spot in the fingerprint region (From 400 cm^{-1} to 1800 cm^{-1}). Control cells incubated in the respective medium for up to 72 h were used to determine spectral changes as a result of particle exposure in PS-NH_2 exposed cells.

5.3.7. Data analysis

In order to observe the signatures of biochemical changes in cells upon PS-NH_2 exposure, the Raman data sets obtained from exposed cells and their controls for different exposure times were transferred to Matlab (Mathworks, USA) for data analysis. All data sets were subjected to pre-processing prior to multivariate analysis. Briefly, a mild smoothing (Savitsky-Golay filter, 3^{rd} order, 9 points) was applied and background was removed by using Classical Least Squares Analysis (CLSA) to remove contributions from the water in the immersion geometry (Bonnier *et al.* 2014; Miljkovic *et al.* 2010). Smoothed and background removed spectra were vector normalised prior to principal components analysis (PCA).

5.3.8. Intracellular Reactive Oxygen Species (ROS) study

Generation of oxidative oxygen species in A549, Calu-1 and BEAS-2B cell lines for selected concentrations were evaluated by using carboxy-H_2DCFDA dye. Cells were seeded onto 96-well plates at a density of $1x10^5$cells/well and incubated at 37 °C in 5%$C0_2$ for 24 h for initial attachment and growth. Following initial attachment, cells were rinsed with 100 µL/well of PBS and 100µL/well of carboxy-H_2DCFDA dye, prepared in PBS at a concentration of 10 µM, were added into the 96-well plates and cells were incubated at 37 °C in 5% CO_2 for 30 min. After 30 min, the dye solution was removed from plates and cells were rinsed with 100µL/well PBS twice. Cells were exposed to 0.6, 1 and 2.5 µM of PS-NH_2 prepared in pre-warmed cell medium with 10% FBS and 2µM L-glutamine for BEAS-2B, Calu-1 and A549 cell lines, respectively. A 100 µM hydrogen peroxide (H_2O_2) solution was used as a positive control for all cell lines. Cells were incubated with test materials for 1, 2, 3, 4, 6 and 24 h. For positive and negative controls and PS-NH_2 exposure, 6 replicates are used in the same 96-well plate and 3 independent experiments were carried out from the same batch of the cells after different passages to evaluate the generation of reactive oxygen species (ROS). The plates were kept away from light throughout the experiment. The fluorescence emission of oxidized DCFDA dye (Excitation/Emission; 485/535 nm) was measured at 535 nm by using a micro plate reader (SpectraMax-M3, Molecular Devices, USA).

5.3.9. Lysosensor study

Lysosensor Green DND-189 was used to monitor lysosomal activity and aberrations in lysosomal activity for A549, Calu-1 and BEAS-2B upon exposure to 2.5, 1 and 0.6 μM concentrations of PS-NH_2. 10% DMSO was used as positive control for all cell lines. Cells were seeded onto 96-well plates at a density of $1x10^5$ cells/mL in pre-warmed medium supplemented with 10% FBS and 2μM L-glutamine and incubated for 24 h at 37 °C in 5%CO_2. Following 24 h initial attachment, cells are washed with PBS and exposed to test materials prepared in the respective medium for periods of 1, 2, 3, 4, 6 and 24 h. Lysosensor was prepared at a concentration of 2 μM in pre-warmed PBS. After the desired exposure time, the cells were washed twice with pre-warmed PBS and cells were exposed to dye solutions for 30 min. After 30 min, plates were rinsed with PBS twice to remove unloaded dye and cells were kept in 100μL/well PBS for the measurements. Lysosensor fluorescence emission was measured by using a micro plate reader (SpectraMax-M3, Molecular Devices, USA) at 535 nm (Exc/Em 488/535 nm).

5.4. Results and Discussion

5.4.1. The cytotoxic effect of PS-NH_2 in cancerous and non-cancerous cell lines

The effect of 100 nm PS-NH_2 on cancerous (A549, Calu-1) and non-cancerous (BEAS-2B) cell lines was evaluated using commercially available and well-established cytotoxicity assays, AB and MTT (Berridge, Herst, & Tan 2005; Rampersad 2012; Vega-Avila & Pugsley 2011).Figure 5.1 shows the dose dependent

changes in cellular viability, at time points from 24 to 72 h, as determined by the AB (Figure 5.1A, C and E) and MTT (Figure 5.1B, D and F) assays. The cell viability assays are based on measurement of a fluorescent marker corresponding to a specific change on the whole cell population under investigation (Riss *et al.* 2004). The AB assay provides information about the cell viability and proliferation while the MTT assay has been shown to have contribution from the mitochondrial activity of the cell (Berridge, Herst, & Tan 2005; Hamid *et al.* 2004; Marshall, Goodwin, & Holt 1995; Mosmann 1983; O'Brien *et al.* 2000). Although MTT reduction can occur in different cellular regions, upon reduction of MTT dye to its fluorescent form by electron transfer after 25 min of incubation, around 25–45% of MTT reduction was shown to be associated with mitochondria by Bernas *et al.* (Bernas & Dobrucki 2002). In the study of Maher *et al.*, MTT assay was found to be more sensitive than AB to the effect of exposure of cells to PAMAM dendrimers, which mainly localise in the mitochondria and cause changes in mitochondrial integrity(Maher & Byrne 2016). Therefore, the MTT results can be interpreted in terms of functional changes of the mitochondria.

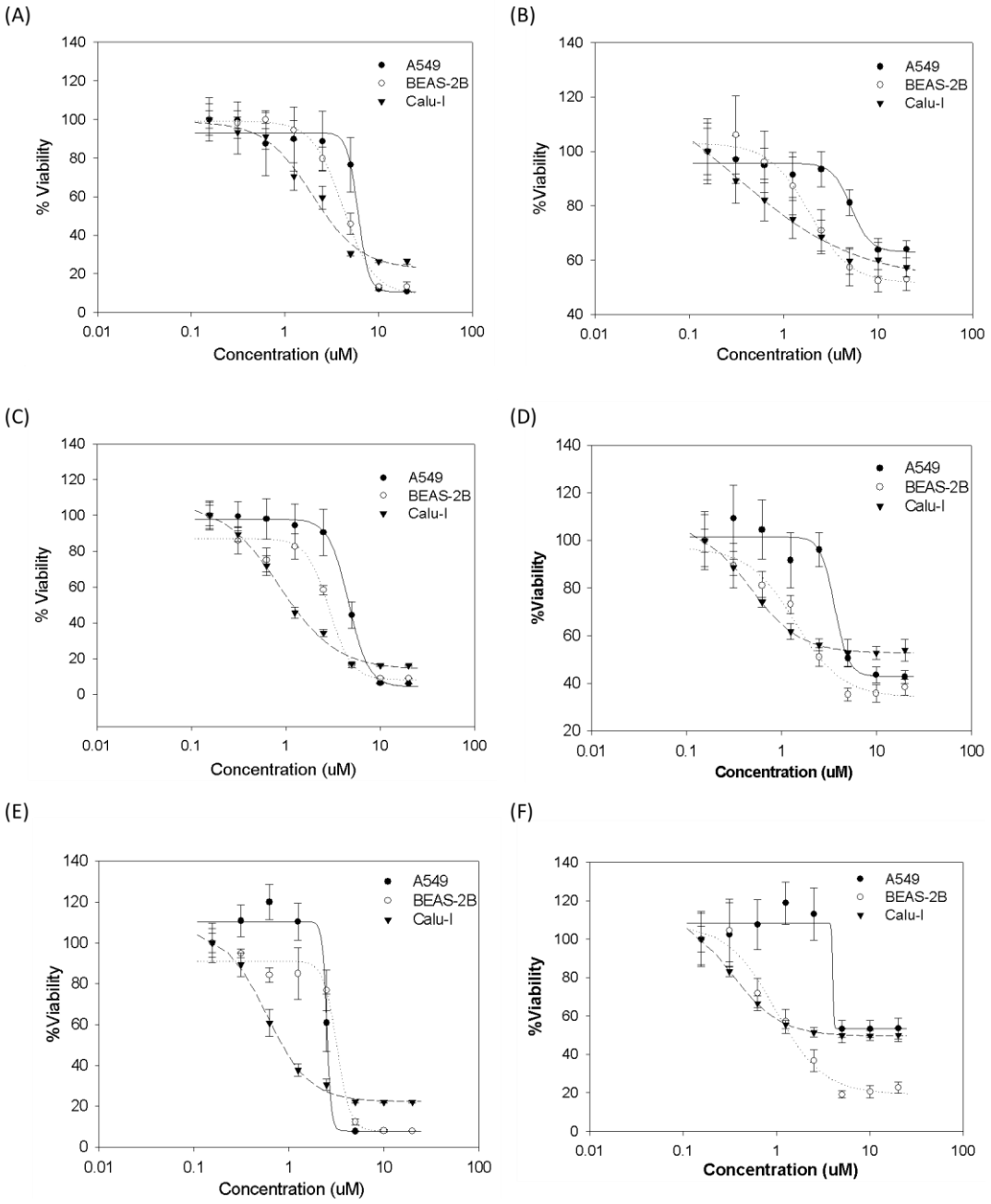

Figure 5.1. Cytotoxicity of 100 nm amine-modified polystyrene nanoparticles ($PS\text{-}NH_2$) after 24 h (A and B), 48 h (C and D) and 72 h (E and F) exposures, as determined by the Alamar Blue (A, C and E) and MTT (B, D and F) assay, for A549, Calu-1 and BEAS-2B cell lines. The concentration range between 20 to 0.15 μM is used throughout the study. Data are expressed as % of control mean ± SD of three independent experiments.

Even though the AB and MTT assays have different mechanisms for measuring toxic effects of the nanoparticles, in terms of applied dose, both assays provided comparable results for all cell lines and the toxicity progressively increased with increasing dose (from 0.15 to 20 μM) as seen in Figure 5.1.When the AB response of A549, Calu-1 and BEAS-2B cells are compared, a general trend of increasing toxicity response in the order Calu-1 > BEAS-2B >A549is observed (Figure 5.1).For all three cell lines and exposure times, viability in exposed cells is observed at around 100% for the lowest concentration of the PS-NH_2, while the percentage approaches zero for higher concentrations (Figure 5.1A, C and D). The half-maximal concentrations for cellular viability (EC_{50}) were calculated by a four parameter sigmoidal fit in SigmaPlot and the results are shown in Table 5.1. However, although the trend, Calu-1 > BEAS-2B > A549, remains the same for three cell lines, the AB assay does not show a significant difference in EC_{50} values between 48 and 72 h exposure for BEAS-2B cells (from 2.87±0.41 to 3.20±0.38μM).When the confidence interval is calculated, EC_{50} is calculated to be in the range between 3.28 - 2.46 μM for 48 h and 3.58 - 2.82 μM for 72h.

Table 5.1. Calculated EC_{50} values with standard deviation for A549, Calu-1 and BEAS-2B cell lines from 24 to 72 hPS-NH_2 exposure.

Cell lines	Viability Assays	EC_{50} Values (μM)		
		24h	48h	72h
A549	AB	6.00(±1.15)	4.62(±0.13)	2.50(±0.5)
	MTT	5.20(±0.59)	3.63(±0.55)	3.99(±0.12)
Calu-1	AB	1.96(±0.33)	0.85(±0.11)	0.58(±0.04)
	MTT	0.30(±0.42)	0.47(±0.03)	0.33(±0.01)
BEAS-2B	AB	4.17(±0.24)	2.87(±0.41)	3.20(±0.38)
	MTT	2.00(±0.06)	1.39(±0.27)	0.97(±0.18)

Notably, whereas the viability as measured by the AB assay for extended exposure times tends towards 10-0% for the cell lines, for the MTT assay, the increase in toxicity is observed to be less systematic for A549 and Calu-1 cells and the minimum viability, even at 72h exposure, is observed around ~50-40% (Figure5.1B, D and F).This is indicative of sustained mitochondrial activity or increase in the number of mitochondria in cells upon exposure to PS-NH_2. In contrast, the viability of the BEAS-2B continues to reduce with increasing dose and extended exposure times, tending towards 10-0%, a similar profile to the AB response (Figure 5.1A, C and E). From a pharmacological point of view, agonists can have partial or full efficacy on a receptor. While 'full agonism' can cause a reduction in viability to 0%,'partial agonism' can cause the loss of viability to saturate at finite values, even at prolonged exposure times

(Pliska 1999). By analogy, the MTT response in A549 and Calu-1 can be described as "partial agonism" as the viability only goes to about 50%, whereas in BEAS-2Bs, there is almost a full loss of viability.

In recent years, the mechanisms underlying the toxicity of nanoparticles have been widely studied and various contributions have been identified, such as induction of oxidative stress upon nanoparticle uptake, cascades of inflammatory responses, counteracted by natural cell defence mechanisms (*e.g*. antioxidants) (Anguissola *et al.* 2014; Bexiga *et al.* 2011; Efeoglu, Casey, & Byrne 2016; Efeoglu *et al.* 2015; Mu *et al.* 2012; Ruenraroengsak & Tetley 2015; Shapero *et al.* 2011; Xia *et al.* 2008). In the case of the PS-NH_2, partial agonism determined by MTT assay is evidence of more than one mechanism governing the toxic response. The partial agonistic MTT response for A549 and Calu-1 cells can also be attributed to more effective defence mechanisms, such as more effective antioxidant quenching of ROS in cancer cell lines compared to non-cancerous cell lines (Liou & Storz 2010). Conversely, for the BEAS-2B cells, the similar response and systematic changes ('full agonistic response' for the all exposure times) determined by both assays can be related to the prevalence of one toxic pathway leading to cell death.

5.4.2. Morphological Changes in cancerous and non-cancerous cells upon PS-NH_2 exposure

Morphological changes also provide valuable information about the cell viability and overall cell health. In the case of cellular stress and activation of cell death pathways leading to apoptosis and necrosis, significant changes occur in the overall cell structure

such as a cell shrinkage or swallow, alterations and aberrations in the cell membrane, cell blebbing or budding and formation of stress related granular structures (Elmore 2007; Kerr, Wyllie, & Currie 1972; Ouyang *et al.* 2012). In order to observe morphological effects of the systematic changes on BEAS-2B cells upon PS-NH_2 exposure, CLSM was employed to visualise exposed cells compared to their corresponding controls from 24 to 72 h (Figure 5.2). Extending exposure times from 24 to 72 h, control cells are observed to be affected by nutrient consumption (Filomeni, De Zio, & Cecconi 2015) and several morphological changes are observed in the cell membrane and cytoplasm. Cellular stress related lipid granules were observed after 48 h (indicated with an arrow in Figure 5.2) and the change in the cellular morphology is observed significantly after 72 h. For PS-NH_2 exposed cells, 0.6 μM concentrations of PS-NH_2 were chosen as sub-lethal dose (~EC_{25}values at 24 h exposure determined by MTT) for the CLSM study. After 24 h particle exposure, PS-$NH_2$are observed to be mainly localised in the perinuclear region. After 72 h, excessive amounts of PS-$NH_2$are observed in the cytoplasmic area and morphological changes become highly visible. For all exposure times, the formation of stress related lipid granules was observed to be increased upon particle exposure. Compared to their controls for each exposure time, significantly higher distortion in cell structure is observed.

Consistent with the known trafficking of PS nanoparticles, after 24 h exposure, the particles are observed to be in the perinuclear region which shows the localisation of the nanoparticles in the endoplasmic reticulum. With the extending exposure times, although uptake and trafficking of the PS-NH_2 continue and the amount of the particles increase inside the cell, no localisation of the particles are observed in nuclear region (Efeoglu *et al.* 2015).

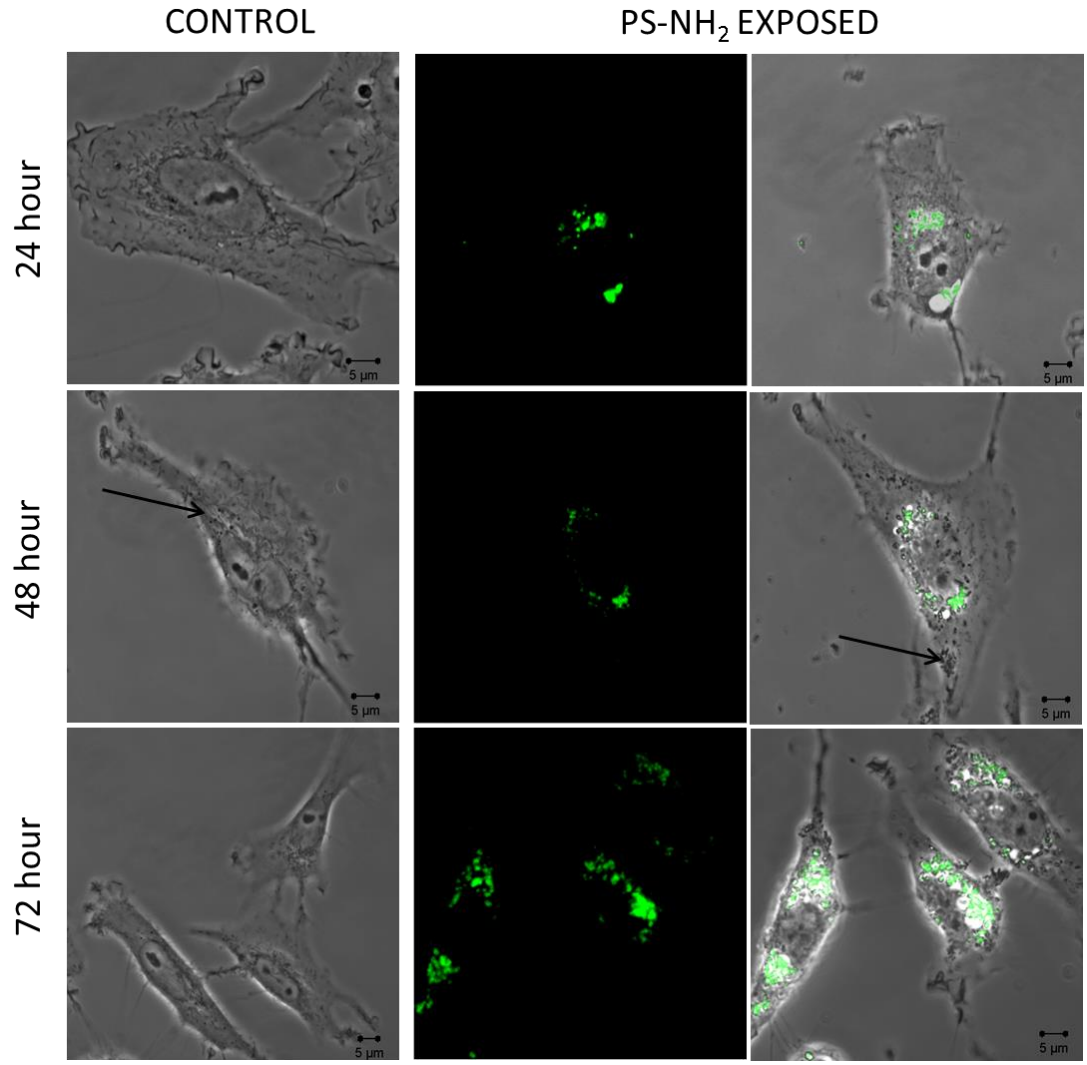

Figure 5.2. CLSM images of BEAS-2B cells and BEAS-2B cells exposed to 100 nm aminated polystyrene nanoparticles (indicated with green fluorescent) from 24 to 72 hours.x60 magnification.

5.4.3. Raman microspectroscopic evolution of the spectral markers of toxicity in cancerous and non-cancerous cell lines

In order to investigate in more detail the systematic changes within PS-NH_2 exposed BEAS-2B cells determined by the MTT assay and CLSM, Raman spectra were acquired from 20 points within the cytoplasm of the exposed cells and their corresponding controls. For the Raman study, the ~EC_{25}at 24 h exposure determined by the MTT assay (0.6 μM concentration of PS-NH_2) was chosen as a sublethal dose at which to observe the time dependent changes in the cell line.

The spectral changes in BEAS-2B, the non-cancerous cell line, upon PS-NH_2 exposure from 24 to 72 h were evaluated by using PCA. The scatter plots of PCA obtained from comparison of the cytoplasm of the exposed and unexposed BEAS-2B cells after 24, 48 and 72 h particle exposure are provided in Supplementary Figure 5.S1. For all exposure times, exposed cells clearly separated from their controls according to PC1, with increasing explained variance with increasing exposure times. In all cases, control cells are observed to form more compact clusters, which indicate higher variance in particle exposed cells, as might be expected. The explained variances are calculated to be 62, 84 and 89% for 24, 48 and 72 h, respectively, which indicates the significant changes in cell composition upon PS-NH_2 exposure. The loadings of PC1for control versus PS-NH_2 exposed BEAS-2B cells, from 24 to 72 h, are provided in Figure 5.3.In each loading, negative features (PC<0) represent the dominant features of the cytoplasm of control cells and positive features (PC>0) represent the features of PS-NH_2 exposed cells. The most significant changes in the loadings are observed in the range between 1000and 1800 $cm^{-1}$and are indicated with black dashes (band

assignments are provided in Table S1). When the loadings of PC1 for different exposure times are compared, significant differences are observed between 24 and 48 h particle exposure, including inversion of bands between control and exposed cells (Figure 5.3). After 24 h exposure, protein (1003 cm^{-1}, Phenylalanine (Phe); 1033 cm^{-1}, Phe; 1248 cm^{-1}, Amide III of proteins, also attributed to nucleic acids, guanine (G) or cytosine (NH_2); 1339 cm^{-1}, Phe, tyrosine (Tyr); 1658 cm^{-1} Amide I (α-helix) (Movasaghi, Rehman, & Rehman 2007) band of proteins) and lipid bands (1440 cm^{-1}, lipids) (Movasaghi, Rehman, & Rehman 2007; Notingher & Hench 2006; Notingher *et al.* 2003) are observed in the positive features of the PC1, which indicates an increased amount of protein and lipids in PS-NH_2 exposed compared to control cells. Although the highest peak observed in the range of 1600 to 1700 cm^{-1} is identified as 1658 cm^{-1}, the region can have many contributions in this region from lipids (C=O and/or C=C band) and also some residual water (bound of semibound -OH) (Abramczyk *et al.* 2014; Vyumvuhore *et al.* 2013). The possible contributions in the range and their assignments are provided in Table 5.S1. The increased signatures of proteins in particle exposed cells compared to their corresponding controls can be attributed to changes in protein template and formation of altered protein structures and also changes in post-translational modifications of the proteins and problems in protein degradation mechanisms due to the changes in cell signalling upon nanoparticle uptake (Frohlich *et al.* 2012; Mohamed *et al.* 2012; Sierra *et al.* 2016). Also, it can be attributed to formation of more Raman active proteins or conformational changes (Saptarshi, Duschl, & Lopata 2013).Uptake and removal mechanism of the nanoparticles also leads to the formation of lipid based structures such as lysosomes to facilitate cellular trafficking of the nanoparticles, which results in an increase in lipid bands. Moreover, formation of stress related lipid granules in

the cytoplasm observed with CLSM can contribute to the increase in the lipid band at 1440 cm^{-1}.

After 48 and 72 h exposure, the most prominent bands are observed in the negative features of loading 1, which represents a higher amount of the corresponding cellular constituents in control cells compared to PS-NH_2 exposed cells. The lipid and protein bands are inverted to negative features of the loading 1 which indicates damage and loss of the protein and lipids in particle exposed cells. The increase of the features in the loading from 48 to 72 h indicates the progress of the cascade of events in the cell, resulting in further degradation in protein and lipid structures due to the toxicity of the particles.

The decrease in lipid composition of the cells after 48 and 72 h exposure can be attributed to the lysosomal aberrations in long exposure times. The uptake mechanism of the PS-NH_2 nanoparticles is known to be endocytosis. Briefly, particles are taken up by endosomes in the first 4 h and carried to lysosomes within 12 h, which are engulfed by golgi apparatus or endoplasmic reticulum after 24 h (Efeoglu *et al.* 2015). However, amine groups located on the surface provide a cationic surface charge to PS-NH_2. Therefore, particles create a proton-sponge effect in the early endosomes and lysosomes which cause protonation in lysosomes (Anguissola *et al.* 2014; Benjaminsen *et al.* 2013; Freeman, Weiland, & Meng 2013; Lullmann, Lullmann-Rauch, & Wassermann 1978; Maher *et al.* 2014; Sonawane, Thiagarajah, & Verkman 2002). Reduction in protein content for these exposure times can be an indicator of follow up damage in the exposed cells due to oxidative stress. After 72 h exposure, the band at 719 cm^{-1} (membrane phospholipidhead, phosphatidylcholine) (Movasaghi,

Rehman, & Rehman 2007; Notingher & Hench 2006; Notingher *et al.* 2003) can be used to track damage to membrane integrity and cellular death phase.

A doublet of peaks at around 785 cm^{-1} (nucleic acids) and 810 cm^{-1} (RNA), associated with changes in the nucleic acid content in the cytoplasm, has previously been identified as a potential marker for oxidative stress in the Raman signatures of nanoparticle exposed cells (Efeoglu, Casey, & Byrne 2016). The increasing amount of the nucleic acid bands in cytoplasm of the particle exposed cells compared to control cells can be attributed to the changes in cytoplasmic RNA and accumulation of non-coding RNAs in the cytoplasm due to oxidative stress. However, they are only weakly observed as positive features of the loading after 24 h particle exposure are not evident at all at the prolonged exposure times, which shows a lack of RNA accumulation in the cytoplasm of exposed BEAS-2B cells for longer time points.

As seen in Figure 5.3, the spectral changes in BEAS-2B cells are found to be systematic after 24 h particle exposure, which correlates with the full agonistic response determined by AB and MTT assays and evolving changes in CLSM. Therefore, the significant changes in the spectroscopic signatures between 24 and 48 h particle exposure (with an increase in explained variance from 62 to 84%) can be related to initiation of toxic events (Molecular initiation event (MIE)) and the lower increase in the explained variance (from 84 to 89%) from 48 to 72 h can be attributed to the cascade of following toxic responses in the cell.

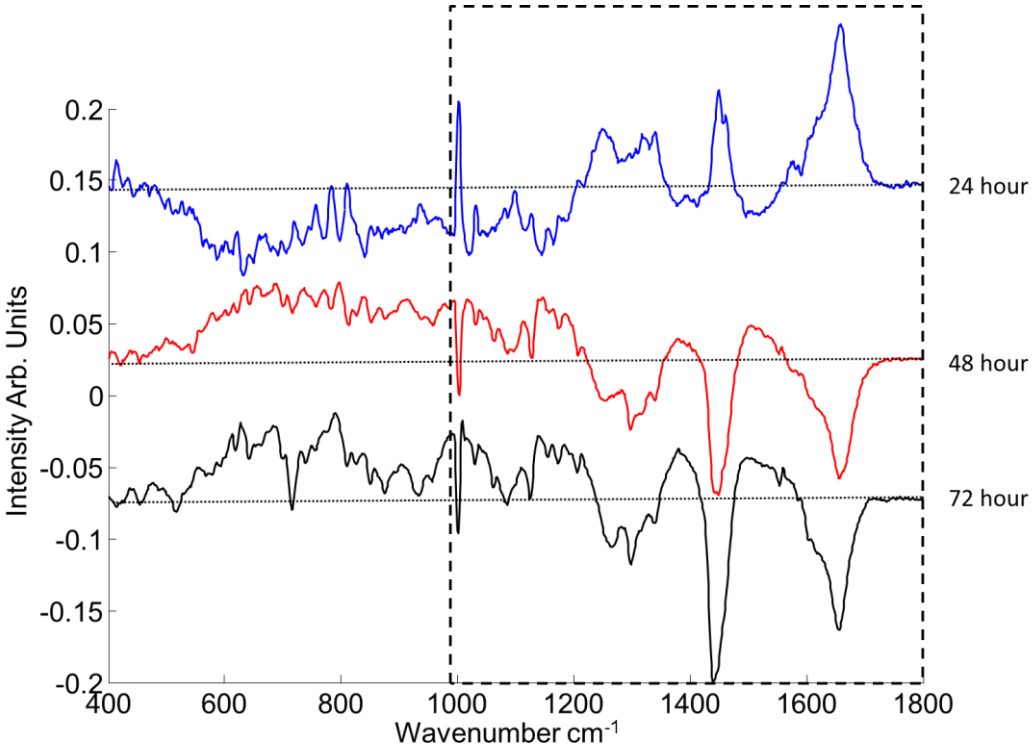

Figure 5.3. Loadings of the first component of PCA (PC1), each exposure time is indicated by a colour from 24 hour to 72 h as following; blue, red and black. The positive side of the loadings represents the spectral features of the particle exposed cells (0.6 μM of PS-NH_2), while the negative side represents the control cells for each loading. Loadings are offset for clarity and the dotted line represents the zero '0' point for each loading. The changing features with extended particle exposure times are indicated with black dashed area.

The differences encountered in AB and MTT assay between BEAS-2B, non-cancerous, and A549 and Calu-1, cancerous, cell lines were also investigated using Raman microspectroscopy. The partial agonistic response obtained by the MTT assay for A549 and Calu-1 cells can be attributed to differences in mitochondrial functionality following the nanoparticle uptake. In order to observe the differences between cell lines in terms of spectroscopy, 20 point spectra from the cytoplasm of

different individual cells were acquired for each exposed cell line and their corresponding controls. For the Raman study, concentrations of 2.5, 1 and 0.6 μM PS-NH_2 were chosen as sub-lethal doses (~EC_{25} values at 24 h exposure) to observe time dependent changes in the cell lines.

The 72 h exposure was chosen to compare cellular responses as more obvious changes ('full agonistic response' for BEAS-2B, 'partial agonistic response' for A549 and Calu-1) are observed for the MTT assay results at this time point (Figure 5.1). PCA was applied pairwise between controls and particle exposed cells after 72 h exposure. The scatter plots of the PCA of cytoplasm of exposed and control cells for A549 and Calu-1 cells after 72 h are shown in Supplementary Figure 5.S2. The exposed cells differentiate according to PC1 from their controls 43% and 46% for A549 and Calu-1 cells, respectively. For BEAS-2Bs, exposed cells largely differentiate from controls (Explained Variance 89%, Figure 5.S1).Figure 5.4 shows the first loadings of PCA for BEAS-2B, A549 and Calu-1 cells, corresponding to cytoplasm. When the first loadings are compared, similar trends in the spectral range from 1000 to 1800 cm^{-1} for A549 and BEAS-2B cells are observed, which can be attributed to similarities in the cascade of events for one type of toxic pathway which also can be attributed to the similarities in full agonistic cellular response determined by the AB assay. The spectral range from 1000 to 1800 cm^{-1} of the so-called fingerprint region includes many characteristic bands related to protein and lipid content of the cells. When the chosen range is considered, for all cell lines, loadings are dominated by negative features. The bands at 1266 cm^{-1} (Amide III-α helix), 1298 cm^{-1} (Lipids) and 1438 cm^{-1} (Lipids and proteins) are observed as positive features of the loading for Calu-1 cells. The band at 1658 cm^{-1}, which can specifically be attributed to the Amide I (α-helix) of proteins

(Movasaghi, Rehman, & Rehman 2007), is observed as negative features of the loadings for BEAS-2B and A549 cells, whereas the peak manifests as a positive feature for Calu-1 cells, indicating a lower amount of damage in Amide I band of the proteins in Calu-1 cells compared to the other cell lines. For A549 cells, the positive features in the range from 1600 to 1700 cm^{-1} can be attributed to partial aberrations in protein and lipid bands (C=C and/or C=O) characteristic of this region. The inverted structure of these bands can be attributed to damage of protein and lipid structures in particle exposed cells after 72 h. Although the cell lines are different to each other, the spectral signatures of cell damage leading to cell death in later stages are found to be similar and cell damage upon toxicity can be determined using Raman microspectroscopy which can be used to utilize a single step analysis of cell-nanoparticle interaction for different cell lines.

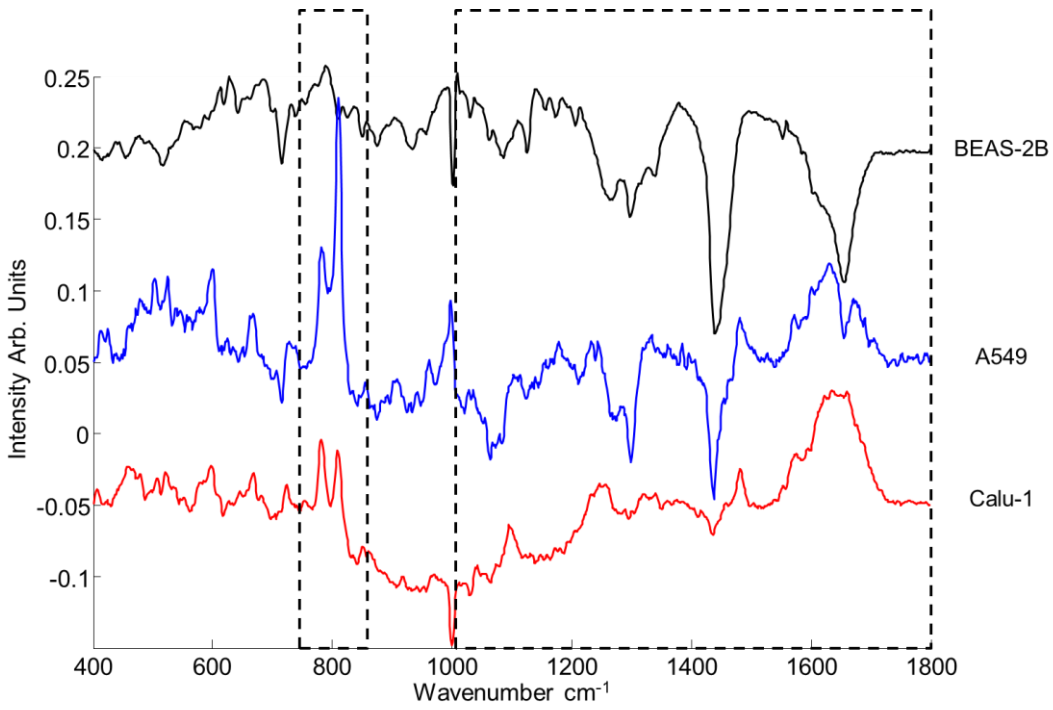

Figure 5.4. First loadings of PCA of cytoplasm of control and 72 hour particle exposed cells for BEAS-2B, A549 and Calu-1 cell lines, respectively; loadings are offset for clarity and the dotted line represents the zero '0' point for each loading. Positive side of the loadings (PC>0) represents the spectral features of the particle exposed cells, while the negative side (PC<0) represents the control cells for each loading. The areas with changing features between cell lines are indicated with dashed lines.

Although a general trend is observed in the AB responses and spectral signatures of cell damage for all three cell lines in the higher wavenumber region of the fingerprint, a significantly different trend is observed for the lower wavenumber region, 785-810 cm^{-1}, which indicates the presence of different molecular initiating events, as well as the presence of a secondary toxic pathway leading to cell death upon toxic nanoparticle exposure.

The prominent peaks at 785 cm^{-1} (nucleic acid) and 810 cm^{-1} (RNA), in the loadings corresponding to the cytoplasm of A549 and Calu-1 cells are indicative of nucleic acid alterations in the cytoplasm due to oxidative stress, as previously discussed for A549 cells (Efeoglu, Casey, & Byrne 2016). However, the peaks are absent in the loading of BEAS-2B cells after 72 h exposure. Although ROS such as hydrogen peroxide (H_2O_2), superoxide anion (O2−•) and hydroxyl radicals (HO•) are known to be Raman inactive and are consumed in cells quickly after they are produced (Casteilla, Rigoulet, & Pénicaud 2001; Mukherjee & Byrne 2013), the 785 and 810 cm^{-1} bands can be used to track oxidative stress inside the cells in a completely label free way (Efeoglu, Casey, & Byrne 2016).

The nucleic acid bands in the cytoplasm have been identified as a signature of formation and accumulation of noncoding RNAs due to oxidative stress upon particle exposure(Efeoglu, Casey, & Byrne 2016). In order to further explore this process in the cytoplasm of the different cell lines, the ROS levels of A549, Calu-1 and BEAS-2B cells were measured by using carboxy-H_2DCFDA dye (Figure 5.5). The concentrations for ROS measurements were kept same with the concentrations used for Raman study for the each line (0.6, 1 and 2.5 μM, for BEAS-2B, Calu-1 and A549, respectively.) in order to see ROS levels corresponding to the doublet of peaks. The results show significantly lower ROS formation in BEAS-2B cells, which is consistent with the absence of the double peak in the lower wavenumber region. For this reason, the formation of ROS can be identified as a molecular initiating event for the A549 and Calu-1 cell line, which leads to cell damage and ultimately cell death.

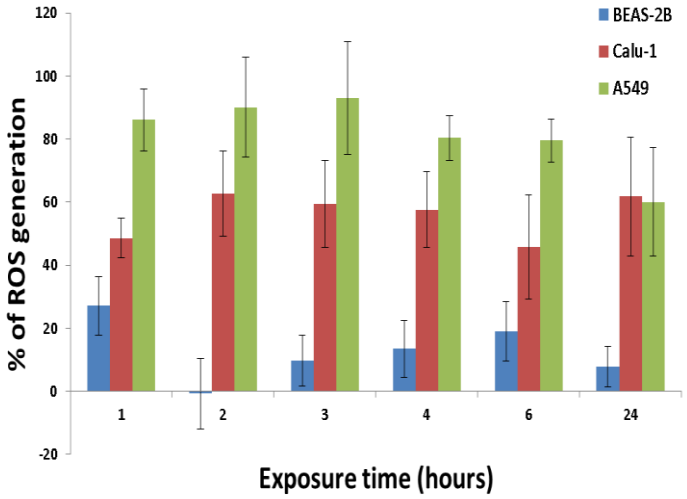

Figure 5.5. % of Reactive oxygen species (ROS) generation compared to controls for A549, Calu-1 and BEAS-2B cell line after 1, 2, 3, 4, 6 and 24 h PS-NH_2 exposure. The concentrations used for BEAS-2B, Calu-1 and A549 are 0.6, 1 and 2.5 μM, respectively.

In order to see earlier effects of the molecular initiating event for the different cell lines, spectral changes were also investigated at shorter exposure times (24 and 48 h) and pairwise PCA of cytoplasm corresponding to the exposed cells and their controls was carried out. The scatter plots of PCA of cytoplasm of exposed and control cells are provided in Supplementary Figure 5.S1 (A and B) for BEAS-2B and Figure 5.S3 for A549 and Calu-1 cells after24 and 48 h. The explained variance between control and exposed cells according to PC1 increases to 64 and 59% for A549 and Calu-1 cells and PS-NH_2 exposed BEAS-2Bs differentiate from their controls 84% after 48 h exposure. The increase in explained variance after 48 h exposure compared to 72 h for A549 and Calu-1 cells can be attributed to higher stress in the control cells due to rapid consumption of medium by metabolically active cancer cell lines (DeBerardinis 2008).A representative example of the morphological changes in control cells after 48 and 72 h exposure, as seen by white light microscopy, is shown for A549 cells in Supplementary Figure 5.S4.Changes in cell shape, membrane integrity and formation of lipid vesicles, relating to the oxidative stress, are observed with increasing exposure time. When the exposure time is reduced to 24 h, A549, Calu-1 and BEAS-2B cells differentiate from the corresponding controls according to PC1, explaining ~50-60% for all cell lines. Figure 5.6 shows the loadings of PC1 corresponding to cytoplasm of exposed and control cells after 24, 48 and 72 h for A549 (A), Calu-1 (B) and BEAS-2B (C) cells. A549 and Calu-1 cell lines show similar responses in the lower wavenumber region and the double peak at 785 and 810 cm^{-1}isprominently observed for all exposure times (Figure 5.6 (A and B)). The change in the bands at 785 and 810 cm^{-1} also shows similarity in terms of intensity ratio of the 785/810 cm^{-1}bands, which indicates comparable changes in RNA accumulation for both cell lines (Figure 5.6). Conversely, the double peak, 785 and 810 cm^{-1}, is absent in the loading of PC1 of

BEAS-5.2B cell line after 48 h exposure. When the exposure time is reduced to 24 h, the double peak is observed with low intensity, which indicates the production of ROS in low levels and rapid consumption for the BEAS-2B cell line. The significantly higher intensity of 785 and 810 cm^{-1} bands can be attributed to higher amounts of accumulated nucleic acids in the cytoplasm of A549 and Calu-1 cells compared to BEAS-2B cells, consistent with the higher levels of ROS observed (Figure 5.5).

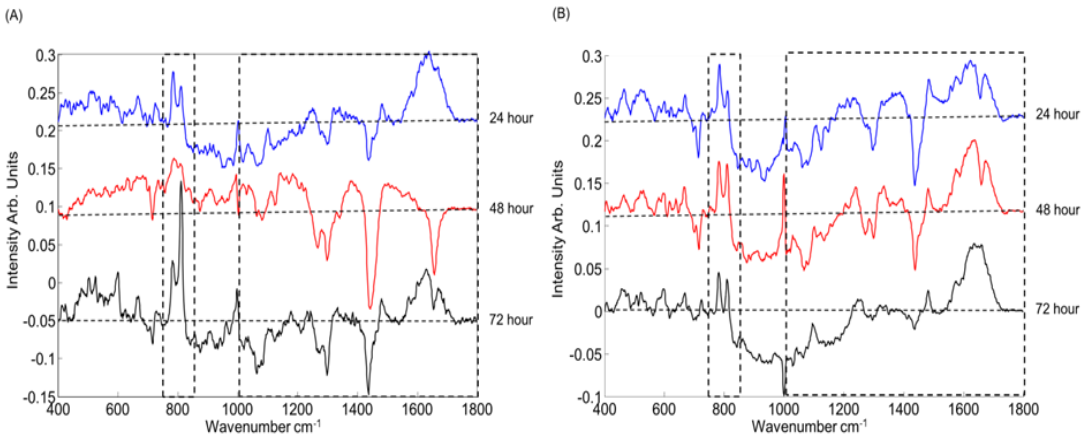

Figure 5.6. Comparison of the first loadings of PCA of cytoplasm of control and particle exposed A549 (A) and Calu-1 (B) cell lines after 24, 48 and 72 hour particle exposure; loadings are offset for clarity and the dotted line represents the zero '0' point for each loading. The positive side of the loadings represents the spectral features of the particle exposed cells, while the negative side represents the control cells for each loading. The changing features between cell lines are indicated with dashed lines.

When different cell lines are compared in the higher wavenumber region of the fingerprint, above 1000 cm^{-1}, after 24 and 48 h exposure, similar trends are observed in A549 and Calu-1 cells, which are mainly an increase or a decrease in protein and lipid related bands in particle exposed cells compared to their corresponding controls.

However, BEAS-2B cells show a significant change between 24 and 48 h, which can be attributed to more rapid and single step mechanism in the cytotoxic response rather than multiple mechanisms. The rapid toxic response can be related to full agonistic mechanism of the BEAS-2B cells (Figure 5.1) determined by the AB and MTT assay, which is also consistent with the less effective defence mechanisms of non-cancerous cell lines (Oberley & Oberley 1997).

As seen in Figure 5.6(A) for A549 cells, after 48 h exposure, the loading of PC1 is dominated by negative features above 1000 cm^{-1}. The bands at 1266 cm^{-1} (Amide III/α-helix), 1298 cm^{-1} (Lipids), 1438 cm^{-1} (lipids, proteins) and 1658 cm^{-1} (Amide I(α-helix)) are observed in the negative features of the loadings, which is consistent with damage to protein and lipid content of the exposed cells. The damage and loss in lipid composition of the cell can be attributed to protonation in lysosomes, lipidosis and ultimately lysosomal rupture as well as higher ROS levels in the cell upon PS-NH_2 exposure. The oxidative stress also causes alterations and damage to proteins in the cytosolic region of the exposed cells. When the exposure time is reduced to 24 h, A549 cells show changes in the same features as the loadings of 48 h, with less damage to protein and lipid structures. For the Calu-1 cell line, similar to the A549 cells, the loading of PC1is dominated by negative features above 1000 cm^{-1}(Figure 5.6(B)). The bands at 1266 cm^{-1} (Amide III/α-helix), 1298 cm^{-1} (Lipids) and 1438 cm^{-1} (lipids, proteins) are observed in the negative features of the loading. However, the range from 1600 to 1700 cm^{-1} of the Calu-1 cells shows significant differences compared to that of A549 cells. This region, as a broad band formed by multiple sub-bands, can be related to different molecular vibrations such as C-C, C=O (Movasaghi, Rehman, & Rehman 2007) and indicates the presence of lipid and proteins (Table S1). Although

the band at 1656 cm^{-1}(Amide I) can be identified as a negative feature in the loading, the general changes in the protein content of exposed cells are observed as positive features after 24 and 48 h exposure, which indicates higher amount of proteins as well as more Raman active proteins in the PS-NH_2 exposed cells compared the corresponding controls. The later effect on protein structures compared to lipid content can be explained by a cascade of events in the cell upon toxic particle exposure. The onset of lipidosis, change in pH gradient and ROS formation can impact on proteins at later stages, compared to the lipid based changes in the earlier stages. Moreover, the change in the spectral markers of proteins and lipids in Calu-1 cells with increasing exposure time is not observed to be as significant as A549 cells which can be attributed to a slower cytotoxic response.

Conversely, for the BEAS-2B cells, the formation of the cellular damage cannot be attributed to ROS due to low levels of measured ROS and the absence of the double peak at 785 and 810 cm^{-1}, even though similar signatures of cell damage response are observed in the range above 1000 cm^{-1} with A549 and Calu-1 cells. Although ROS is one of the mechanisms for cellular damage, other toxic pathways can be identified for cell death. pH gradient of the cells can have a significant contribution to damage in biochemical composition of the cells as well as effecting the working mechanism of the cellular compartments (Jayanth, Bayne, & Varnes 1994).The levels of the protonation in acidic organelles such as endosomes and lysosomes were measured using the Lysosensor dye. Lysosensor is known to be a pH dependent dye which quantifies the lysosomal content. As seen in Figure 5.7, BEAS-2B cells show a continuous protonation in lysosomes over a 24 h period. In contrast, A549 and Calu-1 cells show fluctuations in protonation. Changes and fluctuations in the amount of

protonated lysosomes can be explained by three different events occurring in the cell upon PS-NH_2 exposure. First, the proton pump effect can be initiated byPS-NH_2uptake into cells and formation of endosomes. After 3 to 4 h exposure, fusion of endosomes in lysosomes occurs and lysosomal protonation can initiate the second source of protonation, while the third can be related to lysosomal rupture. The fluctuations in protonation also show these additional protonation stages such as lysosomal rupture in A549 and Calu-1 cells compared to BEAS-2B cells. The lysosomal rupture has a significant effect on ROS formation, which ultimately affects the RNA in cytoplasm and results in accumulation of the noncoding RNAs. Although there are fluctuations in the levels for A549 (A) and Calu-1 (B) cells, the lysosomal protonation can contribute to cellular toxicity, in concert with ROS formation. On the other hand, the main reason for PS-NH_2 toxicity to BEAS-2B cells can be a continuous proton pump effect which affects the internal pH and ultimately pH gradient in the cytosolic region. Continuous changes in the internal pH can show a significant effect on the working mechanism of the mitochondria which needs a proton gradient for energy production and full functionality(Matsuyama & Reed 2000). The effect of PS-NH_2 on the mitochondria of BEAS-2B cells can also be seen from the MTT response and full agonistic feature of PS-NH_2 for BEAS-2B cell line.

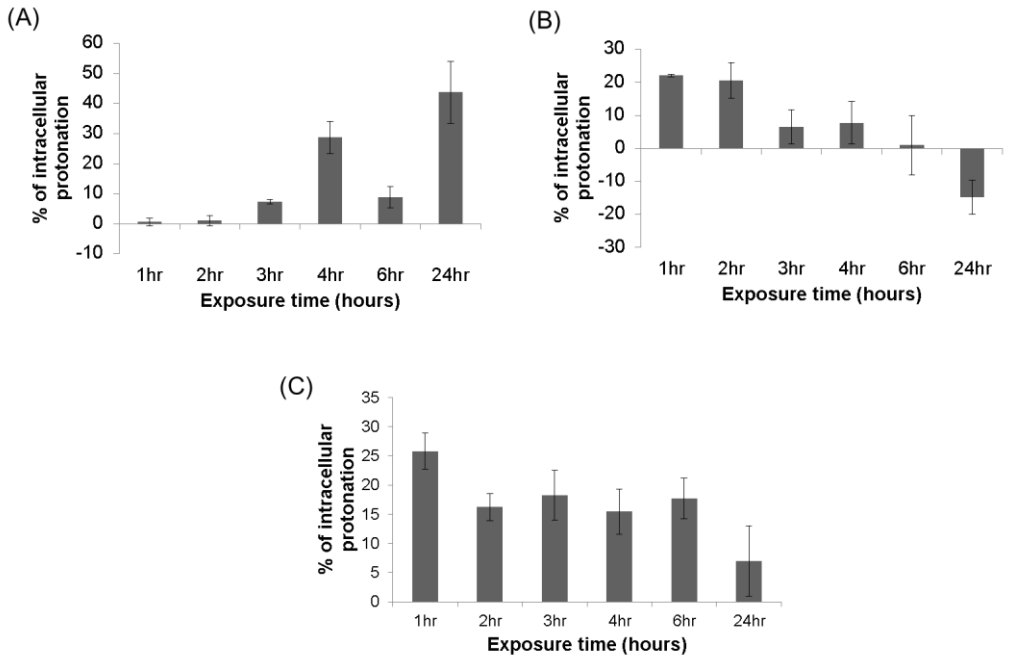

Figure 5.7. Changes in lysosomal protonation measured by Lysosensor activity in A549 (A), Calu-1 (B) and BEAS-2B (C) cell lines.

Overall, the cellular toxicity of PS-NH_2 for A549 and Calu-1 cells can be associated with two mechanisms,whereasBEAS-2B shows only one main mechanism. Briefly, after PS-NH_2 are taken up by A549 and Calu-1 cells, they give rise to the proton pump effect in lysosomes, which elicits a partial MTT response and changes mitochondrial activity as one mechanism. The ROS formation due to subsequent lysosomal rupture can be identified as the main mechanism which leads to cell damage and death, resulting in the full agonistic AB response. Conversely, BEAS-2B cells retain the lysosomal integrity and elicit a full agonistic response in MTT. The proton pump effect and the changes in mitochondrial function leads to cell death. A schematic representation of the different pathways for different cell lines can be seen in Figure 5.8.

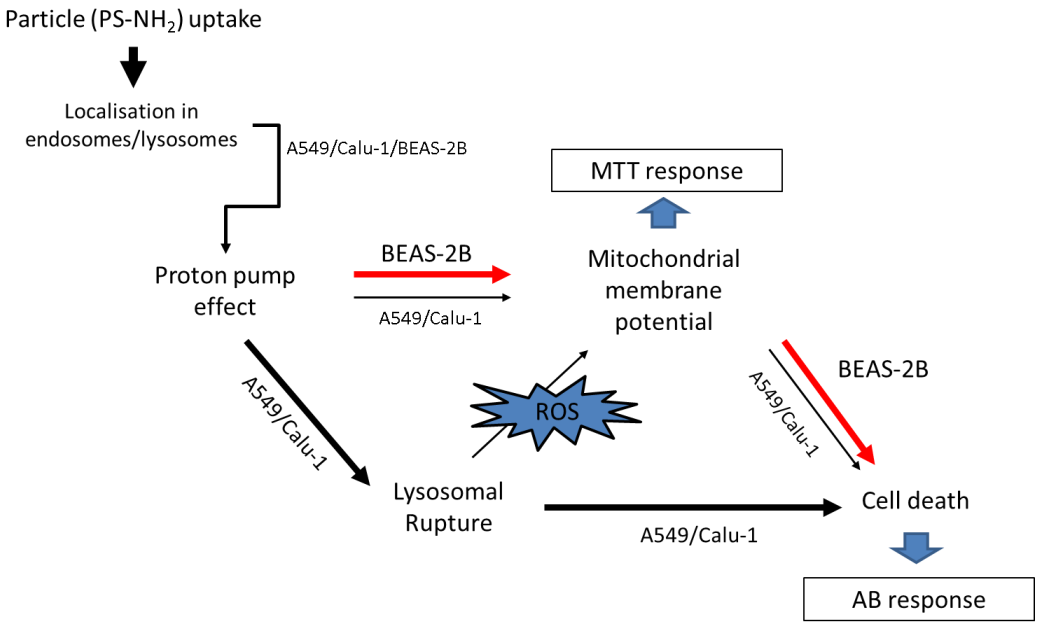

Figure 5.8. Schematic representation of different cell death pathways for A549, Calu-1 and BEAS-2B cell lines. Pathway for BEAS-2B cell line is indicated with red arrows, when A549 and Calu-1 is represented with black arrows.

Previous studies have shown the higher susceptibility of the lysosomal-mediated cell death in cancer cell lines compared to the normal cells(Reginald 2015). The relatively larger size of the lysosomes in the cancer cells are shown to make the lysosomal structure more fragile which makes the lysosomal alterations more common in cancerous cells (LeGendre, Breslin, & Foster 2015). In the study by LeGendre *et al.*, anticancer effects of the (-)-Oleocanthal, a phenolic compound in olive oil, has been demonstrated on the cancerous and non-cancerous cell lines and it has been found to selectively induce cell death in cancer cell lines due to fragility of the lysosomes and changes in lysosomal membrane permeabilization (LeGendre, Breslin, & Foster 2015). Therefore, the differences between cancer and non-cancerous cell lines observed by Raman microspectroscopy which can be attributed to lysosomal rupture resulting in cell death as a second mechanism for cancerous cell lines, A549 and Calu-

1, can also be attributed to lysosomal alterations due to larger size and fragility of the lysosomes. The CLSM images of the PS-NH_2 exposed cells also show a different distribution of the nanoparticles inside the cytoplasmic area after 24 h for A549 and Calu-1 cells compared to BEAS-2B cells (Supplementary Figure 5.S5). For the A549 (A) and Calu-1 (B), PS-$NH_2$are observed to be more spread in the cytoplasm, whereas the particles are observed to localise in perinuclear region for BEAS-2B (C) cells which indicates the evidence of common lysosomal rupture in the cancerous cell lines.

In this study, Raman microspectroscopy is shown to provide information in a rapid way with high sensitivity regarding overall cellular health, lysosomal and mitochondrial changes, changes in the biochemical composition of the cell, oxidative stress, from early stage particle exposure to cell death, as a function of time, in a range of cell lines. Raman microspectroscopy can be applied to different areas, from *in vitro* toxicology to medicinal chemistry (Bankapur *et al.* 2012; Efeoglu, Casey, & Byrne 2016; Keating & Byrne 2013; Kong *et al.* 2015; Owen *et al.* 2006; Pence & Mahadevan-Jansen 2016), as a high content screening technique, due to the multifaceted information contained in the fingerprint region and the technique can potentially replace the cellular and biochemical assays which require the use of multiple assays with multiple labels. The use of labels for the evaluation of cellular processes as well as localisation studies has been widely studied in different areas (Anguissola *et al.* 2014; Basiji *et al.* 2007; Ettinger & Wittmann 2014). However, the labels are known to be specific to one cellular event, whereas a complex series of events can take place inside the cell as a response to a single stimulus. The specificity of the labels brings the requirement of the use of multiple assays which is inefficient in terms of cost and time. Notably, when the complexity of cells, tissues and higher animal models are considered, the amount of assays and analysis required to complete

the picture of interaction mechanisms and efficacies and responses significantly retards the whole process for pharmaceutical and medical applications. As it is label free, Raman microspectroscopy uses the intrinsic properties of the biochemical constituents of the cells and spectral markers of subcellular events occurring inside the cell and allows the detection of the changes without targeting a specific molecule or event. For example, the cytotoxicity assays used in this study are based on measurement of the resorufin (pink and highly fluorescent) and formazan (purple) products inside the cell which are produced as a result of Resazurin and MTT reduction by AB and MTT assays, respectively (Mosmann 1983; O'Brien *et al.* 2000). Therefore, although conventional cytotoxicity assays such as AB and MTT provide valuable indications of the response of a cell population, they are based on measurement of a specific marker and do not provide any information on the mechanism of action or response pathways. Differing responses are commonly obtained from different assays, and the collective responses of multiple assays are not readily interpretable. As a high content screening technique, Raman microspectroscopy, can elucidate the mechanism of action and different pathways leading to the toxicity. The particle dependant (ROS) and cellular dependant (damage in protein and lipid structures, which gives information about cellular viability) spectral markers can be applied to predict nanoparticle toxicity. The consistencies in the spectral markers of the particle and cellular dependant events can be converted into more quantitative measurement with the analysis of spectral marker intensities versus dose and time. Moreover, further refinements of the data analysis and quantification protocols can be achieved by using more sophisticated data mining methods such as PC-LDA (Principal Component-Linear Discriminant Analysis) and Partial Least Squares Regression analysis (PLSR) to achieve improved differentiation and quantification.

5.5. Conclusion

Although conventional cytotoxicity assays, AB and MTT, provide valuable information about the toxicity of PS-NH_2, the techniques have been shown to be limited by the nature of the measurement methodology. The individual technique relies on the colorimetric changes on a specific marker. The varying results obtained from different assessments, which reflects the measurement of a different specific marker, can show a high impact on the evaluation of the nanoparticle toxicity and the reliability of the results. However, Raman microspectroscopy can provide deeper insights into toxic pathways by using intrinsic properties of biological molecules which are produced and consumed during cellular events. Upon exposure to a toxicant, spectral markers of the molecular initiating events and the subsequent cascade of events can be determined using Raman microspectroscopy. The spectral markers of toxicity obtained by Raman microspectroscopy can be observed in multiple cell lines and allow the prediction of mechanism of action of the nanomaterial.

This study has further demonstrated the different cellular responses and mechanisms leading to cell death between cancerous and non-cancerous cell lines can be differentiated by using the spectral markers of the cellular toxic events. The doublet peak, 785-810 cm^{-1}, is identified as a signature of ROS related changes in biochemical composition of the cell upon a toxicant exposure and the changes upon activation of the cell death mechanism has been identified with the region over 1000 $cm^{-1}$with the changes in protein and lipid structures The proof of concept study has demonstrated the consistency of the Raman spectroscopic signatures at a subcellular level, as a result of cell exposure to nanoscale toxicants, for the example of the commercially available

PS-NH_2. It demonstrates that the signatures of the initial responses to oxidative stress are consistent in different cell lines, and furthermore that the subsequent cellular responses can be interpreted in terms of characteristic signatures, including those of the cellular defence mechanisms, which are potentially quantifiable as a function of dose and/or exposure time. The confocal spectroscopic technique therefore provides a holistic view of the initiation stage of the toxicity as well as the cellular response in a high content, label free readout.

5.6. References

Abramczyk, H, Brozek-Pluska, B, Krzesniak, M, Kopec, M and Morawiec-Sztandera, A (2014) The Cellular Environment of Cancerous Human Tissue. Interfacial and Dangling Water as a "Hydration Fingerprint". *Spectrochimica Acta Part A: Molecular and Biomolecular Spectroscopy*, 129, 609-23.

Anguissola, S, Garry, D, Salvati, A, O'Brien, P J and Dawson, K A (2014) High Content Analysis Provides Mechanistic Insights on the Pathways of Toxicity Induced by Amine-Modified Polystyrene Nanoparticles. *PLoS ONE*, 9(9), e108025.

Bankapur, A, Krishnamurthy, R S, Zachariah, E, Santhosh, C, Chougule, B, Praveen, B, Valiathan, M and Mathur, D (2012) Micro-Raman Spectroscopy of Silver Nanoparticle Induced Stress on Optically-Trapped Stem Cells. *PLOS ONE,* 7(4), e35075.

Basiji, D A, Ortyn, W E, Liang, L, Venkatachalam, V and Morrissey, P (2007) Cellular Image Analysis and Imaging by Flow Cytometry. *Clinics in laboratory medicine,* 27(3), 653- 670.

Benjaminsen, R V, Mattebjerg, M A, Henriksen, J R, Moghimi, S M and Andresen, T L (2013) The Possible "Proton Sponge " Effect of Polyethylenimine (Pei) Does Not Include Change in Lysosomal Ph. *Molecular Therapy*, 21(1), 149-57.

Bernas, T and Dobrucki, J (2002) Mitochondrial and Nonmitochondrial Reduction of Mtt: Interaction of Mtt with Tmre, Jc-1, and Nao Mitochondrial Fluorescent Probes. *Cytometry*, 47(4), 236-42.

Berridge, M V, Herst, P M and Tan, A S (2005) Tetrazolium Dyes as Tools in Cell Biology: New Insights into Their Cellular Reduction. *Biotechnol Annu Rev,* 11, 127-52.

Bexiga, M G, Varela, J A, Wang, F, Fenaroli, F, Salvati, A, Lynch, I, Simpson, J C and Dawson, K A (2011) Cationic Nanoparticles Induce Caspase 3-, 7- and 9-Mediated Cytotoxicity in a Human Astrocytoma Cell Line. *Nanotoxicology,* 5(4), 557-67.

Bonnier, F, Mehmood, A, Knief, P, Meade, A D, Hornebeck, W, Lambkin, H, Flynn, K, McDonagh, V, Healy, C, Lee, T C, Lyng, F M and Byrne, H J (2011) *In vitro* Analysis of Immersed Human Tissues by Raman Microspectroscopy. *Journal of Raman Spectroscopy*, 42(5), 888-96.

Bonnier, F, Petitjean, F, Baker, M J and Byrne, H J (2014) Improved Protocols for Vibrational Spectroscopic Analysis of Body Fluids. *Journal of Biophotonics,* 7(3-4), 167-79.

Brayden, D J, Cryan, S-A, Dawson, K A, O'Brien, P J and Simpson, J C (2015) High-Content Analysis for Drug Delivery and Nanoparticle Applications. *Drug Discovery Today,* 20(8), 942-57.

Puppels, G., Greve, J. (1996). Whole Cell Studies and Tissue Characterization by Raman Spectroscopy In *"Biomedical Applications of Spectroscopy"* Vol. 25, John Wiley

and Sons, New York.

Brigger, I, Dubernet, C and Couvreur, P (2012) Nanoparticles in Cancer Therapy and Diagnosis. *Advanced Drug Delivery Reviews,* 64, Supplement, 24-36.

Casteilla, L, Rigoulet, M and Pénicaud, L (2001) Mitochondrial Ros Metabolism: Modulation by Uncoupling Proteins. *IUBMB Life*, 52(3-5), 181-8.

DeBerardinis, R J (2008) Is Cancer a Disease of Abnormal Cellular Metabolism?: New Angles on an Old Idea. *Genetics in medicine : official journal of the American College of Medical Genetics*, 10(11), 767-77.

Ding, G J, Fischer, P A, Boltz, R C, Schmidt, J A, Colaianne, J J, Gough, A, Rubin, R A and Miller, D K (1998) Characterization and Quantitation of Nf-Kappab Nuclear Translocation Induced by Interleukin-1 and Tumor Necrosis Factor-Alpha. Development and Use of a High Capacity Fluorescence Cytometric System. *J Biol Chem*, 273(44), 28897-905.

Dorney, J, Bonnier, F, Garcia, A, Casey, A, Chambers, G and Byrne, H J (2012) Identifying and Localizing Intracellular Nanoparticles Using Raman Spectroscopy. *Analyst*, 137(5), 1111-9.

Dykens, J A, Jamieson, J D, Marroquin, L D, Nadanaciva, S, Xu, J J, Dunn, M C, Smith, A R and Will, Y (2008) *In vitro* Assessment of Mitochondrial Dysfunction and Cytotoxicity of Nefazodone, Trazodone, and Buspirone. *Toxicol Sci*, 103(2), 335-45.

Efeoglu, E, Casey, A and Byrne, H J (2016) *In vitro* Monitoring of Time and Dose Dependent Cytotoxicity of Aminated Nanoparticles Using Raman Spectroscopy. *Analyst*, 141(18), 5417-31.

Efeoglu, E, Keating, M, McIntyre, J, Casey, A and Byrne, H J (2015) Determination of Nanoparticle Localisation within Subcellular Organelles *in vitro* Using Raman Spectroscopy. *Analytical Methods*, 7(23), 10000-17.

Elmore, S (2007) Apoptosis: A Review of Programmed Cell Death. *Toxicologic pathology*, 35(4), 495-516.

Ettinger, A and Wittmann, T (2014) Fluorescence Live Cell Imaging. *Methods Cell Biol*, 123, 77-94.

Farhane, Z, Bonnier, F, Maher, M A, Bryant, J, Casey, A and Byrne, H J (2016) Differentiating Responses of Lung Cancer Cell Lines to Doxorubicin Exposure: *In vitro* Raman Micro Spectroscopy, Oxidative Stress and Bcl-2 Protein Expression. *J Biophotonics*, 10, 151-165.

Filomeni, G, De Zio, D and Cecconi, F (2015) Oxidative Stress and Autophagy: The Clash between Damage and Metabolic Needs. *Cell Death Differ*, 22(3), 377-88.

Freeman, E C, Weiland, L M and Meng, W S (2013) Modeling the Proton Sponge Hypothesis: Examining Proton Sponge Effectiveness for Enhancing Intracellular Gene Delivery through Multiscale Modeling. *Journal of biomaterials science. Polymer edition*, 24(4), 398-416.

Frohlich, E, Meindl, C, Roblegg, E, Ebner, B, Absenger, M and Pieber, T R (2012) Action of Polystyrene Nanoparticles of Different Sizes on Lysosomal Function and Integrity. *Part Fibre Toxicol*, 9, 26.

Gasparri, F, Mariani, M, Sola, F and Galvani, A (2004) Quantification of the Proliferation Index of Human Dermal Fibroblast Cultures with the Arrayscan™ High-Content Screening Reader. *Journal of Biomolecular Screening*, 9(3), 232-43.

Godbey, W T, Wu, K K and Mikos, A G (1999) Tracking the Intracellular Path of Poly(Ethylenimine)/Dna Complexes for Gene Delivery. *Proceedings of the National Academy of Sciences of the United States of America*, 96(9), 5177-81.

Hamid, R, Rotshteyn, Y, Rabadi, L, Parikh, R and Bullock, P (2004) Comparison of Alamar Blue and Mtt Assays for High through-Put Screening. *Toxicol In vitro,* 18(5), 703-10.

Jayanth, V R, Bayne, M T and Varnes, M E (1994) Effects of Extracellular and Intracellular Ph on Repair of Potentially Lethal Damage, Chromosome Aberrations and Dna Double-Strand Breaks in Irradiated Plateau-Phase A549 Cells. *Radiat Res,* 139(2), 152-62.

Keating, M E, Bonnier, F and Byrne, H J (2012) Spectral Cross-Correlation as a Supervised Approach for the Analysis of Complex Raman Datasets: The Case of Nanoparticles in Biological Cells. *Analyst,* 137(24), 5792-802.

Keating, M E and Byrne, H J (2013) Raman Spectroscopy in Nanomedicine: Current Status and Future Perspective. *Nanomedicine (Lond),* 8(8), 1335-51.

Kerr, J F, Wyllie, A H and Currie, A R (1972) Apoptosis: A Basic Biological Phenomenon with Wide-Ranging Implications in Tissue Kinetics. *Br J Cancer,* 26(4), 239-57.

Knief, P, Clarke, C, Herzog, E, Davoren, M, Lyng, F M, Meade, A D and Byrne, H J (2009) Raman Spectroscopy - a Potential Platform for the Rapid Measurement of Carbon Nanotube-Induced Cytotoxicity. *Analyst,* 134(6), 1182-91.

Kong, K, Kendall, C, Stone, N and Notingher, I (2015) Raman Spectroscopy for Medical Diagnostics — from in-Vitro Biofluid Assays to in-Vivo Cancer Detection. *Advanced Drug Delivery Reviews,* 89, 121-34.

LeGendre, O, Breslin, P A and Foster, D A (2015) (-)-Oleocanthal Rapidly and Selectively Induces Cancer Cell Death Via Lysosomal Membrane Permeabilization. *Mol Cell Oncol,* 2(4), e1006077.

Liebel, U and Link, W (2007) Meeting Report: Trends and Challenges in High Content Analysis. *Biotechnol J,* 2(8), 938-40.

Liou, G-Y and Storz, P (2010) Reactive Oxygen Species in Cancer. *Free radical research,* 44(5), 479-496

Lullmann, H, Lullmann-Rauch, R and Wassermann, O (1978) Lipidosis Induced by Amphiphilic Cationic Drugs. *Biochem Pharmacol,* 27(8), 1103-8.

Lunov, O, Syrovets, T, Loos, C, Beil, J, Delacher, M, Tron, K, Nienhaus, G U, Musyanovych, A, Mailander, V, Landfester, K and Simmet, T (2011) Differential Uptake of Functionalized Polystyrene Nanoparticles by Human Macrophages and a Monocytic Cell Line. *ACS Nano,* 5(3), 1657-69.

Lunov, O, Syrovets, T, Loos, C, Nienhaus, G U, Mailander, V, Landfester, K, Rouis, M and Simmet, T (2011) Amino-Functionalized Polystyrene Nanoparticles Activate the Nlrp3 Inflammasome in Human Macrophages. *ACS Nano,* 5(12), 9648-57.

Maher, M A and Byrne, H J (2016) Modification of the *in vitro* Uptake Mechanism and Antioxidant Levels in Hacat Cells and Resultant Changes to Toxicity and Oxidative Stress of G4 and G6 Poly(Amidoamine) Dendrimer Nanoparticles. *Anal Bioanal Chem,* 408(19), 5295-307.

Maher, M A, Naha, P C, Mukherjee, S P and Byrne, H J (2014) Numerical Simulations of *in vitro* Nanoparticle Toxicity – the Case of Poly(Amido Amine) Dendrimers. *Toxicology in vitro,* 28(8), 1449-60.

Marshall, N J, Goodwin, C J and Holt, S J (1995) A Critical Assessment of the Use of Microculture Tetrazolium Assays to Measure Cell Growth and Function. *Growth Regul,* 5(2), 69-84.

Matsuyama, S and Reed, J C (2000) Mitochondria-Dependent Apoptosis and Cellular Ph Regulation. *Cell Death Differ,* 7(12), 1155-65.

Miljkovic, M, Chernenko, T, Romeo, M J, Bird, B, Matthaus, C and Diem, M (2010) Label-Free Imaging of Human Cells: Algorithms for Image Reconstruction of Raman Hyperspectral Datasets. *Analyst,* 135(8), 2002-13.

Mohamed, B M, Verma, N K, Davies, A M, McGowan, A, Crosbie-Staunton, K, Prina-Mello, A, Kelleher, D, Botting, C H, Causey, C P, Thompson, P R, Pruijn, G J M, Kisin, E R, Tkach, A V, Shvedova, A A and Volkov, Y (2012) Citrullination of Proteins: A Common Post-Translational Modification Pathway Induced by Different Nanoparticles *in vitro* and in Vivo. *Nanomedicine (London, England),* 7(8), 1181-95.

Morelli, J K, Buehrle, M, Pognan, F, Barone, L R, Fieles, W and Ciaccio, P J (2006) Validation of an *in vitro* Screen for Phospholipidosis Using a High-Content Biology Platform. *Cell Biol Toxicol,* 22(1), 15-27.

Mosmann, T (1983) Rapid Colorimetric Assay for Cellular Growth and Survival: Application to Proliferation and Cytotoxicity Assays. *J Immunol Methods,* 65(1-2), 55-63.

Movasaghi, Z, Rehman, S and Rehman, I U (2007) Raman Spectroscopy of Biological Tissues. *Applied Spectroscopy Reviews,* 42(5), 493-541.

Mu, Q, Hondow, N S, Krzeminski, L, Brown, A P, Jeuken, L J and Routledge, M N (2012) Mechanism of Cellular Uptake of Genotoxic Silica Nanoparticles. *Part Fibre Toxicol,* 9, 29.

Mukherjee, S P and Byrne, H J (2013) Polyamidoamine Dendrimer Nanoparticle Cytotoxicity, Oxidative Stress, Caspase Activation and Inflammatory Response: Experimental Observation and Numerical Simulation. *Nanomedicine,* 9(2), 202-11.

Nel, A E, Madler, L, Velegol, D, Xia, T, Hoek, E M V, Somasundaran, P, Klaessig, F, Castranova, V and Thompson, M (2009) Understanding Biophysicochemical Interactions at the Nano-Bio Interface. *Nat Mater,* 8(7), 543-57.

Notingher, I and Hench, L L (2006) Raman Microspectroscopy: A Noninvasive Tool for Studies of Individual Living Cells *in vitro*. *Expert Rev Med Devices,* 3(2), 215-34.

Notingher, I, Verrier, S, Haque, S, Polak, J M and Hench, L L (2003) Spectroscopic Study of Human Lung Epithelial Cells (A549) in Culture: Living Cells Versus Dead Cells. *Biopolymers,* 72(4), 230-40.

Nune, S K, Gunda, P, Thallapally, P K, Lin, Y-Y, Forrest, M L and Berkland, C J (2009) Nanoparticles for Biomedical Imaging. *Expert opinion on drug delivery,* 6(11), 1175-94.

O'Brien, J, Wilson, I, Orton, T and Pognan, F (2000) Investigation of the Alamar Blue (Resazurin) Fluorescent Dye for the Assessment of Mammalian Cell Cytotoxicity. *Eur J Biochem,* 267(17), 5421-6.

Oberdörster, G, Maynard, A, Donaldson, K, Castranova, V, Fitzpatrick, J, Ausman, K, Carter, J, Karn, B, Kreyling, W, Lai, D, Olin, S, Monteiro-Riviere, N, Warheit, D and Yang, H (2005) Principles for Characterizing the Potential Human Health Effects from

Exposure to Nanomaterials: Elements of a Screening Strategy. *Particle and Fibre Toxicology*, 2(1), 8.

Oberley, T D and Oberley, L W (1997) Antioxidant Enzyme Levels in Cancer. *Histol Histopathol*, 12(2), 525-35.

Oecd Oecd Guidelines for the Testing of Chemicals (2013) [Online]. Available: http://www.oecd.org/chemicalsafety/testing/oecdguidelinesforthetestingofchemicals.htm [Accessed 01/03/2017]

Ouyang, L, Shi, Z, Zhao, S, Wang, F T, Zhou, T T, Liu, B and Bao, J K (2012) Programmed Cell Death Pathways in Cancer: A Review of Apoptosis, Autophagy and Programmed Necrosis. *Cell Prolif*, 45(6), 487-98.

Owen, C A, Selvakumaran, J, Notingher, I, Jell, G, Hench, L L and Stevens, M M (2006) *In vitro* Toxicology Evaluation of Pharmaceuticals Using Raman Micro-Spectroscopy. *J Cell Biochem*, 99(1), 178-86.

Pence, I and Mahadevan-Jansen, A (2016) Clinical Instrumentation and Applications of Raman Spectroscopy. *Chemical Society Reviews*, 45(7), 1958-79.

Pliska, V (1999) Partial Agonism: Mechanisms Based on Ligand-Receptor Interactions and on Stimulus-Response Coupling. *J Recept Signal Transduct Res*, 19(1-4), 597-629.

Radio, N M, Breier, J M, Shafer, T J and Mundy, W R (2008) Assessment of Chemical Effects on Neurite Outgrowth in Pc12 Cells Using High Content Screening. *Toxicol Sci*, 105(1), 106-18.

Rampersad, S N (2012) Multiple Applications of Alamar Blue as an Indicator of Metabolic Function and Cellular Health in Cell Viability Bioassays. *Sensors,* 12(9), 12347–12360.

Halaby, R., (2015) Role of Lysosomes in Cancer Therapy. *Dove Press: Research and Reports in Biology*, 6, 147-55.

Riss, T L, Moravec, R A, Niles, A L, Duellman, S, Benink, H A, Worzella, T J and Minor, L (2004). Cell Viability Assays In Sittampalam, G S, Coussens, N P, Brimacombe, K, Grossman, A, Arkin, M, Auld, D, Austin, C, Bejcek, B, Glicksman, M, Inglese, J, Iversen, P W, Li, Z, McGee, J, McManus, O, Minor, L, Napper, A, Peltier, J M, Riss, T, Trask, O J, Jr. and Weidner, J (Eds) *Assay Guidance Manual*, Eli Lilly & Company and the National Center for Advancing Translational Sciences, Bethesda (MD).

Ruan, B, Pong, K, Jow, F, Bowlby, M, Crozier, R A, Liu, D, Liang, S, Chen, Y, Mercado, M L, Feng, X, Bennett, F, von Schack, D, McDonald, L, Zaleska, M M, Wood, A, Reinhart, P H, Magolda, R L, Skotnicki, J, Pangalos, M N, Koehn, F E, Carter, G T, Abou-Gharbia, M and Graziani, E I (2008) Binding of Rapamycin Analogs to Calcium Channels and Fkbp52 Contributes to Their Neuroprotective Activities. *Proc Natl Acad Sci U S A,* 105(1), 33-8.

Ruenraroengsak, P and Tetley, T D (2015) Differential Bioreactivity of Neutral, Cationic and Anionic Polystyrene Nanoparticles with Cells from the Human Alveolar Compartment: Robust Response of Alveolar Type 1 Epithelial Cells. *Part Fibre Toxicol,* 12, 19.

Saptarshi, S R, Duschl, A and Lopata, A L (2013) Interaction of Nanoparticles with Proteins: Relation to Bio-Reactivity of the Nanoparticle. *Journal of Nanobiotechnology,* 11(1), 26.

Sarker, K P, Kataoka, H, Chan, A, Netherton, S J, Pot, I, Huynh, M A, Feng, X, Bonni, A, Riabowol, K and Bonni, S (2008) Ing2 as a Novel Mediator of Transforming Growth Factor-Beta-Dependent Responses in Epithelial Cells. *J Biol Chem*, 283(19), 13269-79.

Shapero, K, Fenaroli, F, Lynch, I, Cottell, D C, Salvati, A and Dawson, K A (2011) Time and Space Resolved Uptake Study of Silica Nanoparticles by Human Cells. *Mol Biosyst,* 7(2), 371-8.

Sierra, M I, Valdés, A, Fernández, A F, Torrecillas, R and Fraga, M F (2016) The Effect of Exposure to Nanoparticles and Nanomaterials on the Mammalian Epigenome. *International Journal of Nanomedicine,* 11, 6297-306.

Sonawane, N D, Thiagarajah, J R and Verkman, A S (2002) Chloride Concentration in Endosomes Measured Using a Ratioable Fluorescent Cl- Indicator: Evidence for Chloride Accumulation During Acidification. *J Biol Chem,* 277(7), 5506-13.

Tosi, G, Bortot, B, Ruozi, B, Dolcetta, D, Vandelli, M A, Forni, F and Severini, G M (2013) Potential Use of Polymeric Nanoparticles for Drug Delivery across the Blood-Brain Barrier. *Curr Med Chem*, 20(17), 2212-25.

Vega-Avila, E and Pugsley, M K (2011) An Overview of Colorimetric Assay Methods Used to Assess Survival or Proliferation of Mammalian Cells. *Proc West Pharmacol Soc*, 54, 10-4.

Vyumvuhore, R, Tfayli, A, Duplan, H, Delalleau, A, Manfait, M and Baillet-Guffroy, A (2013) Effects of Atmospheric Relative Humidity on Stratum Corneum Structure at the Molecular Level: Ex Vivo Raman Spectroscopy Analysis. *Analyst,* 138(14), 4103-11.

Walton, A G, Deveney, M J and Koenig, J L (1970) Raman Spectroscopy of Calcified Tissue. *Calcified Tissue Research,* 6(1), 162-7.

Wang, F, Yu, L, Monopoli, M P, Sandin, P, Mahon, E, Salvati, A and Dawson, K A (2013) The Biomolecular Corona Is Retained During Nanoparticle Uptake and Protects the Cells from the Damage Induced by Cationic Nanoparticles until Degraded in the Lysosomes. *Nanomedicine,* 9(8), 1159-68.

Xia, T, Kovochich, M, Liong, M, Zink, J I and Nel, A E (2008) Cationic Polystyrene Nanosphere Toxicity Depends on Cell-Specific Endocytic and Mitochondrial Injury Pathways. *ACS Nano,* 2(1), 85-96.

Zock, J M (2009) Applications of High Content Screening in Life Science Research. *Combinatorial Chemistry & High Throughput Screening,* 12(9), 870-6.

5S Supplementary Material:

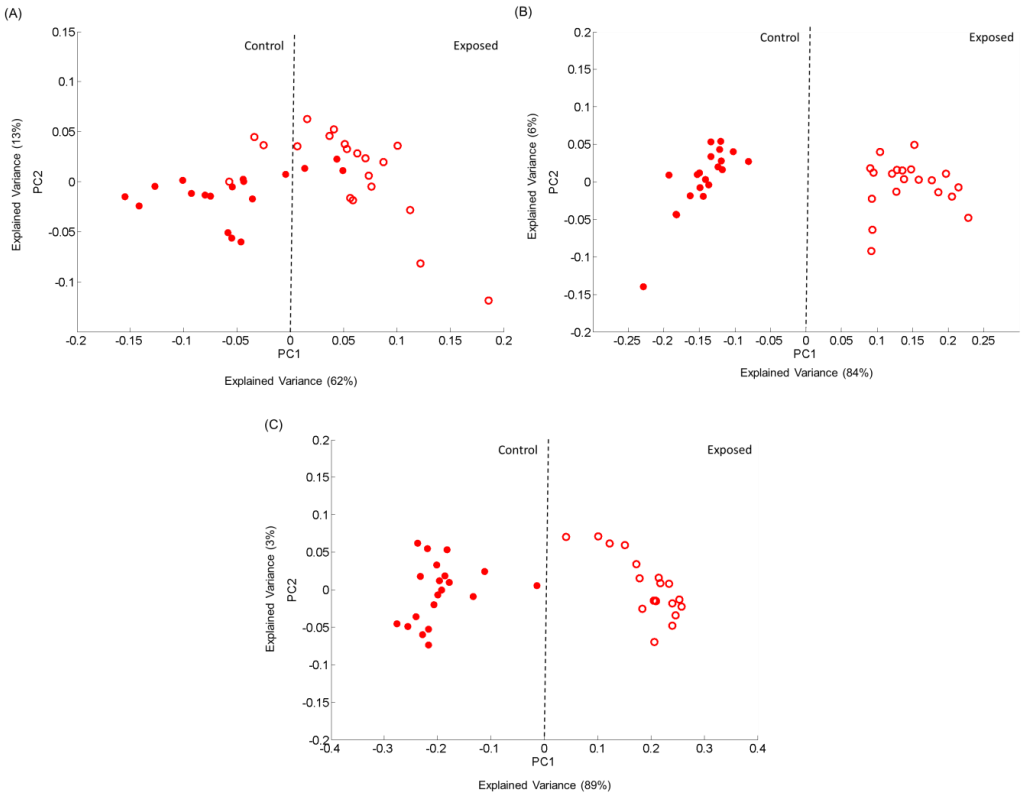

Figure 5.S1. Scatter plot of the PCA of spectra corresponding to cytoplasm of unexposed cells (control) and PS-NH_2 exposed BEAS-2B cells after 24 (A), 48 (B) and 72 (C) h exposure. Unexposed cells and exposed cells are indicated with closed circles and open circles, respectively. '0' line for PC1 is indicated by black dashed outlines.

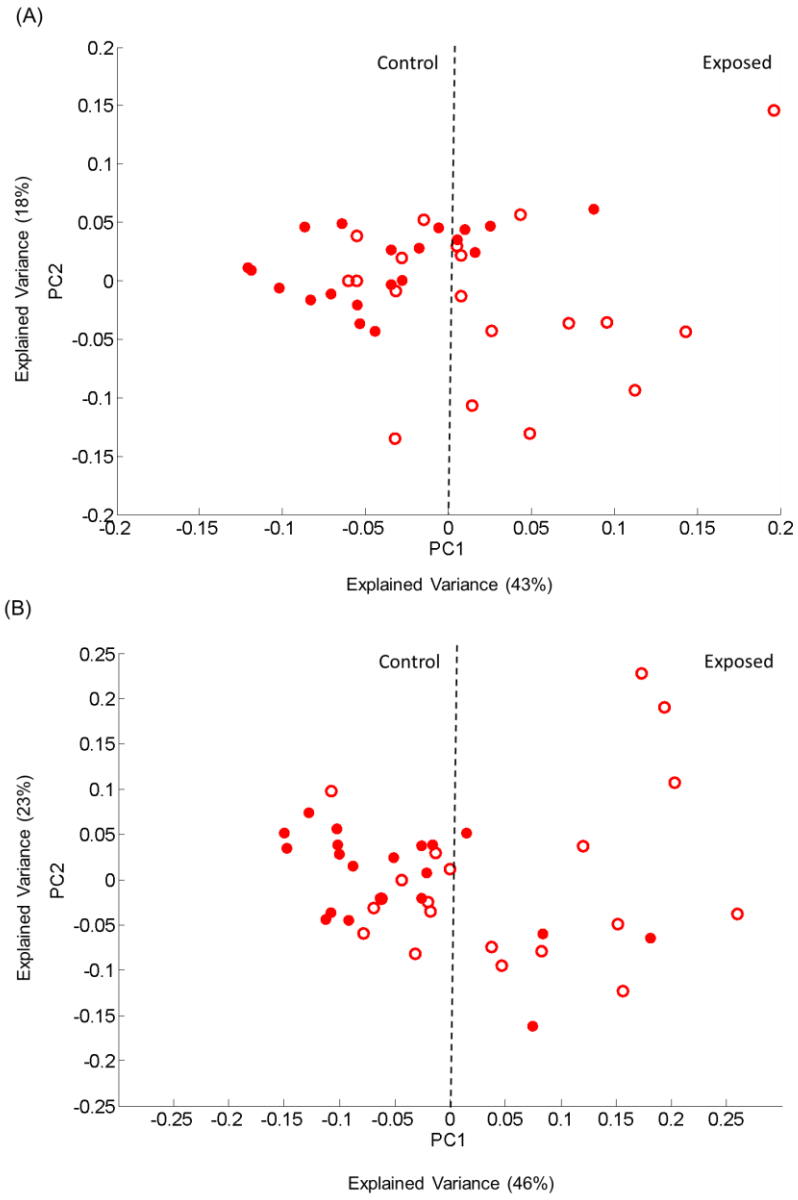

Figure 5.S2. Scatter plot of the PCA of spectra corresponding to cytoplasm cells of the unexposed cells (control) and PS-NH_2 exposed A549 (A), Calu-1 (B) cells after 72 h exposure. Unexposed cells and exposed cells are indicated with closed circles and open circles, respectively. '0' line for PC1 is indicated by black dashed outlines.

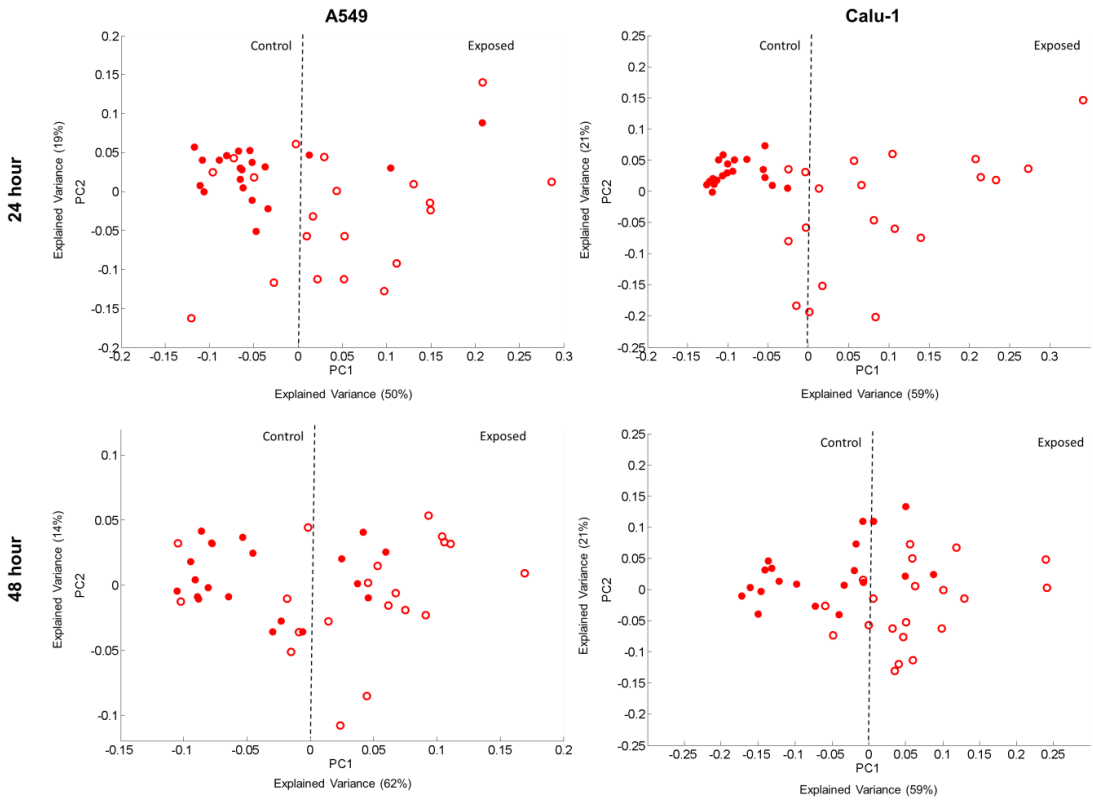

Figure 5.S3. Scatter plot of the PCA of spectra corresponding to cytoplasm cells of the unexposed cells (control) and PS-NH_2 exposed A549 and Calu-1 cells for 24 h exposure. Unexposed cells and exposed cells are indicated with close circles and open circles, respectively.

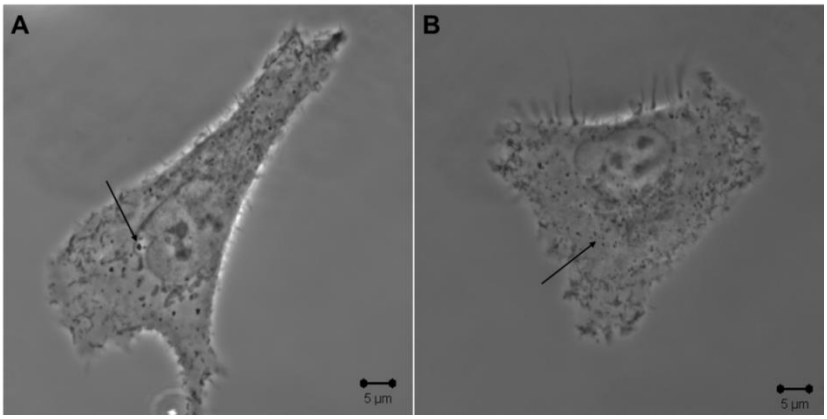

Figure 5.S4. White-light images of A549 cells (unexposed) after 48 (A) and 72 (B) h. x60 magnification. Vesicle formation is indicated with black arrows.

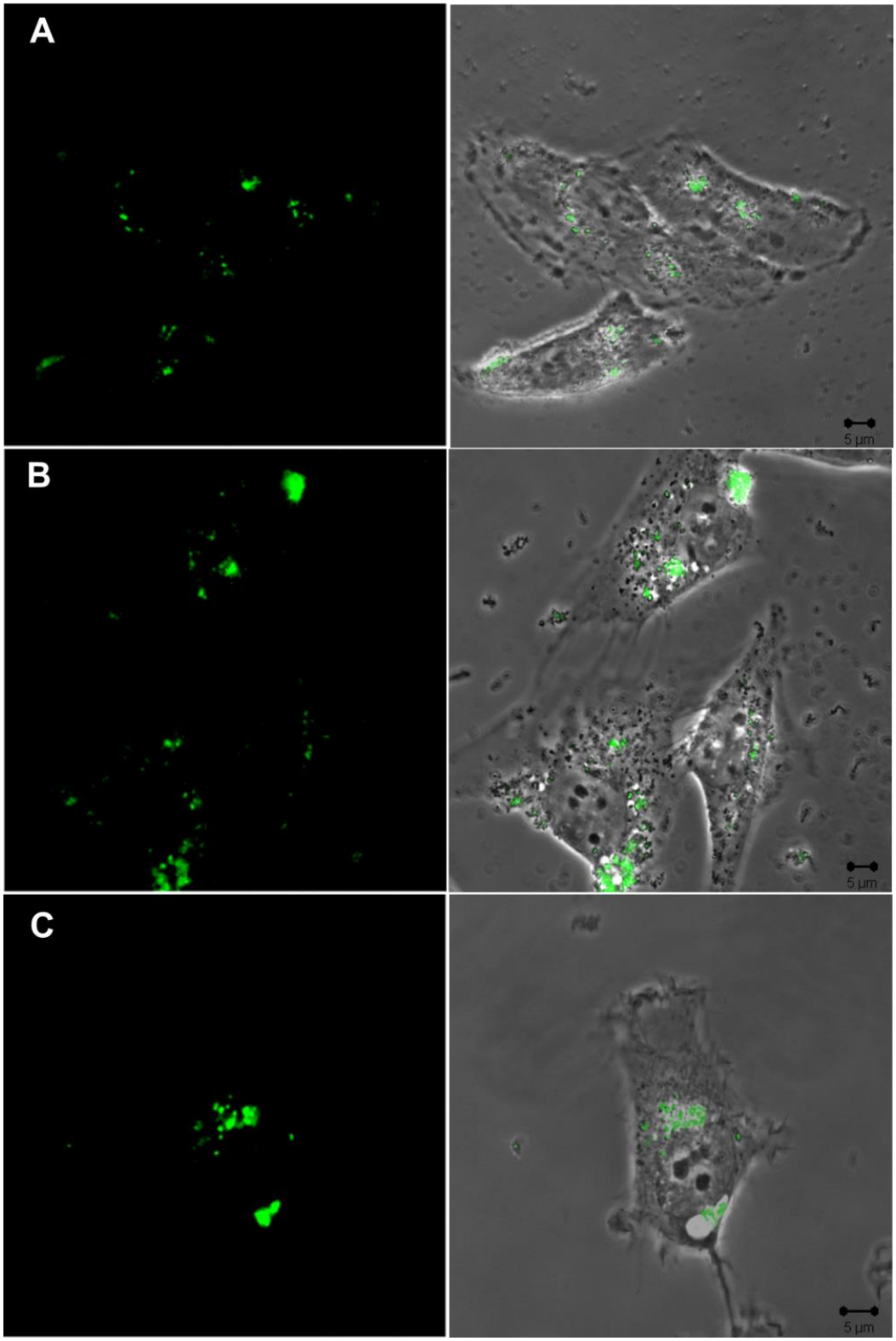

Figure 5.S5. CLSM images of A549 (A), Calu-1 (B) and BEAS-2B (C) cells exposed to 2.5, 1 and 0.6 µM of PS-NH_2 after 24 h with x60 magnification. Green fluorescent indicates the PS-NH_2.

Table 5.S1. Assignments of Raman Bands above 1000 cm^{-1} region of fingerprint (Abramczyk *et al.* 2014; Movasaghi, Rehman, & Rehman 2007; Notingher & Hench 2006; Notingher *et al.* 2003; Vyumvuhore *et al.* 2013).

Band Position (cm^{-1})	Band Assignments
1003	Phenylalanine
1033	Phenylalanine
1248	Amide III of proteins, nucleic acids, guanine (G) or cytosine (NH_2)
1339	Phenylalanine
1658	Amide I(α-helix)
1600-1700	Amide I band of proteins (C=O) Phenylalanine(C=C) Cytosine (NH_2) Tryptophan lipid (C=C) lipids (C=O) phospholipids Fatty acids Residual (-OH)

5S.1. Supplementary References

Abramczyk, H., Brozek-Pluska, B., Krzesniak, M., Kopec, M. and Morawiec-Sztandera, A. (2014) The cellular environment of cancerous human tissue. Interfacial and dangling water as a "hydration fingerprint". *Spectrochimica Acta Part A: Molecular and Biomolecular Spectroscopy*, 14(129), 609-623.

Movasaghi, Z., Rehman, S. and Rehman, I. U. (2007) Raman Spectroscopy of Biological Tissues. *Applied Spectroscopy Reviews*, 42(5), 493-541.

Notingher, I., Verrier, S., Haque, S., Polak, J. M. and Hench, L. L. (2003) Spectroscopic study of human lung epithelial cells (A549) in culture: living cells versus dead cells. *Biopolymers*, 72(4), 230-240.

Notingher, I. and Hench, L. L. (2006) Raman microspectroscopy: A noninvasive tool for studies of individual living cells *in vitro*. *Expert Rev Med Devices*, 3(2), 215-234.

Vyumvuhore, R., Tfayli, A., Duplan, H., Delalleau, A., Manfait, M. and Baillet-Guffroy, A. (2013) Effects of atmospheric relative humidity on Stratum Corneum structure at the molecular level: ex vivo Raman spectroscopy analysis. *Analyst*, 138(14), 4103-4111.

CHAPTER 6

Determination of Spectral Markers of Cytotoxicity and Genotoxicity Using *in vitro* Raman Microspectroscopy: Cellular Responses to Polyamidoamine Dendrimer Exposure

The following chapter has been adapted from the published journal article entitled 'Determination of Spectral Markers of Cytotoxicity and Genotoxicity Using *in vitro* Raman Microspectroscopy: Cellular Responses to Polyamidoamine Dendrimer Exposure', Analyst, 2017, DOI: 10.1039/C7AN00969K.

Author list: Esen Efeoglu, Alan Casey, Hugh J. Byrne

EE performed all measurements, data analysis and is the main drafting author. AC and HJB contributed to manuscript design and final drafting.

6.1. Abstract

Although consumer exposure to nanomaterials is ever increasing, with potential increased applications in areas such as drug and/or gene delivery, contrast agents and diagnosis, determination of cyto- and geno- toxic effect of nanomaterials on human health and the environment still remains challenging. Although many techniques have been established and adapted to determine the cytotoxicity and genotoxicity of nano-sized materials, these techniques remain limited by the number of assays required, total cost, use of labels and they struggle to explain the underlying interaction mechanisms. In this study, Raman microspectroscopy is employed as an *in vitro* label free high content screening technique to observe toxicological changes within the cell in a multi-parametric fashion. The evolution of spectral markers as a function of time and applied dose has been used to elucidate the mechanism of action of polyamidoamine (PAMAM) dendrimers associated with cytotoxicity and their impact on nuclear biochemistry. PAMAM dendrimers are chosen as a model nanomaterial due to their widely studied cytotoxic and genotoxic properties and commercial availability. Point spectra were acquired from cytoplasm to monitor the cascade of toxic events occurring in the cytoplasm upon nanoparticle exposure, whereas the spectra acquired from nucleus and nucleolus were used to explore PAMAM-nuclear material interaction as well as genotoxic responses.

6.2. Introduction

The rapid advances in nanotechnology and potential exploitation of naturally occurring and engineered nanomaterials in various fields, from nanomedicine to diagnostics (Brigger, Dubernet, & Couvreur 2012; Godbey, Wu, & Mikos 1999; Tosi *et al.* 2013), has brought huge interest to the identification of their interaction with living systems and the environment. Nanotoxicology has been developed to monitor the behaviours of these unique materials inside living systems and to determine their mechanism of action (Donaldson *et al.* 2004; Oberdörster *et al.* 2005). Many techniques from cytotoxicity, biochemical assays to bio-imaging techniques have been developed or adapted to investigate nanomaterials. However, these techniques remain limited due to the use of multiple labels, the number of assays required and analysis time. Although the analysis time has been reduced by the adaptation of a high content screening techniques (HCA/HCS) to elucidate nanomaterial toxicity, this technique still requires the use of labels and more development in terms of standardisation, the use of application specific models and data management, is needed (Liebel & Link 2007).

The potential of Raman microspectroscopy for the analysis of biological samples has already been demonstrated, including analysis of bodily fluids and cytological samples as well as tissue sectioning (Bonnier *et al.* 2011; Bonnier *et al.* 2014; Breve 1996; Walton, Deveney, & Koenig 1970). Moreover, Raman microspectroscopy has been used to localise nanoparticles in cellular compartments (Dorney *et al.* 2012; Efeoglu *et al.* 2015; Keating, Bonnier, & Byrne 2012). The dose and time dependent effects of aminated polystyrene nanoparticles (PS-NH_2) on different cell lines has been

spectroscopically characterised (Efeoglu, Casey, & Byrne 2016) and the mechanisms leading to cell death have been differentiated between cancerous and non-cancerous cell lines with the aid of multivariate analysis techniques (Efeoglu *et al.* 2017).

In the current study, the applicability of Raman microspectroscopy as a label-free and *in vitro* high content screening technique to identify spectral markers of cytotoxicity and genotoxicity is demonstrated. The systematic evolution of these spectral markers as a function of time and applied dose is shown for polyamidoamine (PAMAM) dendrimers. PAMAM nanoparticles have attracted attention in nanotechnology and nanomedicine due to their unique and tuneable properties. The potential use of PAMAM dendrimers in gene and/or drug delivery, miRNA delivery and MRI contrast agents has already been explored (Bourne *et al.* 1996; Twyman *et al.* 1999; Zhou *et al.* 2006). The toxic effects of the PAMAM dendrimers on different cell lines have also been widely studied using cytotoxicity assays such as Alamar Blue (AB), MTT, Neutral Red (NR) and Clonogenic assays (Maher & Byrne 2016; Maher *et al.* 2014; Mukherjee & Byrne 2013; Mukherjee, Davoren, & Byrne 2010; Naha & Byrne 2013; Naha *et al.* 2010). Cellular exposure to PAMAM dendrimers has been shown to result in oxidative stress, activation of inflammatory cascades. As a general mechanism, dendrimers are found to cause a generation dependent, systematic cytotoxicity, oxidative stress and genotoxicity due to the proton sponge effect in endosomes and/or lysosomes, which causes lysosomal rupture and mitochondrial accumulation, resulting in cell death. Notably, PAMAM dendrimers were identified among the list of priority nanomaterials for nanotoxicological assessment, drawn up by the Organisation for Economic Co-operation and Development (OECD).(OECD 2010) Therefore,

PAMAM dendrimers are chosen as model nanoparticles due to their widely studied and well-defined toxic properties and commercial availability.

In this study, A549, adenocarcinomic human alveolar basal epithelial cells, were used as a model cell line as they mimic one of the primary routes of nanoparticle exposure, inhalation and also for consistency with previous studies (Dorney *et al.* 2012; Efeoglu, Casey, & Byrne 2016; Efeoglu *et al.* 2015; Efeoglu *et al.* 2017; Keating, Bonnier, & Byrne 2012). PAMAM dendrimers elicit a systematic increase in toxicity with increasing generation (Mukherjee, Davoren, & Byrne 2010), and Generation 5 dendrimers were chosen as they provide a mid-range toxic response. The cells are exposed to various doses of generation 5 PAMAM dendrimers (PAMAM-G5), from sub-lethal to lethal, for 24 h to observe dose dependant changes in the cytoplasmic and nuclear regions. A sub-lethal dose of PAMAM-G5 is also used to elucidate evolving biomolecular changes in the nucleus, nucleolus and cytoplasm, from 4 to 72 h. 20 point spectra were acquired from the cytoplasm, nucleus and nucleolus of the PAMAM-G5 exposed and corresponding controls. Raman spectral data sets were analysed using Principal Components Analysis (PCA) to determine spectral markers of cyto- and geno- toxicity and to observe evolution of spectral markers as a function of time and dose.

6.3. Materials and Methods

6.3.1. Cell Culture and Reagents

Adenocarcinomic human alveolar basal epithelial cells, A549 (CCL-185TM), was obtained from American Type Culture Collection (ATCC) and used as model cell line to determine Raman spectral markers of cyto- and geno- toxicity upon a toxicant exposure. Dulbecco's Modified Eagle's Medium Nutrient Mixture F-12 HAM (DMEM-F12) was purchased from Sigma-Aldrich (Ireland) and cells were cultured in DMEM-F12 supplemented with 2 mM L-glutamine and 10% foetal bovine serum (FBS) at 37 °C in 5% CO_2 humidified incubator. Cells were sub-cultured when the level of confluency reach to 60%-70%, which was approximately 3 to 4 days.

6.3.2. Preparation of Dendrimer Solutions

Generation 5-polyamidoamine (PAMAM-G5) dendrimers (664049) are used as model dendritic nanoparticles throughout the study, due to their well-known toxicity and commercial availability and they were purchased from Sigma-Aldrich (Ireland). The working solutions of the PAMAM dendrimers were freshly prepared from the stock solutions (initial stock concentration: 1.7 mM) in pre-warmed (37 °C) 5% FBS and 2 mM L-glutamine supplemented DMEM-F12 medium. The size of the dendrimers is provided as 5.4 nm by the manufacturer.(Dendritech 2017) The PAMAM dendrimers were also characterised in DMEM-F12 medium by Mukherjee previously using Dynamic light scattering (DLS) and the diameter of the dendrimers are reported to be 6.1 ±0.2 nm (Mukherjee, Davoren, & Byrne 2010).

6.3.3. Cytotoxicity Evaluation and Calculation of Half-Maximal Effective Concentration (EC_{50})

In order to get a general perspective of the toxicity of the PAMAM dendrimers to A549 cells and to determine the concentrations that will be used throughout the Raman microspectroscopy studies, Alamar Blue (AB) and (3-(4, 5-dimethylthiazol-2-yl)-2, 5-diphenyltetrazolium bromide (MTT) assays were carried out and they were purchased from Biosciences Ltd. (Ireland) and Sigma-Aldrich (Ireland), respectively. Both AB and MTT assays are conducted on the same 96-well plates. Cells were seeded in 96-well plates with densities of $1x10^5$, $5x10^4$ and $3x10^4$ cell/mL for 24, 48 and 72 h, respectively and plates were kept in 5% CO_2 at 37 °C for 24 h for initial attachment and growth. After 24 h incubation, cell medium was discarded and cells were washed with pre-warmed (37°C) PBS, twice. Untreated A549 cells were used as negative control, whereas cells exposed to 10% Dimethyl sulfoxide (DMSO) were used as positive control. In each 96-well plate, 6 replicates of controls and samples with PAMAM exposures were prepared and 3 independent experiments were carried out to determine toxicity. PAMAM solutions were freshly prepared prior to the experiment from its stock, over a concentration range from 5.0 to 0.04 μM (8 different concentrations with serial dilutions) in pre-warmed DMEM-F12 medium supplemented with 5% FBS and 2 mM L-glutamine. The cells were exposed to the prepared solutions of the PAMAM for 24, 48 and 72 h. After test exposures, medium containing the particles was removed and cells were rinsed with PBS three times. 100 μl of AB/MTT solution (5% [v/v] AB and 10% [v/v] MTT), prepared in pre-warmed (37 °C) un-supplemented DMEM-F12, were added to the wells and kept at 37 °C in 5% CO_2 humidified incubator for 3 h. Following 3 h incubation of the cells with

AB/MTT solution, fluorescence emission of AB was measured directly at 595 nm using a micro plate reader (SpectraMax-M3, Molecular Devices, USA). For MTT measurement, medium containing dye solutions was removed and cells were washed with PBS, three times. 100 µL of DMSO were added to the wells for dissolution of the formazan product of MTT and plates were kept in a shaker for 10 mins at 200 rpm. The MTT absorbance was measured at 570 nm using the micro plate reader. Data were transferred and analysed in Sigmaplot to determine the half-maximal effective concentration producing a reduction of viability to 50% (EC_{50}). GraphPad was used to predict approximate EC_n values (reduction of viability to n %) based on the EC_{50} calculated in SigmaPlot.

6.3.4. Sample preparation for Raman micro-spectroscopy

For Raman studies, the A549 cells were seeded onto CaF_2 discs with a density of 16,000 cells/ per substrate and incubated in 5% FBS and 2 mM L-glutamine supplemented DMEM-F12 for 24 h at 37 °C in 5% CO_2. Following the 24 h initial attachment and growth, cell medium was discarded and cells were rinsed with pre-warmed PBS, twice. The different concentrations of the PAMAM dendrimers were prepared in pre-warmed and supplemented (5% FBS, 2 mM L-glutamine) DMEM-F12, prior to the experiment. Cells were exposed to the calculated EC_n values for 24 h to determine dose dependant responses, whereas cells were exposed to the EC_{25} from 4 to 72 h in order to monitor time dependant changes on the spectral markers. Fresh DMEM-F12 with the supplements was used for the control samples. At exposure time end points, the medium containing dendrimers was discarded and cells were washed three times with pre-warmed PBS to remove the non-internalized dendrimers. The

samples are fixed using 10% formalin solution and cells were kept in formalin for 10 mins. After fixation, cells were washed with sterilized dH_2O and kept in water for Raman measurements.

6.3.5. Raman Microspectroscopy and Data Analysis

Point spectra from the nucleus, nucleolus and cytoplasm of the 20 individual cells were acquired, for 30 seconds x 2 for each point, using a Horiba Jobin-Yvon LabRAM HR800 spectrometer equipped with a 785 nm diode laser, with laser power on the sample of ~70mW. Raman spectra of the cells were acquired in water throughout the study with a 100x immersion objective (LUMPlanF1, Olympus, N.A. 1) producing a spot size of diameter ~1μm. Prior to the spectral acquisition, the spectrometer was calibrated to the 520.7 cm^{-1} line of silicon. A 300 lines per mm grating, which provides ~1.5 cm^{-1} per pixel spectral dispersion, and a 100 μm confocal pinhole were used and spectra were collected by a 16 bit dynamic range Peltier cooled CCD detector. Spectra were acquired from control and exposed samples in the fingerprint region (400-1800 cm^{-1}). Raman spectral data sets were analysed using Principal Components Analysis (PCA). Pairwise comparison of the control and exposed cells was carried out using data sets, each containing 20 spectra from each cellular compartment. The matrix dimensions of the data sets were kept equal (20 spectra from control and 20 spectra from particle exposed cells) for PCA and mean spectra of the data sets, which are used as input in PCA, are provided in Supplementary Figure S1, S2 and S3 for control, different dose and exposure time, respectively. The data is mean centred as part of the PCA protocol. For all analyses, loadings of the PCA are displayed offset for clarity and the zero '0' line for each loading, which separates the positive and negative

features of the PCA, is indicated with dashed lines. A scaling system based on the '0' line ± 0.05 is used for all figures, which allows inter comparison of the spectral marker intensities.

Prior to analysis, data sets were subjected to pre-processing to improve spectral quality. Data was first subjected to mild smoothing using Savitsky–Golay Filter (3^{rd} order, 9 points) and background, which is predominantly water in the immersion geometry (Bonnier *et al.* 2014; Miljkovic *et al.* 2010), was subtracted using Classical Least Squares (CLS) analysis. CLSA can be carried out two different ways, by use of a factor analysis algorithm (unsupervised) or by manual input of reference spectra. For background correction, a reference background spectrum, which was obtained from the surface of a CaF_2 disc using x100 immersion objective, was subtracted from spectra using CLSA. Baseline correction is carried out by applying a rubberband correction in Matlab. Smoothed, background removed and baseline corrected spectra were vector normalised. All pre-processing and the data analysis is performed in Matlab (Mathworks, USA) using in-house scripts.

6.4. Results and Discussion

6.4.1. Cytotoxicity Evaluation of PAMAM Dendrimers

The effect of PAMAM-G5 dendrimers on the cellular viability of A549 cells was evaluated by using commercially available and commonly used cytotoxicity assays, AB and MTT. For low doses of the PAMAM dendrimers, the cellular viability as measured using the MTT assay is observed to systematically increase from 100% to

>120% compared to controls (Figure 1B). This can be interpreted as an increased mitochondrial activity compared to controls, although a clear toxic response is observed with increasing dose. The mean effective concentration of the cell viability, EC_{50}, was calculated in SigmaPlot by using a four parameter sigmoidal fit and the values are presented in Table 6.1.

Table 6.1. Cytotoxicity of PAMAM-G5 on A549 cell line.

PAMAM-G5 [Concentration Range used(μM)]	Time(h)	EC_{50}(μM) (Standard Deviation)
Alamar Blue Assay [5-0.3]	24	1.04 (±0.04)
	48	0.97 (±0.05)
	72	0.92 (±0.04)
MTT Assay [5-0.3]	24	0.97 (0.05)
	48	0.84 (0.05)
	72	0.77 (0.03)

As seen in Figure 6.1, for all time points, MTT is seen to be more sensitive than AB, consistent with the observations of Mukherjee (Mukherjee & Byrne 2013) and Maher (Maher & Byrne 2016), which can be explained by the mechanism of interaction of PAMAM dendrimers. After PAMAM dendrimers taken up into the cells by endocytosis, they are found to cause endosomal/lysosomal rupture due to the surface amino-groups which provide a high positive charge on the surface (Maher & Byrne

2016; Malik *et al.* 2000; Mukherjee, Davoren, & Byrne 2010; Roberts, Bhalgat, & Zera 1996). The endosomal rupture leads the release of the dendrimers into the cytosol and subsequent localisation in the mitochondria (Maher & Byrne 2016; Watson, Jones, & Stephens 2005). The mechanism results in an early stage (~4hrs) and late stage (>12hrs) increase in intracellular reactive oxygen species.(Mukherjee *et al.* 2010) Although the EC_{50} values determined are similar for AB and MTT, the different trend for the MTT response after 24 h is consistent with the interaction of the PAMAM dendrimers with the mitochondria of the cells (Maher & Byrne 2016; Mukherjee & Byrne 2013; Mukherjee, Davoren, & Byrne 2010; Mukherjee *et al.* 2010).

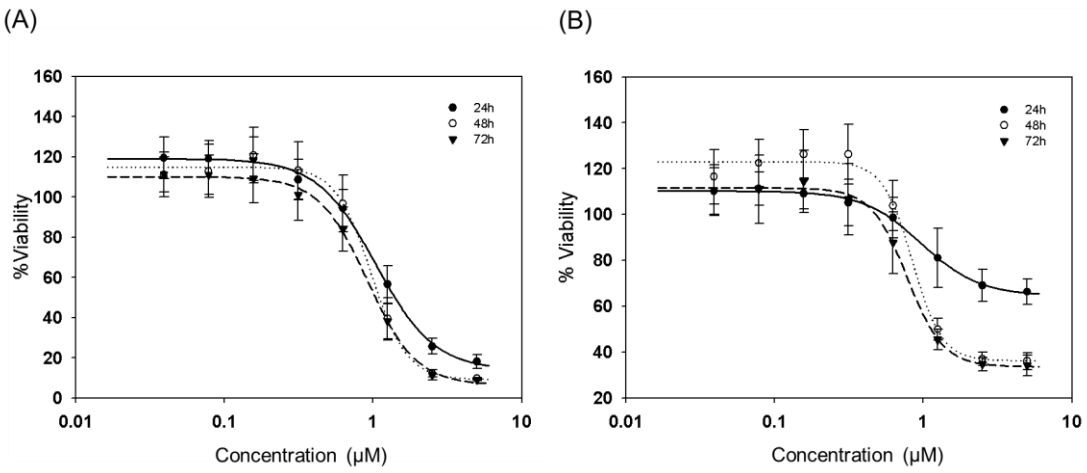

Figure 6.1. Cytotoxicity of generation 5 polyamidoamine (PAMAM-G5) dendrimers after 24, 48 and 72 h exposures determined by the Alamar Blue (A) and MTT assays (B). Data are expressed as % of control mean ± SD of three independent experiments.

In order to monitor these trends with Raman microspectroscopy and to identify spectral markers of cyto- and geno- toxicity upon PAMAM-G5 exposure, 20 point spectra were

acquired from the cytoplasm, nucleus and nucleolus of PAMAM-G5 exposed cells and their corresponding controls.

6.4.2. Raman Spectral Markers of Cytotoxicity: Cytoplasm

The effect of different concentrations of PAMAM-G5 dendrimers on the cytoplasm of A549 cells was evaluated by using a concentration range from EC_{10} to EC_{75}. EC_n values are calculated as 1.72 (±0.08), 1.04 (±0.04), 0.6 (±0.03) and 0.38 (±0.02) μM for EC_{75}, EC_{50}, EC_{25} and EC_{10}, respectively from the responses determined by the AB assay obtained after 24 h exposure and are used to determine dose dependant changes on the spectral markers of cellular responses after 24 h. With increasing dose, significant and progressive changes are observed in the bands corresponding to nucleic acid, protein and lipid structures inside the cytoplasm. Using PCA, for all applied doses, PAMAM-G5 exposed cells clearly separated from their controls according to PC1 (Explained Variance ~69%-82%, Supplementary Figure 6.S4) and PAMAM exposed cells scored positively, whereas control cells scored negatively. Therefore, the positive (PC1>0) features of the loadings represent the biochemical composition of the particle exposed cells, whereas negative (PC<0) features represent the control cells. The changes in the biochemical features of the loadings as a function of time and/or dose can be attributed to increases or decreases in composition of specific component of the cell in particle exposed cells compared to the control cells. As seen in Figure 6.2, the most significant changes in the loadings, corresponding to cytoplasm of PAMAM-G5 exposed cells and their controls, are observed up to the EC_{50} and notably, similar loadings are obtained from the cells which are exposed to EC_{50} and EC_{75} concentrations, which can be explained by a reduction in the toxic response rate

due to saturation of the cell cytoplasm by the nanoparticles. For sub-lethal concentrations (EC_{10} and EC_{25}), the positive side of the loading is dominated by nucleic acid features at 785 (nucleic acids) and 810 (RNA) cm^{-1} (Movasaghi, Rehman, & Rehman 2007; Notingher & Hench 2006; Notingher *et al.* 2003) which have been previously identified as indicators of oxidative stress, resulting in accumulation of the noncoding RNAs or changes on the cytoplasmic RNA (Efeoglu, Casey, & Byrne 2016; Efeoglu *et al.* 2017). When the exposure dose is increased to EC_{50} and EC_{75}, the relative intensity of the band at 785 cm^{-1} is observed to decrease, while the band at 810 cm^{-1} remains almost the same over the dose range, with a slight increase from EC_{10} to EC_{25}. Similar to the band at 785 cm^{-1}, a progressive decrease of the intensity of the nucleic acid bands at 669 cm^{-1} (T and G (DNA/RNA) and 1098 cm^{-1} (Phosphodioxy (PO_2^-) groups) is observed with increasing PAMAM-G5 concentration (Movasaghi, Rehman, & Rehman 2007; Notingher *et al.* 2003).

Although the Amide I region (1600-1700 cm^{-1}) (Movasaghi, Rehman, & Rehman 2007; Notingher & Hench 2006; Notingher *et al.* 2003) does not show a significant change with increasing dose over the range studied, an increase in protein composition of the exposed cells is observed compared to the control cells. The protein bands at 1003 (Phenlyalanine, Phe), 1556 (Tryptophan, Trp) and 1573 (Trp) cm^{-1} are also observed in the positive features of the loadings (Movasaghi, Rehman, & Rehman 2007; Notingher & Hench 2006; Notingher *et al.* 2003). Significant changes are also observed for the bands related to lipid composition of the cell. In the positive features of the loadings, the intensity of the band at 1125 cm^{-1} (skeletal of acyl backbone in lipid) (Movasaghi, Rehman, & Rehman 2007) has reduced significantly when the exposure dose reached EC_{50}. In the negative features of the loadings, lipid based

structures are observed to be dominant, which indicates the loss of lipid in PAMAM exposed cells. A progressive increase is also observed in the intensity of the band at 702 cm^{-1} in the negative features of the loading, which indicates a decrease in cholesterol in PAMAM exposed cells with increasing concentration (Movasaghi, Rehman, & Rehman 2007). Cholesterol is known to be an abundant sterol, especially in the cellular membrane of mammalian cells and is required for viability and cell proliferation. Damage to the cholesterol in the cytoplasm can be attributed to damage to the membrane composition due to the highly positive surface charge. PAMAM dendrimers, as cationic nanoparticles, have been shown to reduce membrane integrity via formation of holes in lipid bilayers which results in membrane erosion (Hong *et al.* 2004; Leroueil *et al.* 2007). Moreover, the band at 715 cm^{-1} (membrane phospholipid head) as well as other lipid features at 1299 and 1438 cm^{-1}, are observed to contribute negatively, also consistent with damage to membrane structures for particle exposed cells (Movasaghi, Rehman, & Rehman 2007; Notingher & Hench 2006; Notingher *et al.* 2003).

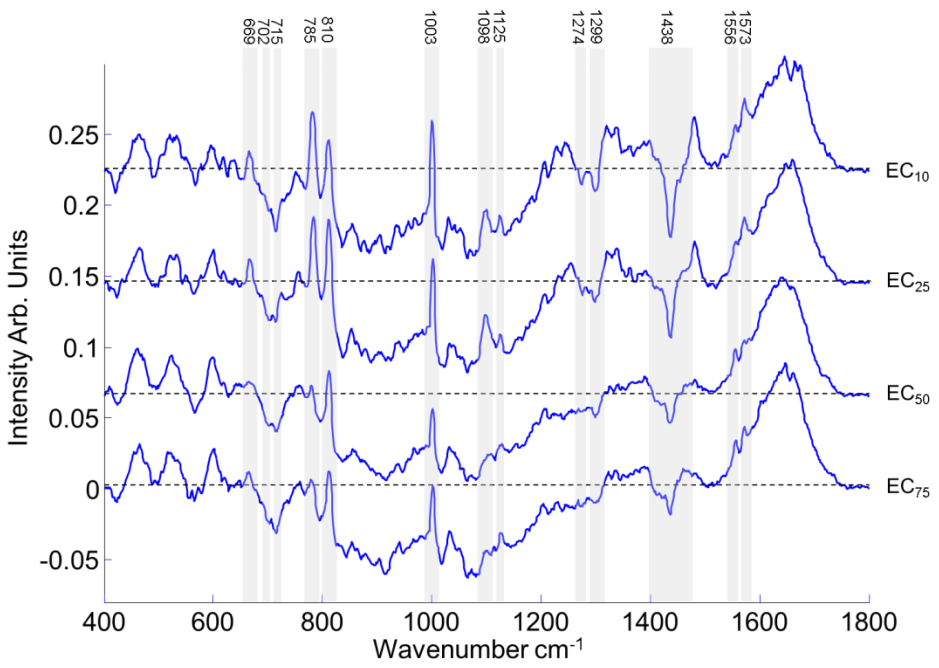

Figure 6.2. Loadings of PC1 for pairwise analysis of cytoplasm of exposed cells (EC_n) and corresponding control after 24 h PAMAM-G5 exposure. The negative side of the loading represents the spectral features of control, whereas positive side represents the cells exposed to PAMAM-G5. Loadings are offset for clarity and zero '0' line for each dose is indicated with black dashes. The progressive changes in the loadings are indicated with grey highlights and corresponding band assignments are provided on top of the highlights.

The changes in the spectral markers associated with toxic events in the cytoplasm were also evaluated as a function of exposure time. The sub-lethal dose (EC_{25}, determined by AB assay after 24 h) of PAMAM-G5 was used to observe progressive changes from 4 to 72 h. The calculated EC_{25} values are found to be similar for each time point from 24-72 h, and therefore, the EC_{25} for 24 h is used for time dependant evaluation of spectral markers.

The scatter plots of the PCA of the cytoplasm of particle exposed cells and corresponding controls are provided in Supplementary Figure 6.S5. The control cells

clearly differentiated from PAMAM-G5 exposed cells according to PC1, with an explained variance ranging from 76%-91%. For 4 h exposure, the loading of PC1 dominated by positive features which show the higher presence of cytoplasmic RNAs, proteins and lipids in PAMAM-G5 exposed cells compared to the control cells (Figure 6.3). The doublet of peaks at 785 and 810 cm^{-1} is again observed to be one of the prominent evolving features in the loadings. A continuous increase is observed in the intensity of the band at 785 cm^{-1} with extended exposure time. An increase is observed in the intensity of the band at 810 cm^{-1} up to 24 h, followed by a decrease after 48 h. The band becomes a negative feature of the loading after 72 h, which can be attributed to a loss of long-noncoding RNAs and secondary changes to the cytoplasmic RNA in the cytoplasm of PAMAM-G5 exposed cells with extended exposure times. The decrease of the band at 600 cm^{-1} (nucleotide conformation) (Movasaghi, Rehman, & Rehman 2007) can also be used as an indicator of RNA damage after 48 h. The next most prominent change after the bands at 785 and 810 cm^{-1} is observed in the band at 1438 cm^{-1}. The band at 1438 cm^{-1}, which can be attributed to CH_2 and CH_3 deformation vibrations of lipids (Movasaghi, Rehman, & Rehman 2007), indicates the total lipid saturation and damage in lipid structures, observed as a negative feature of loading 1 of PCA after 4 h. The other lipid bands in the fingerprint region of the spectra, 702 (cholesterol) and 715 (membrane phospholipids head) cm^{-1}, are also observed as negative features of the loadings for exposure times over 8 h and a progressive increase in the intensity of the bands is observed with extended exposure time. The increase in the intensity of these negative features of the loading can be attributed to higher membrane stability of the control cells compared to PAMAM exposed cells. The different progression of the band at 1438 cm^{-1} (lipid) between different doses (a decrease on the intensity with increasing dose) and exposure times (an increase on the

intensity with extended exposure time), can be attributed to different lipotoxic effects of PAMAM-G5 dendrimers in acute versus long term exposures. The bands at 1274 and 1299 cm^{-1} are observed as negative features of the loading for all exposure times, with increasing intensities, and can be attributed to distortion in Amide II structures of the proteins and also damage in lipids in PAMAM-G5 exposed cells.

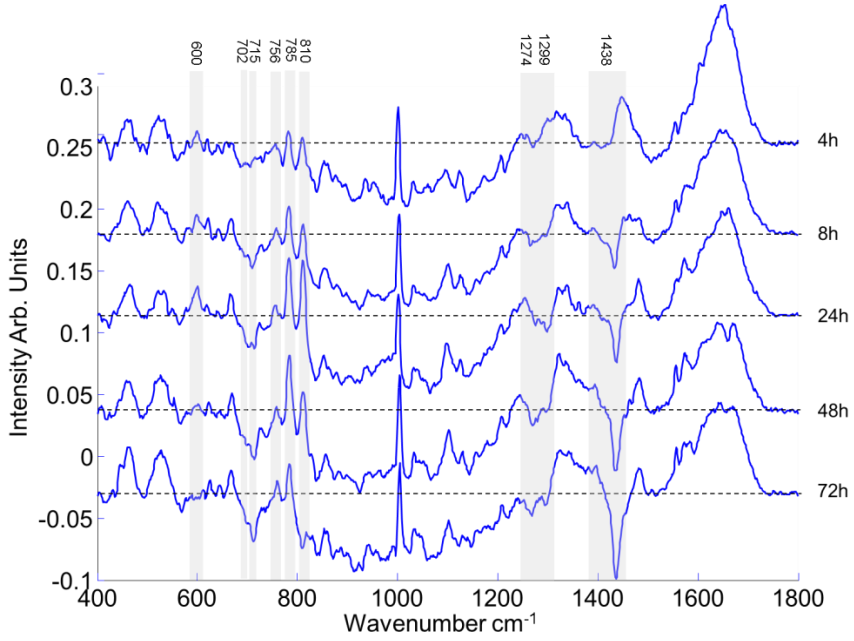

Figure 6.3. Loadings of PC1 for pairwise analysis of cytoplasm of exposed cells and corresponding control from 4 to 72 h PAMAM-G5 (EC_{25}) exposure. The negative side of the loading represents the spectral features of control, whereas positive side represents the cells exposed to PAMAM-G5. Loadings are offset for clarity and the zero '0' line for each dose is indicated with black dashes. The progressive changes in the loadings are indicated with grey highlights and corresponding band assignments are provided on top of the highlights.

The doublet peak at 785 and 810 cm^{-1} has previously been identified as a spectral marker of oxidative stress in aminated polystyrene ($PS\text{-}NH_2$) exposed cells, resulting

in cytoplasmic RNA alterations and damage in the cytoplasm (Efeoglu, Casey, & Byrne 2016; Efeoglu *et al.* 2017). The consistency of the doublet peak following PAMAM exposure provides a validation of the Raman spectral markers for cellular toxic events such as ROS formation. Notably, however, the final localisation of PS-NH_2 has been observed to be in the Endoplasmic Reticulum or Golgi apparatus (Efeoglu *et al.* 2015), and no significant spectral changes were observed in the nuclear regions of the exposed cells (Efeoglu, Casey, & Byrne 2016).

6.4.3. Raman Spectral Markers of Geno-Toxicity: Nucleus and Nucleolus

Although the effect of the PAMAM dendrimers on the genetic material of mammalian cells has been studied, the mechanism leading to the effect still remains unknown due to the size and non-flourescent nature of the PAMAM dendrimers. The use of the labels with PAMAM dendrimers can also change the structure related cell response due to oversize of the used labels compared to the original size of the PAMAM dendrimers. PAMAM dendrimers have been shown to induce DNA damage by using the Comet assay in a study of Naha (Naha & Byrne 2013), although the mechanism leading to the damage remained unclear. The effect of the oxidative stress and formation of reactive oxygen species have been shown to induce DNA damage in various ways, such as 8-hydroxy-2'-deoxyguanosine (8-OHdG) formation, single or double strand DNA breaks, chromatid exchanges and mutations (Henkler, Brinkmann, & Luch 2010; Naha & Byrne 2013; Zhang *et al.* 2009).

Raman microspectroscopy can provide insights into the genetic material-PAMAM interaction by exploring changes of the spectral signatures of the genetic material (DNA, RNA). The changes in the nucleus and nucleolus upon PAMAM exposure were

monitored and spectral markers of the genotoxic events identified. With increasing exposure times, the nucleus of A549 cells exposed to PAMAM-G5 clearly differentiated from their controls according to PC1, with explained variance of 77%-91% (Supplementary Figure 6.S6). The loadings of the PC, for all exposure times, are dominated by features which indicate the presence of biomolecular alterations in particle exposed cells compared to their controls (Figure 6.4). The main changes in the loadings from 4 to 72 h are observed to be in the range between 700-830 cm^{-1} (nucleic acid region) and the band at 1556 cm^{-1} (Tryptophan, Trp).

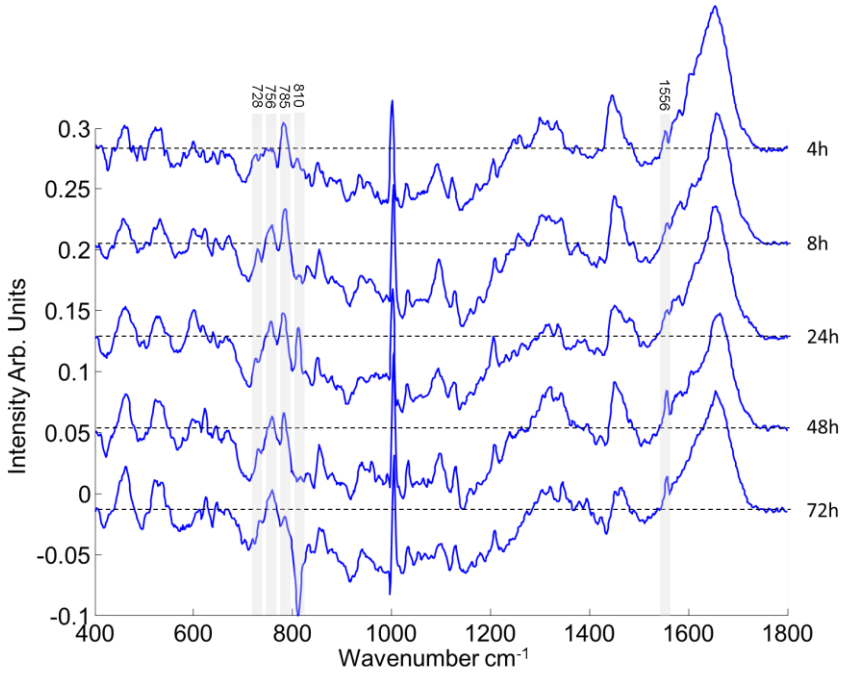

Figure 6.4. Loadings of PC1 for pairwise analysis of nucleus of exposed cells and corresponding control from 4 to 72 h PAMAM-G5 (EC_{25}) exposure. The negative side of the loading represents the spectral features of control, whereas positive side represents the cells exposed to PAMAM-G5. Loadings are offset for clarity and the zero '0' line for each dose is indicated with black dashes. The progressive changes in the loadings are indicated with grey highlights and corresponding band assignments are provided on top of the highlights.

As a function of exposure time, there are slight changes observed in the intensity of the band at 785 cm^{-1} (DNA/RNA), whereas the changes are more pronounced for the intensity of the band at 810 cm^{-1} (RNA) (Supplementary Figure 6.S7 for plotted band intensities). The band at 785 cm^{-1} is known to be a spectral marker for uracil (U), thymine (T), cytosine (C) ring breathing modes in DNA and RNA, whereas the 810 cm^{-1} is more specific to RNA O-P-O band stretching (Movasaghi, Rehman, & Rehman 2007). Therefore, the slight changes in the intensity of the bands at 785 cm^{-1} can be indicative of changes in local conformation, rather than to chemical changes to the

nucleobases in the nucleic acids. However, the intensity of the band at 810 cm^{-1} showed a significant increase between 8 and 24 h, followed by a decrease until 72 h and the band becomes a negative feature of the loading, which shows higher RNA content in nucleus of control cells compared to PAMAM exposed cells. The increase up to 24 h can be attributed to the effect of oxidative stress on RNA content in the nuclear region, whereas reduction after 24 h and damage of the RNA in the nuclear region can be related to genotoxicity of the PAMAM dendrimers.

The other characteristic bands in the loadings of the nucleus corresponding to the PAMAM-G5 exposed cells and their controls are observed to be the bands at 728 (Adenine, DNA) and 756 (Trp and/or DNA, C5-H (cytosine)) cm^{-1}. With extended exposure time, the intensities of the bands are observed to increase, with a more significant increase at 756 cm^{-1} compared to 728 cm^{-1} Figure 6.5A). When different doses of the PAMAM-G5 are exposed to the A549 cells, the band at 728 cm^{-1} does not show a significant change, whereas the band at 756 cm^{-1} is significantly changed for the doses over EC_{25} concentration (Figure 6.5B). The increase in the band at 756 cm^{-1} along with the changes in the 830 cm^{-1} band (PO_2^- stretch of nucleic acids) can be attributed to significant changes in DNA over the extended exposure times (Figure 6.4). Similarly, when the exposure dose is changed between EC_{25} and EC_{50}, the band at 830 cm^{-1} disappears (Figure 6.5C). The band at 1220 cm^{-1} also shows the changes in the phosphate backbone (PO_2^-). In this case, the interaction of PAMAM dendrimers with nuclear material can be related to DNA modifications and cell death.

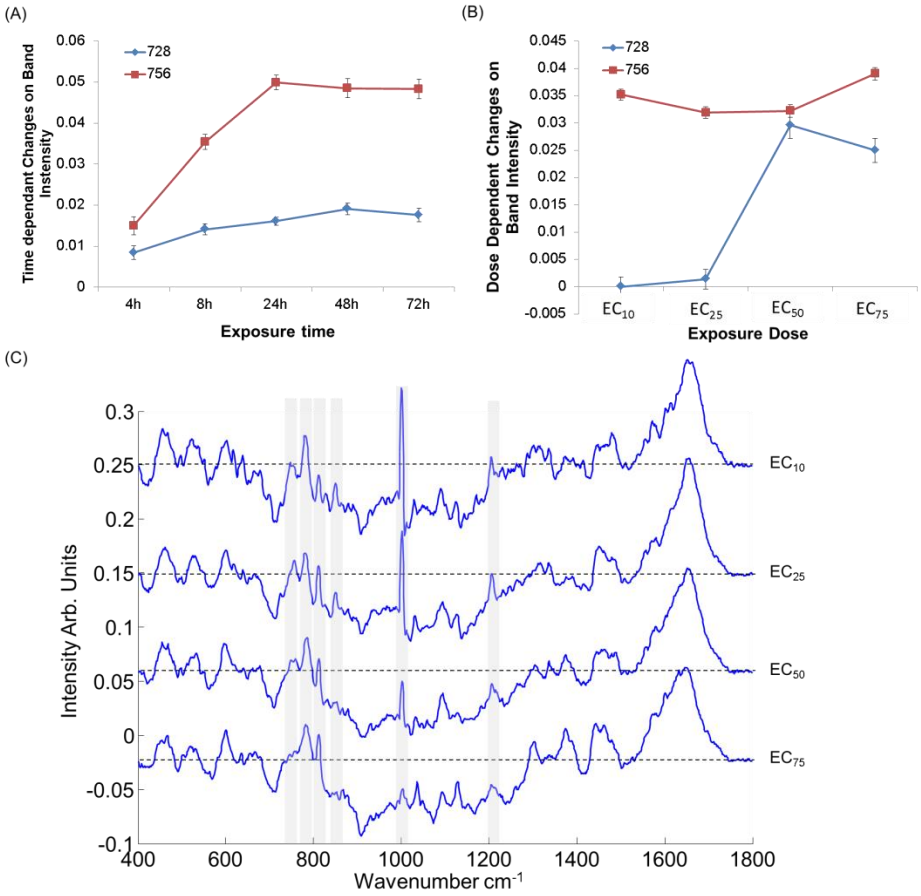

Figure 6.5. A) Comparison of time dependant changes on the band intensities of 728 and 756 cm^{-1} bands calculated from pairwise PCA of nucleus of exposed cells and corresponding control, B) Comparison of dose dependant changes on the band intensities of 728 and 756 cm^{-1} bands calculated from pairwise PCA of nucleus of PAMAM exposed cells and corresponding control, in A and B error bars indicate ± SD of the band intensities, C) Loadings of PC1 for pairwise analysis of nucleus of exposed cells and corresponding control after 24h PAMAM-G5 exposure. The negative side of the loading represents the spectral features of control, whereas positive side represents the cells exposed to PAMAM-G5. Loadings are offset for clarity and zero '0' line is indicated with black dashes. The progressive changes in the loadings are indicated with grey highlights and corresponding band assignments are provided on top of the highlights.

When the intensities of the 785 and 810 cm^{-1} bands are calculated, they are observed to increase with increasing exposure dose and the changes between EC_{10}-EC_{25} and EC_{50}-EC_{75} concentrations are observed to be more pronounced compared to EC_{25}-EC_{50} differences (Supplementary Figure 6.S8). Although it is extremely challenging to determine localisation of PAMAM dendrimer in the nucleus due to the non-fluorescent nature of the dendrimers, and significant increase in the particle size and physicochemical properties upon fluorescent labelling, Raman microspectroscopy can be used to identify PAMAM-G5 presence in the nucleus and nucleolus. PAMAM-G5 dendrimers can pass the nuclear membrane and interact with nuclear material due to their highly positive surface and small size (measured diameter of G5 is 5.4 nm, size in medium ~6.5 nm) (Brunner *et al.* 2000). When the changes in the band at 810 cm^{-1} over time and dose for the nuclear region (nucleus and nucleolus) are considered, the interaction of the PAMAM-G5 with nuclear material can be seen as more a pronounced PAMAM-RNA interaction compared to PAMAM-DNA interaction. When the first loading of the PCA is considered for the cells exposed to the different doses of the PAMAM-G5 dendrimers, the spectra of cytoplasm and nucleus do not show a significant change until the concentration is increased to the EC_{50}. A significant change is observed for the loading of the cell exposed to EC_{75} of PAMAM dendrimers versus corresponding controls, and the features of the loading become completely different compared to previous doses (Figure 6.6A). Atomic simulations of dendrimer-nucleic acid interactions have been conducted by Nandy *et al.* and the study showed the formation of stable DNA and siRNA complexes with PAMAM dendrimers at a physiological pH based on electrostatic interaction (Nandy, Santosh, & Maiti 2012). The strong binding affinity of PAMAM dendrimers to the RNA has also been shown in computational and experimental designs by Pavan *et al.* (Pavan *et al.* 2010). The

dose and time dependent changes on the nucleolus of the A549 cells upon PAMAM-G5 exposure are also evaluated in order to clarify mechanism of action of PAMAM-G5 dendrimers with RNA. The scatter plots of PCA of nucleolus of PAMAM-G5 exposed A549 cells and corresponding controls are provided in Supplementary Figure 6.S9 and S10 for dose dependent and time dependent responses, respectively. For both cases, PAMAM-G5 exposed cells and corresponding controls are clearly separated from each other with calculated high explained variance at different time points (Explained variance ~70%-90%) compared to different doses (Explained variance ~40%-78%). As seen in Figure 6A and B, the most dominant features of the loadings with significant changes as a function of both time and dose are determined to be the bands at 728, 756, 785, 810 and 830 cm^{-1}. When the exposure dose is increased from EC_{25} to EC_{75}, the intensity of the bands at 785, 810 and 830 cm^{-1} are decreased, whereas an increase is observed for the bands at 728 and 756 cm^{-1} and loadings are dominated by the features in the positive side which corresponds to PAMAM-G5 exposed cells. When the exposure dose reached EC_{75}, significant changes are observed in the loadings. In addition to the changes in the bands at 728, 756, 810 and 830 cm^{-1}, changes in the bands at 1033 (C-H in plane Phe), 1095 (PO_2^- str.), 1128 (C-N str. of proteins), 1209 (C-C_6H_5 str. Phe, Trp), 1301 (CH_2 twist of lipids), 1369 (Guanine), 1438 (lipids), 1460 (N_2-H (cytosine), C_4-C_5 (cytosine)), 1600 (Amide I) and 1654 (Amide I) cm^{-1} (Movasaghi, Rehman, & Rehman 2007; Notingher & Hench 2006; Notingher *et al.* 2003), observed as positive features of the loading, are consistent with dramatic changes in protein and nucleic acid content of the nucleus. Recent studies have shown the effect of the nanomaterials on epigenetic modifications such as DNA methylation, post-translasional modifications and formation of non-coding RNAs (Gong *et al.* 2010; Pirela *et al.* 2016; Sierra *et al.* 2016). The changes in the DNA and

protein bands can be attributed to modifications in DNA such as chemical modifications on the C5 position of cytosines (Sierra *et al.* 2016).

The study demonstrates that Raman microspectroscopy can be employed to monitor signatures of the toxic responses of cells to nanoparticle exposures. Although the spectroscopic signatures of the initiating events can consistently be identified, the subsequent evolution of the toxic response is a complex cascade of events,[24] and this, coupled with the limited number of dose and time points, mean that more sophisticated by linear data-mining approaches to data analysis, such as Partial Least Squares Regression are not suitable. However, emerging, more rapid spectroscopic screening technologies will afford more continuous and even real-time monitoring of such toxicological response pathways, which ultimately may be analysed using more sophisticated data mining techniques such as Multivariate Curve Resolution Alternating Least Squares.

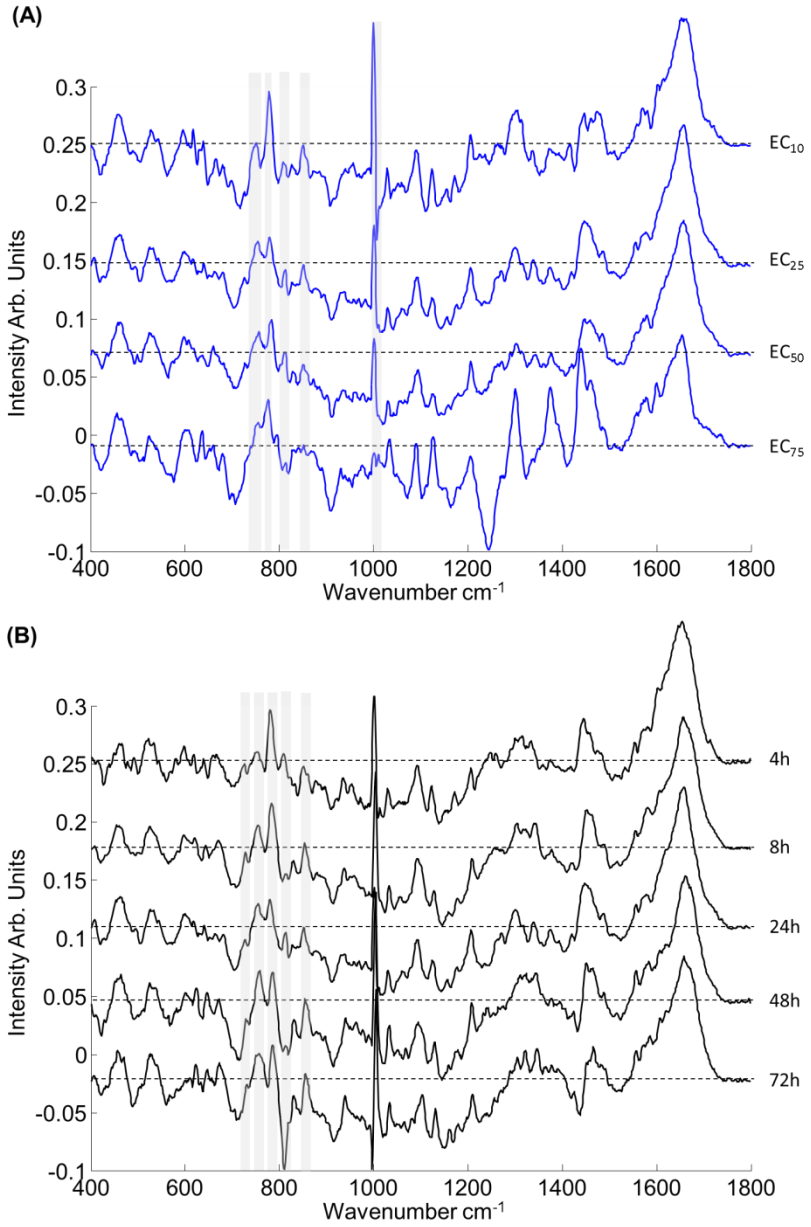

Figure 6.6. **A)** Loadings of PC1 for pairwise analysis of nucleolus of exposed cells and corresponding control after 24h PAMAM-G5 exposure. B) Loadings of PC1 for pairwise analysis of cytoplasm of exposed cells and corresponding control from 4 to 72 h PAMAM-G5 exposure. The negative side of the loading represents the spectral features of control, whereas positive side represents the cells exposed to PAMAM-G5. Loadings are offset for clarity and zero '0' line is indicated with black dashes. The progressive changes in the loadings are indicated with grey highlights and corresponding band assignments are provided on top of the highlights.

6.5. Conclusion

The analysis of a broad range of nanomaterials, in a rapid and multi-parametric fashion, is of significant importance, to identify mechanism of action and possible adverse health and environmental effects. In this study, the potential of Raman microspectroscopy has been shown to identify cyto- and geno- toxic responses in cell upon a toxicant exposure. In PAMAM-G5 exposed cells, ROS formation and oxidative stress has been established as the principal toxic mechanism and is associated a significant impact on mitochondria. The increased levels of the ROS are monitored by evolution of the Raman bands at 785 and 810 cm^{-1}. The secondary impact of PAMAM-G5 dendrimers inside the cell is observed as a lipotoxic effect, which is identified by the spectral marker at 1438 cm^{-1}. When the spectral markers of the cytotoxicity of PAMAM-G5 and PS-NH_2 exposed cells, from a previous study, are considered, a high degree of consistency of the Raman spectral markers is observed. The differences between the spectral markers, especially those in the region above 1000 cm^{-1}, for PAMAM-G5 and PS-NH_2 exposed cells can be attributed to different cell death mechanisms which can be investigated further. The study further shows the applicability of Raman microspectroscopy to determine spectral markers of the genotoxicity and possible PAMAM-DNA/RNA interactions based on the changes of nucleic acid bands in the range from 750 to 830 cm^{-1}. The PAMAM-RNA interaction is observed to be more pronounced compared to the DNA interaction, which can be an indicator of localisation of the PAMAM in the nucleolus. The spectral markers of the post-translational modifications and corresponding biochemical changes are identified, and can be used to characterise biochemical consequences of biomolecular modifications such as changes in Trp and cytosine C5-H.

6.6. References

Bonnier, F, Mehmood, A, Knief, P, Meade, A D, Hornebeck, W, Lambkin, H, Flynn, K, McDonagh, V, Healy, C, Lee, T C, Lyng, F M and Byrne, H J (2011) *In vitro* Analysis of Immersed Human Tissues by Raman Microspectroscopy. *Journal of Raman Spectroscopy*, 42(5), 888-96.

Bonnier, F, Petitjean, F, Baker, M J and Byrne, H J (2014) Improved Protocols for Vibrational Spectroscopic Analysis of Body Fluids. *Journal of Biophotonics,* 7(3-4), 167-79.

Bourne, M W, Margerun, L, Hylton, N, Campion, B, Lai, J-J, Derugin, N and Higgins, C B (1996) Evaluation of the Effects of Intravascular Mr Contrast Media (Gadolinium Dendrimer) on 3d Time of Flight Magnetic Resonance Angiography of the Body. *Journal of Magnetic Resonance Imaging,* 6(2), 305-10.

Breve, G J P a J (1996). Whole Cell Studies and Tissue Characterization by Raman Spectroscopy In *"Biomedical Applications of Spectroscopy"* Vol. 25, John Wiley and Sons, New York.

Brigger, I, Dubernet, C and Couvreur, P (2012) Nanoparticles in Cancer Therapy and Diagnosis. *Advanced Drug Delivery Reviews,* 64, Supplement, 24-36.

Brunner, S, Sauer, T, Carotta, S, Cotten, M, Saltik, M and Wagner, E (2000) Cell Cycle Dependence of Gene Transfer by Lipoplex, Polyplex and Recombinant Adenovirus. *Gene Ther,* 7(5), 401-7.

Dendritech, I (2017) Available: http://www.dendritech.com/pamam.html (Accessed: June 2017)

Donaldson, K, Stone, V, Tran, C L, Kreyling, W and Borm, P J (2004). Nanotoxicology In *Occup Environ Med* Vol. 61 England.

Dorney, J, Bonnier, F, Garcia, A, Casey, A, Chambers, G and Byrne, H J (2012) Identifying and Localizing Intracellular Nanoparticles Using Raman Spectroscopy. *Analyst,* 137(5), 1111-9.

Efeoglu, E, Casey, A and Byrne, H J (2016) *In vitro* Monitoring of Time and Dose Dependent Cytotoxicity of Aminated Nanoparticles Using Raman Spectroscopy. *Analyst,* 141(18), 5417-31.

Efeoglu, E, Keating, M, McIntyre, J, Casey, A and Byrne, H J (2015) Determination of Nanoparticle Localisation within Subcellular Organelles *in vitro* Using Raman Spectroscopy. *Analytical Methods,* 7(23), 10000-17.

Efeoglu, E., Maher, M. A., Casey, A., Byrne, H. J. (2017) Label-Free, High Content Screening Using Raman Microspectroscopy: The Toxicological Response of Different Cell Lines to Amine-Modified Polystyrene Nanoparticles (PS-NH_2), *Analyst*, DOI: 10.1039/C7AN00461C.

Godbey, W T, Wu, K K and Mikos, A G (1999) Tracking the Intracellular Path of Poly(Ethylenimine)/Dna Complexes for Gene Delivery. *Proceedings of the National Academy of Sciences of the United States of America,* 96(9), 5177-81.

Gong, C, Tao, G, Yang, L, Liu, J, Liu, Q and Zhuang, Z (2010) Sio(2) Nanoparticles Induce Global Genomic Hypomethylation in Hacat Cells. *Biochem Biophys Res Commun,* 397(3), 397-400.

Henkler, F, Brinkmann, J and Luch, A (2010) The Role of Oxidative Stress in Carcinogenesis Induced by Metals and Xenobiotics. *Cancers,* 2(2), 376-96.

Hong, S, Bielinska, A U, Mecke, A, Keszler, B, Beals, J L, Shi, X, Balogh, L, Orr, B G, Baker, J R, Jr. and Banaszak Holl, M M (2004) Interaction of Poly(Amidoamine) Dendrimers with Supported Lipid Bilayers and Cells: Hole Formation and the Relation to Transport. *Bioconjug Chem,* 15(4), 774-82.

Keating, M E, Bonnier, F and Byrne, H J (2012) Spectral Cross-Correlation as a Supervised Approach for the Analysis of Complex Raman Datasets: The Case of Nanoparticles in Biological Cells. *Analyst,* 137(24), 5792-802.

Leroueil, P R, Hong, S, Mecke, A, Baker, J R, Orr, B G and Banaszak Holl, M M (2007) Nanoparticle Interaction with Biological Membranes: Does Nanotechnology Present a Janus Face? *Accounts of Chemical Research,* 40(5), 335-42.

Liebel, U and Link, W (2007) Meeting Report: Trends and Challenges in High Content Analysis. *Biotechnol J,* 2(8), 938-40.

Maher, M A and Byrne, H J (2016) Modification of the *in vitro* Uptake Mechanism and Antioxidant Levels in Hacat Cells and Resultant Changes to Toxicity and Oxidative Stress of G4 and G6 Poly(Amidoamine) Dendrimer Nanoparticles. *Anal Bioanal Chem,* 408(19), 5295-307.

Maher, M A, Naha, P C, Mukherjee, S P and Byrne, H J (2014) Numerical Simulations of *in vitro* Nanoparticle Toxicity – the Case of Poly(Amido Amine) Dendrimers. *Toxicology in vitro,* 28(8), 1449-60.

Malik, N, Wiwattanapatapee, R, Klopsch, R, Lorenz, K, Frey, H, Weener, J W, Meijer, E W, Paulus, W and Duncan, R (2000) Dendrimers: Relationship between Structure and Biocompatibility *in vitro,* and Preliminary Studies on the Biodistribution of 125i-Labelled Polyamidoamine Dendrimers in Vivo. *J Control Release,* 65(1-2), 133-48.

Miljkovic, M, Chernenko, T, Romeo, M J, Bird, B, Matthaus, C and Diem, M (2010) Label-Free Imaging of Human Cells: Algorithms for Image Reconstruction of Raman Hyperspectral Datasets. *Analyst,* 135(8), 2002-13.

Movasaghi, Z, Rehman, S and Rehman, I U (2007) Raman Spectroscopy of Biological Tissues. *Applied Spectroscopy Reviews,* 42(5), 493-541.

Mukherjee, S P and Byrne, H J (2013) Polyamidoamine Dendrimer Nanoparticle Cytotoxicity, Oxidative Stress, Caspase Activation and Inflammatory Response: Experimental Observation and Numerical Simulation. *Nanomedicine,* 9(2), 202-11.

Mukherjee, S P, Davoren, M and Byrne, H J (2010) *In vitro* Mammalian Cytotoxicological Study of Pamam Dendrimers - Towards Quantitative Structure Activity Relationships. *Toxicol In vitro,* 24(1), 169-77.

Mukherjee, S P, Lyng, F M, Garcia, A, Davoren, M and Byrne, H J (2010) Mechanistic Studies of *in vitro* Cytotoxicity of Poly(Amidoamine) Dendrimers in Mammalian Cells. *Toxicol Appl Pharmacol,* 248(3), 259-68.

Naha, P C and Byrne, H J (2013) Generation of Intracellular Reactive Oxygen Species and Genotoxicity Effect to Exposure of Nanosized Polyamidoamine (Pamam) Dendrimers in Plhc-1 Cells *in vitro*. *Aquat Toxicol,* 132-133, 61-72.

Naha, P C, Davoren, M, Lyng, F M and Byrne, H J (2010) Reactive Oxygen Species (Ros) Induced Cytokine Production and Cytotoxicity of Pamam Dendrimers in J774a.1 Cells. *Toxicology and Applied Pharmacology,* 246(1–2), 91-9.

Nandy, B, Santosh, M and Maiti, P K (2012) Interaction of Nucleic Acids with Carbon Nanotubes and Dendrimers. *J Biosci,* 37(3), 457-74.

Notingher, I and Hench, L L (2006) Raman Microspectroscopy: A Noninvasive Tool for Studies of Individual Living Cells *in vitro*. *Expert Rev Med Devices*, 3(2), 215-34.

Notingher, I, Verrier, S, Haque, S, Polak, J M and Hench, L L (2003) Spectroscopic Study of Human Lung Epithelial Cells (A549) in Culture: Living Cells Versus Dead Cells. *Biopolymers*, 72(4), 230-40.

Oberdörster, G, Maynard, A, Donaldson, K, Castranova, V, Fitzpatrick, J, Ausman, K, Carter, J, Karn, B, Kreyling, W, Lai, D, Olin, S, Monteiro-Riviere, N, Warheit, D and Yang, H (2005) Principles for Characterizing the Potential Human Health Effects from Exposure to Nanomaterials: Elements of a Screening Strategy. *Particle and Fibre Toxicology*, 2(1), 8.

OECD. (2010). Oecd, Series on the Safety of Manufactured Nanomaterials (pp. 46).

Pavan, G M, Posocco, P, Tagliabue, A, Maly, M, Malek, A, Danani, A, Ragg, E, Catapano, C V and Pricl, S (2010) Pamam Dendrimers for Sirna Delivery: Computational and Experimental Insights. *Chemistry – A European Journal*, 16(26), 7781-95.

Pirela, S V, Miousse, I R, Lu, X, Castranova, V, Thomas, T, Qian, Y, Bello, D, Kobzik, L, Koturbash, I and Demokritou, P (2016) Effects of Laser Printer-Emitted Engineered Nanoparticles on Cytotoxicity, Chemokine Expression, Reactive Oxygen Species, Dna Methylation, and Dna Damage: A Comprehensive *in vitro* Analysis in Human Small Airway Epithelial Cells, Macrophages, and Lymphoblasts. *Environ Health Perspect*, 124(2), 210-9.

Roberts, J C, Bhalgat, M K and Zera, R T (1996) Preliminary Biological Evaluation of Polyamidoamine (Pamam) Starburst Dendrimers. *J Biomed Mater Res,* 30(1), 53-65.

Sierra, M I, Valdés, A, Fernández, A F, Torrecillas, R and Fraga, M F (2016) The Effect of Exposure to Nanoparticles and Nanomaterials on the Mammalian Epigenome. *International Journal of Nanomedicine,* 11, 6297-306.

Tosi, G, Bortot, B, Ruozi, B, Dolcetta, D, Vandelli, M A, Forni, F and Severini, G M (2013) Potential Use of Polymeric Nanoparticles for Drug Delivery across the Blood-Brain Barrier. *Curr Med Chem,* 20(17), 2212-25.

Twyman, L J, Beezer, A E, Esfand, R, Hardy, M J and Mitchell, J C (1999) The Synthesis of Water Soluble Dendrimers, and Their Application as Possible Drug Delivery Systems. *Tetrahedron Letters,* 40(9), 1743-6.

Walton, A G, Deveney, M J and Koenig, J L (1970) Raman Spectroscopy of Calcified Tissue. *Calcified Tissue Research,* 6(1), 162-7.

Watson, P, Jones, A T and Stephens, D J (2005) Intracellular Trafficking Pathways and Drug Delivery: Fluorescence Imaging of Living and Fixed Cells. *Adv Drug Deliv Rev,* 57(1), 43-61.

Zhang, R, Kang, K A, Piao, M J, Maeng, Y H, Lee, K H, Chang, W Y, You, H J, Kim, J S, Kang, S S and Hyun, J W (2009) Cellular Protection of Morin against the Oxidative Stress Induced by Hydrogen Peroxide. *Chem Biol Interact,* 177(1), 21-7.

Zhou, J, Wu, J, Hafdi, N, Behr, J P, Erbacher, P and Peng, L (2006) Pamam Dendrimers for Efficient Sirna Delivery and Potent Gene Silencing. *Chem Commun (Camb)*(22), 2362-4.

6S Supplementary Information:

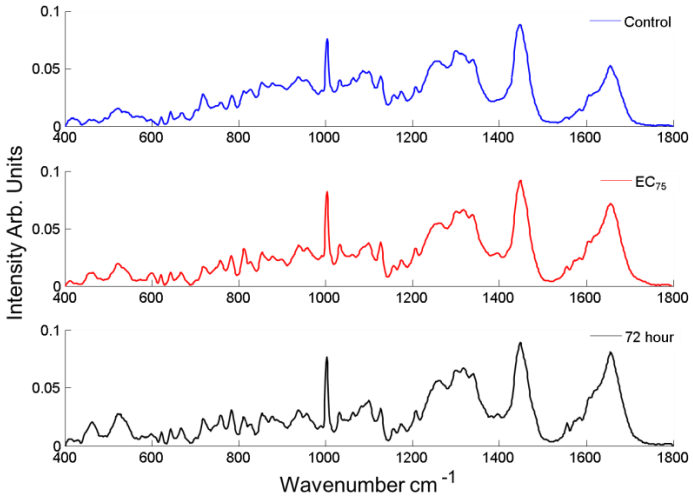

Figure 6.S1. Mean spectra of cytoplasm from control cells and exposed cells (PAMAM dendrimers) as a function of dose (24 hour exposure to EC_{75}) and time (72 hour exposure to EC_{25}).

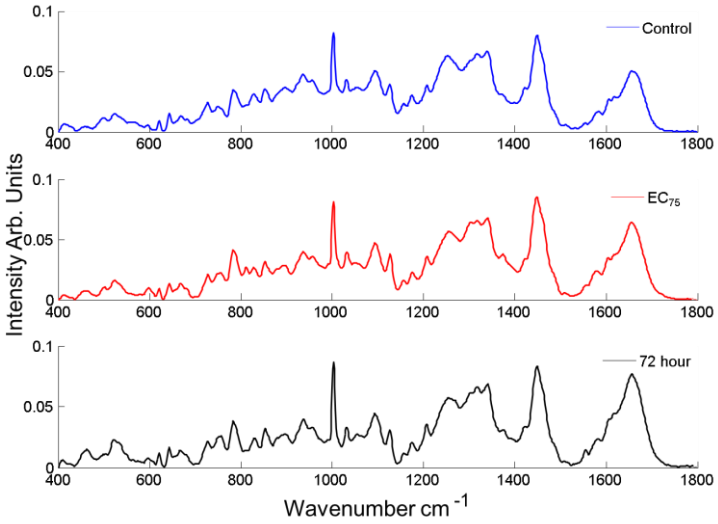

Figure 6.S2. Mean spectra of nucleus from control cells and exposed cells (PAMAM dendrimers) as a function of dose (24 hour exposure to EC_{75}) and time (72 hour exposure to EC_{25}).

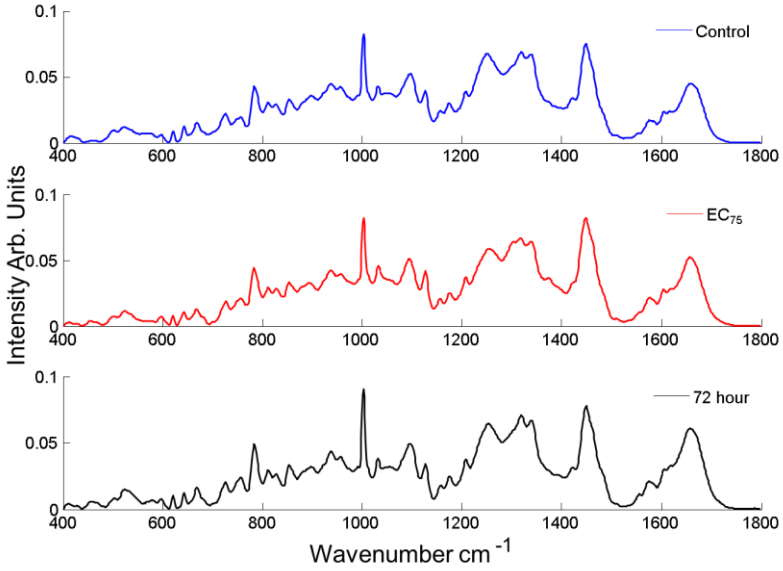

Figure 6.S3. Mean spectra of nucleolus from control cells and exposed cells (PAMAM dendrimers) as a function of dose (24 hour exposure to EC_{75}) and time (72 hour exposure to EC_{25}).

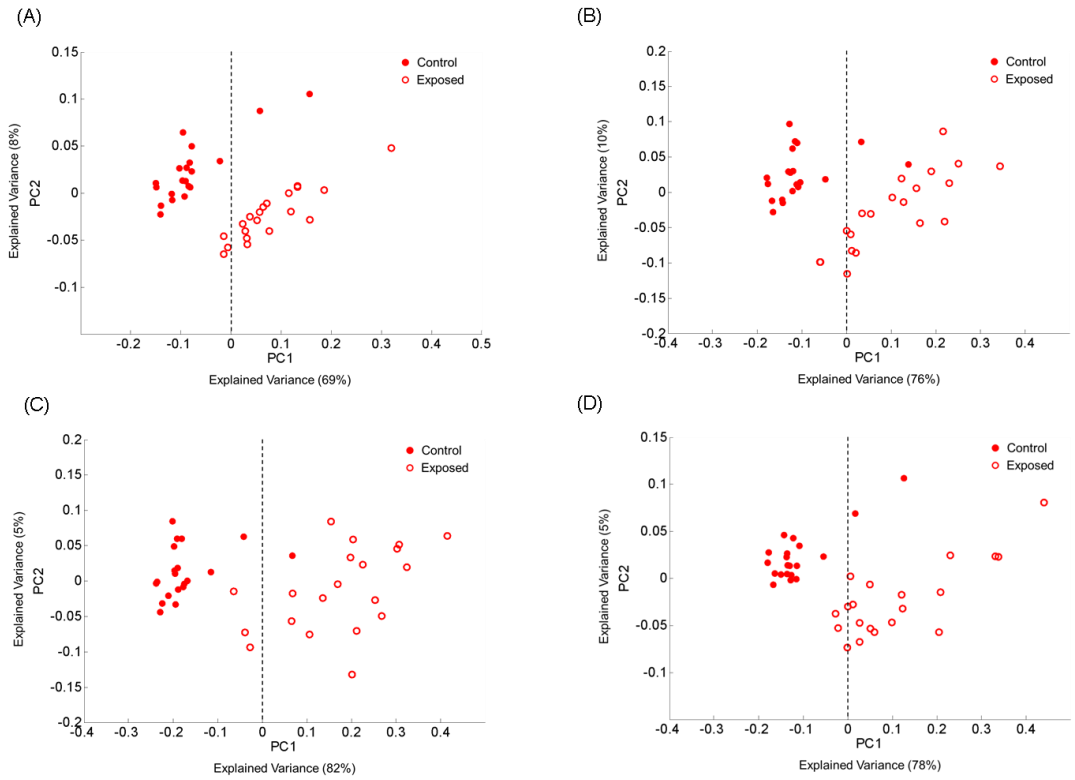

Figure 6.S4. Scatter plots of the PCA of spectra corresponding to cytoplasm of A549 cells (control) and A549 cells exposed to the EC_{10} (A), EC_{25} (B), EC_{50} (C) and EC_{75} (D) concentrations of PAMAM-G5 dendrimers after 24 h. Each graph indicates a pairwise comparison of exposed cells with corresponding control for 24 hour. Unexposed cells and exposed cells are indicated with closed circles and open circles, respectively. '0' line for PC1 is indicated by black dashed outlines.

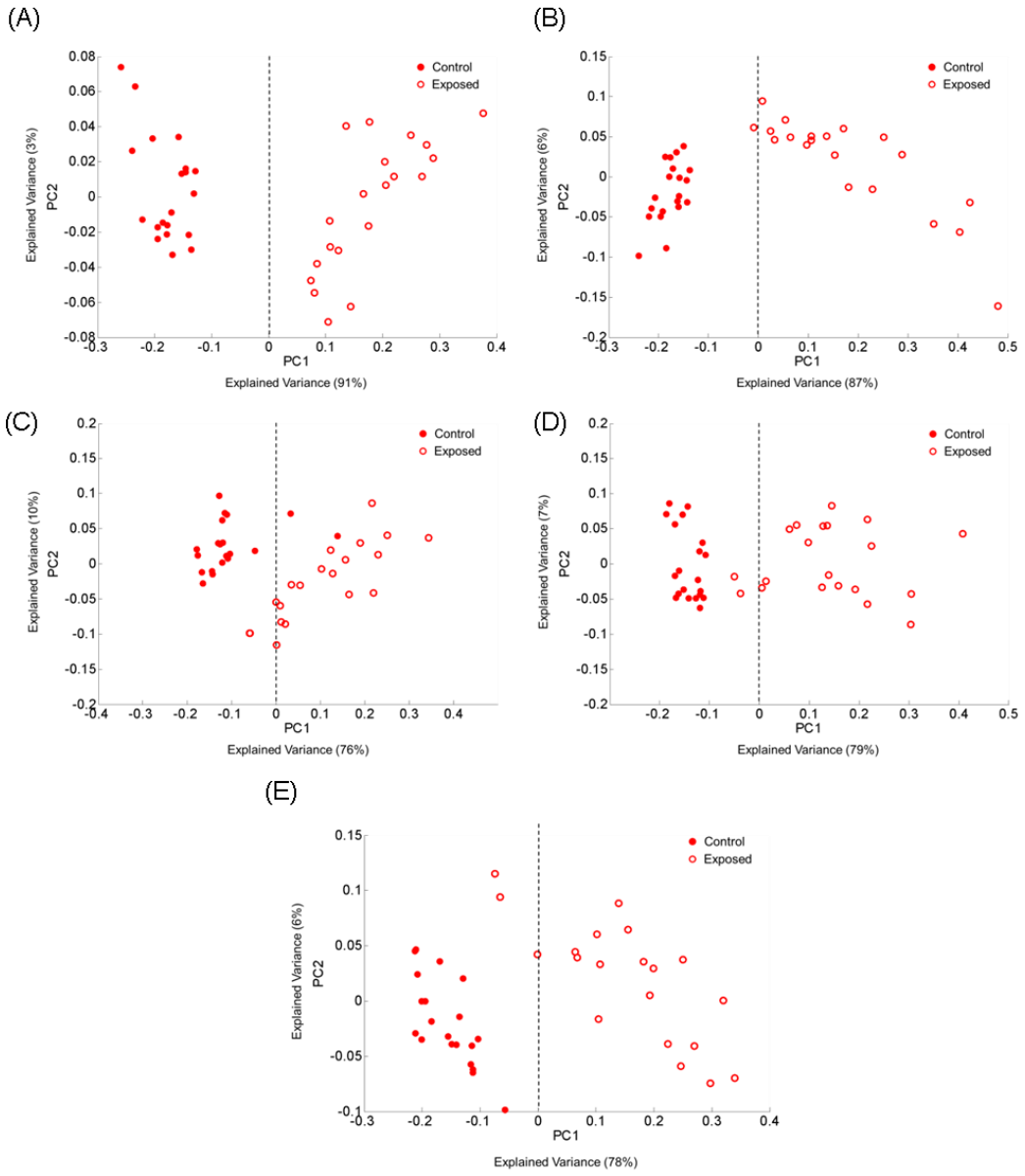

Figure 6.S5. Scatter plot of the PCA of spectra corresponding to cytoplasm of A549 cells (control) and A549 cells exposed to the EC_{25} concentration of PAMAM-G5 dendrimers after 4 (A), 8 (B), 24 (C), 48 (D) and 72 hour. Each graph indicates a pairwise comparison of exposed cells with corresponding control for extending exposure times. Unexposed cells and exposed cells are indicated with closed circles and open circles, respectively. '0' line for PC1 is indicated by black dashed outlines.

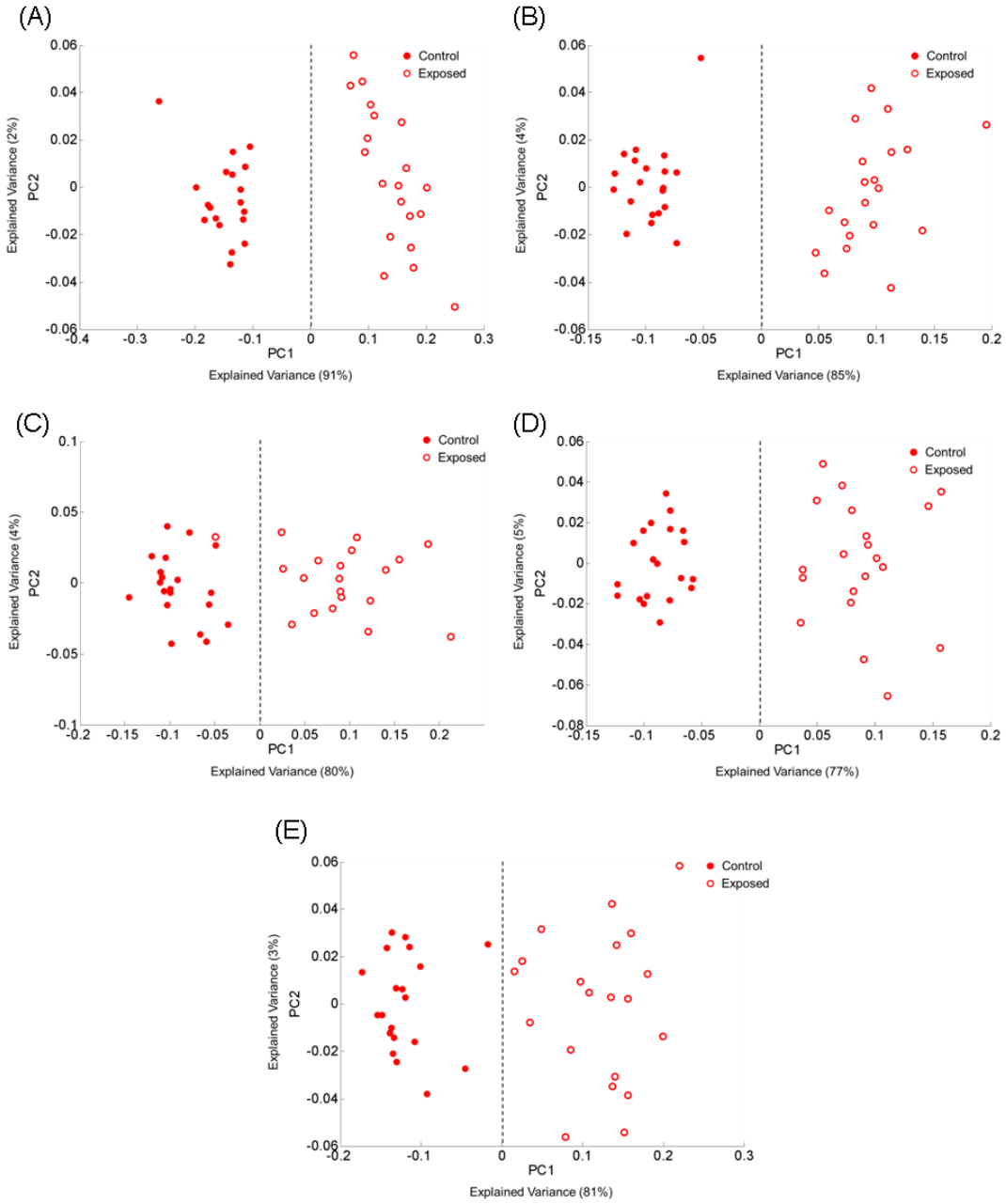

Figure 6.S6. Scatter plot of the PCA of spectra corresponding to nucleus of A549 cells (control) and A549 cells exposed to the EC_{25} concentration of PAMAM-G5 dendrimers after 4 (A), 8 (B), 24 (C), 48 (D) and 72 hour. Each graph indicates a pairwise comparison of exposed cells with corresponding control for extending exposure times. Unexposed cells and exposed cells are indicated with closed circles and open circles, respectively. '0' line for PC1 is indicated by black dashed outlines.

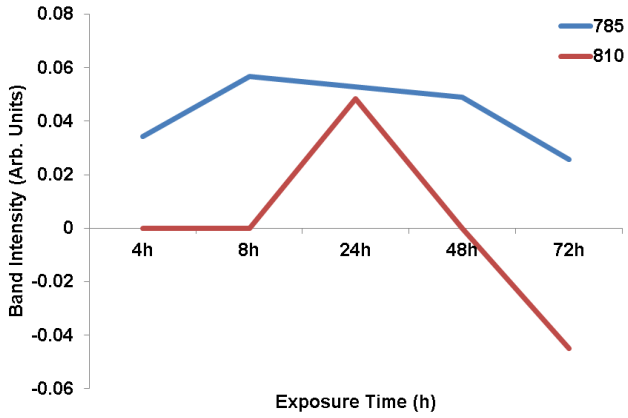

Figure 6.S7. Band intensities of 785 (nucleic acids) and 810 (RNA) cm^{-1} bands calculated from PC1 from pairwise PCA of nucleus of PAMAM-G5 exposed cells and corresponding controls from 4 to 72 h.

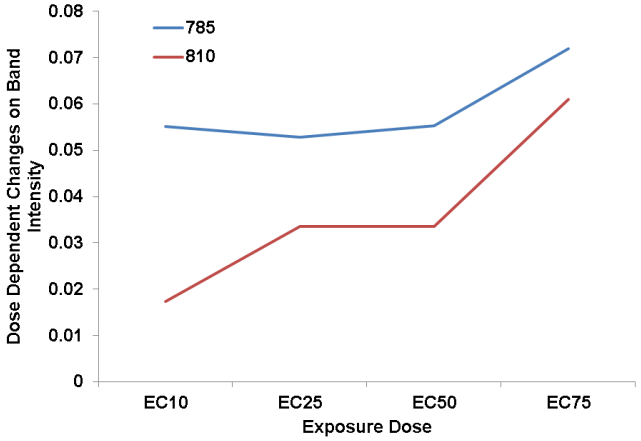

Figure 6.S8. Band intensities of 785 (nucleic acids) and 810 (RNA) cm^{-1} bands calculated from PC1 from pairwise PCA of nucleus of exposed cells and corresponding controls.

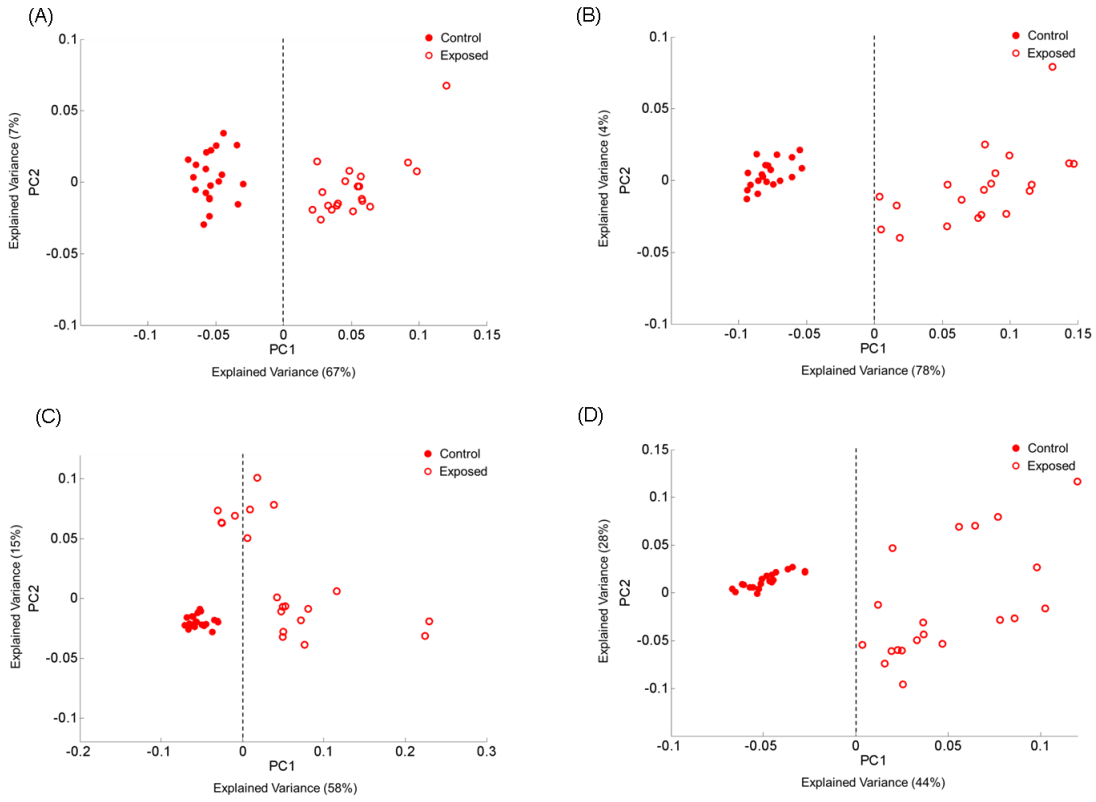

Figure 6.S9. Scatter plots of the PCA of spectra corresponding to nucleolus of A549 cells (control) and A549 cells exposed to the EC_{10} (A), EC_{25} (B), EC_{50} (C) and EC_{75} (D) concentrations of PAMAM-G5 dendrimers after 24 h. Each graph indicates a pairwise comparison of exposed cells with corresponding control for 24 hour. Unexposed cells and exposed cells are indicated with closed circles and open circles, respectively. '0' line for PC1 is indicated by black dashed outlines.

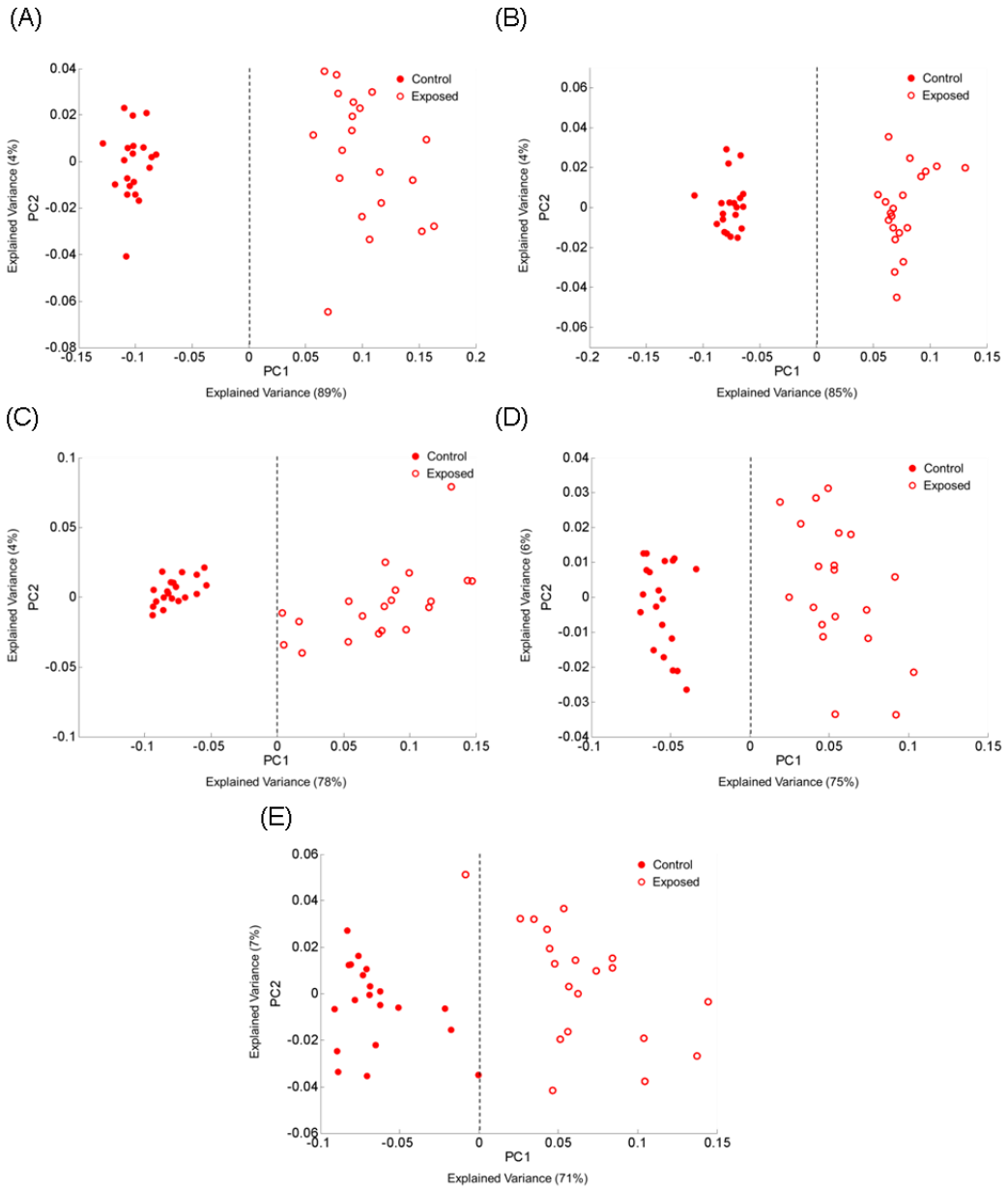

Figure 6.S10. Scatter plot of the PCA of spectra corresponding to nucleolus of A549 cells (control) and A549 cells exposed to the EC_{25} concentration of PAMAM-G5 after 4 (A), 8 (B), 24 (C), 48 (D) and 72 hour. Each graph indicates a pairwise comparison of exposed cells with corresponding control for extending exposure times. Unexposed cells and exposed cells are indicated with closed circles and open circles, respectively. '0' line for PC1 is indicated by black dashed outlines.

CHAPTER 7

Identification of Cell Death Mechanisms based on Raman Spectral Markers of Cyto-/Geno-Toxicity: Comparative Study of Polyamidoamine Dendrimers and Aminated Polystyrene Nanoparticles

The following chapter has been adapted from the submitted journal article entitled 'Identification of Cell Death Mechanisms based on Raman Spectral Markers of Cyto-/Geno-Toxicity: Comparative Study of Polyamidoamine Dendrimers and Aminated Polystyrene Nanoparticles, Journal of Biophotonics, 2017.

Author list: Esen Efeoglu, Maher A. Maher, Alan Casey, Hugh J. Byrne

EE performed all measurements, data analysis and is the main drafting author. MAM, AC and HJB contributed to manuscript design and final drafting.

7.1. Abstract

The determination of the *in vitro* cyto- and geno- toxicity of nanomaterials in a rapid and label-free fashion, with multi-parametric information, is of significant importance for identifying, amongst an enormous range of nanomaterials, candidates which are biocompatible and have high potential for applications in nanomedicine. Raman microspectroscopy has been shown to be capable of monitoring subcellular compartments and the localisation of the nanoparticles in these compartments. The potential of the technique has also been demonstrated to identify the mechanism of action of nanomaterials, and the spectral signatures of the cellular events, from nanoparticle uptake to cell death, have been identified. In this study, common and/or differentiating spectral markers of cyto- and geno- toxicity were identified by comparing the spectral markers of the cellular responses upon exposure to two different toxic nanoparticles, amine-modified polystyrene nanoparticles (PS-NH_2) and polyamidoamine nanoparticles (PAMAM). The study further demonstrates the potential of Raman microspectroscopy to differentiate apoptotic and necrotic cell death mechanisms. In order to elucidate the mechanism of action of PAMAM and PS-NH_2 in human cells as a function of time (from 4 to 72 h) and applied dose (sub-lethal/lethal), point spectra were collected from the cytoplasm and nucleus of particle exposed cells and corresponding controls . The spectral markers of the toxic events and ultimately cell death were identified and compared with the aid of unsupervised Principal Component Analysis (PCA). The results are correlated with flow cytometry and cytotoxicity assays.

7.2. Introduction

Nanomaterials show a great potential, given their unique physicochemical properties, and present tuneable features based on their size, surface modifications and charge (Guisbiers 2010; Jagiello *et al.* 2017; Nel *et al.* 2006; Sperling & Parak 2010). Although there is a bright future for nanomaterials in a wide range of fields, from clinical to pharmaceutical applications, many challenges remain concerning their mechanism of action as well as potential toxic effects in living systems. Many nanoparticles have been reported to cause changes to the biochemical composition of the cells, directing or interrupting the cellular events and responses and even causing changes to genetic material which can lead to epigenetic modifications and ultimately genotoxicity (Efeoglu, Casey, & Byrne 2016; Efeoglu *et al.* 2017; Manke, Wang, & Rojanasakul 2013; Martinez *et al.* 2009; Mukherjee & Byrne 2013; Mukherjee, Davoren, & Byrne 2010; Naha & Byrne 2013; Naha *et al.* 2010; Sierra *et al.* 2016; Wang & Wang 2014). Therefore, determination of nanomaterial toxicity in an efficient, rapid way, yielding multi-parametric information, without using multiple assays and labels is of significant importance when the range of identified and designed nanomaterials is considered.

Previous studies have shown the applicability of Raman microspectroscopy for monitoring of cellular trafficking and localisation of polystyrene nanoparticles (PS) (Dorney *et al.* 2012; Efeoglu *et al.* 2015; Keating, Bonnier, & Byrne 2012) inside the cell and subcellular compartments, based on the intrinsic properties of the nanomaterial. Moreover, the progressive changes in the cytoplasm of A549 cells upon aminated polystyrene nanoparticle (PS-NH_2) exposure compared to controls have been

previously monitored using Raman microspectroscopy and significant changes have been identified based on different exposure times and doses (Efeoglu, Casey, & Byrne 2016). Notably, spectroscopic changes have been identified which can be attributed to distortion of and damage to cytoplasmic RNA due to oxidative stress. Moreover, with extended exposure times and increased doses, significant changes are observed to the spectroscopic signatures related to cellular proteins and lipids, associated with cellular responses to exposure. Previous studies also demonstrated the ability of Raman microspectroscopy to identify signatures of different toxicity pathways in cancerous and non-cancerous cell lines (Efeoglu *et al.* 2017). Compared to the Organisation for Economic Co-operation and Development (OECD) recommended, commonly used and commercially available toxicity assays such as Alamar Blue (AB) and 3-(4, 5-dimethylthiazol-2-yl)-2, 5- diphenyltetrazolium bromide (MTT), which provide information corresponding to a specific marker, the label free and high-content information obtained using Raman microspectroscopy has shown to provide a more holistic spectral profile of the toxic response.

In order to determine the common and/or differentiating spectral markers of cellular toxicity, a second model toxic nanomaterial, polyamidoamine (PAMAM) dendritic nanoparticles, was chosen, due to their well-known structure related toxic properties (Maher & Byrne 2016; Maher *et al.* 2014; Mukherjee, Davoren, & Byrne 2010; Mukherjee *et al.* 2010). PAMAM dendrimers contain a 2-carbon ethylenediamine core and a well-defined number of primary amino groups on the surface, depending on the generation. The number of amino groups systematically increases with increasing generation (Dendritech 2017). The controllable and well-defined structure of the PAMAM dendrimers makes them attractive nanomaterials for many biological

applications, such as targeted delivery of genes and drugs, use as contrast agents as well as biomedical applications (Bourne *et al.* 1996; Twyman *et al.* 1999; Zhou *et al.* 2006). However, the polar surface amino groups carry a high cationic charge which impacts on mammalian cell viability following their endocytosis, due to oxidative stress, mitochondrial activity changes, release of inflammatory factors, DNA damage which ultimately leads to cell death (Leroueil *et al.* 2007; Maher *et al.* 2014; Malik *et al.* 2000; Naha & Byrne 2013; Roberts, Bhalgat, & Zera 1996). Similar to PS-NH_2, PAMAM are taken up into the cells by endocytosis and carry a cationic charge on the surface, which causes significant changes in endosomal/lysosomal integrity and mitochondrial activity, ultimately resulting in cell death (Anguissola *et al.* 2014; Benjaminsen *et al.* 2013; Efeoglu, Casey, & Byrne 2016; Efeoglu *et al.*, 2017; Freeman, Weiland, & Meng 2013; Maher *et al.* 2014).

Cell death is known to be a significant process which allows the regulation of vital activities in organisms. The cell death mechanism can be connected with cell viability and proliferation by its role in regulating the toxic and inflammatory responses (Elmore 2007; Fink & Cookson 2005; Rock & Kono 2008). Although different cell death mechanisms such as apoptosis, necrosis, autophagy etc. have been already described (Fink & Cookson 2005; Nikoletopoulou *et al.* 2013), *in vitro* determination of the cell death mechanisms still remains challenging. The analysis of the cell death mechanisms based on differentiating biochemical and morphological changes in the cell upon exposure to a toxicant normally requires the use of multiple labels. The potential of Raman microspectroscopy has been demonstrated to differentiate live and dead cells from each other (Notingher *et al.* 2003) and the technique has also been

applied to determine cell death stages upon environmental factors such as temperature and heat (Brauchle *et al.* 2014).

In this study, spectral markers of the toxicity as a function of time and applied dose are determined for PAMAM exposure and are compared with those observed for PS-NH_2 exposure. The applicability of Raman microspectroscopy is demonstrated based on intrinsic properties of biomolecules, and by identification of the evolution of spectral markers for particle exposed cells compared to their corresponding controls. The biochemical signatures of the cells related to protein, lipid and nucleic acid content upon toxicant exposure is used to differentiate the mechanisms of apoptotic and necrotic cell death.

7.3. Materials and Methods

7.3.1. Cell Culture and Reagents

The human lung carcinoma cell line, A549 (ATCC number CCL-185TM), was chosen as a model to evaluate cellular responses upon exposure to two different toxicants and to determine Raman spectral markers of cellular toxicity and genotoxicity. A549 cells were cultured in Dulbecco's Modified Eagle's Medium Nutrient Mixture F-12 HAM (DMEM-F12) supplemented with 2 mM L-glutamine and 10% foetal bovine serum (FBS) at 37 °C in 5% CO_2 humidified incubator. Cells were sub-cultured every 3-4 days when they reach a confluency level of approximately 60%-70%.

7.3.2. Nanoparticles and Preparation of Nanoparticle Solutions

Commercially available, extensively studied, Generation 5 dendritic polyamidoamine nanoparticles (PAMAM-G5 dendrimers, (664049)) and 100 nm amine-modified polystyrene nanoparticles (PS-NH_2, (L9904)) were chosen as model nanoparticles for determination of cellular toxicity and were purchased from Sigma-Aldrich, Ireland. According to manufacturer's instructions, the stock concentrations of PAMAM-G5 dendrimers and PS-NH_2 nanoparticles were calculated as 1.7 and 2.05 mM, respectively. The working concentrations of the nanoparticle solutions were prepared in pre-warmed (37 °C) DMEM-F12 with supplements prior to use. The percentage of the FBS supplement in the growth medium was altered to 5% from 10% for PAMAM dendrimers for consistency with previous studies (Maher & Byrne 2016; Naha & Byrne 2013), whereas 10% FBS in DMEM-F12 was used for the PS-NH_2 nanoparticles. No significant effect on the cell viability is observed based on the percentage of the FBS used for PAMAM dendrimers.

7.3.3. Cytotoxicity Evaluation and Calculation of Half-Maximal Effective Concentration (EC_{50})

Alamar Blue (AB) and 3-(4, 5-dimethylthiazol-2-yl)-2, 5- diphenyltetrazolium bromide (MTT) were purchased from Biosciences Ltd. (Ireland) and Sigma-Aldrich (Ireland), respectively and the assays were carried out for cytotoxicity evaluation of the PAMAM-G5 and PS-NH_2 nanoparticles on A549 cells from 24 to 72 h. The A549 cells were seeded on 96-well plates with decreasing densities of the cells as $1x10^5$, $5x10^4$ and $3x10^4$ cell/mL for 24, 48 and 72 h exposure, respectively, to prevent over confluency of the cells with extended exposure times. The seeded A549 cells were incubated at 37 °C and 5% CO_2 for 24 h to provide initial attachment and certain

confluency. Following initial attachment, cell medium was removed and the cells were washed twice with phosphate buffered saline (PBS). A549 cells (negative control) and 10% Dimethyl sulfoxide (DMSO) prepared in supplemented DMEM-F12 (positive control) were used for comparison with test samples. 6 replicates of each test sample and the controls per 96-well plate were used throughout the study and 3 independent experiments were carried out to determine the cytotoxicity. For negative control, a 100 μL/well of fresh growth medium with supplements were added. For the test samples, PAMAM dendrimers were prepared in pre-warmed (37°C) DMEM-F12, supplemented with 5% FBS and 2 mM L-glutamine, in the concentration range from 5.0 to 0.04 μM with serial dilutions, whereas a concentration range from 20 to 0.5 μM was used to prepare test solutions of PS-NH_2 nanoparticles in DMEM-F12, supplemented with 10% FBS and 2 mM L-glutamine. The cells were exposed to the test materials for 24, 48 and 72 h and, after exposure, the medium containing test materials, DMSO (positive control) or DMEM-F12 (negative control) was removed and the cells were washed with PBS, three times. AB/MTT solution was prepared in pre-warmed un-supplemented DMEM-F12 in the ratio of 5% [v/v] of AB- 10% [v/v] of MTT. 100 μL of the solution mix were added onto the wells after which the cells were incubated at 37 °C in 5% CO_2 humidified incubator for 3 h. Fluorescence emission of AB was directly measured at 595 nm following the 3 h incubation using a micro plate reader (SpectraMax-M3, Molecular Devices, USA). In order to measure MTT absorbance, AB/MTT solution was removed and cells were washed twice with 100 μL of PBS and a 100 μL/well of DMSO were added onto the cells. Plates were agitated at 200 rpm for 10 min prior to absorbance measurement at 570 nm in a micro plate reader. Data were analysed and EC_{50} values were calculated using a four parameter sigmoidal fit in SigmaPlot.

7.3.4. Raman Microspectroscopy and Data Analysis

Raman microspectroscopy is used to identify and compare time and dose dependent spectral markers of the cytotoxicity upon exposure to the two different toxic agents, PAMAM-G5 dendrimers and PS-NH_2 nanoparticles. A549 cells were seeded on to CaF_2 discs with a density of 16,000 cells/per substrate and incubated in humidified incubator at 37°C in 5% CO_2 for 24 h for initial attachment and growth. After initial attachment, cell medium was removed and cells were washed with PBS, twice. The cells were exposed to the various (24 h) EC concentrations (EC_{10}, EC_{25}, EC_{50} and EC_{75}) of PAMAM dendrimers, calculated using a SigmaPlot four parameter sigmoidal fit, to evaluate the Raman spectral markers of the dose-dependent toxicity. For the evaluation of the spectral markers of time dependence, the calculated EC_{25} value was used to observe progressive changes with extended exposure times (4, 8, 24, 48 and 72 h). For PS-NH_2 exposure, similar to PAMAM-G5 exposure, cells were exposed to EC_{25} concentration of the PS-NH_2 for 4, 8, 24, 48 and 72 h. For the all exposure times, cells were incubated at 37°C in 5% CO_2. For control cells, cell medium was replaced by fresh medium and incubated with medium for 4, 8, 24, 48 and 72 h. Following the exposure of the test materials to the A549 cells, the media containing test materials were removed and cells were washed with 2 mL of pre-warmed PBS, three times. As a fixative reagent, 10% Formalin was used and the cells were incubated with 3 mL of formalin solution in room temperature for 10 min. After fixation, cells were washed with PBS three times to remove formalin. Fixed cells were kept in sterilized dH_2O and spectra were acquired in dH_2O using x100 immersion objective (LUMPlanF1, Olympus, N.A. 1).

A Horiba Jobin-Yvon LabRAM HR800 spectrometer equipped with a 785 nm diode laser was used for all Raman microspectroscopy studies. The spectrometer was calibrated to the 520.7 cm^{-1} line of silicon prior to spectral acquisition of samples. A 300 lines per mm grating, which provides ~1.5 cm^{-1} per pixel spectral dispersion, and a 100 μm confocal pinhole, were chosen for all measurements and spectra were collected by a 16 bit dynamic range Peltier cooled CCD detector. 20 point spectra from cytoplasm and nucleus of particle exposed cells and corresponding controls were acquired for 30 seconds x 2 for each point. Spectra were acquired in the spectral range between 400 and 1800 cm^{-1} (fingerprint region) and used to compare spectral markers of cellular responses for PAMAM and PS-NH_2 nanoparticle exposed cells. The collected spectra were subjected to pre-processing by following the steps, mild-smoothing using Savitsky–Golay Filter (3^{rd} order, 9 points), background subtraction using Classical Least Squares (CLS) analysis and vector normalisation, to improve spectral quality. The unsupervised PCA analysis was applied to data sets obtained from particle exposed cells and their corresponding controls.

7.3.5. Determination of Apoptosis and Necrosis by Flow Cytometry

The effect of PAMAM-G5 dendrimers and PS-NH_2 nanoparticles on cell death mechanism was evaluated using a BD Biosciences Accuri C6 Flow Cytometer (Becton Dickinson, Oxford, UK). The A549 cells were seeded into T25 flasks (growth area: 25 cm^2, working volume 5 mL) at a density of $1x10^5$ cells/ml in 10% FBS and 2 μM L-glutamine supplemented DMEM-F12 medium and incubated at 37 °C in 5% CO_2 incubator for 24 h for cell attachment and initial growth. Following initial attachment and growth, cell medium was removed and cells were washed twice with PBS. The

A549 cells were exposed to the 5, 2.5, 1.25 and 0.625 μM concentrations of PAMAM-G5 dendrimers and PS-NH_2 nanoparticles individually. The A549 cells and the cells with YO-PRO-1/Propidium iodide stains were used as controls. For control cells, fresh medium was added, whereas for nanoparticle exposures, desired concentrations of nanoparticles were prepared in supplemented DMEM-F12 medium and added in onto the cells. Control and exposed cells were incubated at 37 °C in 5% CO_2 incubator for 24 h. Following 24 h exposure, cells were washed with ice-cold PBS twice and harvested by trypsinization. The harvested cells were then centrifuged at 1200 rpm for 8 min to remove trypsin and cells were washed with PBS. The washing procedure with PBS was repeated twice and the cells were kept in 1 ml PBS prior to staining. Cells were stained with a mixture of 1 μl of each dye (YO-PRO-1/Propidium iodide dye). Cells were incubated on ice for 30 mins and analysed in the flow cytometer within 1 h.

7.4. Results and Discussion

7.4.1. Cytotoxicity of PAMAM and PS-NH_2 nanoparticles

The toxic properties of the PAMAM and PS-NH_2 nanoparticles have been widely studied and the effect of the both nanoparticles on the mitochondria, formation of ROS and ultimately alteration of the energy mechanism of the cells due to their high cationic surface has been demonstrated (Anguissola *et al.* 2014; Efeoglu, Casey, & Byrne 2016; Efeoglu *et al*, 2017.; Maher & Byrne 2016; Mukherjee & Byrne 2013; Naha & Byrne 2013; Naha *et al.* 2010). In this study, the toxicological effects of PAMAM-G5 and PS-NH_2 nanoparticles on proliferative capacity and metabolic activity of the A549

cells were evaluated using the AB and MTT assays. The assay response curves fitted by four parameter sigmoidal fit using SigmaPlot upon PAMAM-G5 and PS-NH_2 exposure from 24 to 72 h are provided in Figure 7.1. The cellular viability determined by the AB assay for both toxic nanoparticles showed similar trends and the viability progressively decreased from ~100% to 0% with increasing concentration of the nanoparticles. In contrast, the metabolic activity measured by MTT showed different profiles for the PAMAM and PS-NH_2 particles. Upon PAMAM exposure, a partial toxic response, which causes a reduction in the viability to 60%, is observed after 24 h exposure, whereas this partial toxic response was observed at later time points for PS-NH_2 exposed cells (48 and 72 h) and the metabolic activity remained around 50%.(Pliska 1999) The changes in the metabolic activity determined by MTT can mostly be attributed to changes in the mitochondria (Bernas & Dobrucki 2002). When the AB and MTT responses are compared, the different responses obtained can be related to the presence of a secondary mechanism due to endosomolysis (Efeoglu *et al.*, 2017) which impacts on the mitochondria. Therefore, monitoring of the partial response of MTT at different time points can be attributed to variations in cell response mechanisms and/or different impact rates of the PAMAM and PS-NH_2 on the cell mitochondria.

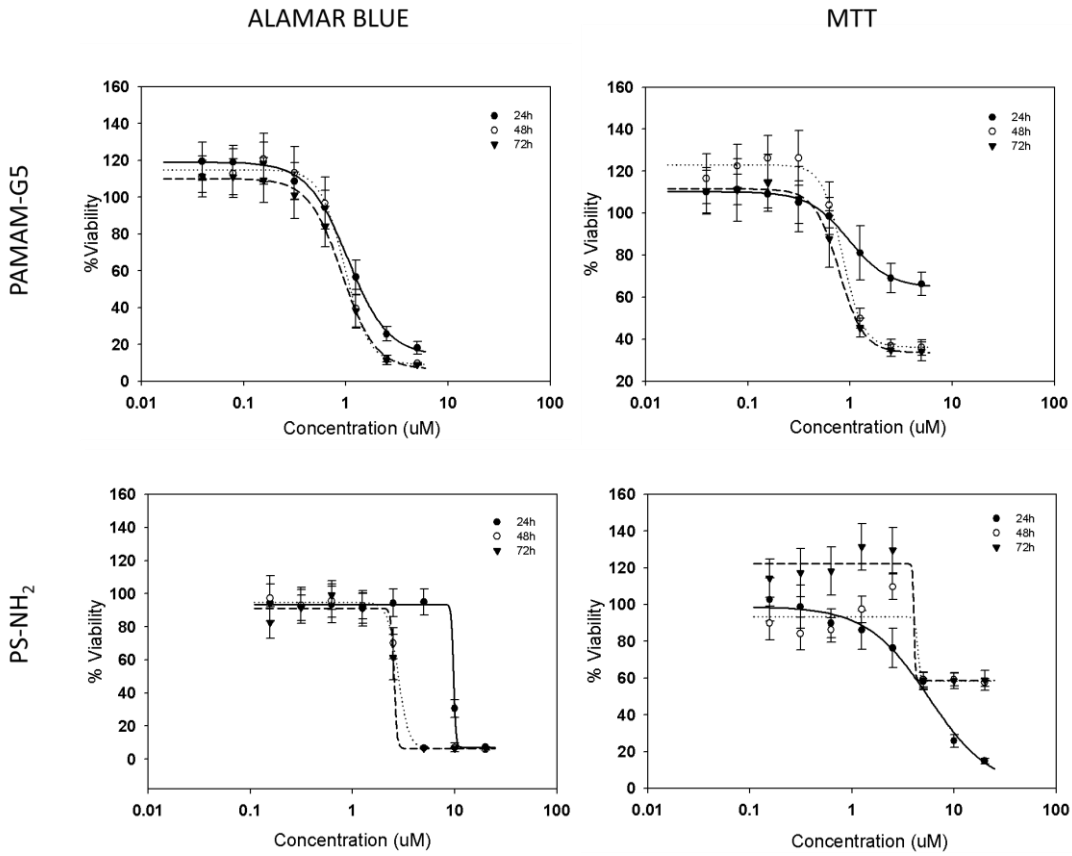

Figure 7.1. Cytotoxicity of generation 5 polyamidoamine (PAMAM-G5) dendrimers and amine-modified polystyrene nanoparticles (PS-NH_2) after 24, 48 and 72 h exposures determined by the Alamar Blue and MTT assays. Data are expressed as % of control mean ± SD of three independent experiments.

As the Alamar Blue assay is more sensitive to nanoparticle exposure in both cases, exposure concentrations are expressed in terms of its response. The half-maximal effective concentrations, EC_{50}, which reduces the cell viability to 50%, for extended exposure times were calculated in SigmaPlot and are provided in Table 7.1.

Table 7.1. Half-maximal effective concentration (EC_{50}) of PAMAM-G5 and PS-NH_2 on A549 cell line from 24 to 72 hour determined by the Alamar Blue assay.

Nanoparticle [Concentration Range used(μM)]	Time(h)	EC_{50}(μM) (Standard Deviation)
PAMAM-G5 Alamar Blue Assay [5-0.3]	24	1.04 (±0.04)
	48	0.97 (±0.05)
	72	0.92 (±0.04)
PS-NH_2 Alamar Blue Assay [20-0.15]	24	6.00 (±1.15)
	48	4.62 (±0.13)
	72	2.50 (±0.5)

When the EC_{50} values of the A549 cells exposed to PAMAM-G5 and PS-NH_2 determined by the AB assay were compared, PAMAM-G5 was found to be significantly more toxic compared to the PS-NH_2, which also can explain the rapid effect on the MTT response as an indicator of mitochondrial disruption. Although both nanoparticles carry a high positive charge on their surface, the more toxic nature of the PAMAM-G5 dendrimers (5.4 nm) compared to PS-NH_2 (100 nm) can be attributed to the size difference between the nanoparticles which leads to more rapid uptake and also the higher degree of surface amination (Gan *et al.* 2012; Rejman *et al.* 2004; Yue *et al.* 2011).

7.4.2. Spectroscopic Responses to PAMAM and PS-NH_2 nanoparticles in the Cytoplasm

Although PS-NH_2 and PAMAM elicit similar processes in terms of toxicology, toxic events can occur at various rates and the determination of the full mechanism of action remains challenging as it requires the use of multiple assays and labels. In this study, Raman microspectroscopy, as a high-throughput screening technique, is used to identify common and/or differentiating spectral markers of the toxicity. The biomarker progression for different nanoparticles was evaluated by comparison of PS-NH_2 exposed cells with PAMAM-G5 exposed cells. A sub-lethal dose of the nanoparticles (EC_{25} determined by AB after 24 h exposure) is used throughout the study to observe progressive changes of the spectral markers. The point spectra from the cytoplasm and nucleus of the cells exposed to the nanoparticles from 4 to 72 h were acquired and compared with corresponding controls for those time points using Principal Component Analysis (PCA). The changes in the biochemical composition of the PAMAM exposed cells were compared with PS-NH_2 exposed cells to reveal the toxic mechanisms leading to the cell death.

Scatter plots of the PCA for cytoplasm of exposed and control cells for each exposure time are provided in Supplementary Figure 7.S1 and 7.S2 for PAMAM-G5 and PS-NH_2, respectively. The control and particle exposed cells are clearly differentiated from each other according to PC1. This separation is observed to be more significant, with higher explained variances, for PAMAM-G5 exposure compared to PS-NH_2 exposure. When the loadings of PC1 corresponding to cytoplasm of exposed and unexposed cells were compared for PAMAM-G5 (Black) and PS-NH_2 (Blue) for

different time points (Figure 7.2, from Figure 7.2A to 2E for 4, 8, 24, 48 and 72 h, respectively), the most dominant features are observed to be the bands at 785 (nucleic acids), 810 (RNA), 1003 (Phenylalanine (Phe)), 1274 and 1299 (Amide II structures of the proteins), 1438 (Lipid) and 1600-1700 (Amide I) cm^{-1} (Ghita *et al.* 2012; Movasaghi, Rehman, & Rehman 2007; Notingher & Hench 2006; Notingher *et al.* 2003). The spectroscopic signatures of the toxic initiating event is identified as ROS formation associated with the presence of the doublet peak at 785 and 810 cm^{-1} (Efeoglu, Casey, & Byrne 2016; Efeoglu *et al*. 2017.). Although the double peak at 785 and 810 cm^{-1} is observed upon exposure to both nanomaterials, the progression of the bands is observed to be different. The double peak is observed after 4 h exposure in the case of PAMAM-G5 exposure, whereas it was absent for PS-NH_2 up to 8 h. When the origin of the doublet peak is considered, ROS formation and alterations of cytoplasmic RNA (Efeoglu, Casey, & Byrne 2016; Efeoglu *et al.* 2017), PAMAM-G5 dendrimers are found to result in a more rapid appearance of the bands compared to PS-NH_2. The higher effect can be attributed to more rapid uptake of PAMAM-G5 dendrimers due to their smaller size (Gan *et al.* 2012; Rejman *et al.* 2004; Yue *et al.* 2011) and/or formation of a higher degree of oxidative stress due to the highly positive surface which is found to be consistent with the response obtained from cytotoxicity assays.

The proton pump effect which causes the endosomal and/or lysosomal protonation and rupture has been shown previously for both PAMAM dendrimers and PS-NH_2 (Efeoglu, Casey, & Byrne 2016; Efeoglu *et al.* 2017 ; Maher & Byrne 2016; Malik *et al.* 2000; Mukherjee, Davoren, & Byrne 2010; Roberts, Bhalgat, & Zera 1996). PAMAM dendrimers are shown to have impact the mitochondria via localisation after

endosomal escape and result in further ROS formation (Maher & Byrne 2016). The second prominent change, which is observed as a more rapid change in the cytoplasm of PAMAM-G5 exposed cells compared to PS-NH_2 exposed cells, is observed in lipid bands, especially at 1438 cm^{-1} (lipid saturation). For PS-NH_2, the band at 1438 cm^{-1} is observed to be inverted to the control side (negative features of the loading) only after 24 h, which indicates damage in lipid structures, whereas it was visible for PAMAM-G5 after 8 h particle exposure. The later effect on lipid saturation for PS-NH_2 can be attributed to a slower mechanism and interaction with mitochondria indirectly. For both toxic agents, protein bands became inverted to the negative side of the loading after 24 h, which shows alterations, damage and loss of protein content. For PAMAM-G5 exposed cells, in contrast to PS-NH_2 exposure, a drop in the intensity of the 810 cm^{-1} band was observed and the band becomes inverted to the control side which shows the cumulative damage in cytoplasmic RNA in PAMAM-G5 exposed cells after 72 h exposure. Conversely, for PS-NH_2 exposed cells, the band at 810 cm^{-1} is observed to be of highest intensity at this time point.

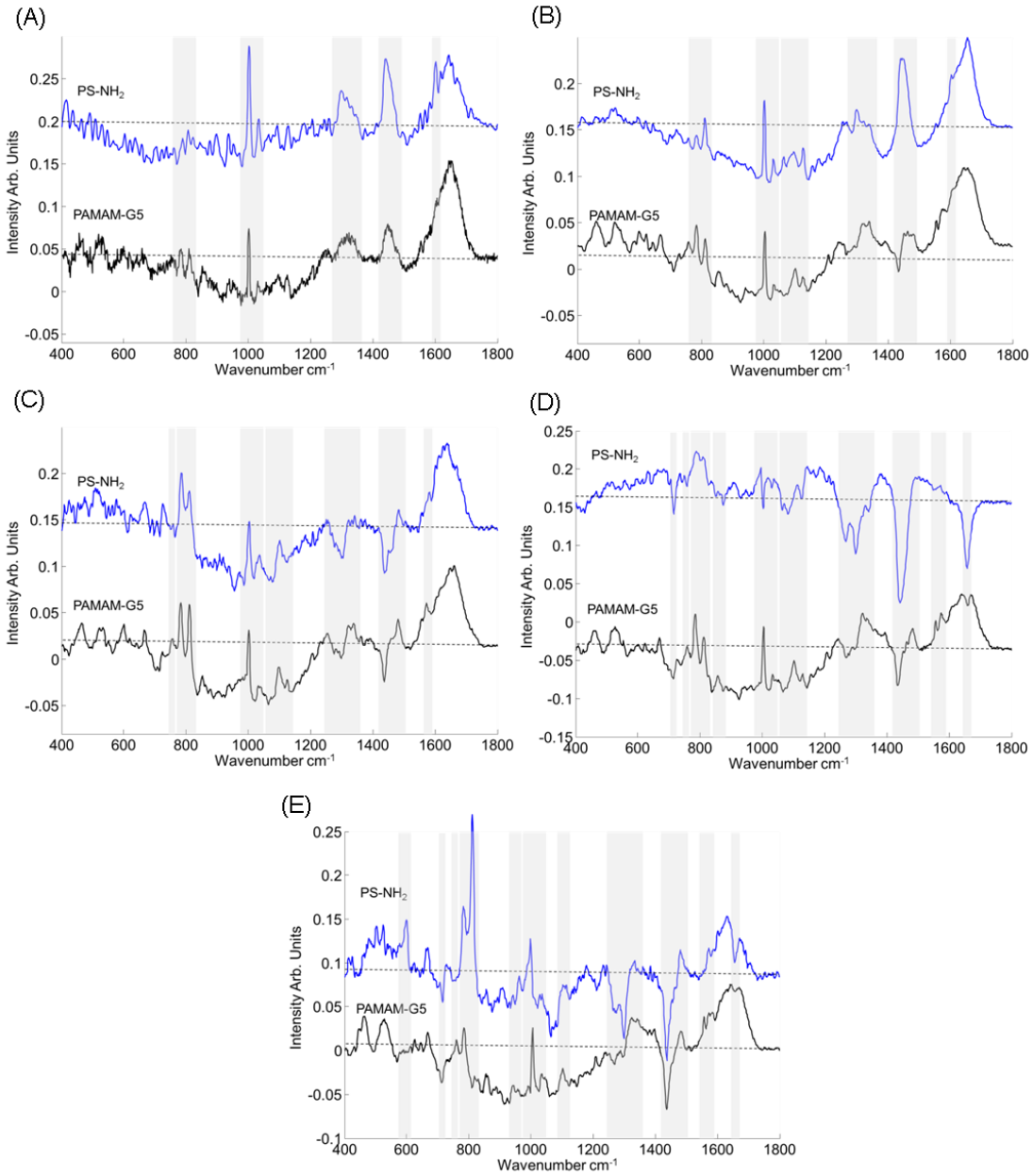

Figure 7.2. Comparison of PC1 obtained from pairwise PCA of cytoplasm of exposed cells and corresponding control for 4(A), 8(B), 24(C), 48(D) and 72 (E) h $PS\text{-}NH_2$ (Blue) and PAMAM-G5 (Black) exposure. The negative side of the loading represents the spectral features of control, whereas positive side represents the cells exposed to $PS\text{-}NH_2$ and PAMAM-G5. Loadings are offset for clarity and the zero '0' line is indicated with black dashes. The progressive changes in the loadings are indicated with grey highlights.

In order to quantify changes in the biochemical composition of the cells upon exposure to EC_{25} concentrations of PAMAM and PS-NH_2 individually, the intensities of four dominant bands of the loadings (785, 810, 1003 and 1438 cm^{-1}) are calculated and shown in Figure 7.3, as a function of exposure time. The intensity of the band at 785 cm^{-1} is observed to be significantly higher for PAMAM-G5 exposed cells compared to those exposed to PS-NH_2, even after 4 h particle exposure (Figure 7.3A). The band progressively increases with extended exposure time and is observed to reach saturation after 24 h exposure for both particles. Although the band maintains the saturation state for PS-NH_2 exposed cells after 24 h, a significant decrease is observed in the intensity of the band in PAMAM-G5 exposed cells after 48 h, which may be indicative of different cell death mechanisms for the different nanomaterials. Similar to the band at 785 cm^{-1}, the band at 810 cm^{-1} is observed to have higher intensity after 4 h for PAMAM-G5 exposure and the band intensity increases up to 24 h exposure. A saturation is observed between 24 and 48 h and the band progression significantly changed after 48 h (Figure 7.3B). For the bands at 1003 cm^{-1} (Phe), no significant change is observed over the 72 h exposure period for PS-NH_2 exposed cells, whereas the band intensity dramatically changed over the same period for PAMAM-G5 exposed cells (Figure 7.3C). For the lipid band at 1438 cm^{-1}, a continuous decrease is observed for both toxic agents with a more pronounced decrease for PAMAM-G5 exposed cells (Figure 7.3D). The more pronounced changes in the intensities of the bands above 1000 cm^{-1} for PS-NH_2 cells compared to PAMAM exposure may be attributed to changes in the cytoplasm as a result of different cell death mechanisms.

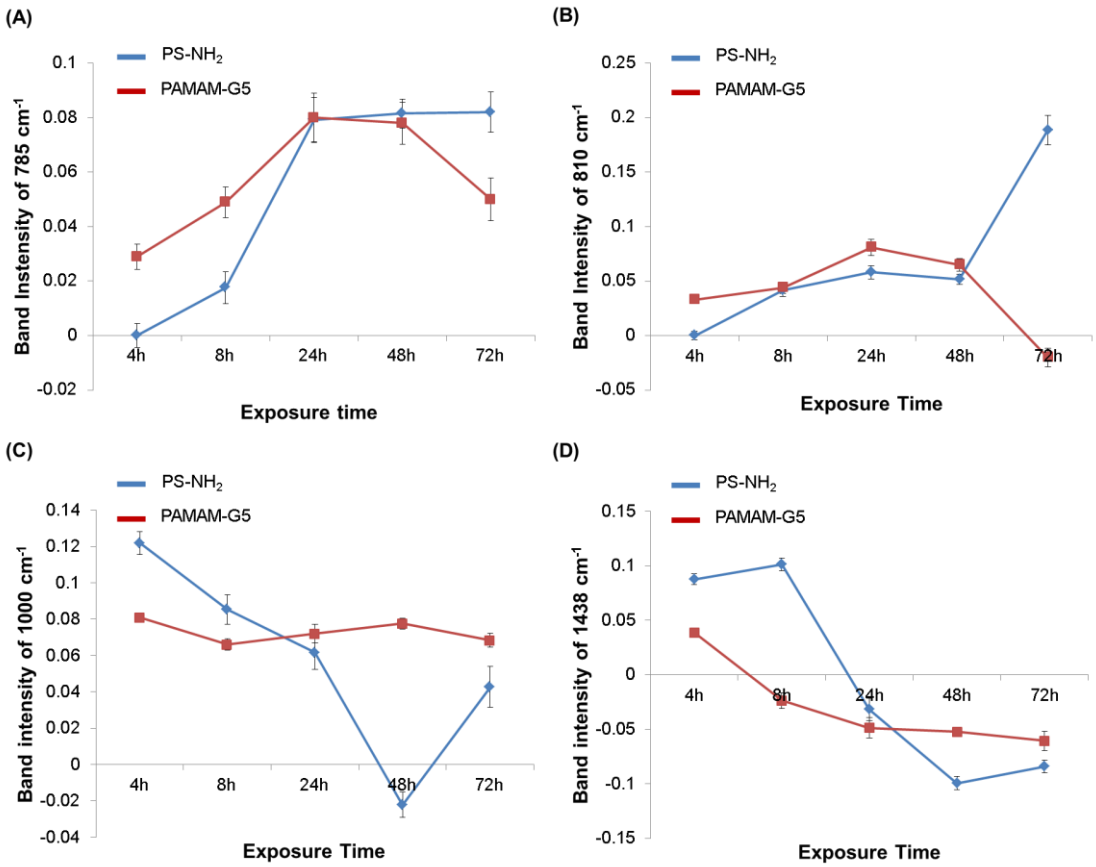

Figure 7.3. Comparison of Band intensities of 785 (nucleic acids), 810 (RNA), 1003 (Phenlyalanine) and 1438 (Lipids) cm^{-1} bands calculated from PC1 from pairwise PCA of cytoplasm of exposed cells (EC_{25}) and corresponding controls. The changes in the band intensities for PS-NH_2 and PAMAM-G5 exposure are indicated with blue and red lines, respectively. Data are expressed as % of control mean ± SD.

7.4.3. Spectroscopic Responses to PAMAM and PS-NH_2 nanoparticles in the Nucleus

Following the identification and comparison of the spectral markers of the cellular toxicity upon PAMAM-G5 and PS-NH_2 exposure of A549 cells from 4 to 72 h, the spectral markers of the genotoxicity were investigated using Raman microspectroscopy. The cellular spectra obtained from nucleus of the cells were

compared with their corresponding controls for PAMAM-G5 and PS-NH_2 exposure as a function of exposure time. The scatter plots of PCA corresponding to comparison of nucleus of PAMAM-G5 exposed cells and their controls for different time points from 4 to 72 h are provided in Supplementary Figure 7.S3. For all exposure times, PAMAM exposed cells clearly differentiated from the corresponding controls and the explained variance is calculated to be ~75%-95% for different exposure times. Conversely, for PS-NH_2 exposed cells, scatter plots of PCA obtained from the nucleus of the exposed and control cells did not show a pronounced separation as observed for PAMAM dendrimers and calculated explained variance stayed at around ~30-50% for all exposure times, except 8 h (Supplementary Figure 7.S4). The lower explained variance between particle exposed cells and their controls for PS-NH_2 compared to PAMAM, can be attributed to indirect changes in the genotoxicity upon PS-NH_2 which are known to localise in the Endoplasmic Reticulum in the cells (Efeoglu *et al.* 2015). The loadings of the PCA are provided in Figure 7.4 for PAMAM-G5 (A) and PS-NH_2 (B), respectively and the areas with progressive changes as a function of exposure time are indicated with black dashes. As seen in Figure 7.4, a significantly different progression in the nucleus of the PAMAM-G5 exposed cells compared to PS-NH_2 exposed cells is observed according to the presence and intensities of the bands in the first loadings of PCA.

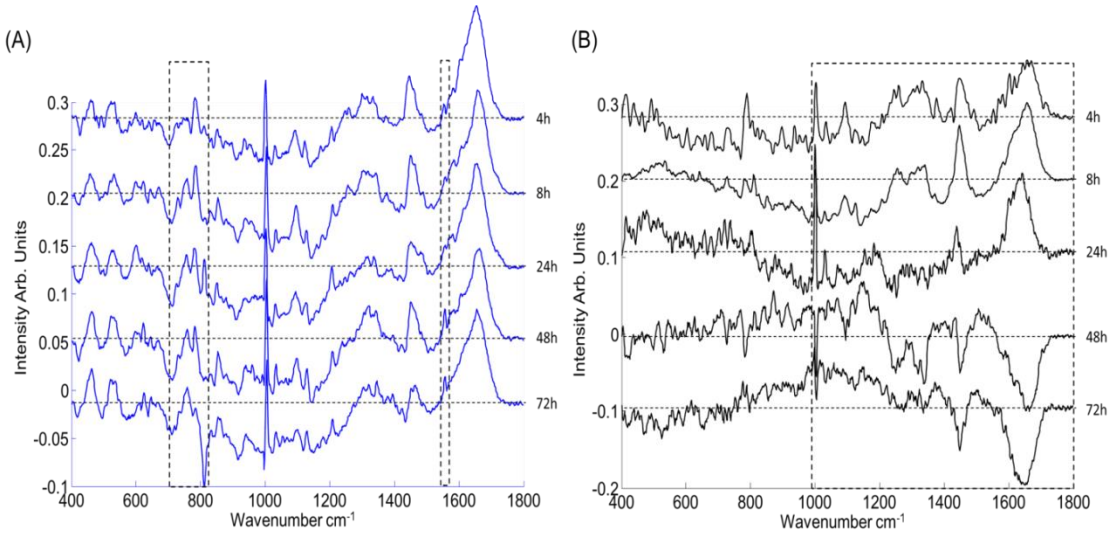

Figure 7.4. Comparison of PC1 obtained from pairwise PCA of nucleus of exposed cells and corresponding control for 4, 8, 24, 48 and 72 h PAMAM-G5 (A) and PS-NH_2 (B) exposure. The negative side of the loading represents the spectral features of control, whereas positive side represents the cells exposed to PS-NH_2 and PAMAM-G5. Loadings are offset for clarity and the zero '0' line is indicated with black dashes. The progressive changes in the loadings are indicated with black dashes.

In the nucleus of the PAMAM-G5 exposed cells, the bands at 728 (Adenine, DNA), 756 (Trp, C_5-H (cytosine)), 785 (nucleic acids) and 810 (RNA) cm^{-1} are observed to change over the exposure time. Also, the band at 1156 (C_5-H, cytosine) cm^{-1} is identified to be another significant change in the loadings with increasing intensity over the time, whereas these bands do not show progressive changes upon PS-NH_2 exposure. Moreover, significant changes for PS-NH_2 exposure are observed in the region from 1000 cm^{-1} to 1800 cm^{-1}, while these changes were not pronounced upon PAMAM-G5 exposure. Spectral changes in the region from 1000 cm^{-1} to 1800 cm^{-1} can potentially be used to identify cell death mechanisms as it provides information about the overall cell health and a cascade of cellular toxic events upon toxic

nanoparticle exposure using the molecular fingerprint of protein and lipid content of the cell.

In order to further elucidate the origins of the differencing spectral profiles, an apoptosis-necrosis assay was carried out by using Flow cytometry (Figure 7.5). As seen in Figure 7.5, A549 cells exposed to PAMAM-G5 (EC_{25}; 0.6 µM), show a necrotic response, especially at low doses, whereas, PS-NH_2 (EC_{25}; 2.5 µM) exposure results in predominantly apoptotic cell death. The significant changes in the band intensities after 48 h can therefore be attributed to different cell death mechanisms originating from exposure to the different nanoparticles.

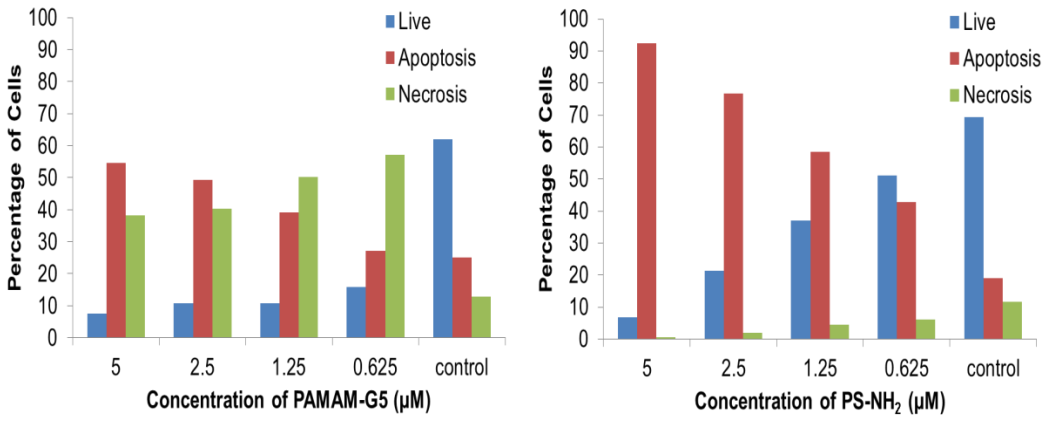

Figure 7.5. Representation of the percentage of cells in different cell death processes upon PAMAM-G5 and PS-NH_2 exposure. Live, apoptotic and necrotic cells were indicated with blue, red and green, respectively. Cells are exposed to 4 different concentrations of the nanomaterials for 24 h. A549 cells without exposure are used as control.

During the apoptosis process, well-defined nuclear changes occur due to proteolysis and DNA fragmentation, whereas nuclear differences are less pronounced in the early

necrosis process (Proskuryakov, Konoplyannikov, & Gabai 2003). As seen in Figure 7.5, cells tend to undergo apoptosis compared to necrotic cell death upon PS-NH_2 exposure, which can be identified by Raman microspectroscopy as inverted bands (1274 and 1299 cm^{-1}, 1438 and 1600-1700 cm^{-1}) from positive features (exposed cells), to the negative features (control cells) of the loading in the spectral region above 1000 cm^{-1}, after 24 h exposure. The inverted bands show the damage in protein and lipid structures in the nucleus of PS-NH_2 exposed cells and identify the mechanism of the cell death as apoptosis. Conversely, the moderate changes in the identified protein and lipid bands upon PAMAM-G5 exposure can be attributed to less pronounced nuclear changes in necrosis.

When the intensities of the nuclear bands at 785, 810, 1003 and 1438 cm^{-1} are compared for exposure to PAMAM-G5 and PS-NH_2, the intensity changes in the PS-NH_2 exposed cells are observed to be more significant compared to PAMAM-G5 exposed cells, which correlates with apoptotic cell death mechanism caused by PS-NH_2 (Figure 7.6). Although critical changes in the spectral region above 1000 cm^{-1} are observed after 48 h, when the loadings of PAMAM and PS-NH_2 exposed cells are compared, the rapid changes in the intensities of the bands up to 48 h for PS-NH_2 exposed cells can be related to the more controlled mechanism of apoptosis compared to necrosis.

An increase in the band at 785 cm^{-1} is observed up to 8 h PAMAM-G5 exposure, followed by a slight decrease over the extended exposure time, whereas the band dramatically decreased upon PS-NH_2 exposure up to 48 h. Although there is an increase on the band intensity after 48 h exposure in PS-NH_2 exposed cells, the band

is observed as a negative feature of the loading, which indicates the higher contribution of nucleic acids in the control cells. Although ROS formation and trafficking of the nanoparticles is observed to be rapid upon PAMAM exposure, and PS-NH_2 does not localise in nucleus, a more rapid change in the band at 810 cm^{-1} is observed (8 h) in PS-NH_2 exposed cells compared to PAMAM-G5 (24 h). and after 8 h exposure, the intensity of the band has reduced and remains the same over the extended exposure times. The change in the RNA band can be explained by a higher increase in RNA activity upon PS-NH_2 uptake compared to PAMAM-G5 uptake. Conversely, the 810 cm^{-1} band reached an intensity which is twice of PAMAM-G5 upon PS-NH_2 exposure. The intensity of the band is significantly reduced after 24 h and became inverted after 48 h exposure. The protein band at 1003 cm^{-1} and lipid band at 1438 cm^{-1} do not show significant changes upon PAMAM-G5 exposure, whereas PS-NH_2 exposure results in a decrease after 24 h.

The biochemical processes such as production of specific proteases and DNA fragmentation do not occur in necrotic cell death. Therefore, no nuclear alteration is observed until damage to the cellular membrane occurs. Conversely, DNA, RNA and protein content are continuously affected by energy dependant caspase activities in apoptotic cells (Elmore 2007; Proskuryakov, Konoplyannikov, & Gabai 2003). Therefore, the intensities of the bands at 785 (nucleic acids), 1003 (Proteins) and 1438 (Lipid) cm^{-1} are observed to be more stable over the time for PAMAM exposed cells (necrosis) compared to PS-NH_2 (apoptosis). The differences in the biochemistry of the cell death mechanisms can contribute the different cytotoxicity profiles and notably can clearly be identified using Raman microspectroscopy.

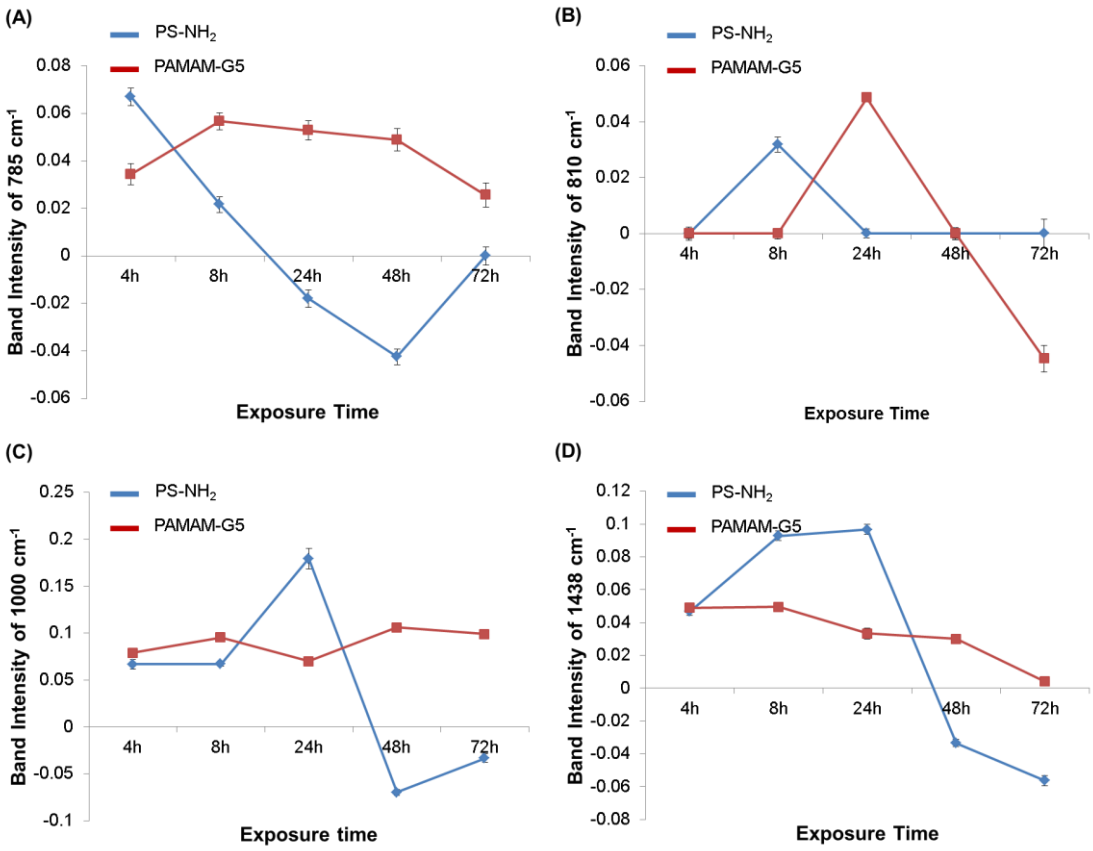

Figure 7.6. Comparison of Band intensities of 785 (nucleic acids), 810 (RNA), 1000 (Phenlyalanine) and 1438 (Lipids) cm^{-1} bands calculated from PC1 from pairwise PCA of nucleus of exposed cells and corresponding control for The changes in the band intensities for PS-NH_2 and PAMAM-G5 exposure are indicated with blue and red lines, respectively. Data are expressed as % of control mean ± SD.

7.5. Conclusion

Raman microspectroscopy can be used to identify cellular responses and monitor cell fate upon exposure to a toxicant, from uptake to final localisation. In this study, Raman microspectroscopy is used as a high content screening technique for cellular exposure to two different nanomaterials PAMAM and PS-NH_2, and common and differentiating spectral markers of the cyto- and geno- toxicity are identified. The common spectral

markers of toxic events for ROS formation and damage in protein/lipid composition of cytoplasm are found to be identical for different toxic materials and variances in spectral marker evolution are on the result of different response rates. The observation of the different response rates which can be determined based on the spectral markers at 810 and 785 (cytoplasmic nuclear material) and 1438 (lipids) cm^{-1}, can be applied to a wide range of nanomaterials and pharmaceuticals with a positive surface charge, to monitor and predict toxicological behaviour. Moreover, significantly different evolution of spectral markers is observed in the spectral region of the fingerprint, above 1000 cm^{-1}, which enables determination of the cell death as apoptosis or necrosis. Although the profile of the apoptosis and necrosis markers, which are determined in this study as 1003 and 1438 cm^{-1}, become more visible at longer exposure times for the nucleus (after 48 h), more pronounced changes in the intensity of the spectral markers in cytoplasm and nucleus up to 48 h can be used for early detection of apoptotic and necrotic cell death. As a label free probe of the cytotoxic responses of the cells, Raman microspectroscopy thus provides a wealth of biochemical information not accessible using conventional cytotoxic assays.

7.6. References

Anguissola, S, Garry, D, Salvati, A, O'Brien, P J and Dawson, K A (2014) High Content Analysis Provides Mechanistic Insights on the Pathways of Toxicity Induced by Amine-Modified Polystyrene Nanoparticles. *PLoS ONE*, 9(9), e108025.

Benjaminsen, R V, Mattebjerg, M A, Henriksen, J R, Moghimi, S M and Andresen, T L (2013) The Possible "Proton Sponge " Effect of Polyethylenimine (Pei) Does Not Include Change in Lysosomal Ph. *Molecular Therapy*, 21(1), 149-57.

Bernas, T and Dobrucki, J (2002) Mitochondrial and Nonmitochondrial Reduction of Mtt: Interaction of Mtt with Tmre, Jc-1, and Nao Mitochondrial Fluorescent Probes. *Cytometry*, 47(4), 236-42.

Bourne, M W, Margerun, L, Hylton, N, Campion, B, Lai, J-J, Derugin, N and Higgins, C B (1996) Evaluation of the Effects of Intravascular Mr Contrast Media (Gadolinium Dendrimer) on 3d Time of Flight Magnetic Resonance Angiography of the Body. *Journal of Magnetic Resonance Imaging*, 6(2), 305-10.

Brauchle, E, Thude, S, Brucker, S Y and Schenke-Layland, K (2014) Cell Death Stages in Single Apoptotic and Necrotic Cells Monitored by Raman Microspectroscopy. *Scientific Reports*, 4, 4698.

Dendritech, I (2017) [Online]. Available: http://www.dendritech.com/pamam.html

Dorney, J, Bonnier, F, Garcia, A, Casey, A, Chambers, G and Byrne, H J (2012) Identifying and Localizing Intracellular Nanoparticles Using Raman Spectroscopy. *Analyst*, 137(5), 1111-9.

Efeoglu, E, Casey, A and Byrne, H J (2016) *In vitro* Monitoring of Time and Dose Dependent Cytotoxicity of Aminated Nanoparticles Using Raman Spectroscopy. *Analyst,* 141(18), 5417-31.

Efeoglu, E, Keating, M, McIntyre, J, Casey, A and Byrne, H J (2015) Determination of Nanoparticle Localisation within Subcellular Organelles *in vitro* Using Raman Spectroscopy. *Analytical Methods,* 7(23), 10000-17.

Elmore, S (2007) Apoptosis: A Review of Programmed Cell Death. *Toxicologic pathology,* 35(4), 495-516.

Efeoglu, E, Maher, M A, Casey, A, Byrne, H J. (2017) Label-Free, High Content Screening Using Raman Microspectroscopy: The Toxicological Response of Different Cell Lines to Amine-Modified Polystyrene Nanoparticles (PS-NH_2), Analyst, DOI: 10.1039/C7AN00461C.

Fink, S L and Cookson, B T (2005) Apoptosis, Pyroptosis, and Necrosis: Mechanistic Description of Dead and Dying Eukaryotic Cells. *Infection and Immunity,* 73(4), 1907-16.

Freeman, E C, Weiland, L M and Meng, W S (2013) Modeling the Proton Sponge Hypothesis: Examining Proton Sponge Effectiveness for Enhancing Intracellular Gene Delivery through Multiscale Modeling. *Journal of biomaterials science. Polymer edition,* 24(4), 398-416.

Gan, Q, Dai, D, Yuan, Y, Qian, J, Sha, S, Shi, J and Liu, C (2012) Effect of Size on the Cellular Endocytosis and Controlled Release of Mesoporous Silica Nanoparticles for Intracellular Delivery. *Biomed Microdevices,* 14(2), 259-70.

Ghita, A, Pascut, F C, Mather, M, Sottile, V and Notingher, I (2012) Cytoplasmic Rna in Undifferentiated Neural Stem Cells: A Potential Label-Free Raman Spectral Marker for Assessing the Undifferentiated Status. *Anal Chem,* 84(7), 3155-62.

Guisbiers, G (2010) Size-Dependent Materials Properties toward a Universal Equation. *Nanoscale Research Letters,* 5(7), 1132-6.

Jagiello, K, Chomicz, B, Avramopoulos, A, Gajewicz, A, Mikolajczyk, A, Bonifassi, P, Papadopoulos, M G, Leszczynski, J and Puzyn, T (2017) Size-Dependent Electronic Properties of Nanomaterials: How This Novel Class of Nanodescriptors Supposed to Be Calculated? *Structural Chemistry,* 28(3), 635-43.

Keating, M E, Bonnier, F and Byrne, H J (2012) Spectral Cross-Correlation as a Supervised Approach for the Analysis of Complex Raman Datasets: The Case of Nanoparticles in Biological Cells. *Analyst,* 137(24), 5792-802.

Leroueil, P R, Hong, S, Mecke, A, Baker, J R, Orr, B G and Banaszak Holl, M M (2007) Nanoparticle Interaction with Biological Membranes: Does Nanotechnology Present a Janus Face? *Accounts of Chemical Research,* 40(5), 335-42.

Maher, M A and Byrne, H J (2016) Modification of the *in vitro* Uptake Mechanism and Antioxidant Levels in Hacat Cells and Resultant Changes to Toxicity and Oxidative Stress of G4 and G6 Poly(Amidoamine) Dendrimer Nanoparticles. *Anal Bioanal Chem,* 408(19), 5295-307.

Maher, M A, Naha, P C, Mukherjee, S P and Byrne, H J (2014) Numerical Simulations of *in vitro* Nanoparticle Toxicity – the Case of Poly(Amido Amine) Dendrimers. *Toxicology in vitro,* 28(8), 1449-60.

Malik, N, Wiwattanapatapee, R, Klopsch, R, Lorenz, K, Frey, H, Weener, J W, Meijer, E W, Paulus, W and Duncan, R (2000) Dendrimers: Relationship between Structure and Biocompatibility *in vitro*, and Preliminary Studies on the Biodistribution of 125i-Labelled Polyamidoamine Dendrimers in Vivo. *J Control Release,* 65(1-2), 133-48.

Manke, A, Wang, L and Rojanasakul, Y (2013) Mechanisms of Nanoparticle-Induced Oxidative Stress and Toxicity. *BioMed Research International,* 2013, 15.

Martinez, E, Lagunas, A, Mills, C A, Rodriguez-Segui, S, Estevez, M, Oberhansl, S, Comelles, J and Samitier, J (2009) Stem Cell Differentiation by Functionalized Micro- and Nanostructured Surfaces. *Nanomedicine (Lond),* 4(1), 65-82.

Movasaghi, Z, Rehman, S and Rehman, I U (2007) Raman Spectroscopy of Biological Tissues. *Applied Spectroscopy Reviews,* 42(5), 493-541.

Mukherjee, S P and Byrne, H J (2013) Polyamidoamine Dendrimer Nanoparticle Cytotoxicity, Oxidative Stress, Caspase Activation and Inflammatory Response: Experimental Observation and Numerical Simulation. *Nanomedicine,* 9(2), 202-11.

Mukherjee, S P, Davoren, M and Byrne, H J (2010) *In vitro* Mammalian Cytotoxicological Study of Pamam Dendrimers - Towards Quantitative Structure Activity Relationships. *Toxicol In vitro,* 24(1), 169-77.

Mukherjee, S P, Lyng, F M, Garcia, A, Davoren, M and Byrne, H J (2010) Mechanistic Studies of *in vitro* Cytotoxicity of Poly(Amidoamine) Dendrimers in Mammalian Cells. *Toxicol Appl Pharmacol,* 248(3), 259-68.

Naha, P C and Byrne, H J (2013) Generation of Intracellular Reactive Oxygen Species and Genotoxicity Effect to Exposure of Nanosized Polyamidoamine (Pamam) Dendrimers in Plhc-1 Cells *in vitro*. *Aquat Toxicol,* 132-133, 61-72.

Naha, P C, Davoren, M, Lyng, F M and Byrne, H J (2010) Reactive Oxygen Species (Ros) Induced Cytokine Production and Cytotoxicity of Pamam Dendrimers in J774a.1 Cells. *Toxicology and Applied Pharmacology,* 246(1–2), 91-9.

Nel, A, Xia, T, Mädler, L and Li, N (2006) Toxic Potential of Materials at the Nanolevel. *Science,* 311(5761), 622.

Nikoletopoulou, V, Markaki, M, Palikaras, K and Tavernarakis, N (2013) Crosstalk between Apoptosis, Necrosis and Autophagy. *Biochimica et Biophysica Acta (BBA) - Molecular Cell Research,* 1833(12), 3448-59.

Notingher, I and Hench, L L (2006) Raman Microspectroscopy: A Noninvasive Tool for Studies of Individual Living Cells *in vitro*. *Expert Rev Med Devices,* 3(2), 215-34.

Notingher, I, Verrier, S, Haque, S, Polak, J M and Hench, L L (2003) Spectroscopic Study of Human Lung Epithelial Cells (A549) in Culture: Living Cells Versus Dead Cells. *Biopolymers,* 72(4), 230-40.

Pliska, V (1999) Partial Agonism: Mechanisms Based on Ligand-Receptor Interactions and on Stimulus-Response Coupling. *J Recept Signal Transduct Res,* 19(1-4), 597-629.

Proskuryakov, S Y, Konoplyannikov, A G and Gabai, V L (2003) Necrosis: A Specific Form of Programmed Cell Death? *Exp Cell Res,* 283(1), 1-16.

Rejman, J, Oberle, V, Zuhorn, I S and Hoekstra, D (2004) Size-Dependent Internalization of Particles Via the Pathways of Clathrin- and Caveolae-Mediated Endocytosis. *Biochem J,* 377(Pt 1), 159-69.

Roberts, J C, Bhalgat, M K and Zera, R T (1996) Preliminary Biological Evaluation of Polyamidoamine (Pamam) Starburst Dendrimers. *J Biomed Mater Res,* 30(1), 53-65.

Rock, K L and Kono, H (2008) The Inflammatory Response to Cell Death. *Annual review of pathology,* 3, 99-126.

Sierra, M I, Valdés, A, Fernández, A F, Torrecillas, R and Fraga, M F (2016) The Effect of Exposure to Nanoparticles and Nanomaterials on the Mammalian Epigenome. *International Journal of Nanomedicine,* 11, 6297-306.

Sperling, R A and Parak, W J (2010) Surface Modification, Functionalization and Bioconjugation of Colloidal Inorganic Nanoparticles. *Philosophical Transactions of the Royal Society A: Mathematical, Physical and Engineering Sciences,* 368(1915), 1333.

Twyman, L J, Beezer, A E, Esfand, R, Hardy, M J and Mitchell, J C (1999) The Synthesis of Water Soluble Dendrimers, and Their Application as Possible Drug Delivery Systems. *Tetrahedron Letters,* 40(9), 1743-6.

Wang, E C and Wang, A Z (2014) Nanoparticles and Their Applications in Cell and Molecular Biology. *Integrative biology : quantitative biosciences from nano to macro,* 6(1), 9-26.

Yue, Z-G, Wei, W, Lv, P-P, Yue, H, Wang, L-Y, Su, Z-G and Ma, G-H (2011) Surface Charge Affects Cellular Uptake and Intracellular Trafficking of Chitosan-Based Nanoparticles. *Biomacromolecules,* 12(7), 2440-6.

Zhou, J, Wu, J, Hafdi, N, Behr, J P, Erbacher, P and Peng, L (2006) Pamam Dendrimers for Efficient Sirna Delivery and Potent Gene Silencing. *Chem Commun (Camb)*(22), 2362-4.

7S Supplementary Information:

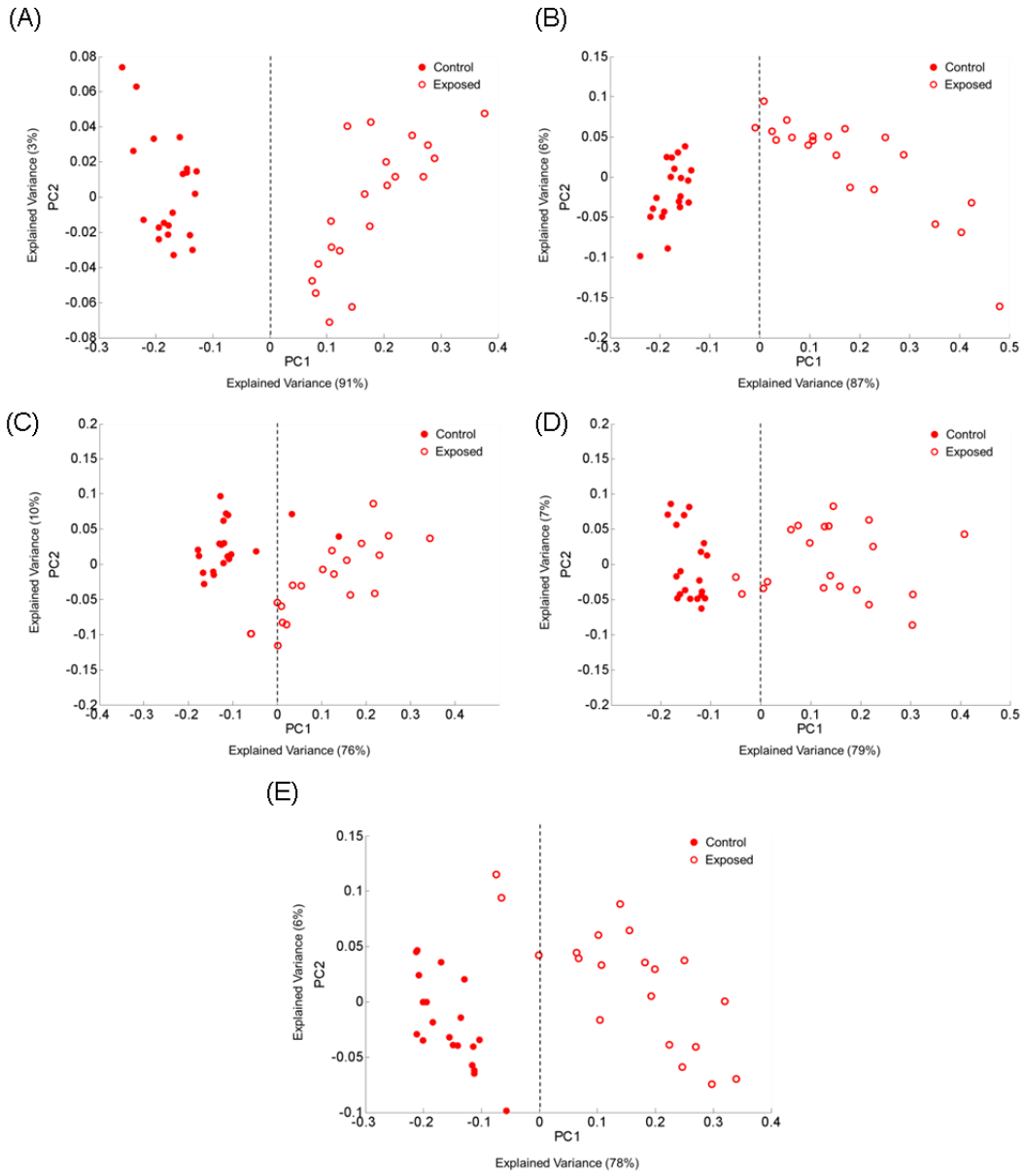

Figure 7.S1. Scatter plot of the PCA of spectra corresponding to cytoplasm of A549 cells (control) and A549 cells exposed to the EC_{25} concentration of PAMAM-G5 dendrimers after 4 (A), 8 (B), 24 (C), 48 (D) and 72 (E) hour. Unexposed cells and exposed cells are indicated with closed circles and open circles, respectively. The zero '0' line for PC1 is indicated by black dashes.

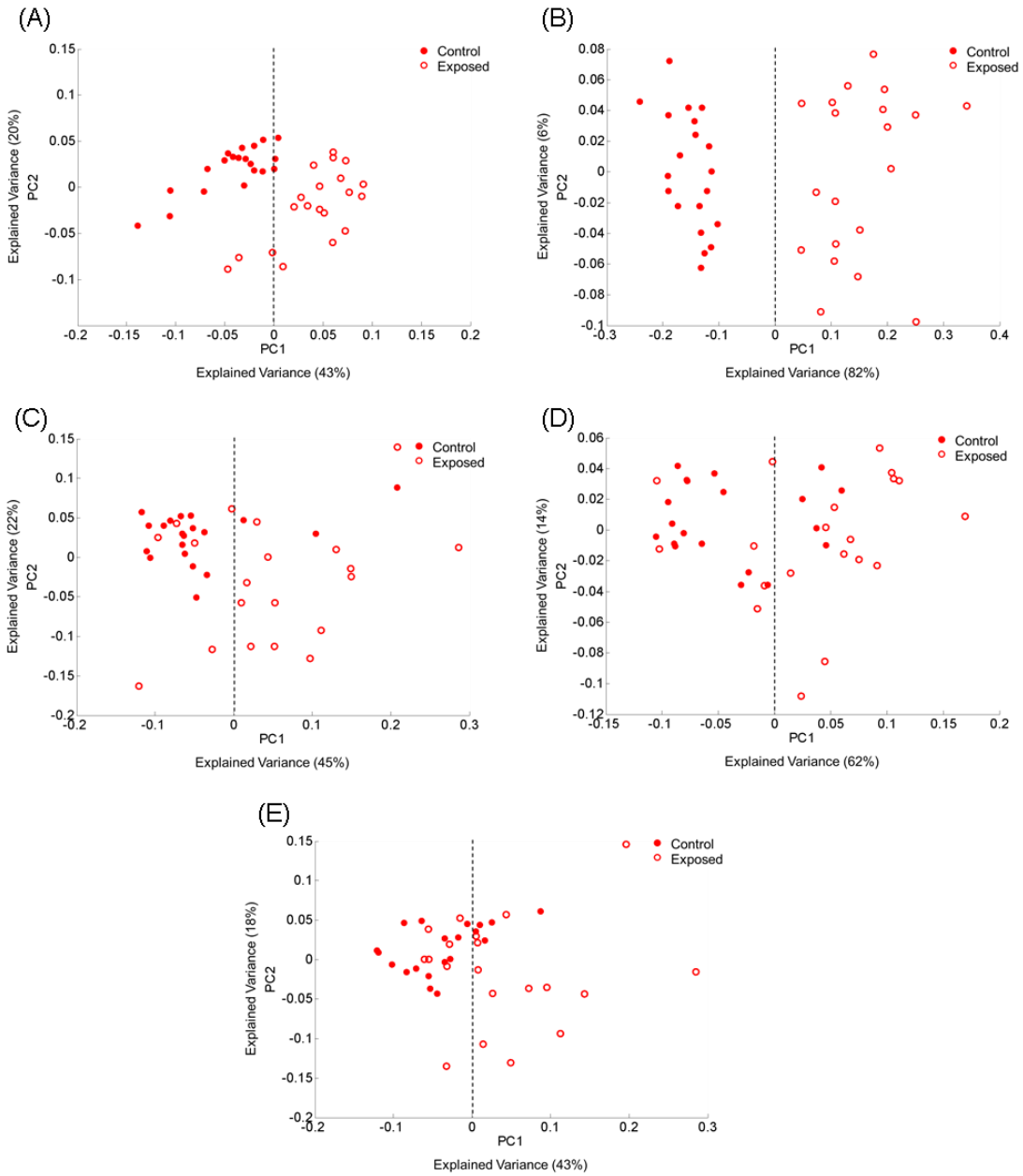

Figure 7.S2. Scatter plot of the PCA of spectra corresponding to cytoplasm of A549 cells (control) and A549 cells exposed to the EC_{25} concentration of PS-NH_2 after 4 (A), 8 (B), 24 (C), 48 (D) and 72 (E) hour. Unexposed cells and exposed cells are indicated with closed circles and open circles, respectively. The zero '0' line for PC1 is indicated by black dashes.

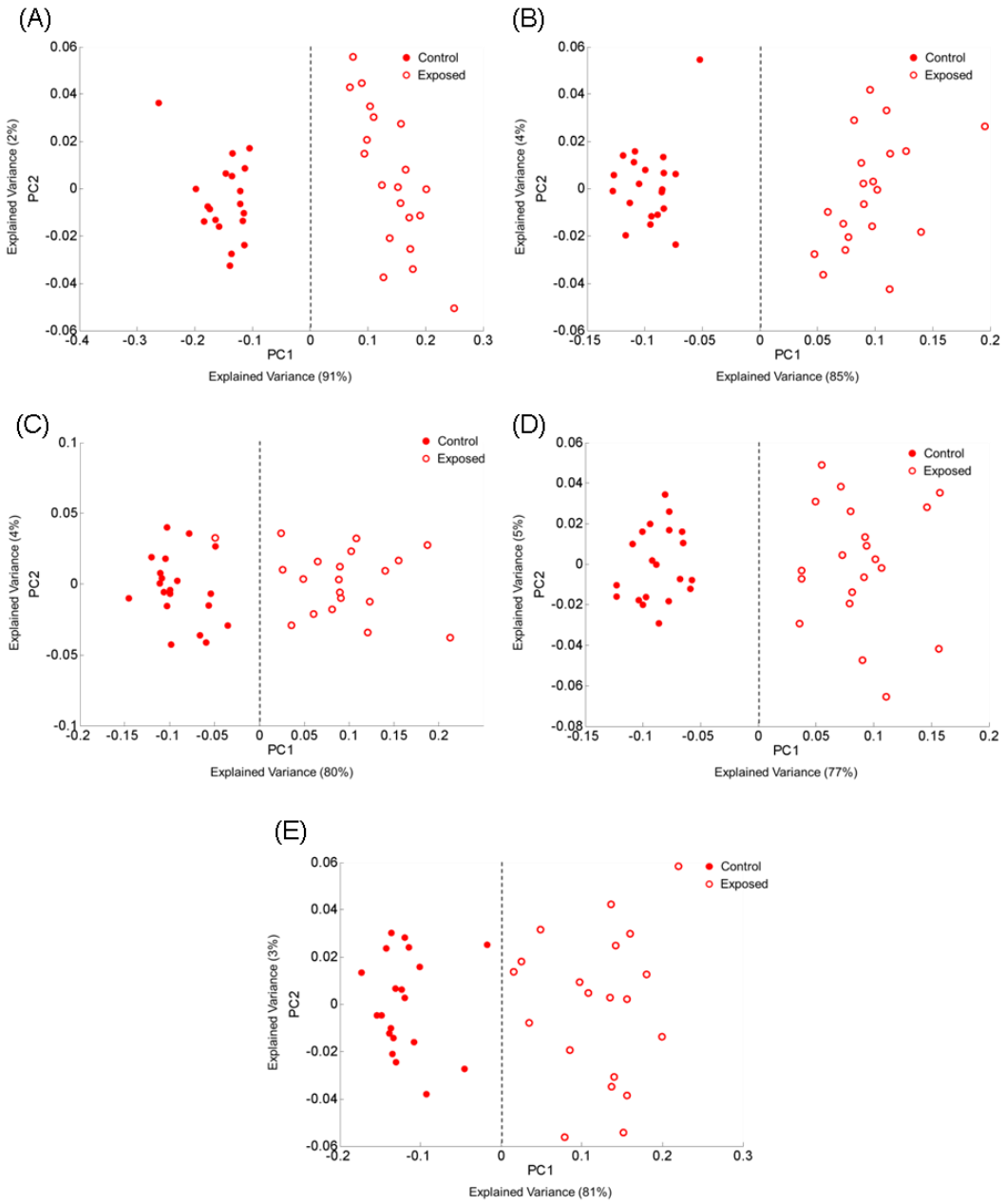

Figure 7.S3. Scatter plot of the PCA of spectra corresponding to nucleus of A549 cells (control) and A549 cells exposed to the EC_{25} concentration of PAMAM-G5 dendrimers after 4 (A), 8 (B), 24 (C), 48 (D) and 72 (E) hour. Unexposed cells and exposed cells are indicated with closed circles and open circles, respectively. The zero '0' line for PC1 is indicated by black dashes.

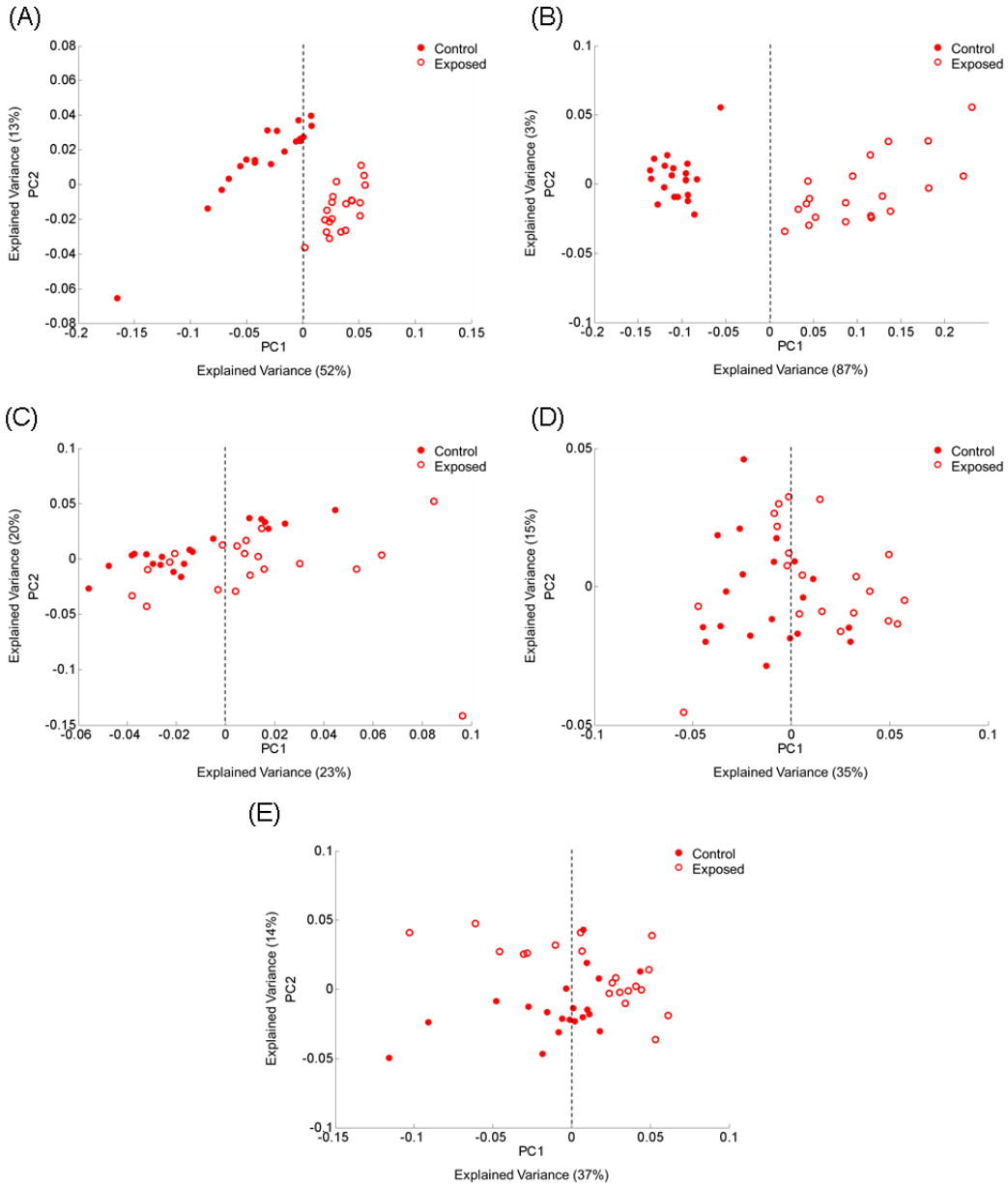

Figure 7.S4. Scatter plot of the PCA of spectra corresponding to nucleus of A549 cells (control) and A549 cells exposed to the EC_{25} concentration of PS-NH_2 after 4 (A), 8 (B), 24 (C), 48 (D) and 72 (E) hour. Unexposed cells and exposed cells are indicated with closed circles and open circles, respectively. The zero '0' line for PC1 is indicated by black dashes.

CHAPTER 8

Summary and Conclusions

Toxicological Assessment of Nanomaterials: The role of *in vitro* Spectroscopic Analysis

The following chapter has been adapted from the accepted journal article entitled 'Toxicological Assessment of Nanomaterials: The role of in vitro Raman Microspectroscopic Analysis', Analytical and Bioanalytical Chemistry, 2017.

Author list: Esen Efeoglu, Marcus A. Maher, Alan Casey, Hugh J. Byrne

EE performed all measurements and data analysis and is the main drafting author. MAM, AC and HJB contributed to manuscript design and final drafting.

8.1. Introduction

The acceleration of nanomaterials research has brought about increased demands for rapid analysis of their bioactivity, in a multi-parametric fashion, to minimise the gap between potential applications and knowledge of their toxicological properties. The potential of Raman microspectroscopy for the analysis of biological systems with the aid of multivariate analysis techniques has been demonstrated. In this study, an overview of recent efforts towards establishing a 'label-free high content nanotoxicological assessment technique' using Raman microspectroscopy is presented. The current state of the art for cellular toxicity assessment and the potential of Raman microspectroscopy are discussed, and the spectral markers of the cellular toxic responses upon exposure to nanoparticles, changes on the identified spectral markers upon exposure to different nanoparticles, cell death mechanisms and the effects of nanoparticles on different cell lines are summarised. Moreover, 3D toxicity plots of spectral markers, as a function of time and dose, are introduced as new methodology for toxicological analysis based on the intrinsic properties of the biomolecular changes, such as cytoplasmic RNA aberrations, protein and lipid damage associated with the toxic response. The 3D evolution of the spectral markers are correlated with the results obtained by commonly-used cytotoxicity assays and significant similarities are observed between band intensity and percentage viability obtained by the Alamar Blue assay, as an example. Therefore, the developed 3D plots can be used to identify toxicological properties of a nanomaterial and can potentially be used to predict toxicity which can provide rapid advances in nanomedicine.

8.1.1. Nanotoxicology

The increasing interest and accelerated research on naturally occurring or engineered nanomaterials, due to their possible impacts on society in terms of science and technological advancements, has raised questions regarding their health and environmental impact and led to the development of 'Nanotoxicology' as a new branch of toxicology to guide the safe deployment and suitable production of these novel materials (Donaldson *et al.* 2004; Institute of Medicine (US) Roundtable on Environmental Health Sciences 2005; Oberdörster *et al.* 2005).

Materials of nanoscale dimensions have been identified as possessing extraordinary and sometimes unique physicochemical and optical properties (Guisbiers 2010; Jagiello *et al.* 2017; Sperling & Parak 2010), which make them invaluable for a wide range of fields such as materials science (*Recent Trends in Nanotechnology and Materials Science* 2014), aerospace (Laurvick & Singaraju 2003), cosmetics (Raj *et al.* 2012), medicine (Kawasaki & Player 2005) and the pharmaceutical industry (Park 2007), to improve structures and to contribute to the develop new treatment strategies and early diagnosis of many diseases (Brigger, Dubernet, & Couvreur 2012; Godbey, Wu, & Mikos 1999; Nune *et al.* 2009; Sailor & Link 2005; Tosi *et al.* 2013). On the other hand, these properties have also been observed to facilitate their interaction with biological systems, which necessitates their responsible use and rapid toxicological analysis to predict possible adverse consequences (Nel *et al.* 2009; Oberdörster *et al.* 2005). Health offices of many governments have already established plans to promote on-going research in nanoscience as well as nanotoxicology (OECD; Society & Engineering 2004). The Organisation for Economic Co-operation and Development

(OECD) has published a list of nanomaterials with high-economic interest which require immediate investigation in terms of Health and Environmental impact (OECD, 2010). The European Union (EU) has established the 'NanoSafety Cluster', which is a consortium of sponsored projects related to toxicology, exposure assessment, mechanism of interaction and risk assessment of nanomaterials in order to maximising the synergy between European level projects (EU NanoSafety Cluster').

8.2. Current Approaches for Toxicological Assessment of Nanomaterial Toxicity

Most of the strategies that have been proposed for the investigation of nanomaterials include the combinational use of toxicity assays, bio-imaging techniques, chemical and biochemical assays to obtain information regarding to metabolic activity, membrane integrities, cellular viability and cell death mechanisms upon exposure. Cytotoxicity assays have been widely employed to determine cellular viability and also cell death rate *in vitro*. For example, the tetrazolium salts, such as MTT (3-(4,5-dimethylthiazol-2-yl)-2,5-diphenyltetrazolium bromide), MTS (3- (4,5-dimethylthiazol-2-yl)-5-(3-carboxymethoxyphenyl)-2-(4-sulfophenyl)-2H tetrazolium), XTT (2,3-bis-(2-methoxy-4-nitro-5-sulfophenyl)-2H-tetrazolium-5-carboxanilide) and WST-1 (2-(2-methoxy-4-nitrophenyl)-3-(4-nitrophenyl)-5-(2,4-disulfophenyl)-2H-tetrazolium) (soluble versions of MTT) assays, have been used to determine cellular viability based on the energy-state of the cell (Mosmann 1983). The Alamar Blue assay (AB), which provides information regarding to overall cell health and proliferative capacity, has also been widely used for determination of nanoparticle toxicity (Berridge, Herst, & Tan 2005; Rampersad 2012; Vega-Avila & Pugsley 2011).

The lactate Dehydrogenase (LDH) (Brzoska *et al.* 2004) and trypan blue (Karlsson *et al.* 2008) assays have been employed to determine cell membrane integrity and cell death rates. For long term toxicity, the clonogenic assay has been employed to determine colony forming efficiency and decreased or increased survival (Casey *et al.* 2008; Herzog *et al.* 2007). Assays such as mitochondrial membrane potential, cellular protonation and reactive oxygen species production have been used to elucidate mechanisms of action of nanomaterials in cells. Assays which measure the activation of caspases, release of inflammatory factors and activation of pro-apoptotic bcl-2 proteins provide further information regarding acute toxic effects of nanomaterials inside the cells. Electron microscopy (EM) and optical microscopy have been used for the visualisation of nanomaterials in cells. Confocal Microscopy (CLSM) has also been used for the visualisation of nanomaterials in cells with the aid of fluorescent labels (Fazlollahi *et al.* 2011; *Handbook of Biological Confocal Microscopy*, 2006; Jan *et al.* 2008; Sandin *et al.* 2012). High Content Analysis/Screening (HCA/HCS), has opened up new perspectives for toxicological assesment by providing multifaceted information with high sensitivity based on automated imaging of 'phenotypic assay endpoints'. The technique has been used for *in vitro* toxicity assesment, animal disease models, drug discovery, neurobiology (Radio *et al.* 2008; Ruan *et al.* 2008), cell signalling (Ding *et al.* 1998; Sarker *et al.* 2008; Zock 2009) and observation of biochemical changes (Brayden *et al.* 2015; Liebel & Link 2007; Zock 2009).

Chronic and genotoxic effects of the nanomaterials have also been widely studied (Efeoglu, Casey, & Byrne 2016; Efeoglu *et al.* 2017 ; Manke, Wang, & Rojanasakul 2013; Martinez *et al.* 2009; Mukherjee & Byrne 2013; Mukherjee, Davoren, & Byrne 2010; Naha & Byrne 2013; Naha *et al.* 2010; Sierra *et al.* 2016; Wang & Wang 2014). The Ames assay has been employed to observe Gene mutations in Chinese hamster

lung (CHL/IU) cells upon exposure to fullerenes (Mori *et al.* 2006). The combination of Ames test, micronuclei assay and comet assay have been used to demonstrate the effect of silver nanoparticles on Chinese hamster ovary cells (Kim *et al.* 2013). High-performance liquid chromatography and immunohistological techniques were employed to observe DNA base modifications based on measurement of oxidized guanine bases upon silica nanoparticle exposure of the human adenocarcinoma cell line (A549) (Jin *et al.* 2007). The comet assay has been used to identify single DNA strand breaks (Naha & Byrne 2013). Northern blot analysis and Polymerase chain reaction (PCR) is widely employed to observe changes in the gene expression (Chew *et al.* 2012; Hillegass *et al.* 2010).

Although conventional techniques have provided invaluable information regarding the interaction of nanomaterials with living systems, they remain limited in various aspects, such as the requirement of multiple labels and assays, interference of nanomaterials with the assay dyes (Casey *et al.* 2007; Casey *et al.* 2008; Holder *et al.* 2012), cost and also time required for the investigation.

Cytotoxicity assays are based on measurement of a biomarker, or so-called 'endpoint', which usually has a fluorescent property and corresponds to a specific change to the state of the whole cell population (Riss *et al.* 2004). Specificity of the 'endpoints' to a single type of toxicological event, within the cascade of events occurring upon toxicant exposure, results in inconsistencies of results obtained from different assays. Moreover, the nanomaterials can interfere with some of these assays. Carbon Nanotubes have been shown to interfere with the MTT and LDH assays, resulting in misleading results (Casey *et al.* 2007; Casey *et al.* 2008; Holder *et al.* 2012). For the

visualisation of the cells, optical microscopy remains limited due to its limited spatial resolution. Even though EM provides very detailed information, some nanomaterials do not provide the contrast and are therefore invisible within the cellular environment (Herzog *et al.* 2007; Shapero *et al.* 2011). CLSM has invaluable advantages for visualisation of the nanomaterials within the cell, although the low resolution of fluorescent based techniques limits its potential. Also, some nanomaterials cannot be functionalised with dyes and the dye can leak to the environment which reduces the reliability of the results (Salvati *et al.* 2011; Suh *et al.* 1998). HCS suffers from the disadvantes of the use of fluorescent dyes and specific'endpoints'. The cost, problems in data management, lack of common standards are also limits in the use of HCS (Liebel & Link 2007).

.

8.3. Raman Microspectroscopy; towards High Content Nanotoxiological Assessment

8.3.1. Raman Spectroscopy

Although the Raman-effect was first demonstrated by Sir C. V. Raman and K. S. Krishnan in 1928 (ACS), the developments in high powered light sources such as ion lasers widened the applications of Raman spectroscopy in the late 1960's. The revolution in Charged Coupled Detector (CCD) arrays in the 1980s and 1990's added to the benefits of high laser source intensities, the significant reductions in acquisition time with multichannel signal detection enabling significant improvements in signal to noise ratio (Adjouri, Elliasmine, & Le Duff 1996). In addition, the development of narrow band laser line rejection filters meant that the huge losses in signal from

traditional triple monochromator systems could be overcome with the combination of a filter set and a single spectroscopic grating.Raman spectroscopy, as a vibrational spectroscopic technique, has now become a really powerful technique for the characterisation and identification of biomolecules and biomolecular species, due to the narrow spectral bandwidths and ease of sample preparation (Butler *et al.* 2016).

The developing technology of Raman Spectroscopy and high potential of the technique in different areas, from medicine to industry, has led to the development of variants of the Raman spectroscopy technique itself, such as surface enhanced Raman spectroscopy (SERS) (Stiles *et al.* 2008), tip enhanced Raman spectroscopy (TERS) (Zhang *et al.* 2016) and coherent anti Stokes Raman spectroscopy (CARS) (Pezacki *et al.* 2011; Zheltikov 2000). These techniques enable Raman spectroscopy to be more sensitive, to perform molecule specific analysis with enhanced signal.

The applicability of Raman microspectroscopy has been widely shown for the analysis of bodily fluids, tumour tissue margining and analysis of cells and cellular compartments (Bonnier *et al.* 2011; Bonnier *et al.* 2014; Breve 1996; Dorney *et al.* 2012; Efeoglu *et al.* 2015; Jermyn *et al.* 2015; Walton, Deveney, & Koenig 1970). Raman microspectroscopy has been employed to visualise cells as well as their sub-cellular organisation (Carey 1982; Dorney *et al.* 2012; Keating, Bonnier, & Byrne 2012). The cellular structures have been identified by combining Raman spectroscopy with immunofluorescence imaging (Klein *et al.* 2012), which enabled label-free imaging of live cells. Raman spectroscopy has been also co-registered with fluorescence microscopy for cellular imaging (Krauss *et al.* 2015). The differing biochemical composition of nucleus, nucleolus and cytoplasm has also been identified

in a completely label free manner, based on intrinsic features of biochemical (Bonnier *et al.* 2010; Carvalho *et al.* 2015; Dorney *et al.* 2012). The changes of the spectral signatures upon cell death have been shown by comparing spectral features of dead and alive cells (Notingher *et al.* 2003). The importance of the use of multivariate analysis techniques such as Spectral Cross Correlation (SCC) and Classical Least Squares (CLS) analysis to extract information from huge Raman data sets has also shown by Keating *et al.* (Keating, Bonnier, & Byrne 2012). Raman spectral phenotyping with the aid of Principal Component Analysis (PCA) has also been studied by comparison of primary cells with cell line models (Swain *et al.* 2010).

Furthermore, as a label-free vibrational spectroscopic technique, both Infrared absorption (IR) and Raman spectroscopy have been employed for the localisation of nanomaterials inside the cell (Carey 1982; Li *et al.* 2013; Li *et al.* 2015; Rhiem *et al.* 2015). Although IR analysis is challenged by the strong contributions of water in biological samples (Draux *et al.* 2009), Raman microspectroscopy is not affected to the same degree and has attract attention for the analysis of biological samples (Miljkovic *et al.* 2010). Raman microspectroscopy also provides higher intrinsic spatial resolution for subcellular imaging compared to IR (Byrne, Sockalingum, & Stone 2011).

The correlation between Raman spectral markers of carbon nanotubes (CNTs) and commonly used cytotoxicity assays has been studied by Knief *et al.* (Knief *et al.* 2009). The studies of Dorney *et al.* and Keating *et al.* have shown the localisation of nanoparticles in cells and the use of multivariate analysis techniques to obtain more detailed information regarding to subcellular environment. Confocal Raman

microscopy has been employed to study the uptake and localisation of surface engineered CNTs, aluminium oxide and cerium dioxide nanoparticlesat single cell level in HepG2liver cells (Donath 2011). The stress effects of silver nanoparticles as a funtion of applied concentration on human mesenchymal stem cells (hMSCs) has also been studied (Bankapur *et al.* 2012). Uptake of titania and iron oxide nanoparticles into the nucleus of epithelial cells have been shown using Raman imaging with the aid of multivariate classification (Ahlinder *et al.* 2013).

Although there has been huge effort and on-going research in the use of Raman microspectroscopy to explore the cellular interactions of nanomaterials, the studies have been somewhat fragmented and a systematic study of cell-nanoparticle interaction as a function of dose and time has not as yet been reported.

This study aims to aggregate the results of Raman microspectroscopic analysis of nanoparticle exposure of cells *in vitro*, considering cell-nanoparticle localisation, spectral marker identification as a function of time and dose, and consistency of the method in different cell lines and for different nanoparticles, with a view towards assessing its potential as a non-invasive, label-free and High Content Nanotoxicological Screening technique.

In order to establish a toxicological assessment protocol based on Raman microspectroscopy, a progressive and congregate route is followed, from nanoparticle localisation to modelling of 3D plots based on spectral markers of toxicity which will ultimately allow the prediction of toxicity. Different commercially available nanoparticles are used as models throughout the study. 40 nm non-toxic carboxyl-

modified polystyrene nanoparticles (PSNPs) are employed to determine nanoparticle localisation and trafficking, whereas 100 nm toxic amine-modified polystyrene nanoparticles (PS-NH_2) are used to determine spectral markers of the toxicity. Generation 5 PAMAM dendrimers are used as a secondary toxic nanoparticle model for comparison of spectral markers of toxicity. Moreover, the consistency of the spectral markers in different cell lines has been investigated using model cell lines for cancerous and non-cancerous cells. Human adenocarcinoma cells (A549, American Type Culture Collection (ATTC) CCL-185TM), human lung epidermoid (Calu 1, European Collection of Authenticated Cell Cultures (ECACC) 93120818) and human bronchial epithelium cell line (BEAS-2B, ATCC CRL-9609™) were chosen as model cell lines as they mimic one of the primary exposure route of nanomaterials, which is inhalation.

8.3.2. Nanoparticle uptake and Trafficking

Raman microspectroscopy has been employed to determine the localisation of non-toxic carboxylated polystyrene nanoparticles inside the cellular transport organelles, including early endosomes, lysosomes and endoplasmic reticulum, as a function of time following their uptake (Efeoglu *et al.* 2015), (Chapter 3). Confocal microscopy with different organelle staining was used to determine the localisation of nanoparticles from 4 to 24 hour. Raman microspectroscopy was used to map the sub-cellular regions, at determined time points by confocal microscopy, to extract information regarding to nanoparticle localisation as nanoparticles are trafficked inside the cell.

Due to the variability of surface properties and size of the nanomaterials, cell-nanomaterial interaction can occur in various ways. However, one of the primary uptake mechanisms of the nanoparticles is known to be endocytosis (Treuel, Jiang, & Nienhaus 2013). Although different mechanisms of endocytosis have been identified (Doherty & McMahon 2009), endocytosis can be described as uptake of nanomaterials in membrane based vesicles. The confocal study showed the uptake mechanism of the carboxylated PSNPs by endocytosis and PSNPs are observed in early endosomes within 4 hours. Then, PSNPs are carried to lysosomes which act as the digestion/recycling system of the cells (12 hour). After 12 hour exposure of cells to the PSNPs, they are further trafficked to the endoplasmic reticulum, considered the final localisation point (Efeoglu *et al.* 2015). The Raman spectroscopic mapping of subcellular regions after 4, 12 and 24 hour exposure to the PSNPs provided invaluable information regarding not only nanoparticle localisation but also identification of Raman signatures of organelles with the aid of multivariate analysis techniques. Early endosomes, lysosomes and endoplasmic reticulum are mainly composed of lipids which make them difficult to differentiate from each other. However, the study showed the potential of Raman microspectroscopy to differentiate organelle signatures based completely on their intrinsic biochemical properties in completely label-free manner. The differentiating spectral signatures are best viewed as the PCA loadings of 4, 12 and 24 hour nanoparticle exposure data sets obtained from pairwise comparison of particle cluster and environment. Figure 8.1 shows varying the spectral signatures of endoplasmic reticulum, lysosome and endosomes after 4, 12 and 24 hour carboxy-PSNP exposure. The main differences on the spectral profiles of different organelles are highlighted with grey and some of the spectral markers are provided in Figure 8.1.

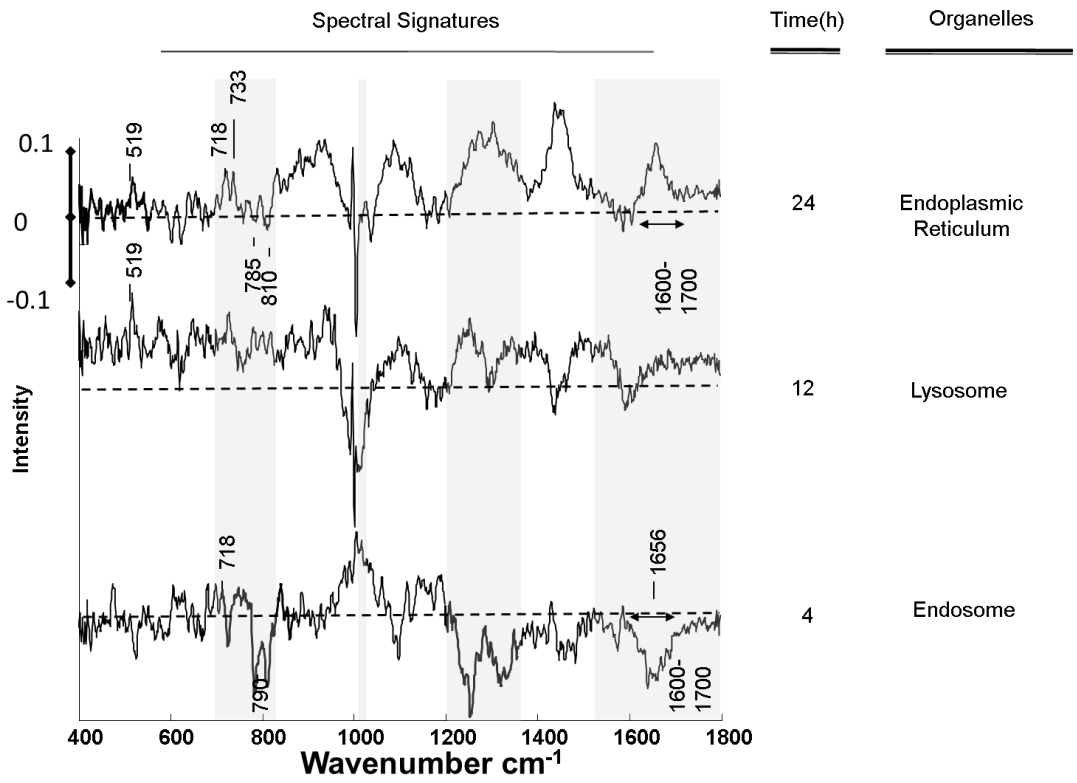

Figure 8.1. Comparison of PCA loadings of 4, 12 and 24 hour nanoparticle exposure data sets. Loadings are offset for clarity. The dotted line represents the zero '0' point for each loading and intensity scale of 0±0.1 is used for comparison. The figure is adapted from a published paper (Efeoglu *et al.* 2015).

8.3.3. Acute toxicity of Nanoparticles

8.3.3.1. Effects of Nanoparticles in Cytoplasm

While carboxylated and neutral PS nanoparticles are known to be non-toxic, their aminated counterparts are known to show acute toxicity as a result of oxidative stress in the endosomal and lysosomal pathway (Dorney *et al.* 2012; Efeoglu, Casey, & Byrne 2016; Efeoglu *et al.* 2015). In order to observe acute toxicity and corresponding responses, time and dose dependant Raman spectroscopic markers of cellular toxic

events were systematically monitored upon PS-NH_2 and PAMAM exposure to cancerous and non-cancerous cells (Efeoglu, Casey, & Byrne 2016; Efeoglu, Casey, & Byrne 2017; Efeoglu *et al.* 2017), (Chapter 4, 5, 6 and 7).

Upon PS-NH_2 exposure, the most dominant spectral marker is observed to be the 'doublet band' at 785 and 810 cm^{-1} in the cytoplasm, which indicates a change in the cytoplasmic RNA as a result of ROS formation and the doublet band is observed in particle exposed cells even at low doses (EC_{25}) and short exposure times (after 4 hour). The intensity of the band systematically and progressively changed as a function of dose and exposure time (Efeoglu, Casey, & Byrne 2016), (Chapter 4). The doublet band was also observed in the biochemical features of Calu-1 cells following PS-NH_2 exposure and progressively changed with extended exposure times (Efeoglu *et al.* 2017), (Chapter 5). When, a second toxic nanoparticle model, PAMAM dendrimers, was introduced to the A549 cells, a similar trend to that for PS-NH_2 is observed for the double peak at 785 and 810 cm^{-1}, which, together, with the results obtained from different cell lines and nanoparticle models, validates the changes in cytoplasmic RNA to be a spectral marker of toxicity (Efeoglu *et al.* 2017), (Chapter 6). The changes in the doublet band, upon exposure to PS-NH_2, are followed by concomitant and subsequent changes in the higher end of the fingerprint which provides information about protein (Amide I region) and lipid damage (1229 and 1438 cm^{-1}). The band at 1438 cm^{-1}, which has been identified upon PS-NH_2 exposure, was also identified after exposure to PAMAM dendrimers and it has been observed to provide information regarding to lipotoxicity (Efeoglu, Casey, & Byrne 2016; Efeoglu, Casey, & Byrne 2017; Efeoglu *et al.* 2017). Therefore, it can be concluded that Raman spectroscopy identifies signatures of the initiating toxic response and following cellular dependant

events, in real-time single assay and notably, brings new aspect to determination of nanomaterial toxicity by identifying cytoplasmic RNA as a spectral marker, which is not normally identified by conventional toxicity assays. Moreover, the doublet band can be seen as the first strong spectroscopic response of oxidative stress. Although, it does not measure the ROS directly, it provides information about the response, which is a ROS related change in cytoplasmic RNA. The onset of ROS formation upon nanoparticle exposure has been observed to be within 2-6 hours (Maher & Byrne 2016; Mukherjee *et al.* 2010), and this initial stage of ROS dies away due to the action of intracellular antioxidants with a similar timescale (Mukherjee *et al.* 2010). In contrast, the doublet band is observed only after 8 hour exposure to PS-NH_2 and increases further with exposure time. Figure 8.2 shows the loadings of PCA obtained from pairwise comparison of particle exposed cells (24 hour) and corresponding controls. Positive and negative features of the loadings relate to exposed and unexposed cells, relatively and the figure summarises spectral markers of acute toxic response in cytoplasm identified by Raman microspectroscopy.

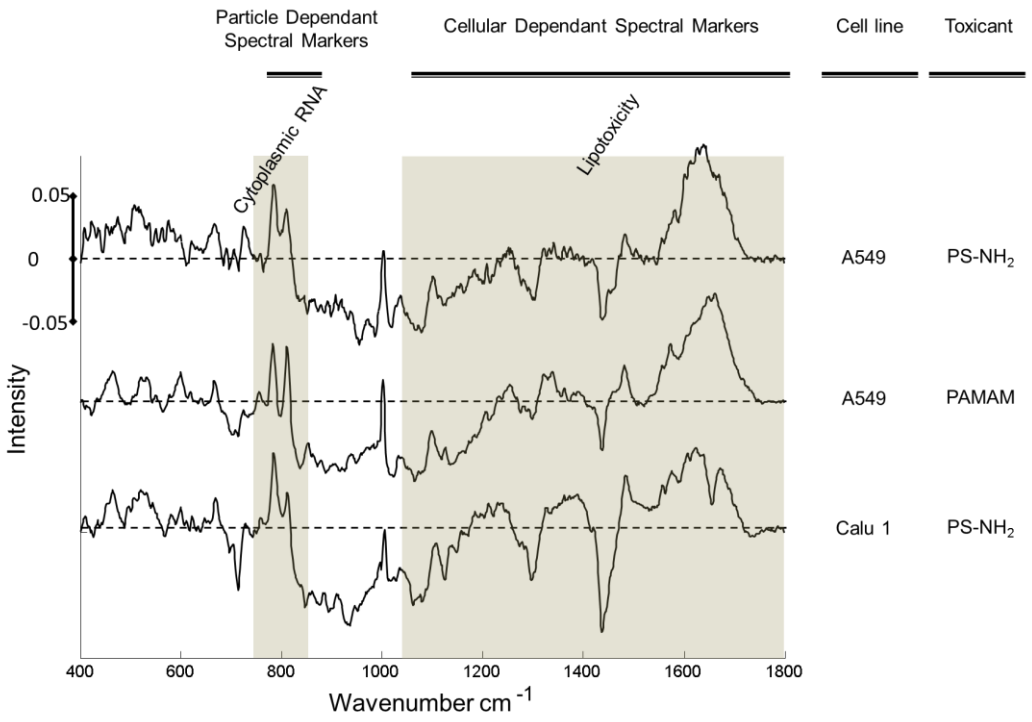

Figure 8.2. Spectral Markers of acute toxic response in cytoplasm of A549 and Calu-1 cells after 24 hour exposure to PS-NH_2 and PAMAM nanoparticles. Positive and negative features of the loadings relate to exposed and unexposed cells, relatively. The 750-830 cm^{-1} and above 1000 cm^{-1}region are indicated with highlights. Loadings are offset for clarity. The dotted line represents the zero '0' point for each loading and intensity scale of 0±0.05 is used for comparison.

The potential of Raman microspectroscopy as a single label-free technique with multi-parametric information was further analysed by focusing on the validation of the technique by comparing spectral marker evolution in non-cancerous cells lines with cancerous cell lines (Efeoglu *et al.* 2017) (Chapter 5) to build a 'high content' and 'label-free' Nanotoxicological assessment protocol. The spectral markers of toxic events such as oxidative stress and lysosomal damage have been identified as a function of time and the study showed that the identified spectral markers for cellular dependant events show consistency across multiple cell lines which allow the

identification of mechanism of action of the nanomaterial. The findings from the comparison of presence and progression of spectral markers, especially in low wavenumber region, have also shown the applicability of Raman spectroscopy to identify different cell death pathways in cancerous and non-cancerous cell lines (Figure 8.3) (Efeoglu *et al.* 2017). Positive and negative features of the loadings relate to exposed and unexposed cells, relatively (Chapter 5). The study showed the potential of Raman spectroscopy to provide further information regarding the mechanism of action as a single label free assay, without use of multiple labels and assays.

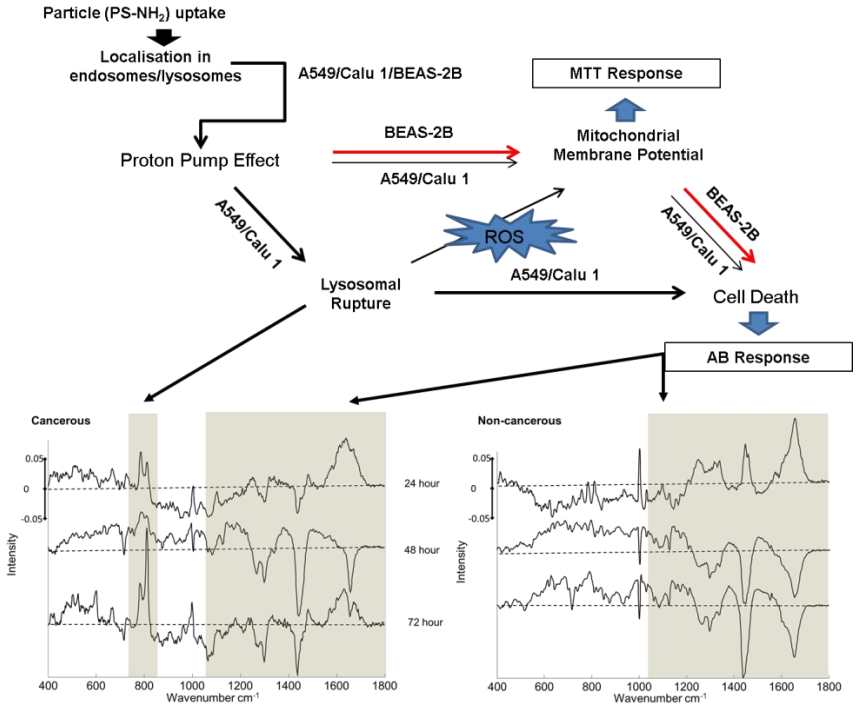

Figure 8.3. The schematic illustration of different cell death pathways on cancerous and non-cancerous cell lines and Raman spectral markers which are used to identify cell death pathways. Loadings are offset for clarity. The dotted line represents the zero '0' point for each loading and intensity scale of 0±0.05 is used for comparison (Efeoglu *et al.* 2017) .

8.3.3.1. Effects of Nanoparticles in the Nucleus and Nucleolus

Another notable outcome from the study has been determined to be the genotoxicity spectral markers. The spectral features of the nucleus and nucleolus showed significant changes as a function of time and dose upon PAMAM exposure. Nanoparticles such as PAMAM dendrimers are not fluorescent and do not provide contrast for EM studies, which makes cellular interaction studies challenging. Moreover, the small size of these dendrimers (~ 2-10nm, depending on dendrimer generation) (Dendritech 2017) makes them unsuitable for fluorescent labelling, which significantly changes their size and potentially their toxic properties. However, the use of Raman spectroscopy and systematic changes to the spectral signatures of biochemical composition of the cells can be used to elucidate their interaction with DNA and RNA inside the nucleus. The spectral range from 750 to 830 cm^{-1} is particularly useful to represent the mechanism of action of small non-fluorescent nanomaterials in nucleus and nucleolus. By comparison of PAMAM/DNA and PAMAM/RNA interactions, possible final localisation in the cells has been identified as the nucleolus which is not possible to observe with other current techniques (Efeoglu, Casey, & Byrne 2017). Spectral signatures of the post-translational modifications and corresponding biochemical changes, information which normally requires the use of multiple assays, have also been identified.

The high degree of consistency upon exposure to different toxicants indicates a promising future for the use of those spectral markers identified by Raman microspectroscopy in nanotoxicology and nanomedicine. Based on the similar trends for the toxicity of different nanoparticles, the evolution of the spectral markers was

further investigated to identify common and/or differing spectral markers of toxicity (Efeoglu *et al.* 2017) (Chapter 7). The findings of the study showed that, although spectral markers of cytoplasmic RNA, lipid and protein damage show consistencies, their evolutions show differences as a result of different response rates. Therefore, it can be concluded that Raman spectroscopy can give not only multi-parametric information based on intrinsic features of biochemicals upon toxicant exposure but also their response rates. Notably, in this study, especially at extended exposure times, a significantly different evolution of spectral markers has been observed for the two different types of toxic nanoparticles, which can be attributed to different cell death mechanisms. Although the changes were more significant at long exposure times, the different response rates of the bands at early time points also provided information regarding the different cell death mechanisms. Cell death upon toxicant exposure can occur in multiple ways, most notably apoptosis and necrosis. The conventional apoptosis/necrosis assays use colorimetric identification based on cellular uptake of dyes and give information related to whether apoptotic or necrotic cell death has occurred. However, Raman microscopy not only provides information regarding whether the cell is apoptotic or necrotic, but also the biochemical path leading to this differentiation (Figure 8.4).

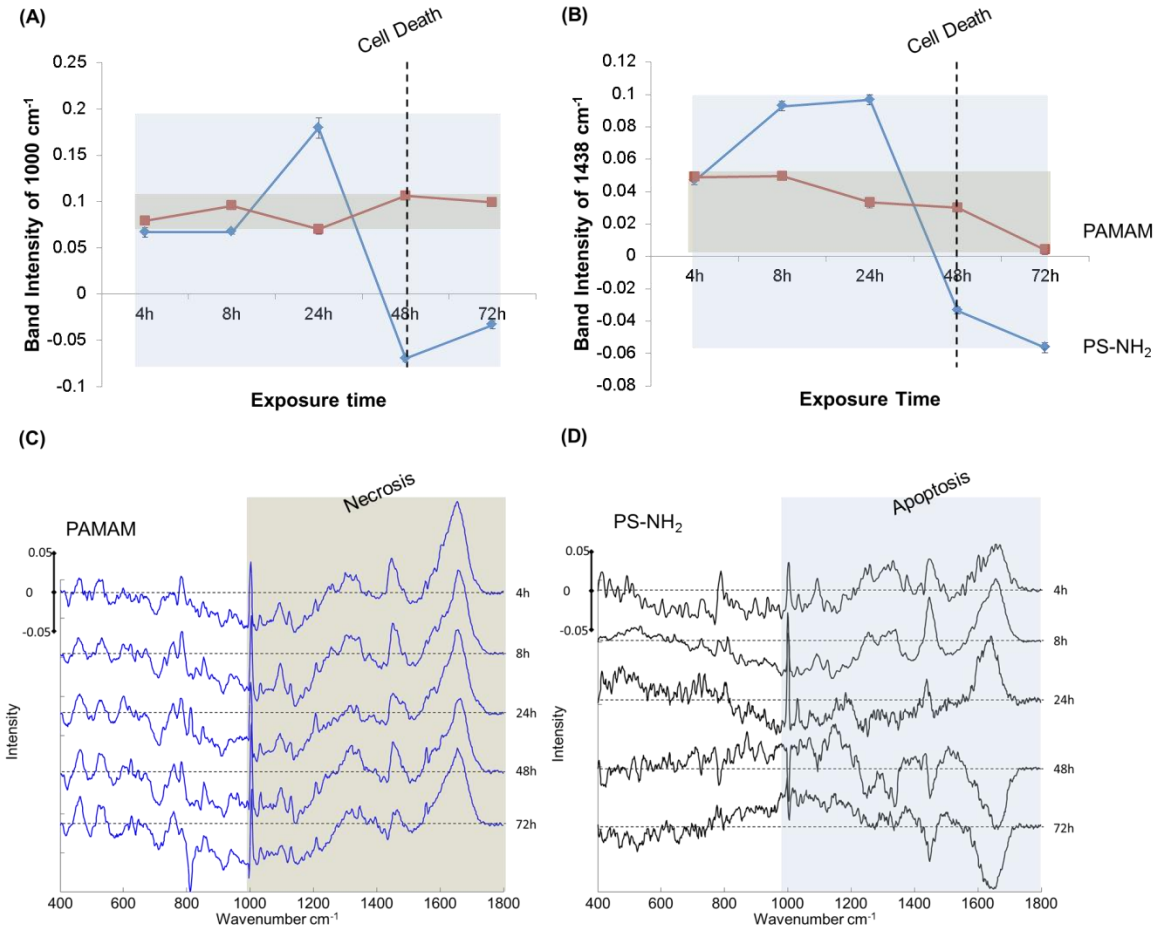

Figure 8.4. Spectral marker profiles of apoptotic and necrotic cell death. Comparison of Band intensities of 1003 (Phenylalanine) (A) and 1438 (Lipids) (B) cm^{-1} bands calculated from PC1 from pairwise PCA of nucleus of exposed cells and corresponding control. Comparison of PC1 obtained from pairwise PCA of nucleus of exposed cells and corresponding control for 4, 8, 24, 48 and 72 h PAMAM-G5 (C) and PS-NH2 (D) exposure. The changes in the band intensities for $PS\text{-}NH_2$ and PAMAM-G5 exposure are indicated with blue and red lines, respectively. Data are expressed as % of control mean ± SD. The negative side of the loading represents the spectral features of control, whereas positive side represents the cells exposed to $PS\text{-}NH_2$ and PAMAM-G5. Loadings are offset for clarity. The dotted line represents the zero '0' point for each loading and intensity scale of 0±0.05 is used for comparison.

Adopting the terminology of the Adverse Outcome Pathway methodology (OECD), upon exposure to a toxicant, the response begins with a molecular initiating event (MIE) which induces a cascade of consequent events. In the current context, the MIE is identified as the initial oxidative stress caused by the ingestion of the nanoparticles in exosomes and ultimately results in a change in cytoplasmic RNA, manifest as changes in the doublet peak of 785 cm^{-1} and 810cm^{-1}. The study of Maher *et al.* (Maher *et al.* 2014) showed that the MIE shows particle dependency and induces cellular dependant events which can include, for example, changes in mitochondrial function, activation of caspases, and release of inflammatory factors. However, conventional and commonly used cytotoxicity assays use specific markers which can be defined as 'endpoints' and identify the toxicity as a function of half-maximal effective dose 'EC_{50}'. Therefore, these assays remain limited to provide information regarding to multiple events that occur concomitantly or consecutively inside the cell. Raman microspectroscopy shows signatures of this cascade as presence of spectral markers of initiating toxic event at low doses and short exposure times in low wavenumber region (cytoplasmic RNA, indirect ROS), followed by concomitant changes (Protein and lipid damage as a result of cellular toxic events) in high wavenumber region of fingerprint.

8.3.2. 3D Toxic Response to Nanoparticles Determined by Raman Microspectroscopy

A notable finding from the studies based on comparison of the spectral profiles was the 3D dimensional correlation of the spectral markers. The 3D response surface of cytotoxicity has previously been highlighted (Maher *et al.* 2014), whereby similar responses are elicited when cells are exposed to higher concentrations of a toxicant for

short exposure time and low concentrations for longer exposure times. This 3D relationship is also evident in the time and dose dependences of the spectral markers identified by Raman microspectroscopy. Figure 8.5 shows the loadings of PC1 obtained from pairwise comparison of cytoplasm of particle exposed cells with their corresponding controls. The positive features represent the biochemical composition of the particle exposed cells, whereas negative features represent the composition of control cells. As seen in Figure 8.5(A),the loadings of the PCA from the cytoplasm of PS-NH_2 exposed cells show similar trends when cells are exposed to 10 μM (lethal dose) of PS-NH_2 for 8 hour and 2.5 μM (sublethal dose) for 48 hour. Moreover, the 3D response effect is observed for PAMAM dendrimers even between sublethal doses and the loadings showed similar features when the cells are exposed to EC_{10} for 24 hour and EC_{25} for 8 hour (Figure 8.5(B)).

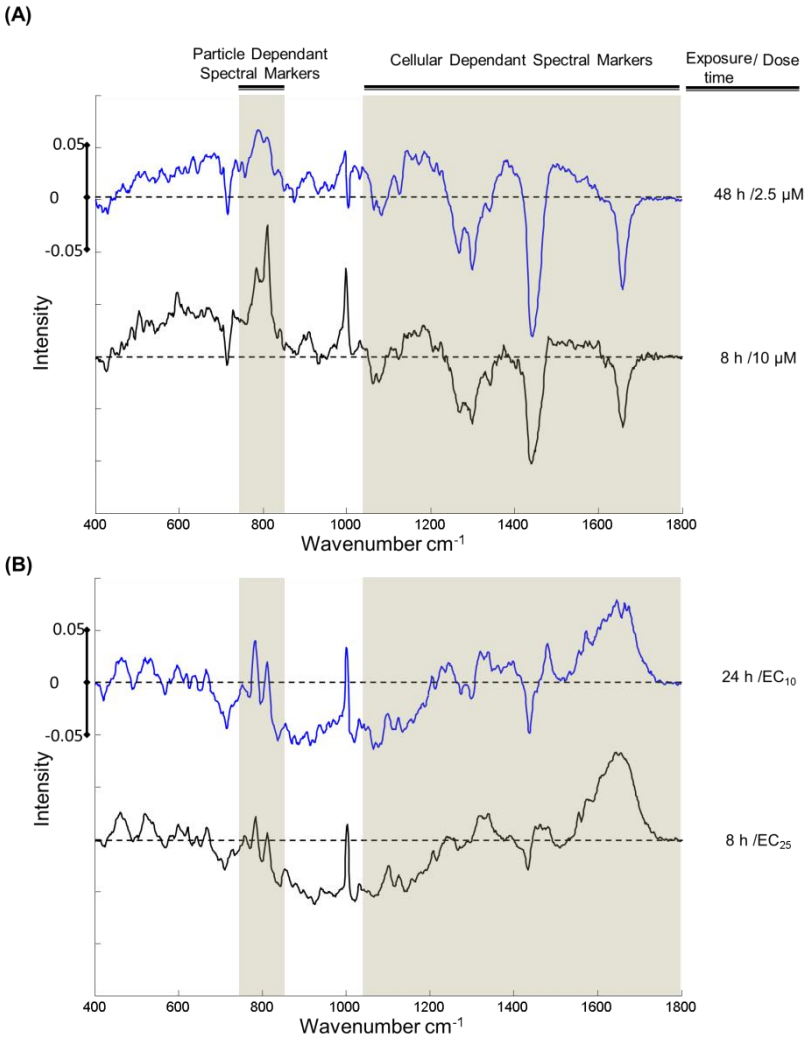

Figure 8.5. Comparisons of the loading 1 of PCA of cytoplasm for exposed and control cells. (A) After 8 h exposure to 10 µM (red) and 48 h 2.5 µM (blue) PS-NH_2. (B) After 8 h exposure to EC_{25} (red) and 24 h EC_{10}µM (blue) PAMAM dendrimers. Positive and negative features of the loadings relate to exposed and control cells, relatively. The areas that show similar responses are indicated with highlights. Loadings are offset for clarity. The dotted line represents the zero '0' point for each loading and intensity scale of 0±005 is used for comparison.

The 3D response has been also been monitored within the nuclear region (nucleus and nucleolus) for cells exposed to PAMAM dendrimers, as seen in Figure 8.6. The

spectral markers of genotoxicity, at 750-830 cm^{-1}, showed similar patterns when cells are exposed to EC_{10} for 24 hour and EC_{25} for 8 hour.

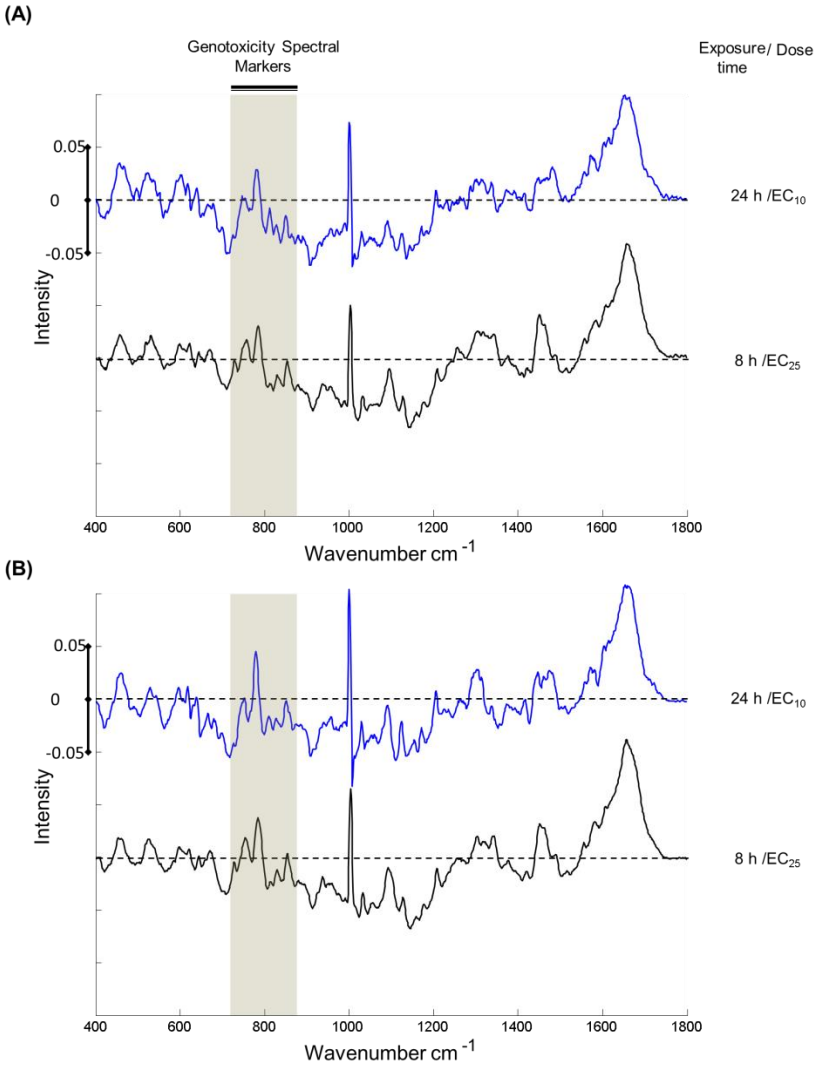

Figure 8.6. Comparison of the loading 1 of PCs of cytoplasm, nucleus and nucleolus for exposed and unexposed cells after 8 h exposure to EC_{25} (red) and 24 h EC_{10} (blue) PAMAM dendrimers. Positive and negative features of the loadings relate to exposed and unexposed cells, relatively. The 750-830 cm^{-1}area is indicated with highlights. Loadings are offset for clarity. The dotted line represents the zero '0' point for each loading and intensity scale of 0±0.05 is used for comparison.

The 3D toxic responses, which are observed based on identified spectral markers of the toxicity, can be represented in 3D plots of Spectral Marker intensities which can be used for the prediction of toxic events of any nanomaterial by observation of the spectral markers. As an example, the Raman spectral data sets for PAMAM dendrimers as a function of time and dose are used as an input to build 3D plots. The four main spectral markers which have been identified throughout the study, 785, 810, 1003 and 1438 cm^{-1}, are simultaneously plotted against time point and dose. The band intensities of the identified markers have been observed to change as a function of dose and time, which is manifest as an increase in the positive features, or inversion to negative features, of the loading of the PCA. The increase of the intensity of positive features can be attributed to an increase, accumulation and/or a conformational change of the biochemical constituent, whereas inversion to the negative features indicates damage and loss of the constituent upon exposure, in both cases compared to unexposed control. Figure 8.7 shows the representative 3D mesh and contour plot created to show spectral marker intensity distribution of the 785 and 810 cm^{-1} in the cytoplasm as a function of time and dose of PAMAM G5 exposure. A colour scale is provided to show intensity of the spectral marker for contour plots. In the 3D plots based on spectral marker intensities, a range of areas from safe to toxic can be identified and the plots can be further applied to different nanoparticles and pharmaceuticals to identify the range they fit into. The 785 and 810 cm^{-1} spectral marker was identified as one of the most significant markers observed throughout the study, showing dramatic and progressive changes as a function of dose and exposure times. The band at 785 cm^{-1} (nucleic acid) showed a progressive decrease with increasing dose, whereas an increase followed by decrease is observed with extended exposure times (Figure 8.7(A)). When the intensity of the spectral marker band at 785

cm^{-1} is correlated with 24 hour cellular %viability determined by AB assay as EC_{10}, EC_{25}, EC_{50} and EC_{75}, a significant correlation is observed and the intensity of the marker is reduced with reducing viability. The approximate viability values obtained from EC_{50} curve fits after 24 hour exposure are presented in Figure 8.7(B) in white text. The origin of the 810 cm^{-1}band has been identified as changes in cytoplasmic RNA as a result of formation of ROS. The intensity reaches its highest value at ~24-48 hour, after which a significant loss of the signature of cytoplasmic RNA can be observed (Figure 8.7(C and D).

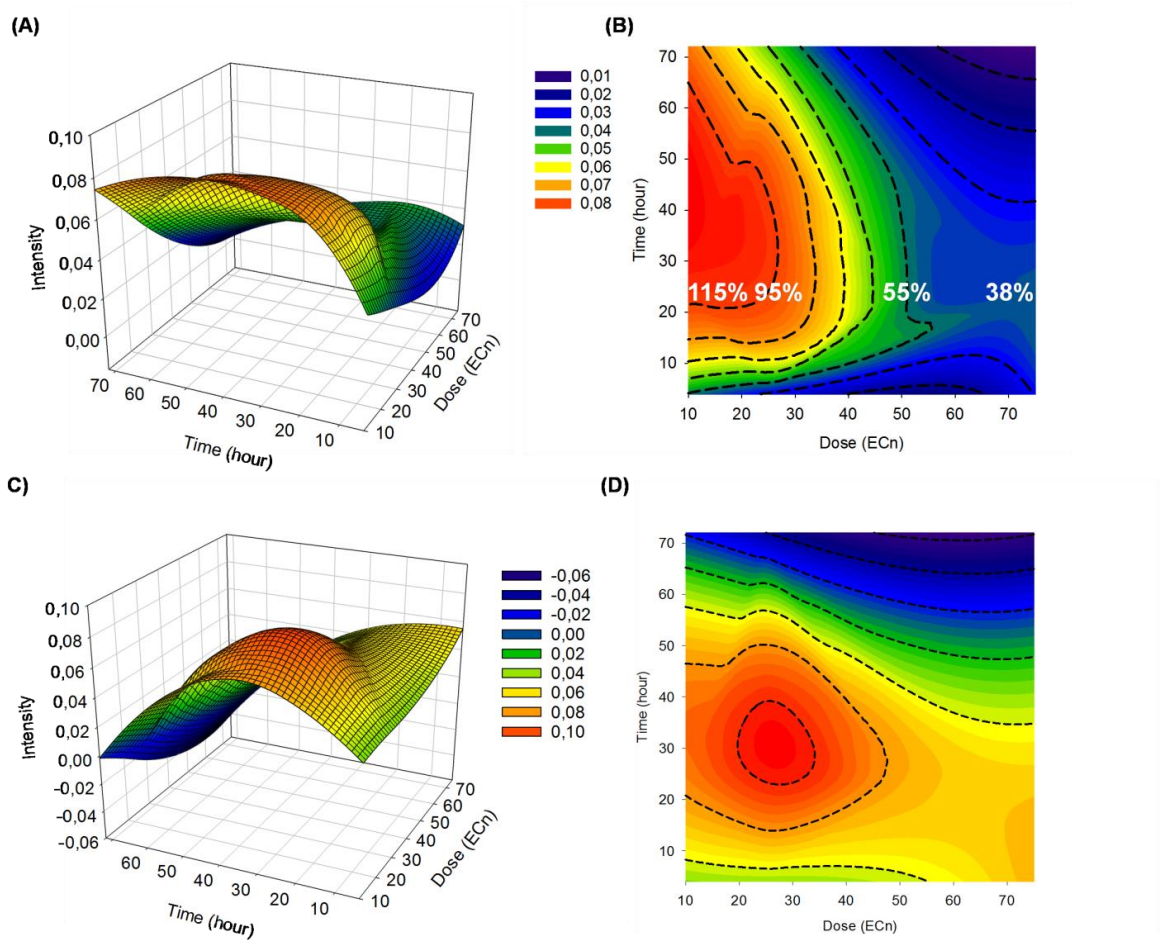

Figure 8.7. 3D mesh and contour plot of 785 (A, B) and 810 cm^{-1} (C, D) spectral marker intensity as a function of time (hour) and dose (EC_n). The 24 hr cellular viability at EC_{10}, EC_{25}, EC_{50} and EC_{75} determined by AB assay are indicated with percentages on the plot (white text).

However, this relation is not observed for the band at 810 cm^{-1} spectral marker. The different dose/time dependencies of the spectral markers can be related to consecutive cascade of events occurring within the cell upon a toxicant exposure. The band at 786 cm^{-1} originates from the ring breathing modes of nucleic acid bases (U, T and C) and also from O-P-O backbone. Therefore, the presence of the band in the features of the loadings can be attributed to nucleic acids, RNA and/or DNA (Movasaghi, Rehman, & Rehman 2007; Notingher & Hench 2006; Notingher *et al.* 2003). On the other hand,

the band at 810 cm^{-1} is known to be more specific to sugar-phosphate diester of RNA (Small & Peticolas 1971; Thomas, Medeiros, & Hartman 1971). The cytoplasmic RNA significantly gets affected by oxidative stress and increased ROS levels results repression of translation and accumulation of non-coding RNAs. A concomitant increase in the 785 cm^{-1} band can also be observed in short exposure times. A secondary increase in 785 cm^{-1} band, which evolves different, compared to 810 cm^{-1} band can be attributed to independent toxic event in the cell.

Notably, time evolution of the ROS dependant cytoplasmic RNA band (810 cm^{-1}) show significant differences to the simulation models of Maher *et al.* (Maher *et al.* 2014) (Figure 8.8). When the simulated cytotoxic (A) and spectroscopic data (B) are analysed, while similar patterns are observed, the evolution occurs over different timescale, which can be related to the formation of ROS as an initiating toxic event followed by changes in cytoplasmic RNA at later times, as response to ROS formation. However, due to the lack of data in our experimental model, the plots remained limited to show time related pattern in extended exposure times.

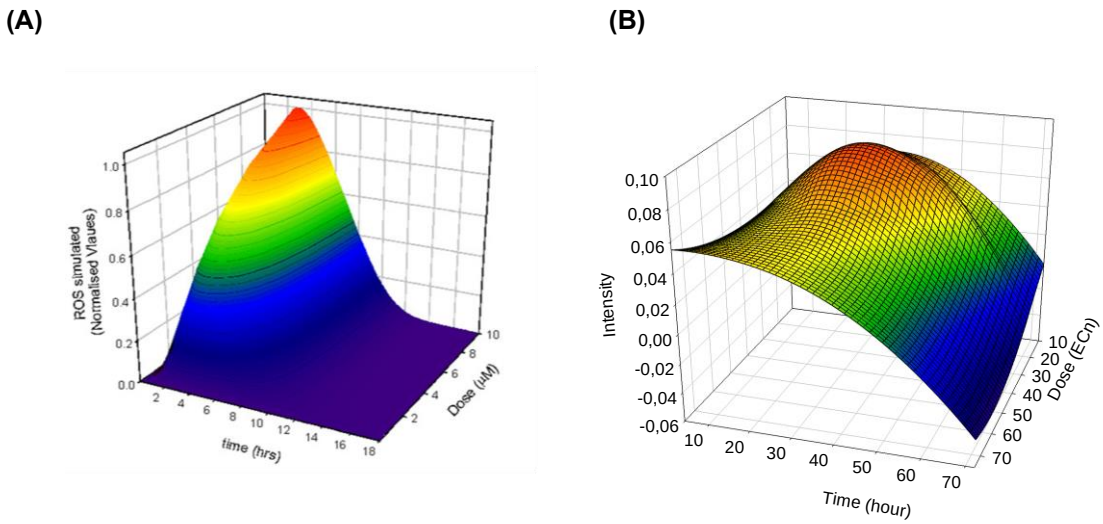

Figure 8.8. 3D mesh plots representing the response of (A) Simulated model of Reactive oxygen species (B) 810 cm^{-1} spectral marker intensity (A) is adapted from Maher *et al.* (Maher *et al.* 2014)

The 1003 cm^{-1} (protein) and 1438 cm^{-1} (lipotoxicity) spectral markers have been also plotted in the same format and are shown in Figure 8.9. The 3D plots show consistency with the 785 cm^{-1} spectral marker in terms of cellular viability. After 24 h exposure, with increasing dose, cellular viability is decreased with concomitant decrease in the intensity of the bands. Especially, at longer time points, the graphs remained limited due to lack of data.

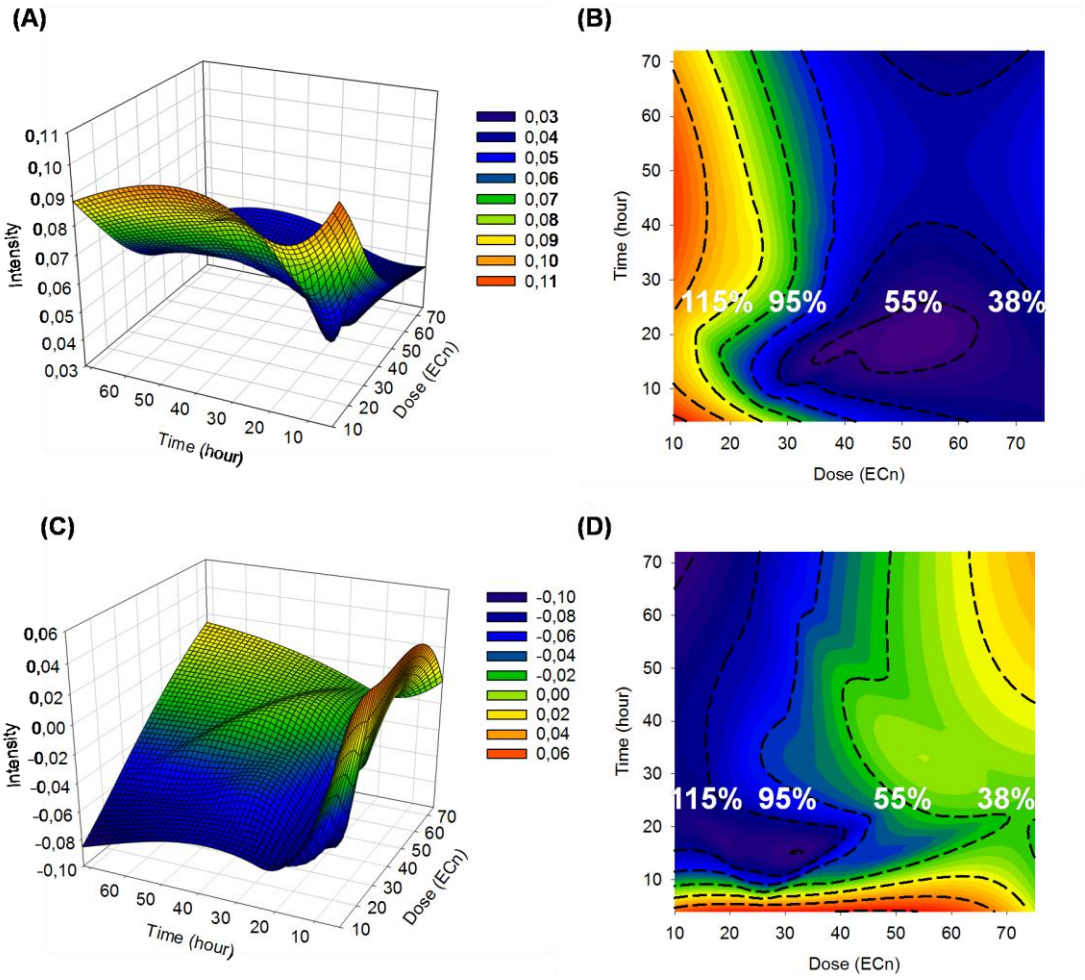

Figure 8.9. 3D mesh and contour plot 1003 (A and B) and 1438 (C and D) cm^{-1}spectral marker intensity as a function of time and dose. The cellular viability at EC_{10}, EC_{25}, EC_{50} and EC_{75} are indicated with percentages on the plot (white).

8.4. Future perspectives

The established 3D plots help to illustrate the potential of Raman microspectroscopy as a 'High Content Nanotoxicological Screening technique', which can be used to determine and predict Nanotoxicity based on spectral intensities. Although the plots are created for PAMAM dendrimers, the markers are derived from intrinsic properties of biochemical constituents of the cells which are related to individual cellular events

and the plots can be applied to a wide range of nanomaterials and potentially even to the pharmaceuticals.

Further refinements on the development of the plots can be achieved by the use of multiple time points and doses. With improved sensitivities of Raman microspectrometers, or through CARS and SRS techniques, real-time live cell monitoring can potentially be achieved. Moreover, the use of more sophisticated and quantitative multivariate techniques, such as Partial Least Squares Regression (PLSR) and Multivariate Curve Resolution Alternating Least Squares (MCR-ALS), for analysis Raman spectral data sets for the identification of spectral marker intensities can enable the establishment of improved 3D plots.

Nanocarrier systems for drug delivery applications has attracted a significant attention to achieve targeted delivery of drugs in area of interest and to develop personalized medicine (Kurzątkowska *et al.* 2017, Santiago *et al.* 2017, Stobiecka *et al.* 2016, Smith *et al.* 2017, Chon *et al.* 2009). The identified spectral markers and spectral features of Raman active nanocarriers can further be utilized to track the localization of the nanocarriers within a cell, as well as to monitor responses produced in cells upon release of drug from carriers. Notably, the nanocarriers are localised within the cell, initially in endosomes, and can be subsequently trafficked to lysosomes and, for example the endoplasmic reticulum, and the local environment of the nanoparticles and therefore the encapsulating vesicle can also be characterised by Raman microspectroscopic mapping (Efeoglu *et al.* 2015). In the case where random points in the cytoplasm or nucleus are recorded, at least at low to moderate doses, little or no contribution of the nanoparticles or their encapsulating environment is observed, and the recorded responses are primarily due to the cellular responses.

8.5. Conclusion

The work presented in this thesis has demonstrated the potential of Raman microspectroscopy as a label free high content toxicological screening technique which can utilized for the rapid advances in nanotoxicology and nanomedicine and investigation of wide range of nanomaterials real-time in a rapid, label-free way. The use of Raman microspectroscopy as a toxicological assessment protocol can provide many advantages over current techniques by using intrinsic features of biomaterials. The technique provides a multifaceted data which gives information about localisation and trafficking, cellular viability, mechanism of interaction, response rates and cell death mechanism as well as pathways leading to cell death. Continued development of instrumental technologies, and the emergence of nonlinear Raman techniques, promise real time, live cell monitoring of nanoparticle uptake and cellular response, for which more sophisticated, multivariate analysis and data-mining techniques will be required.

8.6. References

ACS *American Chemical Society International Historic Chemical Landmarks. The Raman Effect.* [Online]. Available: http://www.acs.org/content/acs/en/education/whatischemistry/landmarks/ramaneffect.html [Accessed July]

Adjouri, C, Elliasmine, A and Le Duff, Y. (1996). Low-Light-Level Raman Spectroscopy Using a Charge-Coupled Device Detectorlow-Light-Level Raman Spectroscopy Using a Charge-Coupled Device Detector (Vol. 11, pp. 46-9). (Eugene, Oregon): Spectroscopy

Ahlinder, L, Ekstrand-Hammarström, B, Geladi, P and Österlund, L (2013) Large Uptake of Titania and Iron Oxide Nanoparticles in the Nucleus of Lung Epithelial Cells as Measured by Raman Imaging and Multivariate Classification. *Biophysical Journal*, 105(2), 310-9.

Bankapur, A, Krishnamurthy, R S, Zachariah, E, Santhosh, C, Chougule, B, Praveen, B, Valiathan, M and Mathur, D (2012) Micro-Raman Spectroscopy of Silver Nanoparticle Induced Stress on Optically-Trapped Stem Cells. *PLOS ONE*, 7(4), e35075.

Berridge, M V, Herst, P M and Tan, A S (2005) Tetrazolium Dyes as Tools in Cell Biology: New Insights into Their Cellular Reduction. *Biotechnol Annu Rev*, 11, 127-52.

Bonnier, F, Knief, P, Lim, B, Meade, A D, Dorney, J, Bhattacharya, K, Lyng, F M and Byrne, H J (2010) Imaging Live Cells Grown on a Three Dimensional Collagen Matrix Using Raman Microspectroscopy. *Analyst,* 135(12), 3169-77.

Bonnier, F, Mehmood, A, Knief, P, Meade, A D, Hornebeck, W, Lambkin, H, Flynn, K, McDonagh, V, Healy, C, Lee, T C, Lyng, F M and Byrne, H J (2011) *In vitro* Analysis of Immersed Human Tissues by Raman Microspectroscopy. *Journal of Raman Spectroscopy,* 42(5), 888-96.

Bonnier, F, Petitjean, F, Baker, M J and Byrne, H J (2014) Improved Protocols for Vibrational Spectroscopic Analysis of Body Fluids. *Journal of Biophotonics,* 7(3-4), 167-79.

Brayden, D J, Cryan, S-A, Dawson, K A, O'Brien, P J and Simpson, J C (2015) High-Content Analysis for Drug Delivery and Nanoparticle Applications. *Drug Discovery Today,* 20(8), 942-57.

Breve, G J P a J (1996). Whole Cell Studies and Tissue Characterization by Raman Spectroscopy In *"Biomedical Applications of Spectroscopy"* Vol. 25, John Wiley and Sons, New York.

Brigger, I, Dubernet, C and Couvreur, P (2012) Nanoparticles in Cancer Therapy and Diagnosis. *Advanced Drug Delivery Reviews,* 64, Supplement, 24-36.

Brzoska, M, Langer, K, Coester, C, Loitsch, S, Wagner, T O and Mallinckrodt, C (2004) Incorporation of Biodegradable Nanoparticles into Human Airway Epithelium Cells-*in vitro* Study of the Suitability as a Vehicle for Drug or Gene Delivery in Pulmonary Diseases. *Biochem Biophys Res Commun,* 318(2), 562-70.

Butler, H J, Ashton, L, Bird, B, Cinque, G, Curtis, K, Dorney, J, Esmonde-White, K, Fullwood, N J, Gardner, B, Martin-Hirsch, P L, Walsh, M J, McAinsh, M R, Stone, N and Martin, F L (2016) Using Raman Spectroscopy to Characterize Biological Materials. *Nat. Protocols,* 11(4), 664-87.

Byrne, H J, Sockalingum, G D and Stone, N (2011). Chapter 4 Raman Microscopy: Complement or Competitor? In *Biomedical Applications of Synchrotron Infrared Microspectroscopy: A Practical Approach*, The Royal Society of Chemistry.

Carey, P R (1982) *Biochemical Applications of Raman and Resonance Raman Spectroscopies / P.R. Carey*, Academic Press, New York.

Carvalho, L F, Bonnier, F, O'Callaghan, K, O'Sullivan, J, Flint, S, Byrne, H J and Lyng, F M (2015) Raman Micro-Spectroscopy for Rapid Screening of Oral Squamous Cell Carcinoma. *Exp Mol Pathol,* 98(3), 502-9.

Casey, A, Herzog, E, Davoren, M, Lyng, F M, Byrne, H J and Chambers, G (2007) Spectroscopic Analysis Confirms the Interactions between Single Walled Carbon Nanotubes and Various Dyes Commonly Used to Assess Cytotoxicity. *Carbon,* 45(7), 1425-32.

Casey, A, Herzog, E, Lyng, F M, Byrne, H J, Chambers, G and Davoren, M (2008) Single Walled Carbon Nanotubes Induce Indirect Cytotoxicity by Medium Depletion in A549 Lung Cells. *Toxicology Letters,* 179(2), 78-84.

Chew, W S, Poh, K W, Siddiqi, N J, Alhomida, A S, Yu, L E and Ong, W Y (2012) Short- and Long-Term Changes in Blood Mirna Levels after Nanogold Injection in Rats--Potential Biomarkers of Nanoparticle Exposure. *Biomarkers,* 17(8), 750-7.

Chon H, Lee S, Son SW, Oh CH and Choo J (2009) Highly Sensitive Immunoassay of Lung Cancer Marker Carcinoembryonic Antigen Using Surface-Enhanced Raman Scattering of Hollow Gold Nanospheres. Anal Chem, 81 (8), 3029–3034.

Dendritech, I (2017) *Pamam Dendrimers* [Online]. Available: http://www.dendritech.com/pamam.html

Ding, G J, Fischer, P A, Boltz, R C, Schmidt, J A, Colaianne, J J, Gough, A, Rubin, R A and Miller, D K (1998) Characterization and Quantitation of Nf-Kappab Nuclear Translocation Induced by Interleukin-1 and Tumor Necrosis Factor-Alpha. Development and Use of a High Capacity Fluorescence Cytometric System. *J Biol Chem*, 273(44), 28897-905.

Doherty, G J and McMahon, H T (2009) Mechanisms of Endocytosis. *Annu Rev Biochem,* 78, 857-902.

Donaldson, K, Stone, V, Tran, C L, Kreyling, W and Borm, P J (2004). Nanotoxicology In *Occup Environ Med* Vol. 61 England.

Donath, I (2011) Nanoparticle Uptake and Their Co-Localization with Cell Compartments – a Confocal Raman Microscopy Study at Single Cell Level. *Journal of Physics: Conference Series*, 304(1), 012017.

Dorney, J, Bonnier, F, Garcia, A, Casey, A, Chambers, G and Byrne, H J (2012) Identifying and Localizing Intracellular Nanoparticles Using Raman Spectroscopy. *Analyst,* 137(5), 1111-9.

Draux, F, Jeannesson, P, Beljebbar, A, Tfayli, A, Fourre, N, Manfait, M, Sule-Suso, J and Sockalingum, G D (2009) Raman Spectral Imaging of Single Living Cancer Cells: A Preliminary Study. *Analyst,* 134(3), 542-8.

Efeoglu, E, Casey, A and Byrne, H J (2016) *In vitro* Monitoring of Time and Dose Dependent Cytotoxicity of Aminated Nanoparticles Using Raman Spectroscopy. *Analyst,* 141(18), 5417-31.

Efeoglu, E, Casey, A and Byrne, H J. (2017). Determination of Spectral Markers of Cytotoxicity and Genotoxicity Using *in vitro* Raman Microspectroscopy: Cellular Responses to Polyamidoamine Dendrimer Exposure, Journal of Biophotonics, Submitted.

Efeoglu, E, Keating, M, McIntyre, J, Casey, A and Byrne, H J (2015) Determination of Nanoparticle Localisation within Subcellular Organelles *in vitro* Using Raman Spectroscopy. *Analytical Methods*, 7(23), 10000-17.

Efeoglu, E, Maher, M A, Casey, A, Byrne, H J. (2017) Label-Free, High Content Screening Using Raman Microspectroscopy: The Toxicological Response of Different Cell Lines to Amine-Modified Polystyrene Nanoparticles (PS-NH_2), *Analyst*, DOI: 10.1039/C7AN00461C.

EU'NanoSafetyCluster' *Nanosafety Cluster* [Online]. Available: https://www.nanosafetycluster.eu/

Fazlollahi, F, Angelow, S, Yacobi, N R, Marchelletta, R, Yu, A S L, Hamm-Alvarez, S F, Borok, Z, Kim, K-J and Crandall, E D (2011) Polystyrene Nanoparticle Trafficking across Mdck-Ii. *Nanomedicine : nanotechnology, biology, and medicine,* 7(5), 588-94.

Godbey, W T, Wu, K K and Mikos, A G (1999) Tracking the Intracellular Path of Poly(Ethylenimine)/Dna Complexes for Gene Delivery. *Proceedings of the National Academy of Sciences of the United States of America*, 96(9), 5177-81.

Guisbiers, G (2010) Size-Dependent Materials Properties toward a Universal Equation. *Nanoscale Research Letters,* 5(7), 1132-6.

Handbook of Biological Confocal Microscopy (2006), Springer US.

Herzog, E, Casey, A, Lyng, F M, Chambers, G, Byrne, H J and Davoren, M (2007) A New Approach to the Toxicity Testing of Carbon-Based Nanomaterials--the Clonogenic Assay. *Toxicol Lett,* 174(1-3), 49-60.

Hillegass, J M, Shukla, A, Lathrop, S A, MacPherson, M B, Fukagawa, N K and Mossman, B T (2010) Assessing Nanotoxicity in Cells *in vitro*. *Wiley interdisciplinary reviews. Nanomedicine and nanobiotechnology,* 2(3), 219-31.

Holder, A L, Goth-Goldstein, R, Lucas, D and Koshland, C P (2012) Particle-Induced Artifacts in the Mtt and Ldh Viability Assays. *Chemical research in toxicology,* 25(9), 1885-92.

Institute of Medicine (US) Roundtable on Environmental Health Sciences, R, and Medicine (2005) *Implications of Nanotechnology for Environmental Health Research*, National Academies Press (US), Washington (DC).

Jagiello, K, Chomicz, B, Avramopoulos, A, Gajewicz, A, Mikolajczyk, A, Bonifassi, P, Papadopoulos, M G, Leszczynski, J and Puzyn, T (2017) Size-Dependent Electronic Properties of Nanomaterials: How This Novel Class of Nanodescriptors Supposed to Be Calculated? *Structural Chemistry,* 28(3), 635-43.

Jan, E, Byrne, S J, Cuddihy, M, Davies, A M, Volkov, Y, Gun'ko, Y K and Kotov, N A (2008) High-Content Screening as a Universal Tool for Fingerprinting of Cytotoxicity of Nanoparticles. *ACS Nano,* 2(5), 928-38.

Jermyn, M, Mok, K, Mercier, J, Desroches, J, Pichette, J, Saint-Arnaud, K, Bernstein, L, Guiot, M-C, Petrecca, K and Leblond, F (2015) Intraoperative Brain Cancer Detection with Raman Spectroscopy in Humans. *Science Translational Medicine,* 7(274), 274ra19.

Jin, Y, Kannan, S, Wu, M and Zhao, J X (2007) Toxicity of Luminescent Silica Nanoparticles to Living Cells. *Chem Res Toxicol,* 20(8), 1126-33.

Karlsson, H L, Cronholm, P, Gustafsson, J and Moller, L (2008) Copper Oxide Nanoparticles Are Highly Toxic: A Comparison between Metal Oxide Nanoparticles and Carbon Nanotubes. *Chem Res Toxicol,* 21(9), 1726-32.

Kawasaki, E S and Player, A (2005) Nanotechnology, Nanomedicine, and the Development of New, Effective Therapies for Cancer. *Nanomedicine,* 1(2), 101-9.

Keating, M E, Bonnier, F and Byrne, H J (2012) Spectral Cross-Correlation as a Supervised Approach for the Analysis of Complex Raman Datasets: The Case of Nanoparticles in Biological Cells. *Analyst,* 137(24), 5792-802.

Kim, H R, Park, Y J, Shin, D Y, Oh, S M and Chung, K H (2013) Appropriate *in vitro* Methods for Genotoxicity Testing of Silver Nanoparticles. *Environmental Health and Toxicology,* 28, e2013003.

Klein, K, Gigler, Alexander M, Aschenbrenner, T, Monetti, R, Bunk, W, Jamitzky, F, Morfill, G, Stark, Robert W and Schlegel, J (2012) Label-Free Live-Cell Imaging with Confocal Raman Microscopy. *Biophysical Journal,* 102(2), 360-8.

Knief, P, Clarke, C, Herzog, E, Davoren, M, Lyng, F M, Meade, A D and Byrne, H J (2009) Raman Spectroscopy - a Potential Platform for the Rapid Measurement of Carbon Nanotube-Induced Cytotoxicity. *Analyst,* 134(6), 1182-91.

Krauss, S D, Petersen, D, Niedieker, D, Fricke, I, Freier, E, El-Mashtoly, S F, Gerwert, K and Mosig, A (2015) Colocalization of Fluorescence and Raman Microscopic Images for the Identification of Subcellular Compartments: A Validation Study. *Analyst,* 140(7), 2360-8.

Kurzątkowska K, Santiago T, Hepel M (2017) Plasmonic nanocarrier grid-enhanced Raman sensor for studies of anticancer drug delivery. Biosens Bioelectron, 91, 780-787.

Laurvick, C A C and Singaraju, B (2003) Nanotechnology in Aerospace Systems. *IEEE Aerospace and Electronic Systems Magazine,* 18(9), 18-22.

Li, J, Strong, R, Trevisan, J, Fogarty, S W, Fullwood, N J, Jones, K C and Martin, F L (2013) Dose-Related Alterations of Carbon Nanoparticles in Mammalian Cells Detected Using Biospectroscopy: Potential for Real-World Effects. *Environ Sci Technol,* 47(17), 10005-11.

Li, J, Ying, G G, Jones, K C and Martin, F L (2015) Real-World Carbon Nanoparticle Exposures Induce Brain and Gonadal Alterations in Zebrafish (Danio Rerio) as Determined by Biospectroscopy Techniques. *Analyst,* 140(8), 2687-95.

Liebel, U and Link, W (2007) Meeting Report: Trends and Challenges in High Content Analysis. *Biotechnol J,* 2(8), 938-40.

Maher, M A and Byrne, H J (2016) Modification of the *in vitro* Uptake Mechanism and Antioxidant Levels in Hacat Cells and Resultant Changes to Toxicity and Oxidative Stress of G4 and G6 Poly(Amidoamine) Dendrimer Nanoparticles. *Anal Bioanal Chem,* 408(19), 5295-307.

Maher, M A, Naha, P C, Mukherjee, S P and Byrne, H J (2014) Numerical Simulations of *in vitro* Nanoparticle Toxicity – the Case of Poly(Amido Amine) Dendrimers. *Toxicology in vitro,* 28(8), 1449-60.

Manke, A, Wang, L and Rojanasakul, Y (2013) Mechanisms of Nanoparticle-Induced Oxidative Stress and Toxicity. *BioMed Research International,* 2013, 15.

Martinez, E, Lagunas, A, Mills, C A, Rodriguez-Segui, S, Estevez, M, Oberhansl, S, Comelles, J and Samitier, J (2009) Stem Cell Differentiation by Functionalized Micro- and Nanostructured Surfaces. *Nanomedicine (Lond),* 4(1), 65-82.

Miljkovic, M, Chernenko, T, Romeo, M J, Bird, B, Matthaus, C and Diem, M (2010) Label-Free Imaging of Human Cells: Algorithms for Image Reconstruction of Raman Hyperspectral Datasets. *Analyst,* 135(8), 2002-13.

Mori, T, Takada, H, Ito, S, Matsubayashi, K, Miwa, N and Sawaguchi, T (2006) Preclinical Studies on Safety of Fullerene Upon Acute Oral Administration and Evaluation for No Mutagenesis. *Toxicology,* 225(1), 48-54.

Mosmann, T (1983) Rapid Colorimetric Assay for Cellular Growth and Survival: Application to Proliferation and Cytotoxicity Assays. *J Immunol Methods,* 65(1-2), 55-63.

Movasaghi, Z, Rehman, S and Rehman, I U (2007) Raman Spectroscopy of Biological Tissues. *Applied Spectroscopy Reviews,* 42(5), 493-541.

Mukherjee, S P and Byrne, H J (2013) Polyamidoamine Dendrimer Nanoparticle Cytotoxicity, Oxidative Stress, Caspase Activation and Inflammatory Response: Experimental Observation and Numerical Simulation. *Nanomedicine,* 9(2), 202-11.

Mukherjee, S P, Davoren, M and Byrne, H J (2010) *In vitro* Mammalian Cytotoxicological Study of Pamam Dendrimers - Towards Quantitative Structure Activity Relationships. *Toxicol In vitro,* 24(1), 169-77.

Mukherjee, S P, Lyng, F M, Garcia, A, Davoren, M and Byrne, H J (2010) Mechanistic Studies of *in vitro* Cytotoxicity of Poly(Amidoamine) Dendrimers in Mammalian Cells. *Toxicol Appl Pharmacol,* 248(3), 259-68.

Naha, P C and Byrne, H J (2013) Generation of Intracellular Reactive Oxygen Species and Genotoxicity Effect to Exposure of Nanosized Polyamidoamine (Pamam) Dendrimers in Plhc-1 Cells *in vitro*. *Aquat Toxicol,* 132-133, 61-72.

Naha, P C, Davoren, M, Lyng, F M and Byrne, H J (2010) Reactive Oxygen Species (Ros) Induced Cytokine Production and Cytotoxicity of Pamam Dendrimers in J774a.1 Cells. *Toxicology and Applied Pharmacology,* 246(1–2), 91-9.

Nel, A E, Madler, L, Velegol, D, Xia, T, Hoek, E M V, Somasundaran, P, Klaessig, F, Castranova, V and Thompson, M (2009) Understanding Biophysicochemical Interactions at the Nano-Bio Interface. *Nat Mater,* 8(7), 543-57.

Notingher, I and Hench, L L (2006) Raman Microspectroscopy: A Noninvasive Tool for Studies of Individual Living Cells *in vitro*. *Expert Rev Med Devices,* 3(2), 215-34.

Notingher, I, Verrier, S, Haque, S, Polak, J M and Hench, L L (2003) Spectroscopic Study of Human Lung Epithelial Cells (A549) in Culture: Living Cells Versus Dead Cells. *Biopolymers,* 72(4), 230-40.

Nune, S K, Gunda, P, Thallapally, P K, Lin, Y-Y, Forrest, M L and Berkland, C J (2009) Nanoparticles for Biomedical Imaging. *Expert opinion on drug delivery,* 6(11), 1175-94.

Oberdörster, G, Maynard, A, Donaldson, K, Castranova, V, Fitzpatrick, J, Ausman, K, Carter, J, Karn, B, Kreyling, W, Lai, D, Olin, S, Monteiro-Riviere, N, Warheit, D and Yang, H (2005) Principles for Characterizing the Potential Human Health Effects from Exposure to Nanomaterials: Elements of a Screening Strategy. *Particle and Fibre Toxicology,* 2(1), 8.

OECD *Adverse Outcome Pathways, Molecular Screening and Toxicogenomics* [Online]. Available: http://www.oecd.org/chemicalsafety/testing/adverse-outcome-pathways-molecular-screening-and-toxicogenomics.htm

OECD *Safety of Manufactured Nanomaterials* [Online]. Available: http://www.oecd.org/science/nanosafety/

OECD. (2010). Oecd, Series on the Safety of Manufactured Nanomaterials (pp. 46).

Park, K (2007) Nanotechnology: What It Can Do for Drug Delivery. *Journal of controlled release : official journal of the Controlled Release Society,* 120(1-2), 1-3.

Pezacki, J P, Blake, J A, Danielson, D C, Kennedy, D C, Lyn, R K and Singaravelu, R (2011) Chemical Contrast for Imaging Living Systems: Molecular Vibrations Drive Cars Microscopy. *Nat Chem Biol,* 7(3), 137-45.

Radio, N M, Breier, J M, Shafer, T J and Mundy, W R (2008) Assessment of Chemical Effects on Neurite Outgrowth in Pc12 Cells Using High Content Screening. *Toxicol Sci,* 105(1), 106-18.

Raj, S, Jose, S, Sumod, U S and Sabitha, M (2012) Nanotechnology in Cosmetics: Opportunities and Challenges. *Journal of Pharmacy & Bioallied Sciences,* 4(3), 186-93.

Rampersad, S N (2012) Multiple Applications of Alamar Blue as an Indicator of Metabolic Function and Cellular Health in Cell Viability Bioassays. *Sensors,* 12(9).

Recent Trends in Nanotechnology and Materials Science (2014), 1 ed, Springer International Publishing.

Rhiem, S, Riding, M J, Baumgartner, W, Martin, F L, Semple, K T, Jones, K C, Schäffer, A and Maes, H M (2015) Interactions of Multiwalled Carbon Nanotubes with Algal Cells: Quantification of Association, Visualization of Uptake, and Measurement of Alterations in the Composition of Cells. *Environmental pollution (Barking, Essex : 1987),* 196, 431-9.

Riss, T L, Moravec, R A, Niles, A L, Duellman, S, Benink, H A, Worzella, T J and Minor, L (2004). Cell Viability Assays In Sittampalam, G S, Coussens, N P, Brimacombe, K, Grossman, A, Arkin, M, Auld, D, Austin, C, Bejcek, B, Glicksman, M, Inglese, J, Iversen, P W, Li, Z, McGee, J, McManus, O, Minor, L, Napper, A, Peltier, J M, Riss, T, Trask, O J, Jr. and Weidner, J (Eds) *Assay Guidance Manual*, Eli Lilly & Company and the National Center for Advancing Translational Sciences, Bethesda (MD).

Ruan, B, Pong, K, Jow, F, Bowlby, M, Crozier, R A, Liu, D, Liang, S, Chen, Y, Mercado, M L, Feng, X, Bennett, F, von Schack, D, McDonald, L, Zaleska, M M, Wood, A, Reinhart, P H, Magolda, R L, Skotnicki, J, Pangalos, M N, Koehn, F E, Carter, G T, Abou-Gharbia, M and Graziani, E I (2008) Binding of Rapamycin Analogs to Calcium Channels and Fkbp52 Contributes to Their Neuroprotective Activities. *Proc Natl Acad Sci U S A,* 105(1), 33-8.

Sailor, M J and Link, J R (2005) "Smart Dust": Nanostructured Devices in a Grain of Sand. *Chemical Communications*(11), 1375-83.

Salvati, A, Aberg, C, dos Santos, T, Varela, J, Pinto, P, Lynch, I and Dawson, K A (2011) Experimental and Theoretical Comparison of Intracellular Import of Polymeric Nanoparticles and Small Molecules: Toward Models of Uptake Kinetics. *Nanomedicine,* 7(6), 818-26.

Sandin, P, Fitzpatrick, L W, Simpson, J C and Dawson, K A (2012) High-Speed Imaging of Rab Family Small Gtpases Reveals Rare Events in Nanoparticle Trafficking in Living Cells. *ACS Nano,* 6(2), 1513-21.

Santiago T, DeVaux RS, Kurzatkowska K, Espinal R, Herschkowitz JI, Hepel M (2017) Surface-enhanced Raman scattering investigation of targeted delivery and controlled release of gemcitabine. Int J Nanomedicine, 12, 7763-7776.

Sarker, K P, Kataoka, H, Chan, A, Netherton, S J, Pot, I, Huynh, M A, Feng, X, Bonni, A, Riabowol, K and Bonni, S (2008) Ing2 as a Novel Mediator of Transforming Growth Factor-Beta-Dependent Responses in Epithelial Cells. *J Biol Chem,* 283(19), 13269-79.

Shapero, K, Fenaroli, F, Lynch, I, Cottell, D C, Salvati, A and Dawson, K A (2011) Time and Space Resolved Uptake Study of Silica Nanoparticles by Human Cells. *Mol Biosyst,* 7(2), 371-8.

Sierra, M I, Valdés, A, Fernández, A F, Torrecillas, R and Fraga, M F (2016) The Effect of Exposure to Nanoparticles and Nanomaterials on the Mammalian Epigenome. *International Journal of Nanomedicine,* 11, 6297-306.

Small, E W and Peticolas, W L (1971) Conformational Dependence of the Raman Scattering Intensities from Polynucleotides. *Biopolymers,* 10(1), 69-88.

Smith M and Hepel M (2017) Controlled release of targeted anti-leukemia drugs azacitidine and decitabine monitored using surface-enhanced Raman scattering (SERS) spectroscopy. Mediterranean Journal of Chemistry, 6(4), 125-132.

Society, R and Engineering, R A o (2004) *Nanoscience and Nanotechnologies: Opportunities and Uncertainties*, Royal Society.

Sperling, R A and Parak, W J (2010) Surface Modification, Functionalization and Bioconjugation of Colloidal Inorganic Nanoparticles. *Philosophical Transactions of the Royal Society A: Mathematical, Physical and Engineering Sciences,* 368(1915), 1333.

Stiles, P L, Dieringer, J A, Shah, N C and Van Duyne, R P (2008) Surface-Enhanced Raman Spectroscopy. *Annu Rev Anal Chem (Palo Alto Calif),* 1, 601-26.

Stobiecka M, Dworakowska B, Jakiela S, Lukasiak A, Chalupa A, Zembrzycki K (2016) Sensing of survivin mRNA in malignant astrocytes using graphene oxide nanocarrier-supported oligonucleotide molecular beacons. Sens. Actuator B-Chem, 235, 136-145.

Suh, H, Jeong, B, Liu, F and Kim, S W (1998) Cellular Uptake Study of Biodegradable Nanoparticles in Vascular Smooth Muscle Cells. *Pharmaceutical Research,* 15(9), 1495-8.

Swain, R J, Kemp, S J, Goldstraw, P, Tetley, T D and Stevens, M M (2010) Assessment of Cell Line Models of Primary Human Cells by Raman Spectral Phenotyping. *Biophysical Journal*, 98(8), 1703-11.

Thomas, G J, Medeiros, G C and Hartman, K A (1971) The Dependence of Raman Scattering on the Conformation of Ribosomal Rna. *Biochemical and Biophysical Research Communications,* 44(3), 587-92.

Tosi, G, Bortot, B, Ruozi, B, Dolcetta, D, Vandelli, M A, Forni, F and Severini, G M (2013) Potential Use of Polymeric Nanoparticles for Drug Delivery across the Blood-Brain Barrier. *Curr Med Chem,* 20(17), 2212-25.

Treuel, L, Jiang, X and Nienhaus, G U (2013) New Views on Cellular Uptake and Trafficking of Manufactured Nanoparticles. *J R Soc Interface,* 10(82), 20120939.

Vega-Avila, E and Pugsley, M K (2011) An Overview of Colorimetric Assay Methods Used to Assess Survival or Proliferation of Mammalian Cells. *Proc West Pharmacol Soc,* 54, 10-4.

Walton, A G, Deveney, M J and Koenig, J L (1970) Raman Spectroscopy of Calcified Tissue. *Calcified Tissue Research,* 6(1), 162-7.

Wang, E C and Wang, A Z (2014) Nanoparticles and Their Applications in Cell and Molecular Biology. *Integrative biology : quantitative biosciences from nano to macro,* 6(1), 9-26.

Zhang, Z, Sheng, S, Wang, R and Sun, M (2016) Tip-Enhanced Raman Spectroscopy. *Analytical Chemistry,* 88(19), 9328-46.

Zheltikov, A M (2000) Coherent Anti-Stokes Raman Scattering: From Proof-of-the-Principle Experiments to Femtosecond Cars and Higher Order Wave-Mixing Generalizations. *Journal of Raman Spectroscopy,* 31(8-9), 653-67.

Zock, J M (2009) Applications of High Content Screening in Life Science Research. *Combinatorial Chemistry & High Throughput Screening*, 12(9), 870-6.

Appendix I: Publications

E. Efeoglu, M. A. Maher, A. Casey, H.J. Byrne, Toxicological Assessment of Nanomaterials: The role of in vitro Raman Microspectroscopic Analysis, (2017), Analytical and Bioanalytical Chemistry, Accepted.

E. Efeoglu, M. A. Maher, A. Casey, H. J. Byrne, Identification of Cell Death Mechanisms based on Raman Spectral Markers of Cyto-/Geno-Toxicity: Comparative Study of Polyamidoamine Dendrimers and Aminated Polystyrene Nanoparticles, (2017), Journal of Biophotonics, Submitted.

E. Efeoglu, A. Casey, H. J. Byrne, Determination of Spectral Markers of Cytotoxicity and Genotoxicity Using Raman Microspectroscopy: Cellular Responses to Polyamidoamine Dendrimers, (2017), Analyst, DOI: 10.1039/C7AN00969K.

E. Efeoglu, M. A. Maher, A. Casey, H. J. Byrne, Label-Free, High Content Screening using Raman Microspectroscopy: The Toxicological Response of Different Cell Lines to Amine-modified Polystyrene Nanoparticles (PS-NH_2), (2017), Analyst, DOI: 10.1039/C7AN00461C.

E. Efeoglu, A. Casey, H. J. Byrne, '*In vitro* monitoring of time and dose dependent cytotoxicity of aminated nanoparticles using Raman spectroscopy', (2016), Analyst 141 (18), 5417-5431.

G. Dadalt Souto, • Z. Farhane, • A. Casey, • E. Efeoglu, • J. McIntyre, • H. J. Byrne, 'Evaluation of cytotoxicity profile and intracellular localisation of doxorubicin-loaded chitosan nanoparticles, (2016), Analytical and Bioanalytical Chemistry, 408 (20), 5443-5455.

E. Efeoglu, M. Keating, J. McIntyre, A. Casey, H. J. Byrne, 'Determination of nanoparticle localisation within subcellular organelles *in vitro* using Raman spectroscopy', (2015), Anal. Methods, 7, 10000–10017.

Appendix II: Seminars and Conferences

Apr 2016	CLIRCON Conference, Manchester, UK. Poster presentation
Sep 2016	SCiX 2016, Minneapolis, Minnesota, USA. Oral presentation
Jun 2016	SPEC 2016, Montreal, Quebec, Canada. Poster presentation
Oct 2015	The 16th European Conference on the Spectroscopy of Biological Molecules (ECSBM), Bochum, Germany. Poster Presentation
April 2015	CLIRSPEC-Clinical Infrared and Raman Spectroscopy for Medical Diagnosis Conference, Exeter, UK. Oral Presentation
Nov 2014	1st Scottish Microscopy Group and Microscopy Society of Ireland Symposium, Glasgow, UK. Poster presentation
Aug 2014	SPEC 2014, Krakow, Poland. Poster presentation
Jun 2014	BIGGS-Biophotonics and Imaging Graduate Summer School
Feb 2014	Annual Meeting of the Irish Cytometry Society, Dublin, Ireland.
Nov 2013	INSPIRE Nanoinduction Week- Introduction to Nanoscience, Dublin, Ireland.